Exploring Stability Landscapes for Optimal Material Design: Application to Wetting of Structured Surfaces

PANTER, JACK,RAMON

Exploring Stability Landscapes for Optimal Material Design: Application to Wetting of Structured Surfaces

Jack Ramon Panter

A thesis submitted for the degree of Doctor of Philosophy

Department of Physics

Durham University

UK

September 2019

Exploring Stability Landscapes for Optimal Material Design: Application to Wetting of Structured Surfaces

Jack Ramon Panter

Abstract

Nature exhibits a diverse and sophisticated range of complex surface micro- and nanostructures which are highly adapted to manipulating liquids. Many exhibit surfaces which are efficient at shedding even wetting or pressurised liquids, self-cleaning, anti-fouling, antimicrobial, abrasion-resistant or able to produce strongly directional liquid motion; properties which are immensely desirable across a broad range of applications, from water purification to absorbent wipes.

Here, optimised surface designs are produced for two wetting applications: superomniphobic surfaces for liquid-repellency, and enclosed fluid diodes for directional flow. In the superomniphobic investigation, we study three key wetting properties: the minimum energy barrier to the breakdown of liquid-repellency, the contact angle hysteresis (liquid mobility), and the critical pressure (maximum sustainable liquid pressure). We then treat all three properties simultaneously to produce optimal superomniphobic designs. In the fluid diode investigation, we study the critical pressures required for liquid to flow into and out of a membrane pore with both chemical and physical gradients. We then maximise the contrast between these two critical pressures, to design pores with optimal liquid directionality.

Previously, two major hurdles have existed to such optimal design. The first is that the wetting properties on complex surface structures feature multiple competing mechanisms, which previously have been inefficient or expensive to investigate. In this thesis, we overcome this by employing and developing computationally efficient, high-dimensional energy landscape methods. The second is that when multiple wetting properties are desired, optimisation of one property can diminish another. We show how this can be overcome through simultaneous optimisation.

Contents

Acknowledgements

First, I would like to thank my supervisor, Dr Halim Kusumaatmaja, for his constant support, insight, guidance in all areas of my academic development. Thanks also to Dr Yonas Gizaw, whose passion for not only wetting phenomena but functional design has been infectious. Further thanks go to Carl M. Jones for re-developing the L-BFGS software so clearly, without which this research would have been significantly more difficult. I would also like to thank a number of researchers for their support in the past four years: Dr Ciro Semprebon and Muhammad Subkhi Sadullah, for fruitful discussions all things wetting; Dr Teng Zhang and Junbo Chen for hosting me in Syracuse, and for the introduction and collaboration on nonlinear buckling phenomena; Prof Glen Mchale, Dr Rodrigo Ledesma-Aguilar, Dr Gary Wells, and their teams at Northumbria University, Dr Marc Pradas, and Dr Matthew Haynes for their significant expertise and collaboration on wetting on patterned SLIPS surfaces.

I would also like to thank my parents for their unfaltering support throughout my entire education. And finally to my wife Paige. My rock. I couldn't have made it nearly this far without you.

Statement of Authorship

I certify that all work described in this thesis is my own research unless otherwise acknowledged in the text or by references and has not been previously submitted for a degree in this or any other university.

Statement of Copyright

Publications

The following published works form the majority of Chapters 3 and 4:

- Panter, J. R. and Kusumaatmaja, H. "The impact of surface geometry, cavitation, and condensation on wetting transitions: posts and reentrant structures", *J. Phys. Condens. Matter*, **29**, 084001, (2017).
- Panter, J. R., Gizaw, Y. and Kusumaatmaja, H. "Multifaceted design optimization for superomniphobic surfaces", *Sci. Adv.*, **5**, eaav7328, (2019).

The following work in Appendix A is currently under review:

- Panter, J. R., Chen, J., Zhang, T. and Kusumaatmaja, H. "The energy landscapes of cylindrical shell buckling".

The following work which forms the majority of Chapter 5 is currently in preparation:

- Panter, J. R., Gizaw, Y. and Kusumaatmaja, H. "Critical pressure asymmetry in the enclosed fluid diode".

Chapter 1

Introduction

1.1 Surfaces of special wettability in nature

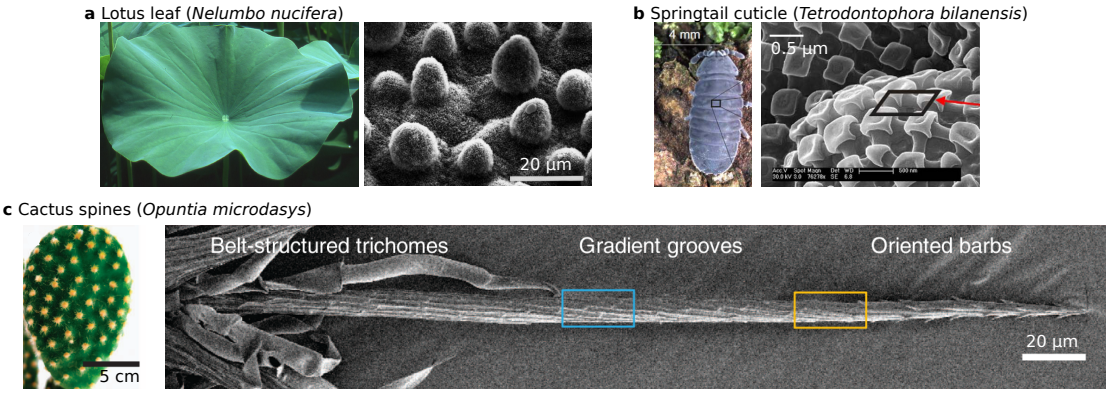

Figure 1.1: (a) Macroscale view of the water-repellent lotus leaf (left) [1], with microscale SEM image of the rough surface (right) [2]. (b) Image of the springtail arthropod (left), with SEM image of the textured skin (right) [3]. (c) The *Opuntia* cactus (left), with SEM image of the textured barb (right) [4].

Nature abounds with surfaces which are highly adapted to the efficient manipulation of liquids, particularly water [5–7]. Throughout this thesis, three organisms shall prove to be mascots for the key wetting phenomena investigated, as shown in Fig. 1.1.

The first is the lotus (*Nelumbo nucifera*), pictured in Fig. 1.1(a), the leaves of which show the extraordinary property of repelling rainwater so effectively that droplets form near-spherical beads on the surface and roll off. This action picks up and removes dust and contaminants from the leaf surface, so that the lotus leaf is self-cleaning, a property termed the lotus-effect [2, 8]. Observed under the scanning electron microscope, as shown in Fig. 1.1(a), the surface of the lotus leaf is found to be textured with a multi-scale rough structure

of wax crystalloids. These structured surface textures inspire investigation in this thesis into water-repellency, and how this repellency breaks down.

The second organism we consider is the springtail, a small, soil-dwelling arthropod which is pictured in 1.1(b). These small organisms typically live in waterlogged environments; however they cannot survive when submerged, as gaseous exchange with the air through their cuticle is required for respiration. The key to their survival is the highly adapted surface micro- and nano-structures on the cuticle surface, which is able to efficiently repel and shed water and even highly-wetting, pressurised liquids; whilst further exhibiting abrasion-resistance and anti-microbial abilities [3, 9–12]. In this thesis, these surfaces inspire the study of wetting of complex geometries under challenging conditions, and how these surfaces can be optimised.

The final organism we consider is the cactus *Opuntia microdasys*, shown in 1.1(c), a closely-studied example of fog-harvesting in plants [4]. In arid desert environments, this species has evolved spines which are able to condense fog into droplets at the tip, which are then directed towards the base for absorption into the storage tissue. The microscale surface texturing of the spine is pivotal to this highly directional liquid motion. We investigate this further in this thesis, to show how directionality can be maximised and exploited for a broad range of applications.

1.2 Chemical aspects of wetting

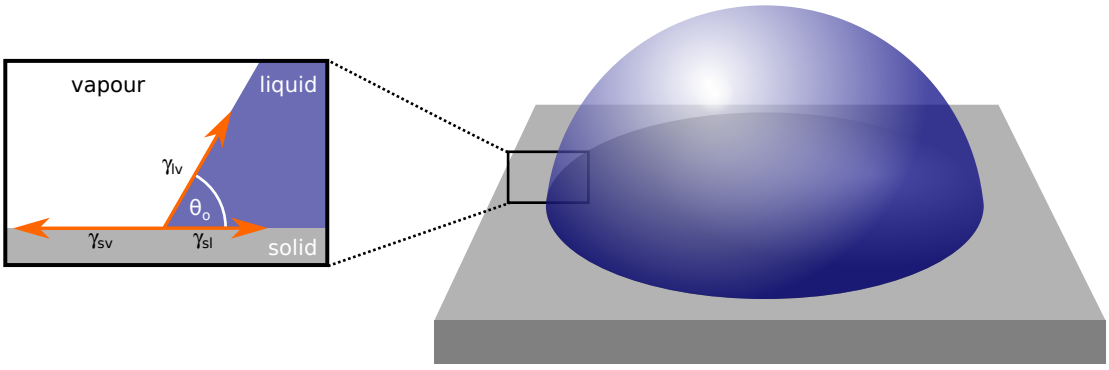

Figure 1.2: Construction of the force balance argument at the three phase contact line for a sessile drop with intrinsic contact angle θ_o.

In order to understand how a surface gives rise to its particular wettability characteristics, we must understand two key aspects: the chemical properties of the surface and the interaction with the contacting fluids, and the physical texturing of the surface. We begin

by summarising the chemical aspect.

In Fig. 1.2, we illustrate a sessile drop on a planar, chemically homogeneous solid surface. The three-phase contact line is defined as the point at which the liquid phase, solid phase and surrounding fluid phase (which we call the vapour phase) meet. The quantification of the contact angle the liquid-vapour interface makes with the solid surface, θ_o, was originally proposed by Thomas Young in 1805, deriving a relationship between θ_o and the surface tensions of the solid-liquid (γ_{sl}), solid-vapour (γ_{sv}) and liquid-vapour (γ_{lv}) interfaces based on the resolution of forces acting at the three-phase contact line [13],

$$\cos\theta_o = \frac{\gamma_{\mathrm{sv}} - \gamma_{\mathrm{sl}}}{\gamma_{\mathrm{lv}}}. \tag{1.1}$$

We now recognise that on the nanoscale the fluid properties change continuously across the interface, with characteristic width ≈1 nm far from the critical point [14], but on much larger scales the interface can be considered to be perfectly sharp. Throughout, we shall typically consider microscale wetting phenomena. Similarly, long-range surface forces are able to distort the interface in the vicinity of the contact line [15], but as this distortion occurs over atomistic ranges, we can accurately model the contact line as meeting the surface with angle θ_o. Another effect which we may neglect by working at the mesoscale is line tension, which is not expected to significantly affect wetting at the contact line above nm length scales [15, 16].

With water droplets, the lotus leaf exhibits contact angles in excess of 150°, but unstructured chemical surfaces cannot approach such high contact angles. Typically, the maximum contact angles are assumed on fluorinated surfaces are ≈ 120° [17]. To achieve larger contact angles than this, we must turn to physical texturing.

1.3 Physical aspects of liquid repellency

1.3.1 Superhydrophobicity

Supended and collapsed states

Far from being a homogeneous surface, the lotus leaf exhibits significant physical texturing, as shown in the scanning electron micrograph of the surface texture in Fig. 1.1(a). Discussions aimed at modifying Young's equation to account for surface heterogeneities were produced

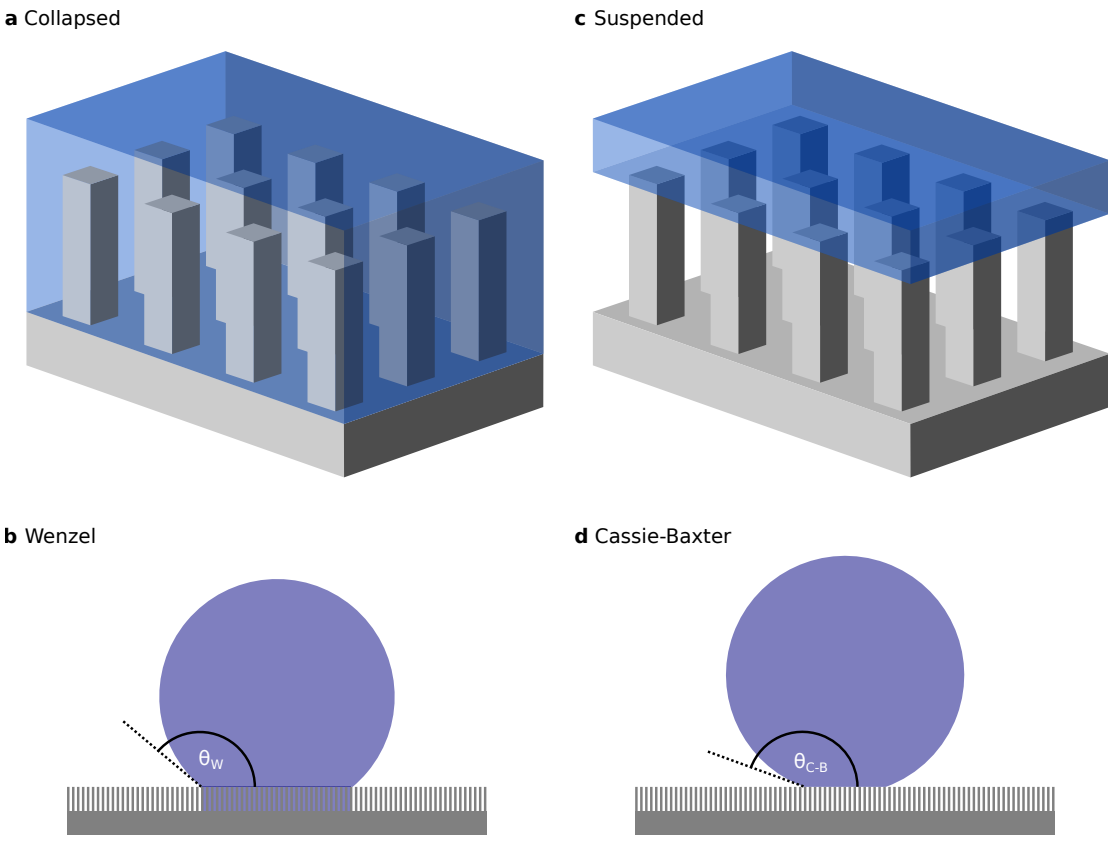

Figure 1.3: (a) Illustration of the collapsed state (i), and the corresponding Wenzel contact angle of a sessile drop (ii). (b) Illustration of the suspended state (i), and the corresponding Cassie-Baxter contact angle of a sessile drop (ii).

initially by Cassie and Baxter [18], and by Wenzel [19]. Wenzel argued that for a physically textured surface, the contact area between the liquid and solid phases is larger than for a droplet of equal contact diameter of a homogeneous surface by a factor r, the roughness factor [19]. It was assumed that the liquid filled the surface texture, as illustrated in Fig. 1.3(a) (which we call the collapsed state for generalised surface structures). This led to the Wenzel equation for determining the contact angle θ_{W} of a sessile droplet in the collapsed state, shown in Fig. 1.3(b), where

$$\cos\theta_{\mathrm{W}} = r\cos\theta_o. \tag{1.2}$$

Unlike the microscopic contact angle θ_o, θ_{W} is a macroscopic contact angle - an effective contact angle measured when the surface structures are much smaller than the length scale of the droplet. For an intrinsically non-wetting surface ($\theta_o > 90°$), $\theta_{\mathrm{W}} > \theta_o$, and for a wetting surface ($\theta_o < 90°$), $\theta_{\mathrm{W}} < \theta_o$.

However, Cassie and Baxter identified a different wetting state for such surfaces, in which the liquid droplet contacted the solid only at the peaks of the surface structures, with the vapour phase residing within the texture [18]. We call this state the suspended state, illustrated in Fig. 1.3(c), although the Cassie-Baxter or fakir states are referred to as well in the literature. The apparent contact angle is therefore reasoned to be a weighted average of the intrinsic contact angles of the materials in contact with the liquid at the base of the drop. The weighting factor of material i, f_i, is the area of material i under the drop projected onto the plane of the surface, relative to the contact area of the drop. Thus, for a droplet in the configuration in Fig. 1.3(d), suspended on the tops of solid pillars of contact angle θ_o with air in between,

$$\cos\theta_{\mathrm{CB}} = f_{solid}\cos\theta_o + f_{air}(-1), \tag{1.3}$$

where $f_{air} = 1 - f_{solid}$, and the contact angle of the drop in air is 180° ($\cos\theta_o = -1$). More recently however, several authors have attempted to correct the erroneous reasoning behind the Cassie-Baxter and Wenzel equations, arguing that there exist no long range interactions between the three phase contact line and the wetting state far from it. As such, the contact angle is determined solely by the surface structure close to the contact line [20, 21].

On minimising the area of solid in contact with the liquid, we see from Eq. (1.3) that contact angles approaching 180° are possible, although $\theta_{\mathrm{CB}} > 150°$ is realised more commonly (see for example [22, 23]). Indeed, a contact angle in excess of 150° has become one of the two de facto characteristics of the *superhydrophobic* state.

Contact angle hysteresis

The second characteristic of a superhydrophobic surface is that the droplet mobility across the texture must be high, manifest as a low-roll off angle, or low contact angle hysteresis. The contact angle hysteresis, CAH, is illustrated in Fig. 1.4. For a sessile droplet on a surface, the equilibrium shape assumed in the absence of external forces is a spherical cap with contact angle θ_o, as shown in Fig. 1.4(a). When a droplet is caused to move across a real surface however, as illustrated in Fig. 1.4(b), the spherical cap shape is distorted: at the advancing (leading) edge of the drop, the advancing contact angle θ_a is greater than θ_o; while at the receding (trailing) edge, the receding contact angle θ_r is less than θ_o. The CAH is defined as

the difference between these advancing and receding contact angles, θ_a and θ_r respectively:

$$\mathrm{CAH} = \theta_\mathrm{a} - \theta_\mathrm{r}. \tag{1.4}$$

θ_a and θ_r are never equal in practice as the contact line will pin to surface defects - either chemical heterogeneities or physical imperfections. Application of a force will distort the contact line up until the point the pinning force is overcome, at which point the sudden relaxation is expected to dissipate energy and slow the motion of a moving drop [15]. This CAH is particularly large for the collapsed (Wenzel) state, caused by a large pinning force arising from the high liquid-solid contact area [24]. For applications which require highly mobile droplets, it is strongly desirable for the collapsed state to be avoided.

In practice, the hysteresis is not measured as illustrated in Fig. 1.4(b). A more reliable methodology is to slowly increase the volume of a droplet on a surface up to the point the contact line moves, defining θ_a, then slowly decrease the volume until the contact line moves, defining θ_r [25].

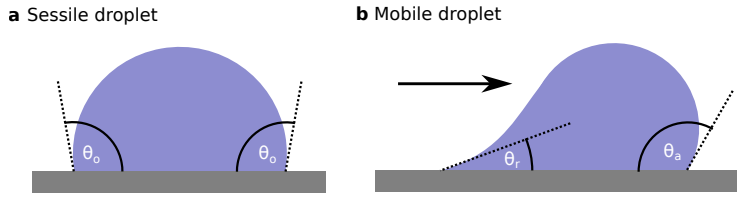

Figure 1.4: (a) Equilibrium spherical cap configuration of a sessile drop. (b) Illustration of the advancing and receding contact angles θ_a and θ_r respectively of a mobile droplet.

Superhydrophobic applications and synthesis

The high contact angle and low CAH (typically less than 10° [23]) of the suspended state means that superhydrophobic surfaces are eminently desirable across a broad range of applications. For example, large scale applications include reducing drag in marine shipping through both the maintenance of high fluid mobility across the surface [26] and reduced biofouling (a significant cause of drag) [27]; as well as for self-cleaning systems, from windows to textiles [28, 29]. Superhydrophobic surfaces are also being investigated in the context of biomedical applications, where a suspended state in implants reduces protein or bacterial adhesion [30, 31] to prevent infection and improve recovery. In small-scale applications, superhydrophobic surfaces are improving the capabilities and performance of microfluidic

devices [32], such as for small-volume biomedical diagnostics [33].

To synthesise superhydrophobic surfaces, myriad materials and techniques have been developed, producing a range of superhydrophobic geometries which numerous reviews are devoted to. To briefly overview the field however, these techniques range from high-performance, precisely-defined geometric structures formed by lithographic techniques (see for example [34]), to stochastic surfaces produced by high-throughput methods such as electrospinning of polymer fibres [29] or nanoparticle deposition [35]. However, increasingly sophisticated and regular surface textures are being developed using, for example, self-assembly of block colopymers [36] and nanotubes [37], or printing techniques [38]. Now, even edible [39] and paper-based structures are being investigated [40].

The collapse transition

Fundamentally, the success of all superhydrophobic applications lies in the ability of physically structured surface textures to maintain the suspended state against transforming into the (usually) more stable collapsed state. This collapse transition can be initiated through a range of external forces: indeed, any perturbation which has the potential to deform the liquid-vapour interface is likely to also precipitate collapse at sufficient strength. Such perturbations include: pressure [41], flow [42], vibration [43], evaporation [44], condensation [45], droplet impact [46], changes to electric [47] or magnetic [48] fields, or thermal fluctuations at the nanoscale [49]. In real-world applications however, several perturbations will be present simultaneously meaning that failure is unlikely to be initiated by only a single perturbation, but instead via their combination.

Several studies have attempted to design surfaces which do not undergo wetting transitions. Two examples have demonstrated how a surface can be patterned with wells so that trapped air is compressed when the transition is attempted, preventing collapse from occurring [50, 51]. However, it was shown that collapse did occur when environmental perturbations (vibrations) were applied [50], meaning true wetting resistance was not achieved. Recently, two studies have instead attempted to destabilise the collapsed state, so that the suspended state can exist indefinitely [52, 53]. One strategy was to show that the addition of a nanoscale texture to a micropillar array effectively accessed contact angles in excess of 135° (when measured on scales much larger than the nanoscale texture), thereby destabilising the collapsed state via wedge-drying [52]. However, it was not shown whether the nanoscale

texture itself exhibited a monostable suspended state. The only study showing true monostability and collapse resistance utilised liquid density functional simulations to show how this time, destabilisation of the collapsed state could be achieved through nano-confinement in nanoscale grooves [53]. However, this still required non-wetting contact angles ($\theta_o = 121°$) to observe this effect, meaning that perfect superhydrophobicity likely remains out of reach for all systems but pure water on pristine fluorinated surfaces.

1.3.2 Superoleophobicity, superamphiphobicity, and superomniphobicity

For liquids which will intrinsically wet a surface ($\theta_o < 90°$), typical of oils, conventional superhydrophobic states break down: the simple post texture has no resistance against collapse. As shall be shown however, through careful design of a surface, even wetting liquids can be maintained in a suspended state. Three terms are frequently used in the literature to describe such suspended states: superoleophobicity [54], describing a specific resistance of a surface against wetting by oils; superamphiphobicity [55], describing a resistance to wetting by both oils and water; and most generally superomniphobicity [56], describing the resistance to wetting by all liquids. Although these three terms have distinct technical definitions, often in the literature they are used interchangeably.

The reentrant and doubly reentrant geometry

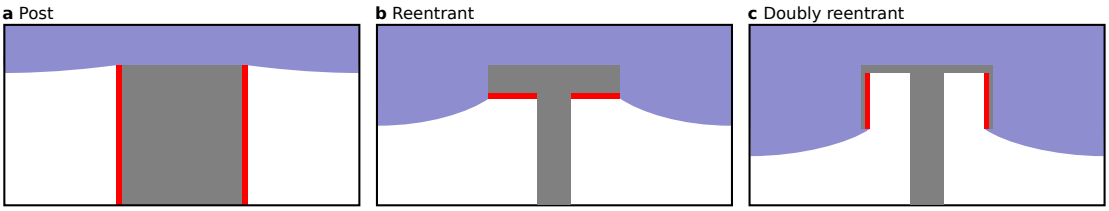

Figure 1.5: (a) The post geometry: a pillar with vertical walls. (b) The reentrant geometry: a pillar with an overhanging cap. (c) The doubly reentrant geometry: A pillar with an undercut cup. Red surfaces highlight the regions relevant for breakdown of the suspended state.

Two promising textures aimed to enable these technologies are the reentrant and doubly reentrant geometries, shown in contrast to the post in Fig. 1.5. The reentrant geometry in Fig. 1.5(b) exhibits an overhanging cap structure, while the doubly reentrant structure in Fig. 1.5(c) advances on this with the addition of a lip structure to the cap. To understand how these additional features enable the reentrant and doubly reentrant geometries to suspend

wetting liquids (unlike the post), we must consider two effects: Gibbs pinning, and Laplace pressure.

The Gibbs pinning criterion

The Gibbs pinning criterion [57] describes the conditions required for a liquid-vapour interface to pin on a solid corner. In Fig. 1.6, this principle is illustrated for a liquid-vapour interface (of intrinsic contact angle θ_o) pinned to a 90° corner. Here, the pinned liquid-vapour interface may take a range of angles β between two extremes. The lower bound is defined as $\beta = \theta_o$, below which the interface will spontaneously depin, and slide to the left. The upper bound is defined as $\beta = \theta_o + 90°$, at which point the interface make an angle of θ_o with respect to the vertical wall. For larger β, the interface will spontaneously depin and slide downwards.

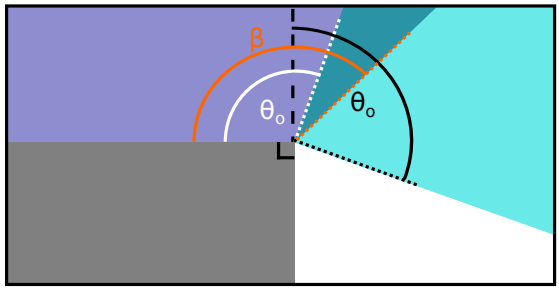

Figure 1.6: Gibbs pinning criterion for pinning on a 90° feature. A liquid-vapour interface of angle β will remain pinned between between two extremes: θ_o, shown in white; and $\theta_o + 90°$, shown in black.

Laplace pressure

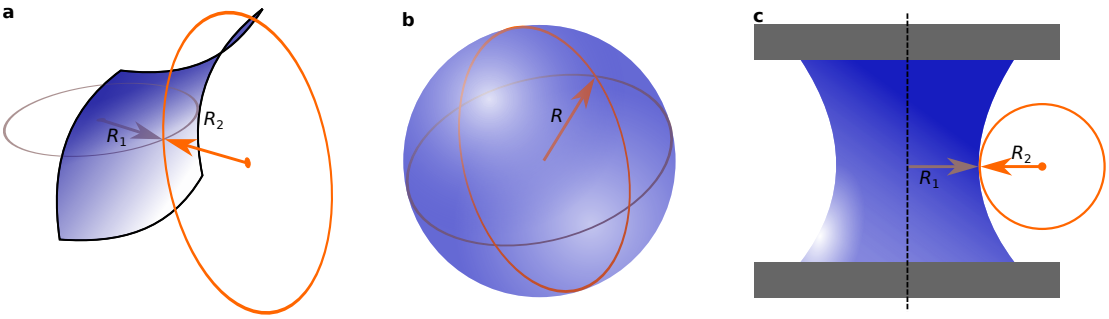

Figure 1.7: (a) General illustration of the two principal radii of curvature, R_1 and R_2, at a point on a surface. (b) The sphere: a surface of constant mean curvature where both principal radii are equal. (c) A capillary bridge: a surface of constant mean curvature where the principal radii are not equal.

In the absence of an external potential acting on the fluids, the Laplace pressure difference

across a liquid-vapour interface was shown by Young and Laplace to arise from the surface tension enacting a stress normal to a curved interface [13, 58], so that in 3D,

$$P_l - P_g = \Delta P = 2\gamma_{\mathrm{lv}} H, \tag{1.5}$$

where P_l, P_g, and ΔP are the liquid pressure, gas pressure and pressure difference respectively. The mean curvature H is calculated from the two principal radii of curvature of a surface, R_1 and R_2, as

$$H = \frac{1}{2}\left(\frac{1}{R_1} + \frac{1}{R_2}\right), \tag{1.6}$$

which is illustrated for a general section of surface in Fig. 1.7(a). Throughout, we define a positive radius of curvature as one which wraps around the liquid phase, while a negative radius wraps around the vapour phase. At mechanical equilibrium, the mean curvature is constant everywhere. As a simple example, for a free surface, a non-zero ΔP will result in a spherical interface, both radii of curvature in this special case being equal everywhere, shown in Fig. 1.7(b). A second example, which will prove to be important throughout this work is the family of Delaunay surfaces. These axisymmetric solutions to the Young-Laplace equation in Eq. (1.5) describe the shapes of capillary bridges that span between two planar boundaries [59], an example of which is illustrated in Fig. 1.7(c).

Stability of the suspended state

We are now able to rationalise how the suspended state is maintained for different geometries. For the post, shown in Fig. 1.5(a), a suspended state is stable against collapse up until the point that the angle the pinned liquid-vapour interface makes with the vertical wall (highlighted in red in Fig. 1.5(a)) is θ_o. For $\theta_o > 90°$, this occurs at a positive Laplace pressure, whereas a negative Laplace pressure would have to be applied for $\theta_o < 90°$. For the reentrant surface shown in Fig. 1.5(b), under conditions where the suspended state would collapse on the post, the interface is able to remain pinned in a suspended state at the bottom of the cap. This suspended state exists up to the point where the pinned interface makes an angle of θ_o with respect to the cap underside, highlighted in red in Fig. 1.5(b). Thus, even for wetting liquids with $\theta_o < 90°$ at positive pressure, a suspended state is maintained. In the limit of a perfectly wetting liquid however ($\theta_o = 0°$), at any positive pressure the suspended state breaks down [60]. It is therefore strictly not correct to describe reentrant geometries

as 'superomniphobic'. Finally, for the doubly reentrant geometry shown in Fig. 1.5(c), the suspended state is stable up until the point where the pinned interface on the inner cap lip makes an angle of θ_o with respect to the inner cap lip, highlighted in red in Fig. 1.5(c). Here, even perfectly wetting liquids may therefore be suspended at positive pressures. A doubly reentrant structure is required for superomniphobicity. Observing the structural changes in Fig. 1.5 from the post, reentrant and doubly reentrant geometry, it could be hypothesised that further improvements in performance could be obtained for even higher generations of the reentrant feature. The triply reentrant geometry as the next generation however offers no benefit over the doubly reentrant geometry, and moreover is more difficult and expensive to fabricate. Triply reentrant structures have been synthesised, but only to guarantee that on pillar deformation the cap always retained a doubly-reentrant nature [61].

Reentrant and doubly reentrant geometries in nature

In Section 1.1, we introduced the springtail cuticle as a natural example of surface texturing. The mushroom-shaped surface features exhibit a doubly reentrant geometry, allowing even highly-wetting liquids to be repelled from the skin [10]. This may be important for life in waterlogged soils, in which water incident on the skin may be contaminated with a variety of organic or inorganic compounds which both lowers the surface tension of water, and decreases θ_o. As an aside, it is tempting to be led into thinking that doubly reentrant geometries are bio-inspired by the springtail cuticle - but this is not true. Instead, the doubly reentrant geometry was conceived in the 80's through rational design methods in an effort to control nucleate boiling in heat transfer applications [62, 63]; the doubly reentrant geometry on the springtail was not realised until 2011 [3].

Surprisingly, despite being an emblem of superhydrophobicity, it has also been revealed that the lotus effect is not actually caused by a hydrophobic pillared structured [64]. It was found that the surface waxes are actually hydrophilic ($\theta_o \approx 74^\circ$). The superhydrophobicity is instead caused by hair-like structures in the wax creating reentrant features, which are able to suspend water even though it wets an unstructured surface.

As a final example, bacterial biofilms (colonies of *Bacillus subtilis*) have been observed to be repellent to even low-surface tension liquids [65]. Instead of hairs or surface pillars, the biofilm was shown to be highly wrinkled and folded over several length scales, which created the reentrant structure required for suspesion of wetting liquids. Overall, these examples

highlight the diverse strategies for creating reentrant structures and extreme liquid repellency across several phylogenetic kingdoms.

Applications and synthesis of reentrant and doubly reentrant geometries

As the most general liquid-repellent texture, superomniphobic surfaces have significant potential to be transformative across a broad array of important applications. Examples range from tackling current global-scale crises, via sustainable technologies for water purification [66, 67] and anti-microbial surfaces in biomedicine [68, 69], through everyday applications such as anti-fingerprint coatings [70] and packaging designed to reduce food waste [39], to digital microfluidics as a versatile biological and chemical technology [71].

Reentrant and particularly doubly reentrant surface textures currently represent the forefront in complex surface texture fabrication methods, due to the requirement of creating undercut structures. However, a number of innovative approaches have been developed (many of which can be found in the recent review [72]). For doubly reentrant geometries, lithographic methods are currently time-consuming and expensive to perform: the first true doubly reentrant structure synthesised on a silicon wafer in 2014 [60] required seven steps, including etching, patterning and thermal oxidation. Recently, although the number of synthesis steps has not decreased, sub-micron fabrication has been achieved to faithfully replicate the springtail cuticle [73]. Two further techniques have been used successfully: fluidisation of the top of polymer micropillars to create an overhanging, undercut cap [74]; and 3D printing [61]. However high-throughput and scalable techniques are yet to emerge. Greater success is to be found for manufacturing the simpler reentrant structures, as random porous textures of particles readily show reentrant pores (a notable example was synthesised by soot deposition from a candle flame onto a glass slide [75]). However, an open problem remains in manufacturing overhanging, undercut geometries which are mechanically stable to impacts and abrasion for real-world applications [76, 77].

1.4 Surface gradients and directional flow

So far we have considered surfaces with uniform physical and chemical properties over a macroscopic area. We now extend our interest to consider surfaces which have a local gradient in these properties, which favour directional liquid motion. Surfaces which bias the direction

of liquid flow are often referred to as fluid diodes [78] or fluid rectifiers [79]. As terrestrial life is highly adapted to manipulate water, it is little of surprise that a vast range of different fluid diodes are exhibited in nature (see [80] for a comprehensive review). Examples include the textured conical spines of the cactus *Opuntia microdasys* [4], shown in Fig. 1.1(c); but also the spindle-knots of spider silks [81], and the ratcheted surface of butterfly wings [82].

Inspired by these naturally occurring strategies, there is a significant interest in developing synthetic analogues for use across many different fields of applications [83]. These fields range from environmental and sustainable strategies [84], with principal applications such as oil-water separation [85], oil spill clean-up [86], and water purification or fog harvesting [87]; to microfluidic systems, for chemical synthesis [88] and bio(chemical) analysis [89]. Matching this breadth of applications, fluid diodes are not limited to a single geometry but show a diverse range, such as across surface structures [90], along porous strips [91], and within microfluidic channels [92–95]; although currently the predominant interest is in through-thickness designs for manufacturability and scalability (see for example [85, 86, 96–98]).

The fluid diode functions through the creation of a unidirectional driving force acting on a liquid. This is caused by asymmetry in the chemical and physical structure experienced by the fluid within the diode. A chemical gradient under a liquid droplet results in a driving force due to the gradient in surface energy [15, 99–101]. Meanwhile, driving forces due to the physical structure arise from two causes. In the first case, a smooth change in surface curvature creates a Laplace pressure difference across a droplet such as on conical surfaces [102, 103] - a strategy employed by *Opuntia* cactus spines [4]. In the second case, a ratcheted structure, in which a difference in pinning forces acts on a fluid-air interface, favours unidirectional liquid propagation [104] - a strategy employed for example by fleas [105] and the Texas horned lizard [106].

1.5 Thesis outline

Throughout this thesis, theoretical techniques and computational simulations are developed and utilised in order to explore and optimise the stability landscapes in soft-matter systems. This is applied in particular to the optimal design of surfaces for surface wettability applications.

In Chapter 2, we discuss in detail the concept of free energy landscapes which feature

multistable states, with special focus on the binary fluidic model used in simulations. We then introduce the general computational techniques for finding these free energy minima in high-dimensional energy landscapes, as well as the pathways between them.

Chapter 3 employs the energy landscape methods to study the free energy landscape of wetting on complex geometries: posts, reentrant and doubly reentrant structures. We will explore the stable states in the landscape, before showing the multiple possible collapse mechanisms. We end Chapter 3 with a comprehensive survey of how the structural and chemical properties of the texture affect the wetting transition.

Following on from this, in Chapter 4 we consider two further important wetting properties on structured surfaces: the CAH and critical pressure. These properties are both systematically surveyed over the range of structural parameters of the reentrant and doubly reentrant geometries. We then combine the surveys from Chapter 3 and Chapter 4 to demonstrate how surfaces can be designed with optimal wetting properties.

In Chapter 5, we then move from surfaces of uniform wetting properties, to consider how physical and chemical gradients combine to direct liquid motion through a fluid diode. The key outcome will be to show how both gradients can be tailored to impart maximum asymmetry across the diode: in that liquid is spontaneously imbibed across the diode membrane in one direction, but faces a large pressure barrier to transport across the membrane in the reverse direction.

Finally, the results presented in this thesis are summarised in Chapter 6, in which we also discuss perspectives for future research.

However, the methods and techniques applied throughout to wetting on structured surfaces are general to many problems which can be represented through high-dimensional energy landscapes. This is demonstrated in Appendix A, where we investigate the minima and transition pathways in buckled elastic shells. This is then exploited to design the energy landscape in order to exert control over the buckling responses.

Chapter 2

Methods for exploring the energy landscapes

In this chapter, we begin by introducing the concept and utility of free energy landscape methods to explore continuum bifluidic systems interacting with solid surfaces. Two principal features of the landscape we investigate in the results chapters are the free energy minima, and the pathways through the landscape between these minima.

In Section 2.1, we construct the free energy of a bifluidic system interacting with a solid surface. We wish to construct a model which is applicable generally, in which it is facile to simulate complex fluid-fluid interfaces of arbitrary topology, as well as complex surface structures. To study complex fluid morphologies, we choose the diffuse interface model initially proposed by van der Waals in 1893 [107], but advanced notably by Cahn and Hilliard [108], and more recently by Jacqmin [109], Briant and Yeomans [110, 111], among others. Diffuse interface models describe a multi-phase system through an order parameter which changes continuously across an interface. Their principal advantage over sharp interface models is that the interfaces do not need to be explicitly tracked, nor are special treatments required to deal with the topological singularities that occur when sharp interfaces split or merge [112]. To study the interaction of the bifluidic system with complex surface geometries, in Section 2.1 we also pay special attention to the boundary conditions imposed by the solid surface.

In Section 2.2, we introduce the algorithms used to efficiently find the minima in the high-dimensional free energy landscapes. In particular, we describe how the limited-memory Broyden-Fletcher-Goldfarb-Shanno (L-BFGS) algorithm [113, 114] enables computational efficiency on two fronts, through reducing both the number of operations required and the memory requirements.

Over a range of simulation parameters, the results chapters demonstrate multistability in the landscape: many minima coexist as stable or metastable states simultaneously. In Section 2.3, we describe the algorithms we use to investigate how these states transform into each other via minimum energy pathways (MEPs). An MEP is a pathway between two minima which passes through at least one index-one saddle point (the transition state) - a stationary point on the landscape with exactly one negative eigenvalue. Descending from the saddle point in both directions via the steepest descent paths, a connected minimum-transition state-minimum triplet is formed. Note that along the steepest descent paths, the local path tangent vector lies along the gradient of the underlying landscape. In general, an MEP may pass through several minima and transition states, such that an MEP is a union of triplets [115]. It is also important to note that a system evolving along an MEP evolves quasi-statically: in the context considered here therefore, the pathway does not depend on the dynamic fluid properties.

As the restriction of following the fluid dynamics physically is removed, finding free energy minima and pathways in the landscape is made more efficient than in explicit fluid-dynamics solvers. For simulating multiphase or multicomponent fluid flow, a variety of approaches are employed. Molecular dynamics or dissipative particle dynamics [116, 117] are well-suited for nanoscale systems, but mesoscale methods include the lattice Boltzmann method [118], and smoothed-particle hydrodynamics [119].

The transition state (TS) has special significance in this quasi-static regime, with direct implications for engineering applications. As the maximum energy point along the minimum energy pathway, the minimum-TS energy barrier provides an absolute lower bound to the energy required to be input into the system to achieve the transition. In real-world applications in which a system is subject to random perturbations, if the energy supplied to the system is never larger than this barrier, the system will remain in the initial minimum indefinitely. As will be shown in the results chapters, this is important for applications in which we would like to preserve the state of a system against transitioning. In Section 2.4, we show how, starting from our estimation of the MEP, we may precisely locate the TS. We go on to develop a method for performing this TS location efficiently over wide ranges of parameter space while minimising the number of computationally-expensive path-finding algorithms required.

2.1 The free energy functional

The bifluidic, diffuse interface potential used throughout has the general form,

$$E[\phi] = E_i[\phi] + E_s[\phi] + E_P[\phi], \tag{2.1}$$

where here the free energy E has been decomposed into the sum of isotropic, surface-interaction, and pressure terms E_i, E_s, and E_P respectively. Each term shall soon be discussed separately. As in [120], the scalar order parameter $\phi(\mathbf{r})$ is chosen to represent the local composition at each point $\mathbf{r}$ in space. Although throughout we shall refer to the two fluids as 'liquid' and 'vapour', the analysis and discussions are equally applicable to any pair of immiscible fluids.

2.1.1 E_i - bulk and interfacial energies

E_i is the free energy contribution arising from an isotropic multiphase system [108],

$$E_i[\phi] = \int_V \left(\psi_b + \frac{\epsilon}{2}|\boldsymbol{\nabla}\phi|^2\right) dV, \tag{2.2}$$

in which the first term of the integrand is a Landau-type free energy density for a homogeneous (bulk) system $\psi_b = \frac{1}{\epsilon}\left(\frac{1}{4}\phi^4 - \frac{1}{2}\phi^2\right)$. Minima in this potential occur at $\phi = 1$, which we shall refer to as the pure liquid phase, and $\phi = -1$ referred to as the pure vapour phase. When the system is inhomogeneous, the second term of the integrand energetically penalises the formation of fluid-fluid interfaces through associating an energy density to gradients in the composition.

Both the liquid-vapour interfacial tension γ_{lv} and composition profile across the diffuse interface can be derived by minimising Eq. (2.2), this is done for example in [121, 122]. Assuming a planar interface (so that we can effectively reduce Eq. (2.2) to one dimension), at equilibrium,

$$\frac{dE_i[\phi]}{d\phi} = \mu = \frac{1}{\epsilon}(\phi^3 - \phi) - \epsilon\frac{d^2\phi}{dx^2} = 0, \tag{2.3}$$

where μ is the chemical potential. This admits the solution for the interfacial profile,

$$\phi(x) = \tanh\left(\frac{x}{\sqrt{2}\epsilon}\right). \tag{2.4}$$

The parameter ϵ therefore defines the width of the liquid-vapour interface. Experimentally, the width of the liquid-vapour interface varies from ≈1 nm far from the critical point [14], to ≈100 nm close to the critical point [123]. Treating ϵ as a physical width would limit phase-field models to nanoscale systems. We can perform mesoscale simulations however by ensuring that the simulated system size (and features therein) are much larger than ϵ. This separation of length scales ensures that mesoscale phenomena observed are not dominated by the finite width of the interface.

Finally, the surface tension is calculated by computing the excess free energy per unit area associated with the compositional gradient at the interface, as done in [122] for example, so that

$$\gamma_{\mathrm{lv}} = \sqrt{\frac{8}{9}}. \tag{2.5}$$

2.1.2 E_s - fluid-surface interaction energy

According to Cahn [124], treating the fluid-surface interactions as short range enables the solid-liquid interaction energy E_s to be approximated as an integral over the surface,

$$E_s = \int_S \psi_s dS. \tag{2.6}$$

A number of choices exist in how to define the surface energy density ψ_s so long as the two following conditions for μ and ϕ at the surface are satisfied [109]: (1) $\boldsymbol{\nabla}\mu \cdot \widehat{\mathbf{n}} = 0$, (2) $\epsilon\boldsymbol{\nabla}\phi \cdot \widehat{\mathbf{n}} + \partial\psi_s/\partial\phi_s = 0$. The first (zero-flux) condition ensures that there is no gradient in the chemical potential perpendicular to the solid boundary. Here, $\widehat{\mathbf{n}}$ is the local normal vector to the solid surface. The second condition arises when minimising the free energy in Eq. (2.1), shown in [125].

To a first approximation, the surface energy density is represented as $\psi_s = -h\phi_s$ [124,126]. ϕ_s is the value of the order parameter at the surface. Regarding condition (2), the effect of this is to impose a composition profile with a constant gradient of $-\frac{h}{\epsilon}$ normal to the surface. The wetting potential h sets the contact angle of a liquid droplet on a planar surface θ_o through

$$h = \mathrm{sign}\left(\frac{\pi}{2} - \theta_{\mathrm{o}}\right)\sqrt{2\cos\left(\frac{\alpha}{3}\right)\left[1 - \cos\left(\frac{\alpha}{3}\right)\right]}, \tag{2.7}$$

where $\alpha = \arccos(\sin\theta_o)$ and the function 'sign' returns the sign of the argument [127].

The solid-liquid and solid-vapour surface tensions, $\gamma_{\mathrm{sl}}, \gamma_{\mathrm{sv}}$, can be derived by considering

the excess bulk free energy density in the presence of a solid surface [122],

$$\gamma_{\mathrm{sl}} = \frac{\gamma_{\mathrm{lv}}}{2}\left(1 - (1+\sqrt{2}h)^{3/2}\right), \tag{2.8}$$

$$\gamma_{\mathrm{sv}} = \frac{\gamma_{\mathrm{lv}}}{2}\left(1 - (1-\sqrt{2}h)^{3/2}\right). \tag{2.9}$$

One feature of the linear model $\psi_s = -h\phi_s$, is that local enrichment of either phase may occur at the surface. To evaluate the magnitude of this enrichment, the order parameter at the surface can be solved, as in [118], yielding the set of solutions $\phi_s = \pm\sqrt{1 \pm \sqrt{2}h}$. Choosing the physical solutions, this means that liquid on a surface with contact angle $\theta_o = 0^\circ$ has $\phi_s \approx 1.30$, and liquid on a surface with contact angle $\theta_o = 180^\circ$ has $\phi_s \approx 0.56$ (compare these values to the bulk equilibrium value $\phi = 1$). Although this enrichment is more detrimental for dynamic simulations due to the generation of non-physical wall layers [109], in static simulations the accuracy of the contact angle is reduced, and the liquid-vapour interface shape is modified in the vicinity of the three-phase contact line. These effects are explored further at the end of this section.

To nullify local enrichment, we also implement a cubic expansion of the surface energy density, based on [128], where

$$\psi_s = g(-\phi_s^3/6 + \phi_s/2 + 1/3). \tag{2.10}$$

The derivative,

$$d\psi_s/d\phi_s = g(-\phi_s^2/2 + 1/2), \tag{2.11}$$

is minimised to zero when $\phi_s = \pm 1$. Thus, at equilibrium the surface composition is the same as in the bulk, so that no enrichment occurs. It is now facile to compute the solid-liquid and solid-vapour surface tensions:

$$\gamma_{\mathrm{sl}} = -\frac{1}{4\epsilon} + \frac{2}{3}g, \tag{2.12}$$

$$\gamma_{\mathrm{sv}} = -\frac{1}{4\epsilon}, \tag{2.13}$$

and using Young's equation, $\gamma_{\mathrm{lv}}\cos\theta_o = \gamma_{\mathrm{sv}} - \gamma_{\mathrm{sl}}$, this yields the relationship between the prescribed contact angle and g,

$$g = -\sqrt{2}\cos\theta_o. \tag{2.14}$$

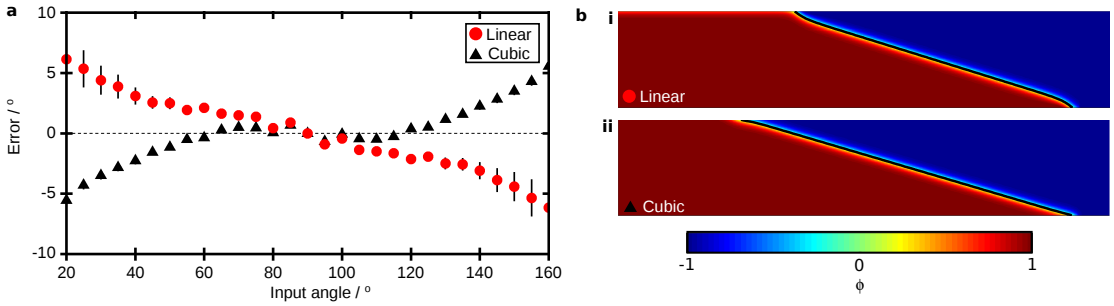

Figure 2.1: Comparison of the linear and cubic surface boundary conditions. **a** Accuracy of both models in reproducing the input contact angle. Error bars indicate the standard error in the linear fit to the contact line gradient. **b** Images of the phase field at an input angle of 20° for: **i** the linear model, **ii** the cubic model.

In Fig. 2.1, we compare the linear and cubic surface boundary conditions. In the 2D simulation setup, we pin the liquid-vapour interface to a point in the bottom of the channel, and vary the prescribed input angle at the top of the channel. The contact angle is then measured by fitting a straight line to the interface (the $\phi = 0$ contour) in the vicinity of the three-phase contact line. The difference between the input angle and measured angle is shown in Fig 2.1a, labelled 'error'. In all cases, the cubic surface treatment is more accurate by up to 2°. The difference between the linear and cubic models is made most apparent however in Fig. 2.1b, in which the equilibrium phase fields are imaged at the input angle $\theta_o = 20°$. Here, the local enrichment in the linear model distorts the liquid-vapour interface in the vicinity of the contact line, whereas the interface in the cubic system remains largely unaffected. A number of other different forms of ψ_s are trailed in [129], but the linear and cubic models maintain competitive accuracy in static simulations.

2.1.3 E_P - imposed pressure difference across the fluid interface

Finally, the effect of pressurising the system is incorporated into the free energy functional through the addition of the term $E_P = -P_l V_l - P_v V_v$. The liquid and vapour pressures are denoted P_l and P_v respectively, and volumes V_l and V_v respectively. Within this phase field model,

$$V_l = \int_V \frac{\phi + 1}{2} dV, \tag{2.15}$$

and by using $V_v = V - V_l$ and $\Delta P = P_l - P_v$, with V as the simulation volume, the pressure terms can be rearranged into the form $-\Delta P V_l + P_v V$, where ΔP is the Laplace pressure difference across the interface. Throughout, $P_v V$ is chosen as a reference energy, against

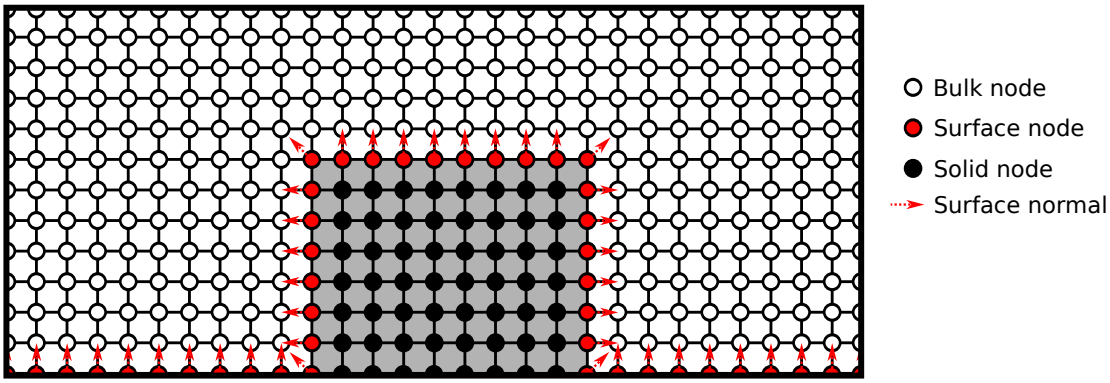

Figure 2.2: 2D slice through a 3D computational domain, showing the cubic discretisation mesh, the three node types, and the direction of surface normals. The shaded grey box marks the location of a post feature on the surface.

which all energies are reported.

2.1.4 Discretisation

To minimise $E[\phi]$ in Eq. 2.1 for general fluid configurations and solid boundary conditions, the computational domain is discretized into a $N_x \times N_y \times N_z$ cubic lattice of points (nodes). Each node is associated with a value ϕ_{ijk}, where $i, j, k \in \{1, ..., N_{x,y,z}\}$. A spatial separation between adjacent points is defined, labelled G. These nodes are classified according to whether they are at the surface of a solid boundary (surface nodes), within the solid (solid nodes), or within the bulk system (bulk nodes). Although the solid nodes are always assigned an initial ϕ, they do not contribute to the free energy or the free energy gradients of the system, and are not updated in the energy minimisation. The surface nodes are each assigned a normal vector $\widehat{\boldsymbol{n}}$. At edges and vertices of the structure, the direction of the normal is defined as the average of the normals of the incident planes. The node arrangement and assignment is illustrated in Fig. 2.2.

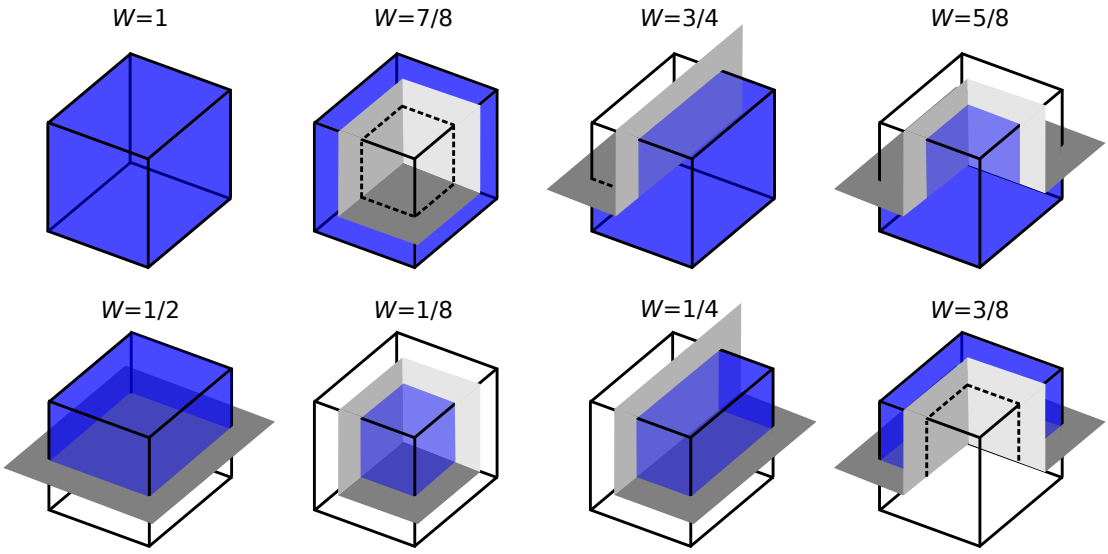

Figure 2.3: Visualisations of the surface structures leading to the node weights W_{ijk}. Each cube has side length G, and is centred on a node. Blue regions indicate the fluid -filled volume, while unfilled regions are inside the solid

$E[\phi]$ in Eq. 2.1 is discretized term by term as follows:

$$\int_V \psi_b dV \rightarrow \sum_{ijk} \frac{1}{\epsilon}\left(\frac{1}{4}\phi_{ijk}^4 - \frac{1}{2}\phi_{ijk}^2\right) W_{ijk} G^3, \tag{2.16}$$

$$\int_V \frac{\epsilon}{2}|\boldsymbol{\nabla}\phi|^2 dV \rightarrow \sum_{ijk} \frac{\epsilon}{2}\left(\left(\frac{\partial \phi_{ijk}}{\partial x}\right)^2 + \left(\frac{\partial \phi_{ijk}}{\partial y}\right)^2 + \left(\frac{\partial \phi_{ijk}}{\partial z}\right)^2\right) W_{ijk} G^3, \tag{2.17}$$

$$\int_S \psi_S dS \rightarrow \sum_{\text{surface}} -h\phi_{ijk} S_{ijk} G^2 \quad \text{or} \quad \sum_{\text{surface}} g\left(-\frac{1}{6}\phi_{ijk}^3 + \frac{1}{2}\phi_{ijk} + \frac{1}{3}\right) S_{ijk} G^2, \tag{2.18}$$

$$\Delta P V_l \rightarrow \Delta P \sum_{ijk} \frac{\phi_{ijk}+1}{2} W_{ijk} G^3. \tag{2.19}$$

The volume weights W_{ijk} describe the fraction of the volume associated with each node that lies outside a solid surface, illustrated in Fig.2.3. For all bulk nodes, $W_{ijk} = 1$, but for surface nodes, $W_{ijk} < 1$ and depends on the local surface structure. The surface weights S_{ijk} describe the surface area associated with each node, in units of G.

Here, the spatial derivatives are approximated using a stencil accurate to second order to avoid the checkerboard instability [120], calculated as,

$$\left(\frac{\partial \phi_{ijk}}{\partial x}\right)^2 = \frac{1}{2G^2}\left(\left(\phi_{(i+1)jk} - \phi_{ijk}\right)^2 + \left(\left(\phi_{(i-1)jk} - \phi_{ijk}\right)^2\right)\right). \tag{2.20}$$

When the simulation boundaries are not capped by solid surfaces, periodic boundary conditions are employed in the x and y directions (in the plane of the surface texture). In

the z-direction, perpendicular to the texture plane, the z-gradient at $k = N_z$ is fixed at zero. This enforces bulk fluid behaviour at the top of the system.

Overall, the gradient in the free energy with respect to the order parameter at each node can be computed:

$$\frac{\partial E}{\partial \phi_{ijk}} = \frac{\partial E_i}{\partial \phi_{ijk}} + \frac{\partial E_s}{\partial \phi_{ijk}} - \Delta P \frac{\partial V}{\partial \phi_{ijk}}, \tag{2.21}$$

where we explicitly differentiate the discretised equations with respect to ϕ_{ijk}.

2.2 Free energy minimisation

In order to capture the interaction of the bifluidic system with complex surface geometries precisely, the computational domain will be discretised into ≈ 100 lattice points in each dimension. Typically, this results in systems with $10^5 - 10^6$ independent ϕ_{ijk}, each representing a degree of freedom.

To efficiently minimise systems containing such large numbers of degrees of freedom, we employ the limited-memory Broyden-Fletcher-Goldfarb-Shanno (L-BFGS) algorithm [113, 114]. This algorithm is efficient in both computational time and memory usage. Detailed analyses of how this algorithm is formed are reported elsewhere (see for example [130]), but as the L-BFGS algorithm is foundational to many of the applications presented here, we shall now examine a brief overview.

Beginning with the Newton method for multivariate optimisation: we begin by evaluating the optimisation function f of coordinate vector $\boldsymbol{x_n}$, where n is the iteration index. Taking a step $\boldsymbol{\Delta x}$ away from $\boldsymbol{x_n}$, the new value of f is approximated to second order as,

$$f(\boldsymbol{x_n} + \boldsymbol{\Delta x}) \approx f(\boldsymbol{x_n}) + \boldsymbol{\nabla} f(\boldsymbol{x_n})^{\mathrm{T}} \boldsymbol{\Delta x} + \frac{1}{2} \boldsymbol{\Delta x}^{\mathrm{T}} H \boldsymbol{\Delta x}, \tag{2.22}$$

and the new gradient of f is approximated as,

$$\boldsymbol{\nabla} f(\boldsymbol{x_n} + \boldsymbol{\Delta x}) \approx \boldsymbol{\nabla} f(\boldsymbol{x_n}) + H \boldsymbol{\Delta x}, \tag{2.23}$$

where H is the Hessian matrix.

To locate stationary points of f, we attempt to find the $\boldsymbol{x_n}$ for which the gradient $\boldsymbol{\nabla} f(\boldsymbol{x_n})$ $= 0$. Given the quadratic approximation to the local behaviour of f, the optimal step $\boldsymbol{\Delta x}$ is

found from Eq. (2.23) by setting the updated gradient, $\boldsymbol{\nabla} f(\boldsymbol{x_n} + \boldsymbol{\Delta x})$ to zero. This yields,

$$\boldsymbol{\Delta x} = -H^{-1} \boldsymbol{\nabla} f(\boldsymbol{x_n}). \tag{2.24}$$

In practice, f may not be quadratic, so that several iterations of taking a step and approximating the next step will be required to approach $\boldsymbol{\nabla} f(\boldsymbol{x_n}) = 0$ to within some tolerance.

For large systems (where the number of elements of $\boldsymbol{x_n}$ is large), this algorithm becomes computationally inefficient due to the necessity of both calculating H and H^{-1}, and storing such large matrices. Quasi-Newton methods alleviate the first issue by iteratively updating an approximate Hessian (denoted B) using the $\boldsymbol{\nabla} f(\boldsymbol{x_n})$ throughout the optimisation process. In such methods, B is chosen to satisfy the secant equation,

$$\boldsymbol{\nabla} f(\boldsymbol{x_n} + \boldsymbol{\Delta x}) = \boldsymbol{\nabla} f(\boldsymbol{x_n}) + B \boldsymbol{\Delta x}. \tag{2.25}$$

The BFGS algorithm provides a effective method for performing the updates to B at each iteration step [131]. Finally, the limited-memory version of the BFGS algorithm removes the problem of storing the large matrix B. Instead, only the past m coordinate and gradient updates are stored, which can be used to perform future approximate Hessian updates without ever forming B itself [113]. One important feature of the L-BFGS updates is that B remains positive-definite throughout, such that only minima of f (with all positive eigenvalues) can be converged upon. This means that the algorithm will never converge on saddle points (with one negative eigenvalue) and higher-index saddle points (more than one negative eigenvalue), unless the initial position $\boldsymbol{x_0}$ is exactly located at one of these points.

2.3 Path finding

To compute the MEP between two minima in the landscape, a broad range of path finding algorithms have been proposed and used [115]. Here, we overview two of the most competitive double-ended search algorithms: the doubly-nudged elastic band (DNEB) algorithm [132, 133], and the simplified string method [134]. Both of these algorithms are used to compute the MEPs in the results chapters, giving equivalent results. In some cases, such as the paper presented in Appendix A, the string method is found to be more reliable.

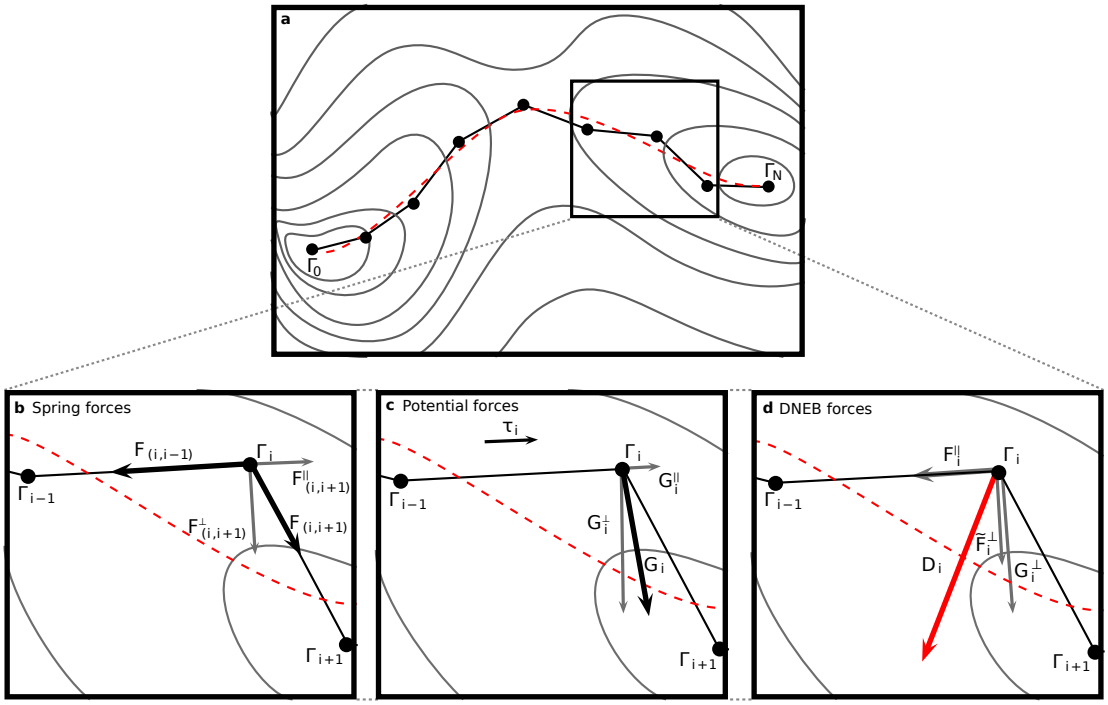

Figure 2.4: Illustration of the construction of the DNEB force at image $\mathbf{\Gamma}_i$, $\mathbf{D}_i$. (a) An example contour plot of the underlying free energy surface, showing a snapshot of the chain of images (black circles) as they are evolved towards the true MEP (red, dashed). (b) The parallel ($\mathbf{F}_i^{\parallel}$) and perpendicular ($\mathbf{F}_i^{\perp}$) components of the spring force ($\mathbf{F}_i$) acting on $\mathbf{\Gamma}_i$. (c) The parallel ($\mathbf{G}_i^{\parallel}$) and perpendicular ($\mathbf{G}_i^{\perp}$) components of the force ($\mathbf{G}_i$) due to $\boldsymbol{\nabla} E$. (d) The force components which contribute to the overall DNEB force $\mathbf{D}_i$, shown as the red vector.

2.3.1 Doubly nudged elastic band algorithm

The first method employed is the doubly-nudged elastic band (DNEB) algorithm [132, 133], used within the program OPTIM [135]. Fig. 2.4 illustrates the principles of the algorithm. The DNEB method is a double-ended chain of states method, in which an MEP between two known endpoints is found. We begin by initialising a discrete chain of images $\{\mathbf{\Gamma}_1, ..., \mathbf{\Gamma}_N\}$ (replicas of the system) across the free energy landscape between the two fixed endpoints $\mathbf{\Gamma}_0$ and $\mathbf{\Gamma}_N$. This chain of images is evolved evolved by enacting a force between them which favours convergence to the MEP [133]. An illustrative setup is shown in Fig. 2.4a, in which a chain of images (black) approximates the true MEP (red-dashed).

The DNEB force is constructed sequentially as follows. To begin with, if we evolved each image according to only the local gradient of the free energy landscape $-\boldsymbol{\nabla} E$, this would result in all images sliding towards the minima. Hence, an elastic interaction potential is applied between adjacent images, such that the elastic potential energy associated with

image i is the sum of the interactions with images $i-1$ and $i+1$,

$$V_i^{\text{spring}} = \frac{k}{2}\left[(\mathbf{\Gamma}_i - \mathbf{\Gamma}_{i-1})^2 + (\mathbf{\Gamma}_{i+1} - \mathbf{\Gamma}_i)^2\right]. \tag{2.26}$$

However, such a potential cannot be expected to result in the close convergence of the images to the true MEP, due to the interaction between the spring potential and the true potential. If the spring force constant k is too large, the true energy at each point on the path is overestimated, and in curved regions the chain will cut the corner. If k is too small, the images will tend to slide towards the landscape minima, leaving a low resolution about the transition states [136].

In the original nudged elastic band (NEB) formulation, this effect was reduced by considering the components of the spring force and $-\boldsymbol{\nabla}E$ in the directions parallel to and perpendicular to the tangent vector $\widehat{\boldsymbol{\tau}}_i$ between each image, illustrated in Fig.2.4b and c. The components of the elastic force acting on image i, F_i, are

$$\mathbf{F}_i^{\parallel} = \left(-\boldsymbol{\nabla}V_i^{\text{spring}} \cdot \widehat{\boldsymbol{\tau}}_i\right)\widehat{\boldsymbol{\tau}}_i, \tag{2.27}$$

$$\mathbf{F}_i^{\perp} = -\boldsymbol{\nabla}V_i^{\text{spring}} - \mathbf{F}_i^{\parallel}, \tag{2.28}$$

and the components of the force from the underlying free energy, $\mathbf{G}_i = \boldsymbol{\nabla}E_i$, are

$$\mathbf{G}_i^{\parallel} = (-\boldsymbol{\nabla}E_i \cdot \widehat{\boldsymbol{\tau}}_i)\,\widehat{\boldsymbol{\tau}}_i, \tag{2.29}$$

$$\mathbf{G}_i^{\perp} = -\boldsymbol{\nabla}E_i - \mathbf{G}_i^{\parallel}. \tag{2.30}$$

The resultant NEB force acting on each image is then $\mathbf{F}_i^{\parallel} + \mathbf{G}_i^{\perp}$. $\mathbf{F}_i^{\parallel}$ controls the image separation, ensuring they are equidistant, while $\mathbf{G}_i^{\perp}$ acts to force the image into the valley of the MEP.

At high image densities, kinks in the chain may occur [132]. However, kinking is reduced by calculating the tangent vector of image i, $\widehat{\boldsymbol{\tau}}_i$ with respect to its highest free energy-

neighbour (when $\mathbf{\Gamma}_i$ is not at a turning point along the chain) [132],

$$\widehat{\boldsymbol{\tau}}_i = \begin{cases} \widehat{\boldsymbol{\tau}}_i^+ = \frac{\mathbf{\Gamma}_{i+1}-\mathbf{\Gamma}_i}{|\mathbf{\Gamma}_{i+1}-\mathbf{\Gamma}_i|}, & \text{if} \quad E_{i+1} > E_i > E_{i-1}, \\ \\ \widehat{\boldsymbol{\tau}}_i^- = \frac{\mathbf{\Gamma}_i-\mathbf{\Gamma}_{i-1}}{|\mathbf{\Gamma}_i-\mathbf{\Gamma}_{i-1}|}, & \text{if} \quad E_{i+1} < E_i < E_{i-1}. \end{cases} \tag{2.31}$$

If image i is however at a turning point along the chain, the weighted average of $\widehat{\boldsymbol{\tau}}_i^+$ and $\widehat{\boldsymbol{\tau}}_i^-$ is used:

$$\widehat{\boldsymbol{\tau}}_i = \begin{cases} \widehat{\boldsymbol{\tau}}_i^+ \Delta E_i^{\max} + \widehat{\boldsymbol{\tau}}_i^- \Delta E_i^{\min}, & \text{if} \quad E_{i+1} > E_i, \\ \\ \widehat{\boldsymbol{\tau}}_i^+ \Delta E_i^{\min} + \widehat{\boldsymbol{\tau}}_i^- \Delta E_i^{\max}, & \text{if} \quad E_{i+1} < E_i, \end{cases} \tag{2.32}$$

where

$$\Delta E_i^{\max} = \max\left(|E_{i+1} - E_i|, |E_{i-1} - E_i|\right), \tag{2.33}$$

$$\Delta E_i^{\min} = \min\left(|E_{i+1} - E_i|, |E_{i-1} - E_i|\right). \tag{2.34}$$

However, complete removal of $\mathbf{F}_i^\perp$ from the NEB force is able to result in unstable convergence to the MEP: when the gradient of the potential is small perpendicular to the path, the lack of perpendicular spring restoring force means the images can undergo large perpendicular oscillations on successive NEB iterations [133]. In the Doubly Nudged Elastic Band method, the stability is improved through re-introducing the component of $\mathbf{F}_i^\perp$, denoted $\widetilde{\mathbf{F}}_i^\perp$, which does not lie along $\mathbf{G}_i^\perp$ [133],

$$\widetilde{\mathbf{F}}_i^\perp = \mathbf{F}_i^\perp - \left(\mathbf{F}_i^\perp \cdot \mathbf{G}_i^\perp\right) \mathbf{F}_i^\perp. \tag{2.35}$$

This leads to an overall expression for the DNEB force, illustrated in Fig.2.4(d),

$$\mathbf{D}_i = \mathbf{F}_i^\parallel + \mathbf{G}_i^\perp + \widetilde{\mathbf{F}}_i^\perp. \tag{2.36}$$

It is important however that as the chain of images converges on the MEP, $\widetilde{\mathbf{F}}_i^\perp$ is gradually switched off, otherwise corner cutting again becomes problematic [133]. It is shown that this form of the DNEB implementation is highly efficient when optimization is carried out using the L-BFGS algorithm, with all images and the inter-image interactions included in

the approximate inverse Hessian [137].

2.3.2 String method

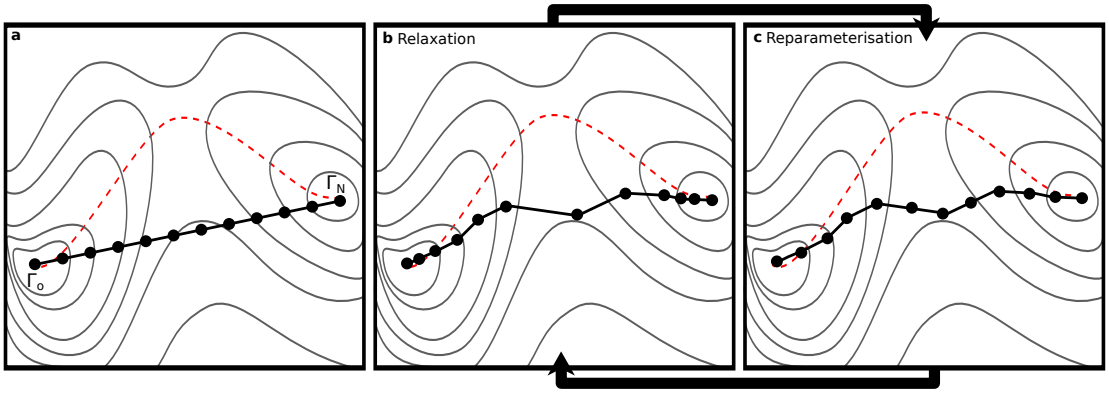

Figure 2.5: Illustration of the string method. (a) The true MEP (red, dashed line) shown across a contour plot of the free energy landscape. An initial string of images (black points) is also shown. (b) Image distribution after partial relaxation of each. (c) Redistribution of the images to be equal-spaced along the interpolated path.

The second path-finding method we employ is the simplified string method [134], illustrated in Fig. 2.5. Like DNEB, the string method is also a double-ended chain of states method for finding the MEP. To begin with, as before, a string of images is initialised across the landscape, illustrated in Fig. 2.5a. Apart from the two fixed end points Γ_0 and Γ_N (although end-point fixing is not strictly necessary), each image is then evolved according to some force $\mathbf{G}_i$. In the original string implementation [138], this force was the component of the free energy gradient lying perpendicular to the local path tangent vector. However, this projection of $-\boldsymbol{\nabla} E$ was later found to be unnecessary (due to the subsequent reparameterisation step), so that each image is simply evolved according to the free energy gradient $\mathbf{G}_i = -\boldsymbol{\nabla} E$. Thus, in the relaxation step, illustrated in Fig. 2.5b, each image is partially evolved downhill in the free energy landscape. We perform this relaxation using the L-BFGS algorithm, terminating the algorithm after a number of iterations to avoid complete relaxation. The iteration number is tuned for a given free energy functional to approach optimum convergence.

The next step in the iteration is to interpolate the path between the relaxed images. Although a cubic spline is recommended in [134], we find a linear interpolation to be sufficient for the large systems dealt with. The images are then redistributed along this interpolated path, to complete the reparameterisation step illustrated in Fig. 2.5c. For the high image

densities typically used, redistributing the images to be equidistant along the path is found to yield the most accurate path estimates. To elaborate, if the total path length L is the sum over the segment lengths

$$L = \sum_{i=0}^{N-1} |\mathbf{\Gamma}_{i+1} - \mathbf{\Gamma}_i|, \tag{2.37}$$

the images are redistributed such that along the piecewise-defined path, the images are separated by distance L/N.

Overall, the relaxation and reparameterisation steps are iterated until sufficiently converged to the MEP: when the local tangent vectors lie to within some tolerance along $\boldsymbol{\nabla} E$.

2.4 Transition state refinement

The highest energy transition state between any pair of minima is important to determine accurately, as this supplies a lower bound for the energy required to be input into the system to achieve the transition. Frequently, after the use of a path finding algorithm to obtain the MEP, the highest energy point, as an approximation to the the transition state, is refined via a variety of techniques. Such techniques include eigenvector following [115,120], the climbing image method [137, 139], and the mountain pass method [140]. For a broad comparison of methods, see for example [141, 142].

2.4.1 Gradient-squared method

In Chapter 3, we perform large-scale surveys of how the transition states vary with the structural parameters of complex surface geometries. This requires many hundreds of pathways to be obtained. The traditional approach of path-finding and subsequent transition state refinement therefore becomes computationally prohibitive. To overcome this, we develop an efficient transition state search algorithm, the gradient-squared technique, combining a landscape transformation with incremental parameter continuation methods.

The gradient squared technique begins by considering that all stationary points (SPs) on the free energy landscape become minima in the $|\boldsymbol{\nabla} E|^2$ landscape, with $|\boldsymbol{\nabla} E|^2 = 0$. In principle, the transition state may be accessed in this landscape via a single minimisation, so long as the initial coordinates are within the basin of attraction of the transition state. However, many additional minima are also present in the $|\boldsymbol{\nabla} E|^2$ landscape which are not stationary points of E, but rather extrema of the gradient. These points are termed non-

stationary points of E (NSPs) and are distinguished from SP's in that $|\boldsymbol{\nabla} E|^2 > 0$ [115, 143]. To worsen matters, in physical systems, it has been found that the basins of attraction of the NSP's are able to dominate the landscape [143]. In order to use gradient-squared minimisation to converge on the transition state and not an NSP, an accurate estimate of the transition state must therefore be made. Although with expert knowledge of the complex systems studied an accurate initial guess is now eminently feasible, a more robust technique is developed when intuition is not forthcoming.

In this, we start by performing a single double-ended search method to find an MEP, with the highest-energy image forming a close approximation to the transition state. This approximation is minimised to the true transition state using gradient-squared minimisation. We then adopt an incremental parameter continuation method (see for example [144] for a review on continuation methods). In this, a small change to the structural parameters in the system is made, and the previous, well-defined transition state used as the approximate candidate for the transition state in the new system. The magnitude of parameter change may be made sufficiently small so the candidate is within the basin of attraction of the new transition state. A gradient-squared minimisation on the new system therefore yields a well-defined new transition state. This parameter continuation is then iterated across the range of structural parameters we wish to sample.

An alternative method using the $|\boldsymbol{\nabla} E|^2$ landscape to find transition states is the biased gradient squared technique [145]. In this, the $|\boldsymbol{\nabla} E|^2$ landscape is biased with a $(E - E_t)$ potential, to target a level-set of E at the target energy E_t . However, in our high-dimensional systems, we find this technique is of limited utility as a good initial guess of the transition state is still required to avoid convergence to NSPs.

Chapter 3

The energy landscapes of wetting on complex surface geometries

3.1 Introduction

In this chapter, our primary aim is to investigate how superhydrophobicity and superomniphobicity break down due to the collapse of the suspended state, and infiltration of liquid into the surface texture. To do this, we apply the energy landscape methods detailed in Chapter 2, beginning by obtaining the stable wetting states possible on posts, reentrant and doubly reentrant geometries in Section 3.3. We then introduce the multiple collapse mechanisms in Section 3.4, and systematically survey how the minimum energy barriers depend on the surface physical properties in Section 3.5, before finally exploring the role of the surface intrinsic contact angle in Section 3.6.

The minimum energy collapse mechanism has proven extremely challenging to probe experimentally, and to date has never been observed. Several works however attempt to examine alternative causes of collapse as proxies for the true minimum energy mechanism, most notably pressure-driven collapse caused by evaporating droplets on pillar arrays [146, 147], or hydrostatic pressure increase on submerged well arrays [148–150]. Even for such pressure-driven collapse, the transition was shown to occur over a time-scale of less than 1 ms [146], making the time-resolution of the interface challenging.

A large range of both theoretical and computational studies have introduced two collapse mechanisms for simple 2D or 3D post structures, termed the 'sagging' and 'depinning' transitions [146, 147, 151–157]. The sagging transition, expected on short pillars, occurs when the liquid-vapour interface sags between the solid pillars, while the three-phase contact line remains pinned to the pillar top. The depinning transition however is expected on tall pil-

lars, where the interface again sags between the pillars but depins from the pillar top before sliding down into the texture. However, the majority of these studies do not follow the true minimum energy pathway of the wetting transition, but rather the transitions are forced by a gradual increase in the Laplace pressure difference across the liquid-vapour interface.

A small number of specialist studies have however managed to track the minimum energy pathway for the collapse transition. For the simplest 2D post geometries, forward flux sampling was used in molecular dynamics simulations to show two collapse mechanisms much like the sagging and depinning mechanisms described previously [158]. This has been corroborated using other techniques such as via the string method using diffuse interface potentials [159], atomistic simulations [160], and sharp interface models [161]. In 3D, atomistic simulations were also used to examine the nano-scale sliding mechanism on posts [162].

For more complex geometries, namely reentrant structures, atomistic and sharp interface models have been used to probe the transition pathway on 2D reentrant wells, showing a number of symmetry breaking events during the pathway [49,163]. The most complex systems tested to date however have been 3D reentrant geometries, [164, 165], in which atomistic simulations showed a nano-drop to undergo two collapse pathways, similar to the sag and depinning mechanisms. Prior to this study, the collapse mechanisms on doubly reentrant geometries were unknown.

In systems comprised of multiple posts, the wetting transition mechanism is consensually characterised as being initiated through the local collapse about a single feature, followed by lateral propagation of the liquid to fill the texture [164, 166–169]. Predominantly, the transition state was shown to be associated with the first local collapse (although the second local collapse was greater in energy on very short pillars [170]). The transition barrier was greater in energy for reentrant geometries compared to posts, as the reentrant geometry imposed a larger liquid-vapour interface area at the transition state. In the presence of multiple posts however, the complex local collapse - propagation mechanism means that the roles of each structural aspect of the surface geometry in the wetting transition are difficult to probe individually.

It is our aim here to comprehensively elucidate the geometrical influence of the surface structure on the wetting states and collapse mechanism through minimising the extraneous effects present in previous works. These include finite size effects when simulating liquid droplets, or liquid propagation effects for transitions on arrays of multiple posts. This is most

effectively performed by simulating systems featuring a single structure, with the texture immersed in a continuous liquid phase. By using a diffuse interface model (allowing for the facile simulation of topological changes), assumptions about the liquid vapour interface morphology are negated. It is important however to acknowledge recent studies which show the minimum energy barrier to collapse is reduced upon increasing the simulated domain from featuring one structure to an array of structures [168, 169]. However, this decrease was small (approximately 10%). Furthermore, as we shall see here, the wetting mechanisms at the most fundamental level already show remarkably rich behaviour, such that the influence of the arrangements of pillars in an array on the mechanism is retained for future study.

3.2 Methods

The simulation systems are set up for the post, reentrant and doubly reentrant geometries as shown in Fig. 3.1. Throughout, the simulation domain includes a single structural replica, with periodic boundary conditions in the plane of the texture to simulate a square array. The boundary condition at the top of the system enforces zero-gradient in the order parameter ϕ, so that bulk fluid behaviour is observed.

The domain size used to obtain the free energy minima in the phase diagrams was $N_\mathrm{x} \times N_\mathrm{y} \times N_\mathrm{z} = 60 \times 60 \times 50$ where the lattice spacing G was equal to the interface width ϵ.

For the transition state survey, the z-height of the domain was increased to $N_\mathrm{z} = 60$ to allow for taller structures to be simulated. In all cases, the system size parameter B, shown in Fig. 3.1 to be the simulation domain length, was fixed at $B = 60G$.

Throughout, the structural parameters labelled in Fig. 3.1 are reported relative to the system size B, which we denote with a subscript 'r'. For example, the reduced pillar width $A_\mathrm{r} = A/B$. We also nondimensionalise the pressure difference ΔP across the liquid-vapour interface, so that $\Delta P_\mathrm{r} = \Delta P/(\gamma_\mathrm{lv}/BG)$. Finally, we nondimensionalise reported energies E, so that $E_\mathrm{r} = E/\gamma_\mathrm{lv}(BG)^2$.

The size of the structural features was chosen to balance the computational cost of the simulation with the Cahn number, C_n, defining the ratio of the interface width to the smallest structural length scale in the system. It has been suggested that $C_n \leq 1/2$ is sufficient for the diffuse interface to not influence the behaviour of the system significantly [128]. To ensure this condition here, $C_n \leq 1/3$.

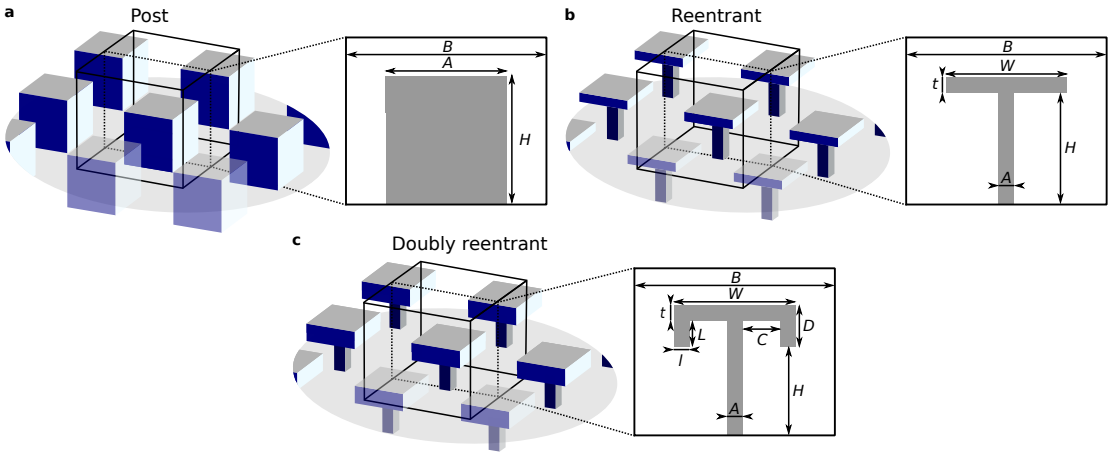

Figure 3.1: Illustration of the three types of surface geometry considered throughout: the simple post (a), reentrant geometry (b), and doubly reentrant geometry (c). The variable structural parameters are labelled in a 2D cross-section for each. The structures are arranged in a square lattice, with the simulation domain being a single unit cell with periodic boundary conditions.

In the free energy minimum survey, to obtain each stable state, the phase field was initialised by approximating the state using planar interfaces. For example, to simulate the suspended state, whereby liquid sits atop a pillar with vapour underneath, we initialised the order parameter at each node, $\phi_{ijk} = 1$ for $z > H + t$, and $\phi_{ijk} = -1$ elsewhere. In each minimisation, to ensure small-number errors had negligible effect on the computation of the energy of a state, the free energy E was multiplied by a constant factor of 10^5. The minimisation was deemed to have converged when the gradient at each node, $\partial E/\partial\phi_{\mathrm{ijk}}$, was separately converged to a tolerance of 10^{-11}.

In the transition state survey using the gradient-squared technique, again the free energy E was multiplied by a constant factor of 10^5, and convergence completed when $\partial|\nabla E|^2/\partial\phi_{\mathrm{ijk}} \leq 10^{-11}$. Transition pathways obtained via the DNEB method featured an initial string of 37 images (inclusive of the minimum end-points). As the MEP converged upon by DNEB is sensitive to the initial string, we trialled strings which both preserved and broke the system symmetry. In the systems used here however, the DNEB algorithm was always observed to converge on the same pathway. For pathways obtained via the string method, an initial string of 50 images was used, and convergence obtained once the total distance change between the images on successive iterations was less than 10^{-7}. The distance measure was defined as the norm of the difference between the old and new ϕ_{ijk} vectors. The DNEB method was used initially to obtain pathways, but we found the string method had two advantages, in

that it more reliably converged to the transition pathway, and was often quicker to converge (offering a speedup of up to 10 times).

For the minimum energy survey, and DNEB pathway searches, the linear surface potential, detailed in Chapter 2, was used to obtain the desired contact angles. For the gradient-squared and string method, the cubic potential was used as a precaution against local enrichment of the phase field at the solid surface. However, the choice of surface potential was found to not substantially influence the wetting pathway.

3.3 Free energy minima

3.3.1 Posts and reentrant geometries

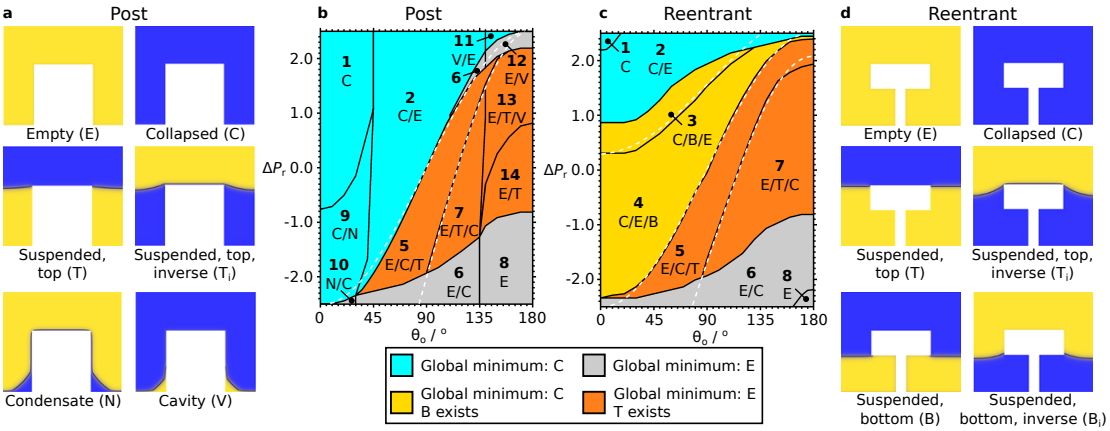

Figure 3.2: Diagonal cross sectional images of the phase field at the free energy minima for the short post (a) and short reentrant geometry (d). The solid structure is shown in white, the liquid phase ($\phi = 1$) in blue, and the vapour phase ($\phi = -1$) in yellow. The ($\phi = 0$) interface is highlighted in black. Also shown are the phase diagrams for the post (b) and reentrant geometries (c). Numbered regions indicate the stable states, listed in order of increasing energy, white dashed lines are flat-interface theoretical approximations to selected phase boundaries.

Our description of the free energy landscape of wetting on complex geometries begins with a characterisation of the stable states - the free energy minima. As shall be shown, the types of minima which exist are largely insensitive to the specific structural dimensions, but do depend on the pressure across the liquid-vapour interface, as well as the intrinsic contact angle θ_o. We therefore survey the free energy minima for the contact angle range $0° \leq \theta_o \leq 180°$, and the pressure range $-2.5 \leq \Delta P_r \leq 2.5$.

As a representative example, we choose the dimension of the post geometry to have width $A_\mathrm{r} = 0.48$ and height $H_\mathrm{r} = 0.5$. To make a fair comparison between the phase diagram of

the post and reentrant structure, the reentrant structure we use can be cut from the post, so that the cap width $W_\mathrm{r} = 0.48$, and the total height $H_\mathrm{r} + t_\mathrm{r} = 0.5$. Here, we also choose the cap height $t_\mathrm{r} = 0.2$, and the pillar width $A_\mathrm{r} = 0.08$.

In Fig. 3.2(a), the posts structure is shown to exhibit six possible minimum energy states. In addition to the vapour-filled (Empty), liquid-filled (Collapsed) and suspended minima (Suspended, top), the product of heterogeneous nucleation of the liquid phase in the empty state (Condensate) is observed, as is the product of nucleation of vapour within the liquid-filled system (Cavity). Finally, the surface texture may also imbibe the liquid phase (Inverse Suspended).

For the reentrant geometries, six minima are highlighted and shown in Fig. 3.2(d). As with the posts, the reentrant geometry also admits Empty, Suspended (top) and Collapsed solutions. However, unlike for the post, the reentrant geometry may maintain a suspended state under conditions that are favourable for the liquid-vapour interface to slide down the cap. For example at modest positive pressures and $\theta_o < 90^\circ$, the interface is pinned at the base of the cap (Suspended, bottom). This latter minimum highlights the ability of the reentrant structure to suspend liquids which would otherwise wet an unstructured or post-structured surface texture. As with the post system, the reentrant texture may also imbibe the liquid phase, resulting in the phase-inverted equivalents of the two suspended states (Suspended, top inverse, and Suspended, bottom inverse). Cavity- and Condensate-type states are also observed for the reentrant geometry. However, as their scale is small, the nucleated fluid does not exhibit bulk behaviour and so is not distinguished from the Collapsed and Empty states.

Evaluation of the existence and energy of each minimum type across the range of $\theta_o - \Delta P_r$ coordinates enables a phase diagram to be constructed for the post and reentrant geometries, shown in Figs. 3.2 (b) and (c) respectively. For both visual clarity, and the choice to focus on the suspended-collapsed transition, the inverse suspended states are omitted from both diagrams. In the absences of surfaces and pressure terms, the diffuse interface potential is symmetric with respect the the exchange of the two fluids, whereas the surface and pressure terms E_s and $-\Delta PV$ are antisymmetric. Therefore, full phase diagrams would have inversion symmetry about $\theta_o = 90^\circ, \Delta P_r = 0$.

Two key comparisons can be made between the post and reentrant phase diagrams. Firstly, the reentrant geometry exhibits a substantially increased region in θ_o and ΔP_r in which a suspended state (B or T) exists. Secondly, a much greater number of distinct regions

are identified for the post than for the reentrant phase diagram. We therefore partition the diagrams into three approximate regimes: 1) a cavity/condensate dominated regime ($\theta_o > 135°$, $\theta_o < 45°$), 2) a regime characterised by high liquid-vapour interfacial curvature ($\Delta P_r > 1.5$, $\Delta P_r < -1.5$), and 3) the remaining region in which cavitation/condensation is insignificant and the interfaces are accurately described as planar.

First, we focus on regime 3 in the region defined by $45° < \theta_o < 135°$, $-1.5 < \Delta P_r < 1.5$. Here, a macroscopic (sharp interface) model is constructed to describe the three phase boundaries in this region: the boundary at which the suspended (top) and collapsed states become isoenergetic (5-7), the boundary at which the suspended (bottom) and empty states become isoenergetic (3-4 for the reentrant geometry), and the stability limit of the suspended (top) state (2-5 for the post, 4-5 for the reentrant geometry). Here, the energies of the collapsed, empty, suspended (top), and suspended (bottom) states are expressed as

$$E_C = \gamma_{sl} A_{sl} - \Delta P V, \tag{3.1}$$

$$E_E = \gamma_{sv} A_{sv}, \tag{3.2}$$

$$E_{T,B} = \gamma_{sl} A_{sl} + \gamma_{sv} A_{sv} + \gamma_{lv} A_{lv} - \Delta P V. \tag{3.3}$$

A_{sl}, A_{sv}, and A_{lv} are the solid-liquid, solid-vapour and liquid-vapour interfacial areas respectively, V is the liquid volume. As the shape of the interface is not analytically available, a planar interface is assumed.

The boundaries where T and C are isoenergetic (5-7) are shown in the phase diagrams in Fig. 3.2(c) and (d), and were constructed through interpolating between adjacent simulation points (black lines). In the planar interface approximation, E_C and E_T were equated to yield an analytic expression for the phase boundary, which is shown in Fig. 3.2(c) and (d) as white dashed lines. This is observed to agree with the simulation boundaries for both the post and reentrant geometry to within a maximum discrepancy of 3% in ΔP_r, and 1% in θ_o at the limits of regime 3.

For the reentrant geometry, the boundary where B and E have equal energy is shown in Fig. 3.2(d) (3-4 boundary). This boundary was modelled by equating E_E and E_B, and as shown in Fig. 3.2(d) as white dashed lines, is also in agreement with the simulation boundary: the maximum difference between the two being a reduced pressure difference of 0.1.

The stability limit of T, shown in Fig. 3.2(c) (2-5) and (d) (4-5), can be evaluated through

consideration of the θ_o-ΔP_r coordinate at which it becomes energetically favourable for the liquid-vapour interface to slide down the structure. This yields the critical pressure, ΔP_c, for a post of square cross section [171]. The same derivation will be shown later in the context of wetting transitions in Section 3.5.2. The same interpretation applied to the reentrant geometry accurately yields the suspended (top)-suspended (bottom) phase boundary. For both phase diagrams, the theoretical critical pressure, which is shown in Fig. 3.2(c) and (d) as white dashed lines, is in agreement with the interpolated simulation results to within an accuracy of 2% in ΔP_r, and 1% in θ_o. The planar interface approximation is therefore a suitable model for the liquid-vapour interface in regime 3.

In regime 2 ($\Delta P_r > 1.5$, $\Delta P_r < -1.5$), the high pressure difference across the liquid-vapour interface causes a high interfacial curvature (according to the Young-Laplace relation). Therefore in this regime, the planar interface approximation underestimates the area of the liquid-vapour interface. As a consequence of the curvature, it is observed that in the suspended states the interface may depin from the edges of the cap. At large negative ΔP_r, this leads to T becoming destabilised relative to E, observed as the (5-6) and (7-6) phase boundaries for the post and reentrant structure in Fig. 3.2(c) and (d). At large positive ΔP_r, the B state for the reentrant structure becomes unstable with respect to the interface depinning from the underside of the cap to fill the surface texture (2-3 boundary).

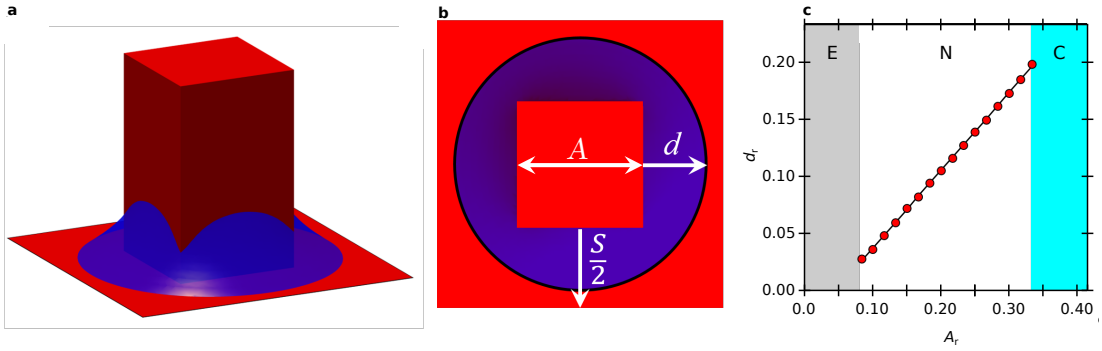

Figure 3.3: (a) Image of the liquid-vapour interface of the condensate about a square pillar, $\theta_o = 20°$, $\Delta P_r = 0.15$. (b) Top view of the system showing the lateral extent of the condensate, d, pillar width A, and separation between the structures S. (c) Plot of the increase in d as the pillar width increases with linear trendline shown (black). Shaded regions indicate where the condensate state (N) is not observed, either due to complete filling of the system (C), or no condensation occurring (E).

Regime 1 is characterised by the tendency for liquid condensation at the base of the post structure for $\theta_o < 45°$ (approximately), or vapour cavitation for $\theta_o > 135°$ (approximately),

and is largely a consequence of the 90° angle between the side of the post and the base [172, 173]. This is evidenced in Fig. 3.2(c) by the presence of condensates (minimum N) in phases 9 and 10, and cavities (minimum V) in phases 11, 12 and 13. At equilibrium, the liquid-vapour interface is a surface of constant mean curvature defined by the Young-Laplace equation, as discussed in Chapter 1.

Of particular interest is the observation of condensates and cavities about the post ($A_\mathrm{r} = 0.48$), but not about the reentrant pillar of substantially reduced width ($A_\mathrm{r} = 0.08$). The extent of condensation about a post of variable width is shown in Fig. 3.3, in which d_r is the maximum lateral extent of the three phase contact line from the post. The variation of d_r with A_r is quantified in Fig. 3.3 (c) for a post with $\theta_o = 20°, \Delta P_r = 0.15$. For all post widths, the separation S_r between the posts was maintained at $S_\mathrm{r} = 0.52$, as has been used throughout this work. It is firstly observed that, independent of A_r, the shape of the three-phase contact line on the base of the system is indistinguishable from a circle at the scale of the system resolution. For $A_\mathrm{r} < 0.08$, no condensate is observed in the empty state. In the range $0.08 < A_\mathrm{r} < 0.33$, d increases with the post width. Within the simulation resolution this is accurately described by a linear relationship and is comparable to the analytically determined behaviour of a condensate at the base of a cylindrical post [172]. For $A_\mathrm{r} > 0.03$, the condensates centred on adjacent posts merge, leading to the collapsed state.

The width of the post relative to the radius of curvature of the interface (imposed by ΔP_r) therefore critically influences the stability of the free energy minima, when condensation and cavitation effects are dominant. This has several consequences for the design of surfaces used to suspend highly wetting or highly non-wetting liquids. Crucially, for the reentrant geometry used here, the pillar is sufficiently narrow that cavity and condensate formation is not observed across all θ_o at the level of the simulation resolution. Therefore, an effective method to stabilise a suspended state with respect to condensation is to fabricate a reentrant surface texture in which the pillar width is minimised.

An increase in the suspended-collapsed coexistence range has been observed previously using a diffuse interface model, but for a droplet on a square array of reentrant posts [167]. However, the suspended and collapsed states were not stable over all θ_o. In this system, the ratio between the reentrant pillar width and the post width was only 0.5, compared to 0.17 here, meaning that the maximisation of the suspended range was not effectively realised.

A consequence of reducing the occurrence of cavitation in the 3D reentrant geometries

is that the suspended states always coexist with the collapsed state. This is in contrast to region 14 of Fig. 3.2(b) for the post structure where, neglecting the empty state, the suspended state is monostable even at positive pressures. The occurrence of a monostable microscale-suspended state on a square array of posts has been recently suggested to occur experimentally for hierarchically textured, superhydrophobic surfaces [52]. The addition of a nanoscale texture to the microscale structuring effectively accesses contact angles in excess of 135° (for surfaces without the microscale texture), although it was not shown whether the nanoscale texture exhibited a monostable suspended state. Conditions for both nanoscale and microscale monostability have recently been proposed through liquid density functional simulations in quasi-3D [53].

3.3.2 Doubly reentrant geometries

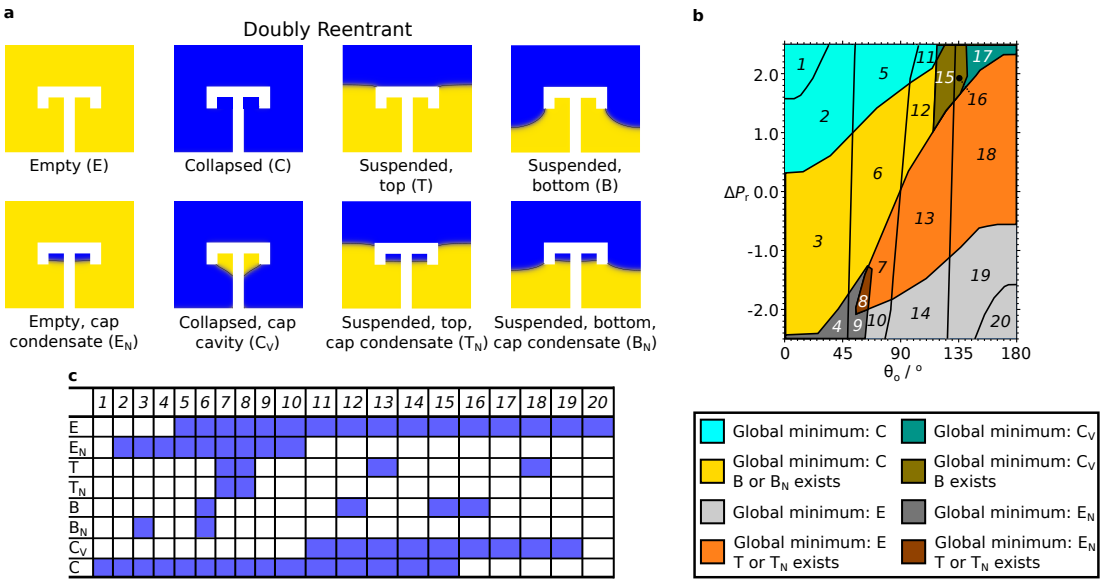

Figure 3.4: (a) Diagonal cross sectional images of the phase field at the free energy minima for the short doubly reentrant geometry. (b) Phase diagram showing the global free energy minima, and existence ranges of a number of key (meta)stable states. The observed minima within each numbered region are highlighted in blue in (c).

We conclude this section by discussing the stable states on the doubly reentrant geometry. Before, a fair comparison was made between the post and reentrant phase diagrams by preparing the reentrant geometry from a 'cut-out' of the post. Here, we make a fair comparison again by choosing a doubly reentrant structure which is a 'cut-out' of the reentrant geometry. In this, the cap width $W_r = 0.48$, total height $H_r + D_r = 0.5$, total cap height

$D_r = 0.2$ and pillar width $A_r = 0.08$. For the doubly reentrant cap, we choose the lip depth $L_r = 0.15$, lip width $l_r = 0.05$, and cap thickness $t_r = 0.05$.

The set of minima on the doubly reentrant surface geometry shows a substantial increase in size compared to the post and (singly) reentrant geometry. A selection of this set most pertinent to the discussion of liquid-repellent surfaces is illustrated in Fig. 3.4(a). As with the reentrant geometry, the empty, collapsed, suspended top, and suspended bottom states are able to exist. However, the doubly reentrant cap in each of these four states may be filled with a liquid or vapour, leading to the four additional cap-condensate and cap-cavity states shown in Fig. 3.4(a). Not shown are the inverse suspended states, which are equivalent to the four suspended variants shown, but with the fluid identities swapped. As these liquid-imbibed states are not important for the discussion on liquid-repellency, we neglect them from further analysis. As with the reentrant geometry, states exist in which small condensates or cavities are formed in the corner regions of the geometry, but as they are either never large compared to the interface width ϵ, or quickly merge to fill the cap, they are not distinguished from the states already presented.

Due to the number of minima which coexist at each (θ_o, ΔP_r) coordinate, the phase diagram shown in Fig. 3.4(b) departs from the format presented for the post and reentrant geometries in Fig. 3.2(b,c). Here, each region, denoted by an italic numeral, marks a distinct set of coexisting minima. Fig. 3.4(c) indicates which minima exist within each region (highlighted blue). For simplicity, we do not distinguish between regions containing the same sets of minima that are only reordered in their relative energies.

Unlike for the post or reentrant geometries, the collapsed and empty states are no longer the only global free energy minima present for the doubly reentrant geometry. In regions *4*, *8*, and *9*, at low contact angles and large negative pressures, the global minimum is the empty state with the cap filled with a liquid condensate: it becomes energetically favourable for the liquid to wet the large cap-underside surface area, despite the pressure penalty for forming bulk liquid. The opposite scenario occurs at large contact angles and large positive pressures in regions *15*, *16*, and *17* . Here, the global energy minimum is a collapsed state with a vapour cavity filling the cap: it is energetically favourable to de-wet the cap underside, even though a large positive pressure favours the presence of the liquid.

More generally, the doubly reentrant geometry is susceptible to spontaneous condensation for approximately $\theta_o < 45°$, and cavitation for approximately $\theta_o > 135°$. As with the post,

this is caused by the large solid surface area associated with corner structures, which are capable of lending large stabilising surface energy contributions to condensates and cavities. This spontaneous condensation causes a reduction in the high-pressure stability range of the bottom-suspended (B) state, compared to the reentrant structure. In this, the $\theta_o < 45°$ portion of region 3 for the reentrant geometry in Fig. 3.2(c) is no longer present for the doubly reentrant geometry in Fig. 3.4(b). This is because the bottom suspended state under high pressure encroaches under the cap at the corners, to contact the cap-condensate. This contact leads to spontaneous breakdown of the suspended state as the system fills with liquid.

However, regions *15* and *16* in Fig. 3.4(b) show that for non-wetting liquids, this example doubly reentrant geometry shows increased pressure resistance against collapse of the B-state, compared to the reentrant geometry. This increase in pressure-resistance is explored in detail in Chapter 4.

Overall it is reasonable to anticipate that despite the increased pressure-resistance, condensate formation will be problematic in designing doubly reentrant surfaces which are resistant to the collapse transition - a point discussed in detail in Section 3.4.

3.4 Minimum energy transition mechanisms

We now continue our description of the free energy landscape by using the double-ended search methods detailed in Chapter 2 to link minima via minimum energy pathways. As we are primarily interested in the breakdown of the suspended state on liquid-repellent geometries, we focus throughout on the suspended-collapsed transition. On the post, reentrant and doubly reentrant geometries, we observe three different transition mechanisms which we term Base Contact, Pillar contact, and Cap Contact. In this section, we perform qualitative analyses on these transition types. In the proceeding section (Section 3.5), we then quantify how the minimum energy barrier depends on the structural parameters and the surface wettability.

3.4.1 Base Contact

The Base Contact mechanism (BC) is observed on all three geometries studied, and is able to occur whenever the interface is able to pin to the cap top or bottom, while sagging into the texture. This mechanism is highly prevalent across a broad range of structural and chemical

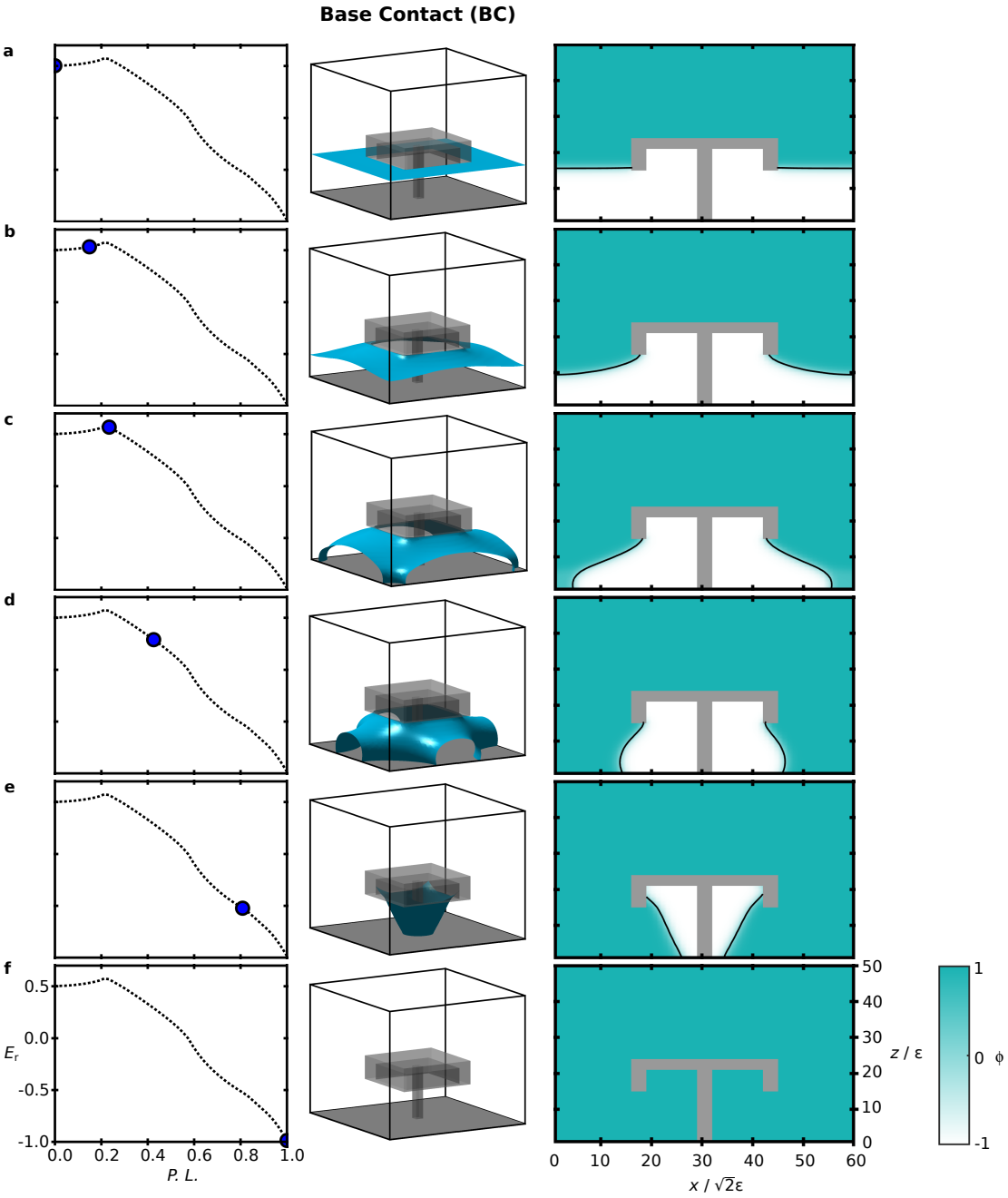

Figure 3.5: (a-f) Snapshots of Base Contact on a doubly reentrant geometry, obtained via the string method. The energetic profile of the pathway is shown as a function of the normalised path length *P.L.* in the left-hand column, the blue data point indicates the current position along the path. The centre column shows a 3D visualisation of the phase field at each point: the geometry is shown as the grey structure, with the liquid-vapour interface shown in blue. The right-hand column shows a 2D diagonal cross section through the 3D system, blue indicating the liquid phase, and white the vapour phase.

properties, such as on non-wetting geometries as well as pillars and nails [49,164,167,170,174]. A representative example of this mechanism is shown in Fig. 3.5, in which Base Contact is occurring on a doubly reentrant geometry.

The system begins in the suspended state in row (a), and the interface begins to sag under the cap in (b). The increase in area of the liquid-vapour interface results in the energy increasing along the transition pathway. This sagging continues until the interface contacts the base of the system, to form the transition state in (c). From this point, collapse becomes spontaneous: the liquid wets the bottom surface and fills in under the cap in (d). Finally, the interface ascends the pillar in (e) to fill the cap and enter the collapsed state in (f). For the reentrant geometry and post, the mechanism proceeds in an almost identical manner, excluding the cap-filling at the end of the transition.

3.4.2 Pillar Contact

The Pillar Contact mechanism (PC) is also observed on all three geometries for $\theta_o > 90°$, but only for the reentrant geometry for $\theta_o < 90°$, and shows more variability in the location and symmetry of the transition state. The representative example shown in Fig. 3.6 highlights the two common features of all Pillar Contact variants: an initial depinning of the interface, followed by a sliding of the contact line down the pillar. In Fig. 3.6, Pillar contact starts from the suspended state (a), from which the interface sags slightly under the cap. The interface depins from one corner in (b), and propagates under the cap. In (c), the interface detaches from the cap at the opposite corner. The near-planar interface then slides down the pillar in (d), before touching the base of the system in (e) to form the collapsed state in (f). As will be shown in Section 3.5, for non-wetting contact angles, the depinning event preserves the system symmetry for reentrant and doubly reentrant geometries. For the post, there is no cap-underside wetting event, so sliding occurs as soon as the interface has depinned. Depending on the contact angle and pressure, if it is energetically favourable for the interface to slide down the pillar, the transition state occurs at the top, as shown in Fig. 3.6 (c); otherwise, the transition state occurs at the bottom of the pillar as the interface meets the base of the system.

The pillar contact mechanism has been observed partially before [164, 165]. In these molecular dynamics simulations, a nano-droplet on tall reentrant geometries was also observed to intrude under the cap, before sliding to the base. However, the droplet size was of the same

scale as a single pillar, and the role of geometry on the transition energy remained largely unexplored.

3.4.3 Cap Contact

The final transition discussed, Cap Contact (CC), is observed exclusively on doubly reentrant geometries when the surface is intrinsically wetting ($\theta_o < 90°$). The mechanism, shown in Fig. 3.7, begins in (a) with the suspended state. Next, a liquid condensate forms in a corner of the cap underside, shown in (b). This condensate continues to grow until the maximum energy point is reached, forming the first (and largest-energy) transition state. The interface morphology at the transition state depends on the structural parameters. Once this transition state is overcome, the cap fills to form the stable cap-condensate state in (c). The cap condensate then merges with the liquid outside of the cap, overcoming a small energetic barrier to do so, shown in (d). From here, the transition proceeds in an identical manner to Pillar contact, with the interface sliding down the pillar (e), meeting the base of the system (f) and forming the collapsed state (g).

Of further note is that the Cap Contact transition is an MEP regardless of liquid volatility. The pressure treatment in the free energy functional used in these simulations effectively contacts every point of the system with an external fluid reservoir at constant pressure. Thus, fluids may be exchanged anywhere within the system. For non-volatile liquids, although the Cap Contact condensation mechanism is a minimum energy pathway on the doubly reentrant geometry, CC may not be realised on an experimental timescale. The transition will therefore occur via a non-condensing route, the minimum energy path of which is Base Contact.

3.5 Structural effects on the MEP and minimum energy barrier

3.5.1 Wettable surfaces

We now survey the wetting mechanisms across the range of structural parameters, by utilising the gradient-squared algorithm. Here, we begin by considering transitions on wettable surfaces, for which we use a representative intrinsic contact angle $\theta_o = 60°$. Our primary aim will be to quantify the minimum energy barrier to wetting, ΔE_{r}, which is the difference between the transition state energy and suspended state energy. Throughout this work, the

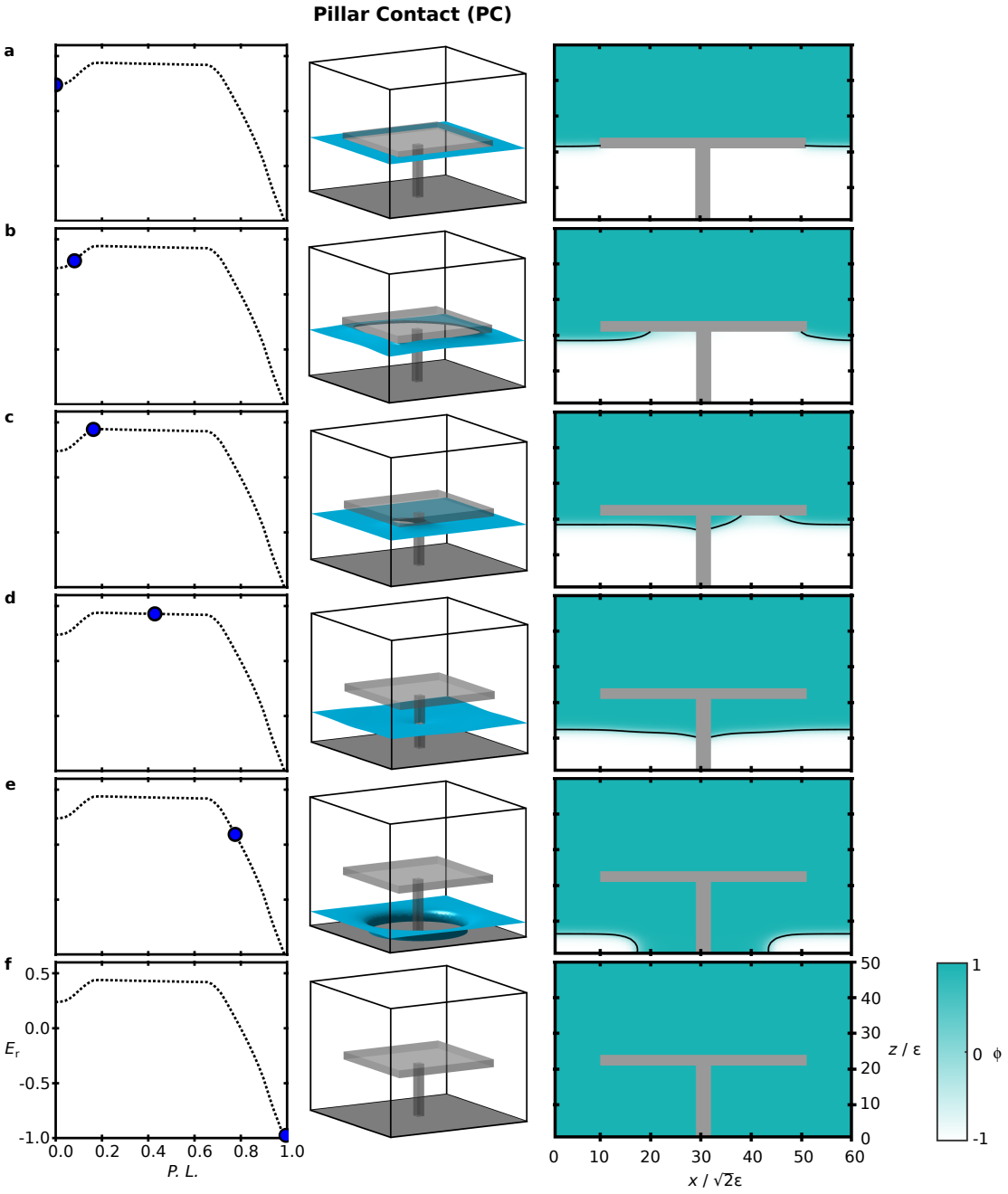

Figure 3.6: (a-f) Snapshots of Pillar Contact on a reentrant geometry, obtained via the string method. The energetic profile of the pathway is shown as a function of the normalised path length *P.L.* in the left-hand column, the blue data point indicates the current position along the path. The centre column shows a 3D visualisation of the phase field at each point: the geometry is shown as the grey structure, with the liquid-vapour interface shown in blue. The right-hand column shows a 2D diagonal cross section through the 3D system, blue indicating the liquid phase, and white the vapour phase.

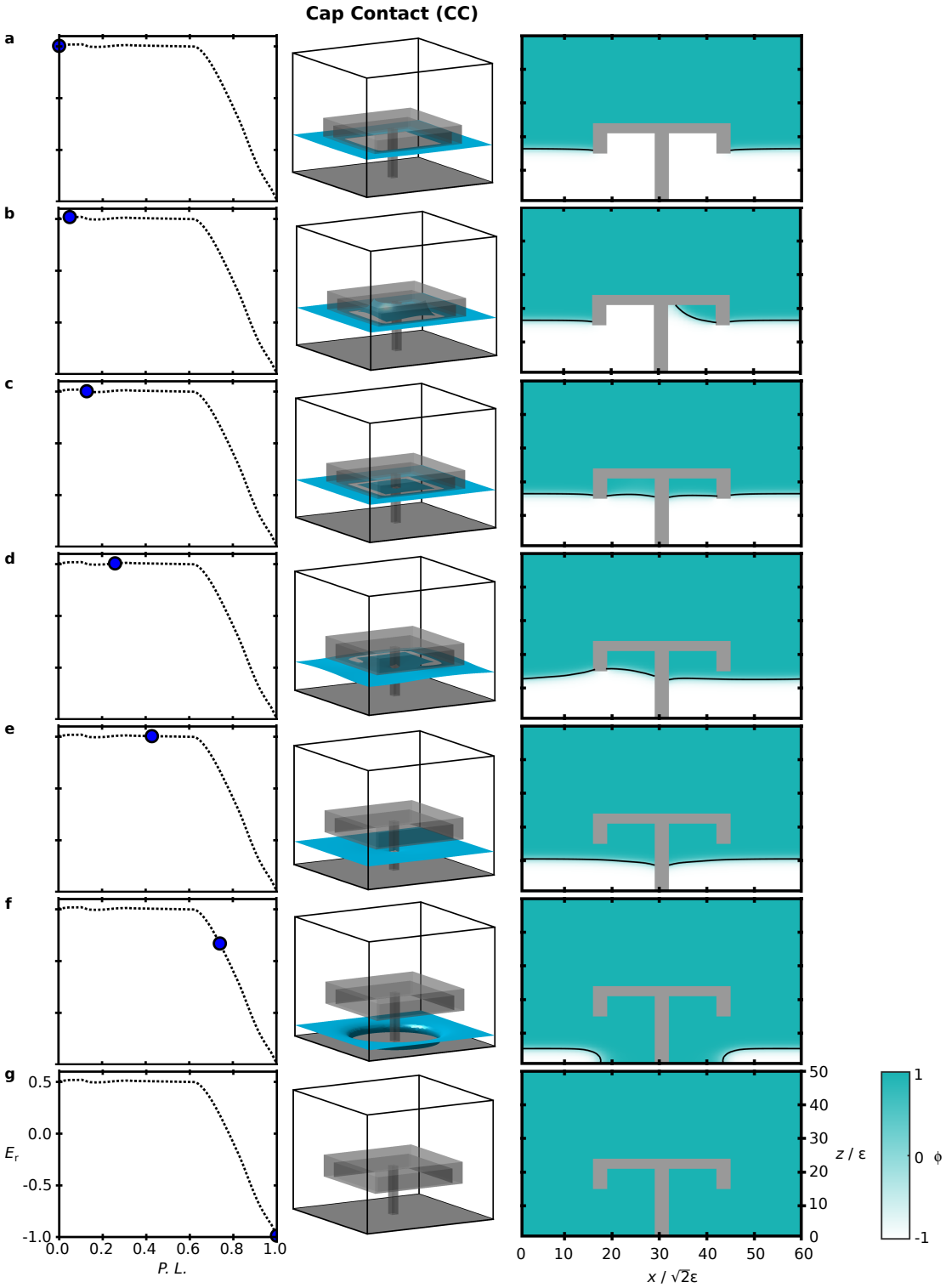

Figure 3.7: (a-f) Snapshots of Cap Contact specific to the doubly reentrant geometry, obtained via the string method. The energetic profile of the pathway is shown as a function of the normalised path length *P.L.* in the left-hand column, the blue data point indicates the current position along the path. The centre column shows a 3D visualisation of the phase field at each point: the geometry is shown as the grey structure, with the liquid-vapour interface shown in blue. The right-hand column shows a 2D diagonal cross section through the 3D system, blue indicating the liquid phase, and white the vapour phase.

energy barrier ΔE_r is expressed relative to the reference energy $\gamma_{lv}(BG)^2$. As the suspended state is not stable on the post geometry for $\theta_o < 90°$, we reserve discussion of the post transitions to the proceeding Section 3.5.2.

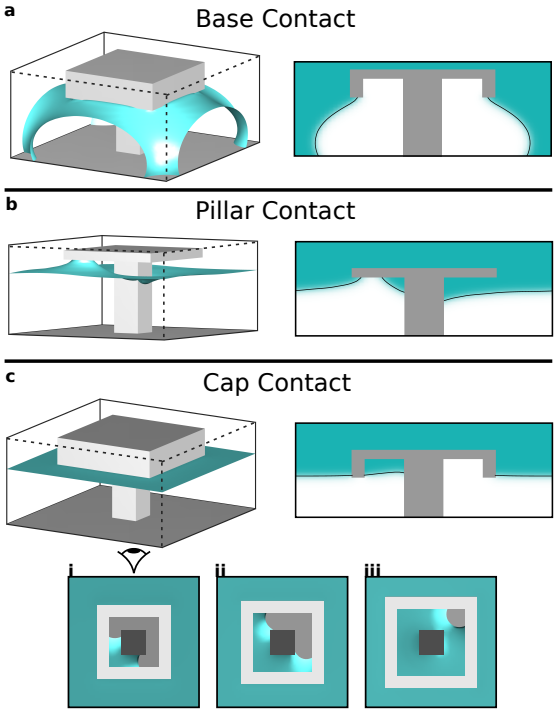

Figure 3.8: (a-c) 3D visualisations of the transition states of each transition pathway (liquid-vapour interfaces shown in blue) with associated diagonal cross sections (liquid-vapour interface outlined in black). In panel (c), under-cap views show the three Cap Contact transition state morphologies.

In Fig. 3.8, we visualise in detail the three possible transition state types which may occur on the reentrant and doubly reentrant geometries. Fig. 3.8(a) shows the Base Contact transition state, common to both reentrant and doubly reentrant geometries. Fig. 3.8(b) shows the pillar contact transition state, which is specific to the reentrant geometry, while Fig. 3.8(c) shows the Cap Contact transition state which is specific to the doubly reentrant geometry. The Cap Contact transition exhibits three morphological variants of the liquid-vapour interface, visualised in (c) in an under-cap perspective. These characteristic examples do not smoothly interpolate as the structural parameters change, but represent distinct morphologies which occur early, middle, or late in the transition for variants (i), (ii), and (iii) respectively.

To overview the energy barrier survey, we summarise the structural parameters which affect the energy barrier for each transition type in Table 3.1. For the Base Contact mecha-

	Reentrant		Doubly Reentrant	
	BC	PC	BC	CC
H_r	●		●	
W_r	●	●	●	●
A_r		●		●
L_r	-	-		●
t_r				

Table 3.1: The geometrical parameters which affect ΔE_r for each transition mechanism, indicated with filled circles. Dashes indicate where a structural parameter is not featured on a geometry.

nism, the transition state is only sensitive to the size of the pinned contact line on the outer cap edge (dependent on the cap width W), and the sag height (dependent on the pillar height H). In contrast, the Pillar Contact mechanism is insensitive to the pillar height. Instead, the solid cap-underside area to be covered with liquid affects the transition state energy; a function of W and the pillar width A. Finally, the Cap Contact energy barrier is sensitive to all structural parameters affecting the cap underside geometry: W, A, and the lip depth L. The cap thickness t never affects the energy barrier, because for $\theta_o < 90°$ the cap outside edge is always completely wetted by the liquid from the start of the transition, in suspended (bottom) state, through to the end, in the collapsed state.

We now quantify the energy barrier of each mechanism on both the reentrant and doubly reentrant geometries. For the reentrant geometry, the two possible mechanisms are the Base Contact and Pillar Contact modes, shown in Fig. 3.9(a). For Base Contact, at large pillar heights H_r, the three-phase contact line is no longer able to remain pinned to the base of the cap, and is unstable with respect to depinning and sliding inwards. This places an upper height limit on the existence range of Base Contact, shown in Fig. 3.9(a)(i). This upper height limit decreases with decreasing cap width W_r in a manner similar to the suppressed critical height at low W_r in the critical pressure discussion, which will be presented later in Chapter 4. To summarise here however, the small, negative radius of curvature of the liquid-vapour interface around the cap enforces an even smaller, positive radius of curvature outwards from the cap. The effect of this is to increase the contact angle the liquid-vapour interface makes with the cap underside, meaning that sliding occurs at smaller pillar heights H_r than for structures with larger cap widths W_r.

For Pillar Contact on the reentrant geometry, the energetic barrier does not depend on the pillar height H_r, and is therefore the only possible transition mechanism at large pillar heights where Base Contact is inoperative. However, two parameters which do influence the

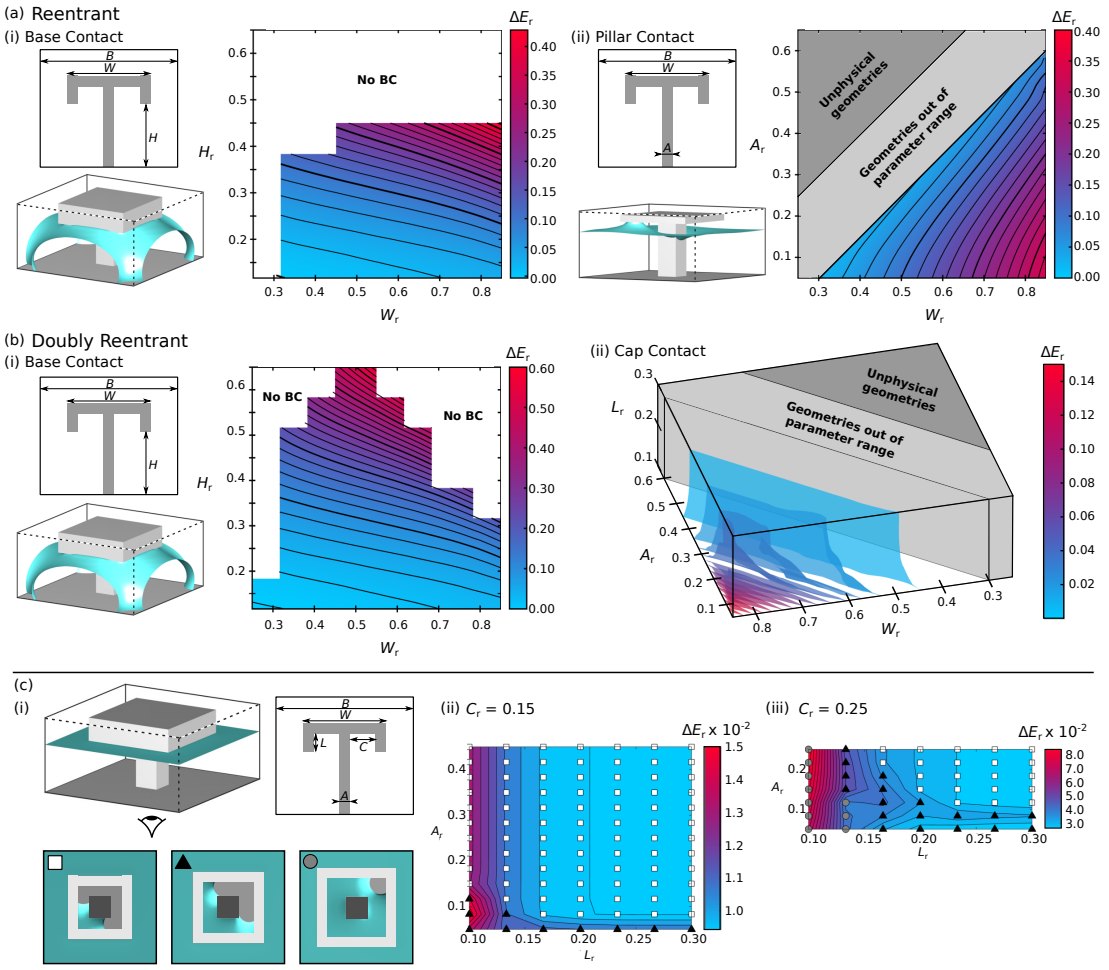

Figure 3.9: (a) 3D illustration and contour plot of the two reentrant transition mechanisms: (i) Base Contact, (ii) Pillar Contact. Impossible geometries with pillar widths A_r wider than the cap width W_r are shaded in dark grey. Geometries approaching this limit and requiring infeasibly large computational domains are shaded in light grey. (b) 3D illustration and contour plot of the two doubly reentrant transition mechanisms: (i) Base Contact, (ii) Cap Contact. (c) Extended description of the cap contact transition mechanism. (i) 3D illustration and under-cap views of the three transition variants (each labelled with a square, triangle, or circle). (ii, iii) Two slices through the 3D contour plot at constant cap width values $C_r = 0.15$ and $C_r = 0.25$ respectively. Each datum is labelled with a symbol corresponding to the transition variant shown in (i).

Pillar Contact barrier are the cap width W_r and pillar width A_r. The energetic barrier is increased when the area of the liquid-vapour interface at the transition state is increased. This is observed to occur by maximising W_r and minimising A_r, as shown in Fig. 3.9(a)(ii).

For the doubly reentrant geometry, the two transition mechanisms, Base Contact and Cap Contact, are shown in Fig. 3.9(b). For cap widths $W_r < 0.7$, the Base Contact mechanism, shown in Fig. 3.9(b)(i), is operative over a greater range of pillar heights H_r than for the reentrant geometry. This is due to the inner cap lip being an effective pinning site, so

preventing the liquid-vapour interface from sliding inwards. However, at cap widths $W_r > 0.7$, it becomes energetically favourable for the liquid-vapour interface to depin from the cap corners, leading to liquid filling the underside of the cap. In these scenarios, Base Contact becomes unstable with respect to the cap-filling, Cap Contact mechanisms.

For the doubly reentrant geometry, the Cap Contact mechanism exists over the entire parameter range tested, shown in Fig. 3.9(b)(ii). Because Cap Contact is a heterogeneous condensation mechanism, in which nucleation proceeds from one cap corner, we expect Cap Contact to be operative for all physical doubly reentrant geometries. As with pillar contact on the reentrant geometry, the energetic barrier is increased by increasing the area of the liquid-vapour interface at the transition state. This is shown in Fig. 3.9(b)(ii) to be achieved by maximising the cap width W_r and minimising the pillar width A_r.

However, three mechanistic variants of Cap Contact are observed, shown in Fig. 3.9(c)(i), and their existence ranges are shown in Figs. 3.9(c)(ii,iii). For ease of comparing the transition mechanisms, in Fig. 3.9(b)(ii) we expressed the Cap Contact energy barrier as a function of the cap width W_r. However, the more pertinent parameter for the internal condensing mode is the inner cap width C_r. We show contour plots for the Cap Contact energy barrier at constant $C_r = 0.15$ and $C_r = 0.25$ in Figs. 3.9(c)(i) and (ii) respectively. When the internal cavity width C_r is small, at large lip depths L_r and large pillar widths A_r, liquid is most readily able to condense within the cavity as the energetic penalty for forming a liquid-vapour interface is offset early in the transition by forming a large energetically favourable liquid-solid contact area. Thus, under these conditions, the critical nucleus is relative small (labelled with the white square). As the cavity size C_r increases, the lip depth L_r decreases, or the pillar widths A_r decreases, the energetic offset for forming the liquid-vapour interface is reduced in magnitude. Thus, the critical nuclei occur later in the transition pathway, with larger energy barriers to overcome. These higher-energy critical nuclei are labelled with black triangles, or grey circles in the most extreme cases.

Over large ranges of structural parameters, we see that two mechanisms are able to be present simultaneously. To conclude this section, in the style of traditional phase diagrams, we present the lowest energy-barrier mechanism at each parameter value tested in Fig. 3.10(a) and (b), and so are able to predict the dominant collapse mechanism for the reentrant and doubly reentrant geometries respectively. For visual clarity, three additional panels are included for each, which represent cuts through the 3D contour plots at constant values of W_r

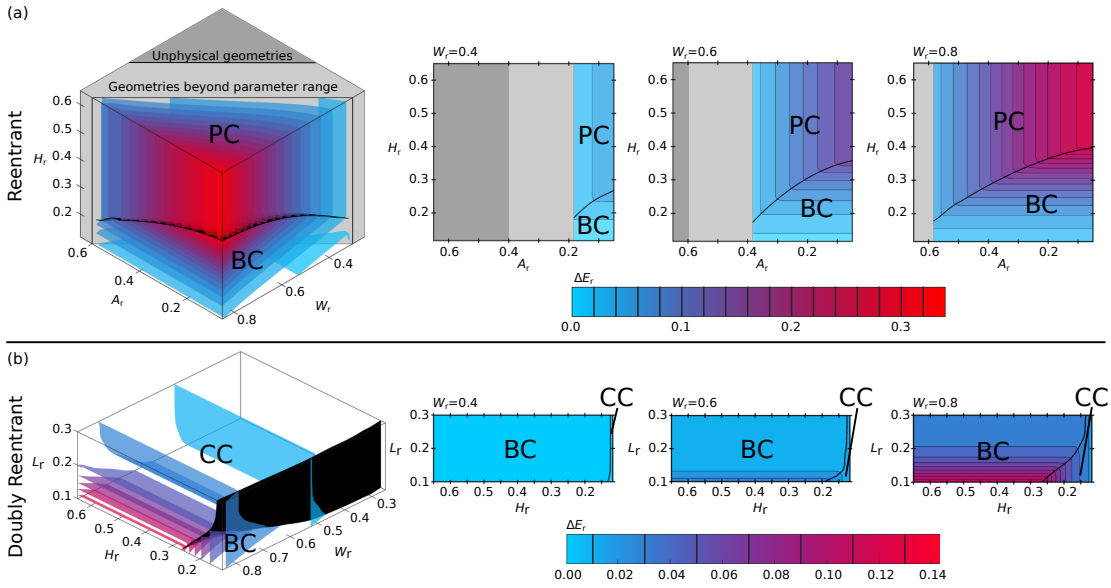

Figure 3.10: (a) 3D contour plot of the lowest energy reentrant geometry transition mechanisms: Base Contact, BC; and Pillar Contact, PC. Three slices through the 3D contour plot are also shown for W_r = 0.4, 0.6, and 0.8. Impossible geometries with pillar widths A_r wider than the cap width W_r are shaded in dark grey. Geometries approaching this limit and requiring infeasibly large computational domains are shaded in light grey. (b) 3D contour plot of the lowest energy doubly reentrant geometry transition mechanisms: Base Contact, BC; and Cap Contact, CC. Three slices through the 3D contour plot are also shown for W_r = 0.4, 0.6, and 0.8.

= 0.4, 0.6, and 0.8. For both geometries these panels highlight the increasing barrier with increasing cap width W_r (all other parameters fixed), as well as the competition between the transition mechanisms.

Beginning the reentrant geometry, Table 3.1 shows that the interface morphology of Base Contact depends on the pillar height H_r and cap width W_r. As both of these structural parameters increase, the liquid-vapour interface increases in area leading to an increase in ΔE_r. However, ΔE_r cannot be increased indefinitely by increasing H_r, as at a critical pillar height, the height-independent Pillar Contact mechanism becomes the lowest energy transition pathway. As the Pillar Contact transition state is associated with the liquid wetting the reentrant cap underside, ΔE_r is increased by expanding the liquid-vapour interfacial area required to do so. This requires W_r to be maximised, and the pillar width A_r to be minimised. In designing a reentrant structure exhibiting the maximum energy barrier, the mechanistic switch upon increasing H_r is a key point to highlight as, assuming taller pillars are mechanically weaker than shorter pillars [76, 175], at a given W_r and A_r the optimal structure height is that on

the BC-PC boundary.

For the doubly reentrant geometry, we find in Table 3.1 that the minimum energy barriers depend on four parameters: the Cap Contact energy barrier depends on W_{r}, A_{r}, and the lip depth L_{r}, whereas the Base Contact barrier depends on W_{r} and also H_{r}. However, ubiquitously the lowest Cap Contact barriers are obtained by minimising A_{r}, such that the barrier diagram shown in Fig. 3.10(b) is at constant $A_{\mathrm{r}} = 0.05$.

Regarding the Base Contact mechanism, the only effect on changing from a reentrant to doubly reentrant geometry is to increase the range of W_{r} and H_{r} for which the Base Contact mechanism is operative. However, except for the smallest pillar heights, the Cap Contact mechanism has a significantly smaller ΔE_{r} compared to the Base Contact barrier. This is principally caused by the condensing critical nucleus having a relatively small, energetically unfavourable liquid-vapour interfacial area, compared to the large, energetically favourable solid-liquid interfacial area. Therefore to maximise the Cap Contact barrier, the liquid-vapour interfacial area must be maximised, whilst minimising the solid-liquid contact area. This is effectively realised by maximising W_{r} and minimising L_{r} and A_{r}. As the Cap Contact mechanism is independent of the height of the structure, in a similar manner to the reentrant structure the optimal pillar height is located on the boundary between the two failure mechanisms.

3.5.2 Non-wettable surfaces

Next, we discuss and quantify how the transition energy barriers on non-wetting geometries depend on the structural parameters. For this survey, we use a representative non-wetting intrinsic contact angle $\theta_o = 110^\circ$. We begin by discussing the wetting barrier on a post, which will prove to have different characteristics to the later reentrant and doubly reentrant transitions.

The energy barrier of the post is quantified in Fig. 3.11(a). Here, two collapse mechanisms are observed, which are related to the Base Contact and Pillar contact mechanisms highlighted previously, and are suitably described by the general pathways descriptions in Section 3.4. However, there is a significant difference for the post mechanisms: unlike for the reentrant and doubly reentrant geometries, the post mechanisms cannot exist simultaneously for a given structure. For short posts, only the Base Contact mechanism is operative, but above a critical height only the Pillar Contact mechanism is operative. We make this distinction explicit by

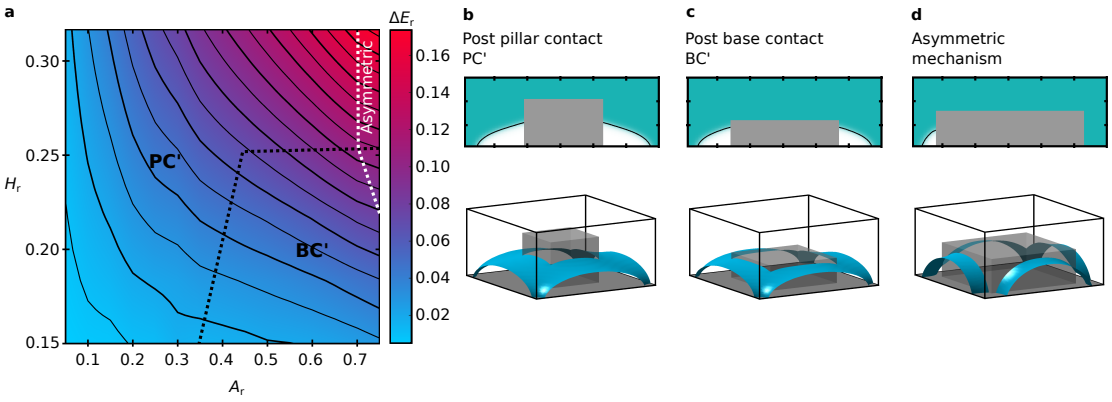

Figure 3.11: (a) Contour map of the reduced energy barrier ΔE_r against the two post structural parameter: the pillar width A, and the post height H. (b,c) 3D images and diagonal cross sections of the two identified transition state types BC' and PC'. (d) 3D image and diagonal cross section of the asymmetric transition state morphology, which may be part of a BC' or PC' transition (the BC' type is shown).

labelling the post Base Contact mechanism BC', and the post Pillar Contact mechanism PC' in Figs. 3.11(b) and (c).

At sufficiently wide and tall post geometries, the system symmetry is broken along the transition pathway. As the liquid-vapour interface sags towards the base of the system, one corner of the base is contacted first, before the others. This can be seen in Fig. 3.11(d). This asymmetric collapse is observed to occur in both BC' and PC' mechanisms. It is speculated that symmetry breaking occurs when there is a large separation of length scales in the system: there is a short gap between the posts, but a long distance along the side of the post from one corner to the next. Thus, each corner is able to act independently, such that at the transition state it is energetically more favourable for one corner to locally increase the liquid-vapour surface area and contact the base of the system, than it is for all four corners increasing the liquid-vapour surface area simultaneously.

As can be seen in the contour plot of Fig. 3.11(a), and summarised in Table 3.2, the energy barrier is increased for increasing pillar height H, and increasing pillar width A. For the BC' transition state, this is because the energetically-unfavourable liquid-vapour interfacial area is increased. For the PC' transition state, the pillar height no longer affects the transition state morphology, and instead the energetic penalty arising from increasing H is attributed to wetting the surface area of the post as the interface descends.

We now examine wetting at $\theta_\circ = 110°$ for the reentrant and doubly reentrant geometries. For both, Base Contact and Pillar Contact mechanisms are observed, and illustrated in Fig.

	Post		Reentrant		Doubly Reentrant	
	BC'	PC'	BC	PC	BC	CC
H_r	●	○	●	○	●	○
W_r	●	●	●	○	●	○
A_r	-	-		●		●
L_r	-	-	-	-	○	○
t_r	-	-	○	○	○	○

Table 3.2: The geometrical parameters affecting ΔE_r for each transition mechanism, labelled by filled and empty circles. Empty circles indicate that the parameter affects ΔE_r, but not the TS liquid-vapour interface morphology. Dashes indicate where a structural parameter is not featured on a geometry.

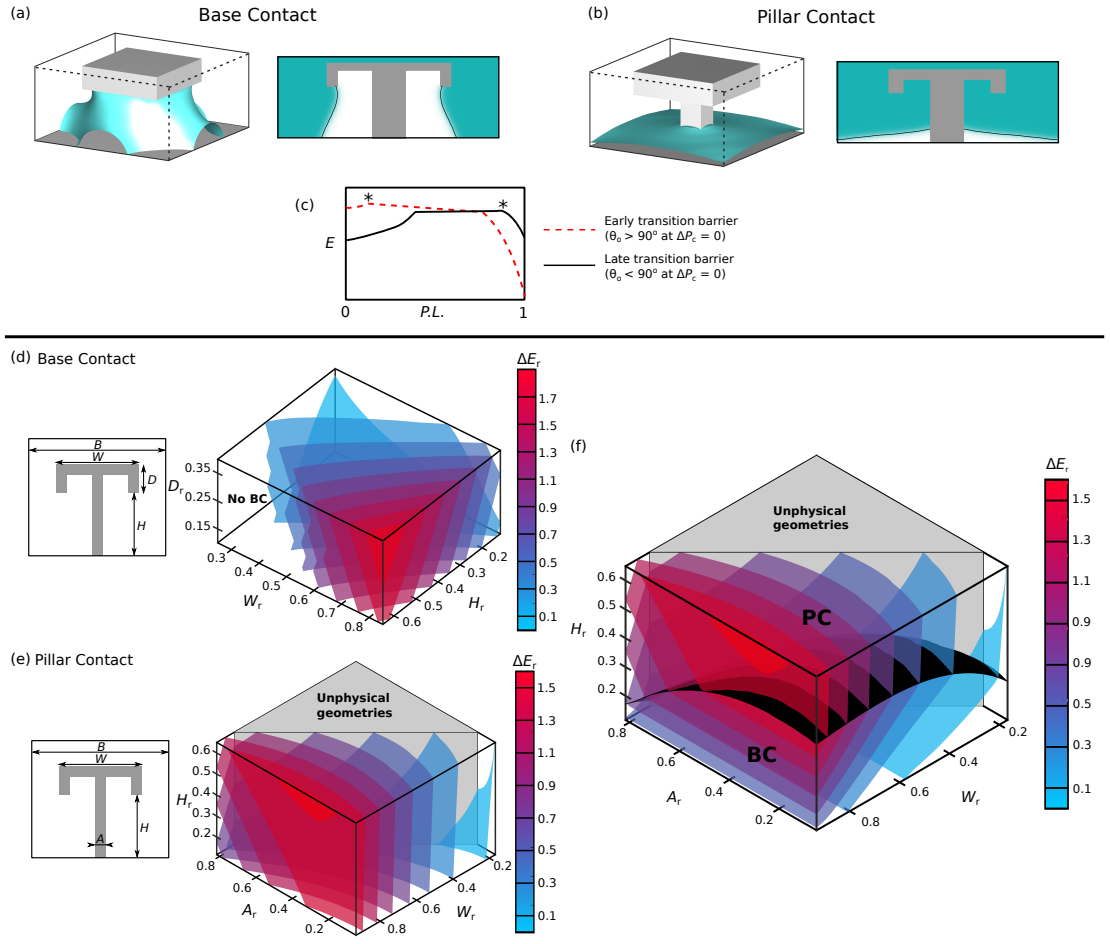

Figure 3.12: (a) 3D visualisation and 2D diagonal cross sections of a representative Base Contact example. (b) 3D visualisation and 2D diagonal cross section a representative Pillar Contact example. (c) Illustration of the two forms of Pillar Contact energetic profiles E as a function of the transition path length $P.L.$, with barriers labelled with a *. $P.L. = 0$ is the suspended state and 1 in the collapsed state. (d-f) 3D contour plots showing the minimum energy barrier for Base Contact (d) and Pillar Contact (e), and the minimum energy transition path (f) as a function of the height H_r, cap width W_r, pillar width A_r, and total lip depth D_r. Markings on the colour bars indicate the energies of each constant-barrier surface.

3.12(a,b). Throughout however, there is negligible difference between the wetting mechanisms for reentrant and doubly reentrant geometries. Both the Base Contact and Pillar contact mechanisms are similar to the $\theta_\circ = 60^\circ$ cases. However for Pillar Contact, as illustrated in Fig. 3.12(c), the energy barrier (*) occurs much later in the reaction pathway for $\theta_\circ = 110^\circ$ (black line) than for $\theta_\circ = 60^\circ$ (red dashed line). Despite the complex interface morphologies, a simple relationship is derived to predict which Pillar Contact variant is operative for a given set of structural parameters. If the total energy of the system is lowered by the liquid-vapour interface sliding down the pillar, the minimum energy barrier occurs early in the transition pathway. This occurs prior to sliding when the liquid contacts the cap, as observed at $\theta_\circ = 60^\circ$. Otherwise, the minimum energy barrier will occur late in the transition, after the sliding process, and immediately before the interface contacts the base of the system, in an identical manner to the post. More generally, we may consider the energy change of an interface sliding down the pillar at constant interface shape. If

$$\Delta P_\mathrm{r} > \frac{4\cos\theta_\circ}{A_\mathrm{r} - \frac{1}{A_\mathrm{r}}}, \tag{3.4}$$

sliding is energetically favourable, and the energy barrier will occur early in the transition mechanism. As we restrict ourselves here to the study of transitions at zero pressure, this explains why the early barrier is observed for $\theta_\circ < 90^\circ$, whilst the late transition is observed for $\theta_\circ > 90^\circ$.

We now consider the minimum energy barrier as a function of the structural parameters. For both mechanisms on the reentrant and doubly reentrant geometries, these dependencies are summarised in Table 3.2. For Base Contact, shown in Fig. 3.12(d), the liquid-vapour interface morphology depends on the pillar height H_r and cap width W_r. As the interfacial area is maximised at large H_r and W_r, the largest minimum energy barriers occur under these conditions. However, upon increasing the height, there exist heights above which the contact line can no longer remain pinned to the outer cap edge, meaning that Base Contact is prevented. For non-wetting liquids, the suspended free energy minimum sees the interface pinned to the top of the cap (at zero applied pressure), whereas the liquid must wet the entire sides of the cap to overcome the minimum energy barrier. Thus, in contrast to $\theta_\circ = 60^\circ$, at $\theta_\circ = 110^\circ$, the minimum energy barrier is increased by increasing the total lip depth D_r.

In the Pillar Contact mechanism, shown in Fig. 3.12(e), the liquid-vapour interface

morphology at the minimum energy barrier is affected only by the pillar width A_r. However, during the transition, almost the entire solid area of the reentrant or doubly reentrant pillar becomes wetted, yielding a concomitant energetic penalty. Therefore, the minimum energy barrier depends on all structural parameters, but in Fig. 3.12(e) we choose to fix $D_r = 0.15$. Although the doubly reentrant cap structure has a larger surface area than the reentrant cap, for the parameter ranges considered here this only marginally impacts the minimum energy barrier.

Finally, over the range of structural parameter values, we evaluate the minimum energy transition mechanism, shown in Fig. 3.12(f). In this, we fix $D_r = 0.15$. At the lowest pillar heights, the Base Contact mechanism is operative, but changes to Pillar Contact once the energetic penalty for forming the large liquid-vapour interface in Base Contact becomes too large. Unlike in the $\theta_o = 60°$ case, here the barrier can be increased indefinitely by increasing the total solid area of the structure which is wetted during the transition. This can be achieved effectively through extending H_r (as with the post) or D_r.

3.6 Contact angle effects of the MEP

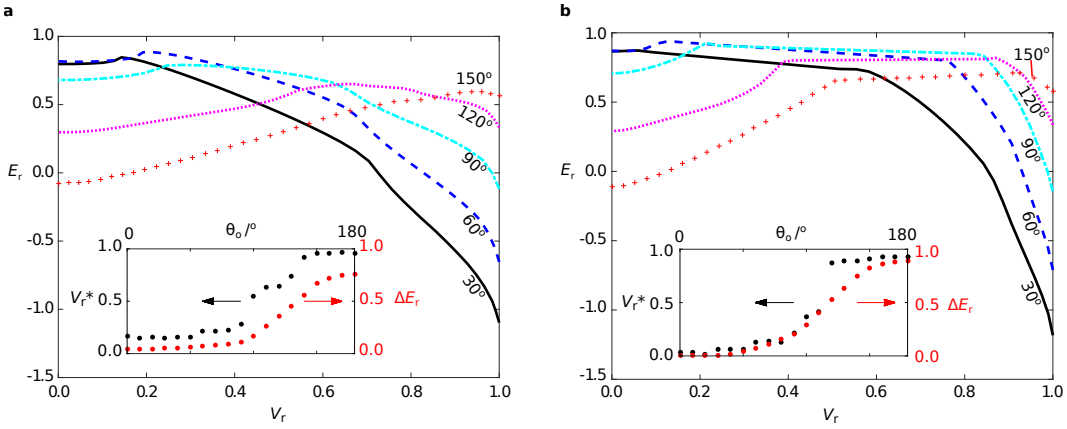

Figure 3.13: The influence of θ_o (labelled) on the energetic profiles of the Base Contact (a) and Pillar Contact (b) mechanisms. The transition profiles are obtained via DNEB. All transitions are carried out at $\Delta P_r = 0.15$. Inset: the variation of the position (black) and energy (red) of the transition state (relative to the suspended minimum free energy) as θ_o is varied.

We conclude this chapter by examining the effects of the intrinsic contact angle on the wetting energy pathway. We begin with the reentrant geometry, as we are able to examine both the Base Contact and Pillar Contact mechanisms across a large range of θ_o. The

dependence of BC and PC on θ_o are shown in Fig. 3.13 (a) and (b) respectively, in which the transitions here are carried out at $\Delta P_r = 0.15$. The transitions are followed through consideration of the reduced liquid volume, V_r,

$$V_r = \frac{V - V_S}{V_C - V_S}. \tag{3.5}$$

Here, V is the absolute liquid volume within the system at a point along the MEP. V_C and V_S are the liquid volumes in the collapsed and suspended states respectively.

For the base contact mode, as θ_o is increased, the energy barrier ΔE_{r} evidences a large increase between 90° and 140°. At low contact angles, the transition state occurs when the sagging liquid-vapour interface first contacts the system base. However, for $\theta_o \geq 140°$, although the same Base Contact mechanism is followed, the transition state occurs immediately prior to the interface contacting the pillar in the final stages of the transition. A crossover regime is observed close to $\theta_o = 130°$, in which the transition state occurs between the interface contacting the base and the pillar. This change in transition state position are evidenced by and increase in the reduced liquid volume at the transition state, V_r^*.

Pillar Contact also shows a jump in both the transition state energy and location between $\theta_o = 110°$ and $\theta = 120°$. We may therefore test Eq. (3.4) to estimate when it becomes energetically favourable for the interface to slide down the pillar. Here, for a reduced width $A_{\mathrm{r}} = 0.083$ at pressure $\Delta P_r = 0.15$, (3.4) predicts that the change in transition state location at $\theta_o = 117°$, consistent with the observation in Fig. 3.13 (b).

Qualitatively, the same characteristics are observed on the post and doubly reentrant geometries, but with the post, no transition is possible when the suspended state is unstable, and for the doubly reentrant geometry, Cap Contact occurs for $\theta_o > 90°$.

We further investigate the dependence of Cap Contact on θ_o in Fig. 3.14. As the transition state occurs within the cap filling process, we show only the transition profiles between the suspended bottom (B), and suspended bottom, cap-filled ($\mathrm{B_N}$) states. Here, the transitions are followed through consideration of the reduced liquid volume, V_r':

$$V_r' = \frac{V - V_B}{V_{B_N} - V_B}. \tag{3.6}$$

In Fig. 3.14, it can be seen that as θ_o increases, the transition state is located increasingly late in the pathway. For $\theta_o = 60°$, the transition state is of type i (shown in Fig. 3.9(c)),

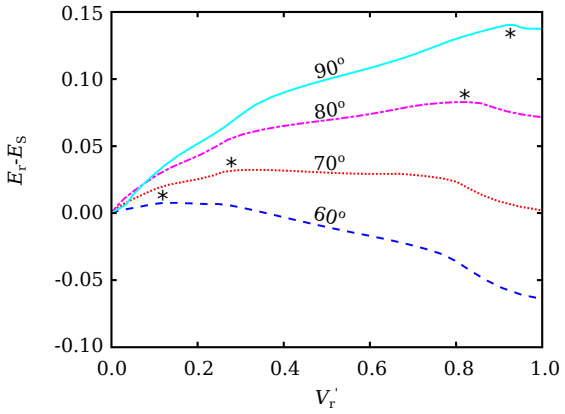

Figure 3.14: The influence of θ_o (labelled) on the energetic profiles of Cap Contact, for the cap-filling process. The energy shown is referenced to the suspended bottom energy in each case, E_B. The transition profiles are obtained via the string method with 30 images. All transitions are carried out at $\Delta P_r = 0.0$. The path distance measure V_r' is the reduced liquid volume in the system, compared to the suspended state. Transition states are highlighted with a '*'.

increasing in liquid volume to type ii at $\theta_o = 70°$, and again to type iii at $\theta_o = 80°$ and $90°$. As θ_o increases, two effects occur to increase the energy of the transition state: firstly, wetting the solid surface becomes more energetically expensive, and secondly, the area of the energetically unfavourable liquid-vapour interface increases in moving from type i to ii to iii.

3.7 Discussion and conclusions

In this chapter we began by showing a selection of the broad range of possible minimum energy configurations of a liquid interacting with a post, reentrant, and doubly reentrant surface geometry. We also showed the existence ranges of a selection of these minima pertinent to liquid-repellent surfaces, over a range of intrinsic contact angles and pressure differences across the liquid vapour interface. On the post, a suspended state was observed to exist over a limited contact angle and pressure range, compared to the reentrant and doubly reentrant geometries. These latter two geometries demonstrated how pinning to the bottom of the cap allowed for a suspended state, even for wetting, pressurised liquids. The wide base of the post was also observed to facilitate condensation below approximately $\theta_o = 45°$, and facilitate cavitation above $\theta_o = 135°$. This cavitation led to a monostable suspended state (neglecting the empty state), a phenomenon also observed recently in experiments [52]. Condensation and cavitation was also prevalent over similar contact angle ranges within the doubly reentrant cap. For highly-wetting liquids, condensation of liquid to fill the cap actually

resulted in a decrease in the high-pressure existence limit of the suspended state, compared to the reentrant geometry. It was hypothesised at this point that condensation within the cap may be problematic for practical doubly reentrant surface.

Leading on from this, three minimum energy wetting mechanisms between the suspended and collapsed state were presented: Base Contact, Pillar Contact, and Cap Contact. The minimum energy barriers for each of these mechanisms, where they existed, were systematically surveyed across the range of structural parameters. This was performed firstly for a wetting liquid ($\theta_o = 60^\circ$) in contact with the reentrant and doubly reentrant geometries. Base Contact and Pillar Contact were able to operate on the reentrant geometry, while Base Contact and Cap Contact operated in the doubly reentrant geometry. Where there was a competition in mechanisms, we evaluated which had the lowest energy barrier, forming the true lower bound to the collapse process. Notably, on the doubly reentrant geometry, the Cap Contact condensation mechanism featured a lower barrier than Base Contact for all but the shortest pillar heights. A large cap cavity size and small lip depth was shown to be effective at increasing this barrier to condensation, but we shall return to this important issue in more detail in Chapter 6.

For non-wetting liquids ($\theta_o = 110^\circ$), Base Contact and Pillar Contact competed for the minimum energy mechanism over a range of structural parameters on the reentrant and doubly reentrant geometries. On the post however, there was never a competition - only one pathway was available on a given structure.

Finally, we investigated the impact of changing the intrinsic contact angle on the transition energy profile. For Base Contact and Pillar Contact, increasing the contact angle resulted in the transition state occurring later in the pathway. This was also observed for Cap Contact, but the transition state was observed to jump between three distinct morphologies.

The principal aim of this chapter was to investigate how the structure of a single feature influenced the wetting transition, and in particular the barrier to wetting. The systematic surveys performed mean that this investigation is complete for the square post, reentrant and doubly reentrant geometries. However, as has been shown recently, the transition mechanism on arrays of geometries differs from a single geometry (with periodic boundary conditions), as the transition breaks the symmetry of the system to lower the overall energy barrier [168,169]. This symmetry breaking is a property of the arrangement of geometries, so that in real systems, we anticipate that the minimum energy pathway is affected by an interaction between

the local structure of the geometry, and the global structure of the arrangement of geometries. A key future investigation will be to investigate this interaction, not only for a square array, but other surface tilings or even stochastic surfaces. Related to this latter point, for defective surfaces where pillars are removed (or presumably stochastic surfaces where a low pillar density occurs), collapse is readily initiated from this site to propagate through the entire surface texture [176]. An interesting and important avenue for future work will therefore be how to design structures which are capable of preventing global collapse, if local failure occurs.

Chapter 4

Designing optimal superomniphobic surfaces for real-world applications: Contact angle hysteresis, critical pressure, and simultaneous optimisation

4.1 Introduction

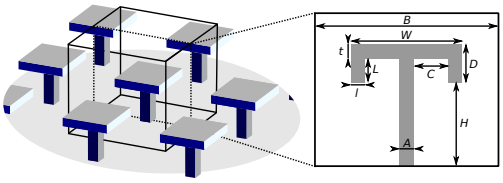

Figure 4.1: Illustration of the 3D simulation repeat unit (left), with 2D cross section showing labelled structural parameters (right).

In Chapter 1, a wide range of potential applications were highlighted for reentrant and doubly reentrant geometries, due to their ability to suspend highly wetting liquids, even when pressurised. Currently, breakthroughs are being made in techniques to fabricate these complex surface structures [60,61,73,74]. However, a large obstacle still exists to widespread development: it is not known how to design the surface structures to enable optimal performance in real-world applications. Successful superomniphobic designs must exhibit three key wetting properties: (1) a low contact angle hysteresis to maximise liquid mobility [56], (2) a high critical pressure, the maximum sustainable pressure at which the suspended state is stable [177], (3) a high energetic barrier to failure, in which liquid infiltrates the surface texture and the high liquid mobility is lost [154]. The complex surface designs mean that

both computational and experimental studies have been expensive and time-consuming to perform, and so are largely restricted in scope to considering only single wetting properties - never all three.

In this chapter, we investigate how the surface design parameters illustrated in Fig. 4.1 affect both the contact angle hysteresis and critical pressure. We then incorporate the minimum energy barrier investigation from Chapter 2 to design optimum geometries for real-world applications. The specialist methods used to simulate these wetting properties, and perform the optimisation are presented first in Section 4.2.

In Section 4.3, we present a detailed analysis of the contact angle hysteresis, CAH, which on intrinsically non-wetting geometries is well-studied. The advancing mechanism is found to be simple and geometry-independent. For large drops, or at zero Laplace pressure, the liquid advances when the liquid-vapour interface spans two adjacent pillar tops, achieved ubiquitously at $\theta_a = 180^\circ$ [178].

The receding mechanisms do however depend on the pillar geometry, with two models extensively discussed. In the differential-area model [179], it is assumed that the receding contact angle depends only on the energetics of moving the contact line by a small distance. This is shown to be adequate at describing θ_r on large area-fraction pillars in experiments and simulations [180, 181]. However, in experiments at small pillar area fractions, a significant distortion of the liquid-vapour interface has been observed in the vicinity of the contact line. In this, a capillary bridge is strained between the top of the pillar and the bulk receding liquid, [147, 178, 182–186], with detachment of the bridge leading to residual droplets on the pillar tops [187, 188].

Prior to this work, only a very small number of previous experimental studies investigated the contact angle hysteresis on intrinsically wetting structured surfaces (see for example the CAH on reentrant geometries in [183] and [175]). A principal outcome of Section 4.3 will therefore be a quantitative analysis of the CAH on wettable surfaces, alongside new receding models to effectively describe the multiple receding mechanisms.

Next, in Section 4.4, we explore the stability limit of the suspended state upon the application of a pressure difference across the liquid-vapour interface. These axisymmetric solutions to the Young-Laplace equation in Eq. (1.5) describe the shapes of capillary bridges that span between two planar boundaries [59]. We will show how a capillary bridge description can be used in a new way to successfully approximate the critical pressure interface morphologies.

In Section 4.5, we finally consolidate our quantitative analyses of the contact angle hysteresis, critical pressure and the minimum energy barrier, to design structures with optimised wetting properties for real-world applications. However, this optimisation will prove to be non-trivial, as the structural parameters of the design couple each wetting property antagonistically. For example, we will show that two effective ways to increase the critical pressure are to decrease the pillar-pillar separation, and decrease the system scale. However, decreasing the separation results in an increase in the contact angle hysteresis, whereas decreasing the system scale decreases the energetic barrier to the wetting transition due to the liquid-vapour interfacial area decreasing in squared proportion. It has been previously suggested that optimised superhydrophobic surfaces can be achieved through minimising the scale of low surface-fraction pillars [185], but as we shall see, the new minimum energy barrier considerations bound from below the optimal system scale. We also note that the three-aspect perspective has been introduced and advocated before [56], but the lowest-energy failure mechanisms have never been calculated nor incorporated into an optimisation strategy.

To illustrate the importance of multifaceted optimisation, we go on to consider two relevant example applications: water purification via membrane distillation, and droplet-based digital microfluidics. Membrane distillation shows significant potential as a sustainable, low-energy water purification technology, capable of extracting potable drinking water from highly contaminated water sources (see [189] for an overview and [66, 67] for recent reviews). A significant challenge however is that oils readily foul the membranes, leading to a breakdown in device performance. Meanwhile, digital microfluidics is a droplet-on-surface technology [190] that is anticipated to enable re-usable, re-configurable, and material-efficient lab-on-chip devices [71]. In this technology, the major challenge is that commonly-used but low surface tension solvents pin strongly to the surface, leading to drop immobilisation and device failure [191]. We find here that the doubly reentrant surface geometry is ideally situated to meet these challenges, as it is robust to pressure even for highly-wetting or surfactant-contaminated liquids.

In such complex surface designs featuring many antagonistically-coupled wetting properties, we recognise that it is not always desirable to perform large-scale wetting property surveys. Thus, we also develop a genetic algorithm, described in Section 4.2.3, to perform the simultaneous optimisation with high efficiency, offering a speedup of up to 10,000×.

4.2 Methods

4.2.1 Contact angle hysteresis

To simulate the advancing and receding liquid morphologies, we adapted the microchannel setup used by Mognetti and Yeomans [181]. In this, a single column of surface structures patterned the base of the microchannel with microscopic contact angle $\theta_\circ = 60°$ to model wetting surfaces, and $\theta_\circ = 110°$ for non-wetting surfaces. These contact angles were chosen to be representative of commonly used solvents and surfaces (see for example [192]).

The base of each individual structure was centred within a square of $N_\mathrm{x} \times N_\mathrm{y} = 60 \times 60$ lattice spacings, where each lattice spacing was equal to the interface width ϵ. Thus, in units of ϵ the system size $B = 60$. Throughout, the variable surface structure dimensions shown in Fig. 4.1 are reported relative to the system size B and indicated with a subscript 'r'. For example the reduced cap width is $W_\mathrm{r} = W/B$. We fixed the cap thickness t_r and lip width l_r at 0.05. For the reentrant geometries, the lip depth was set to $L_\mathrm{r} = 0$.

The top of the channel was capped with a smooth surface of variable contact angle θ, and was set above the top of the surface structures at a height of 40 lattice units. This height was chosen to ensure that the top surface did not influence the advancing and receding interface morphologies, which is evidenced as the interface being planar at the top surface.

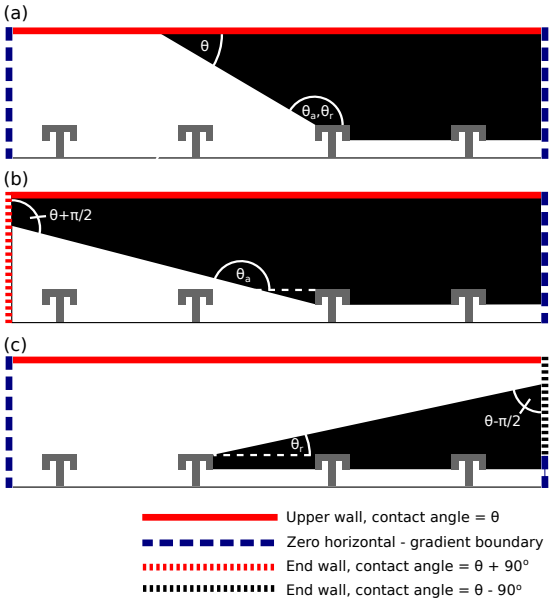

Figure 4.2: Microchannel boundary conditions for: (a) the conventional setup, (b) the advancing case where $\theta < 20°$, (c) the receding case where $\theta > 160°$.

For the majority of CAH simulations, the boundary conditions employed were as shown

in Fig. 4.2(a). Here, the gradient in ϕ perpendicular to the end walls was fixed at zero, enforcing bulk fluid behaviour. To determine θ_{a}, an iterative process was used in which θ was incremented and the free energy minimised, up to the point at which the advancing interface morphology was obtained to a precision of 0.1°. At convergence, the advancing contact angle $\theta_{\mathrm{a}} = 180^\circ - \theta$. An identical process was used to determine the receding interface morphology. At convergence, the receding contact angle $\theta_{\mathrm{r}} = 180^\circ - \theta$. The relationships between θ_{a}, θ_{r}, and θ are indicated in Fig. 4.2(a). Due to the small inherent inaccuracy of the prescribed contact angle in the phase field method, as shown in Chapter 1, after convergence we then determined the true contact angle through a linear fit to the interface in the vicinity of the contact line. The typical uncertainty associated with this measurement was 1°.

Special modifications to the microchannel were required when advancing at $\theta < 20^\circ$, or receding at $\theta > 160^\circ$, as the diffuse interface caused a reduction in contact angle accuracy. In the former case, as shown in Fig. 4.2(b), the advancing-end boundary was replaced by a wall with contact angle equal to $\theta + 90^\circ$. As before, $\theta_{\mathrm{a}} = 180^\circ - \theta$. In the latter case, as shown in Fig. 4.2(c), the receding-end boundary was partially replaced by a wall with contact angle equal to $\theta - 90^\circ$. As before, $\theta_{\mathrm{r}} = 180^\circ - \theta$. The height at which this wall started was between the lip bottom and top, so as not to artificially affect the interface morphology, or receding contact angle. In both cases, the end walls were located sufficiently far from the contact line pinning location that the interface was planar in the end wall vicinity.

4.2.2 Critical pressure

For each critical pressure simulation, a double-resolution system was employed in which the solid structure was centred within a simulation volume of $N_{\mathrm{x}} \times N_{\mathrm{y}} \times N_{\mathrm{z}} = 240 \times 240 \times (H + D + 16)$ where the lattice spacing was equal to $\epsilon/2$. Thus, in units of ϵ, the system size $B = 120$. This was used to ensure that the contact line pinning at the critical pressure was not sensitive to the diffuse interface width. As the critical pressure interface morphologies never broke the square symmetry of the system, computational efficiency was increased by simulating one quarter of the system: $x \in [0, N_{\mathrm{x}}/2], y \in [0, N_{\mathrm{y}}/2], z \in [0, N_{\mathrm{z}}]$. Mirror boundary conditions at $x = 0, N_{\mathrm{x}}/2$ and $y = 0, N_{\mathrm{y}}/2$ maintained the square symmetry. The z-gradient at $z = N_{\mathrm{z}}$ was set to zero to enforce bulk fluid behaviour. Each system was initiated in a zero-pressure suspended state, then the critical pressure was found by an iterative process of pressure increase and energy minimisation. The largest ΔP_{r} at which the suspended state remained

stable was determined with a precision of $0.01\gamma_{\mathrm{lv}}/B$.

4.2.3 Genetic algorithm

For efficient multifaceted optimisation of the structures, a genetic algorithm was established. We began by randomly sampling the parameter space to generate an initial population of 40 surface structures. These were ranked based on score, and the top 20 retained for breeding. Candidate pairs for breeding were selected at random, and breeding occurred if the geometric mean of their scores was greater than a random number between 0 and 1. The offspring were equally likely to inherit each attribute from either parent. Each attribute was then mutated if a random number bewteen 0 and 1 was less than the current mutation probability p_i (set initially at 0.5). For the discrete structural variables, a mutation changed the attribute randomly by between -3 and 3 lattice spacings. For the continuous variable (system scale), the change in $\log(B/B_{\mathrm{ref}})$ was selected randomly from the range -0.3 and 0.3. The mutation probability was reduced each generation, such that $p_{i+1} = p_0 \times$ (standard deviation of scores in previous generation)$^{1/2}$. Any offspring bred or mutated outside the testable parameter range were mutated back into the testable parameter range. The algorithm was deemed to have converged when the mutation rate decreased to zero.

4.3 Contact angle hysteresis

4.3.1 Wettable surfaces

We begin by quantifying the CAH in Fig. 4.3(a), and its deconstruction into θ_a in Fig. 4.3(b) and θ_r Fig. 4.3(c). We then devote the remainder of this section to discussing the mechanisms leading to the observed advancing and receding contact angles.

The advancing and receding interfaces are simulated across the range of structural parameters illustrated in Fig. 4.1. As shown in Fig. 4.3(a), only two parameters are found to affect the CAH: the area fraction $F_r = (W_r/B)^2$, and the total lip depth D_r. The CAH is minimised at low area fractions and maximised at high area fractions, in agreement with previous observations [175]; however at a fixed F_r, the total lip depth that minimises the CAH occurs at an intermediate value in the range tested. This is caused by a competition in the rate of decrease in both θ_a and θ_r as D_r increases.

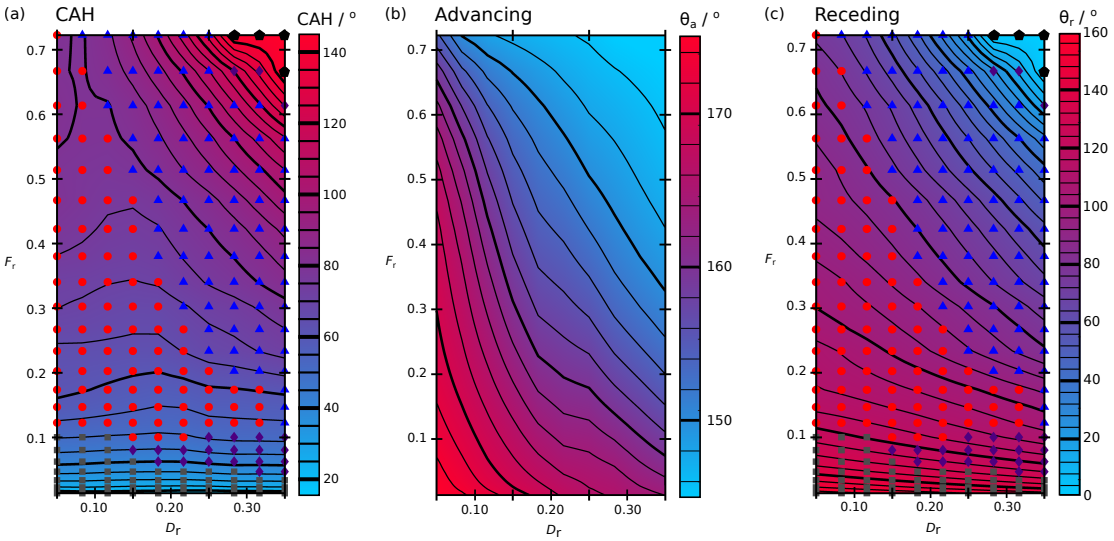

Figure 4.3: (a) Contour plot showing the variation in CAH with the cap area fraction F_{r} and total cap height D_{r}. This is decomposed into the advancing contact angle θ_{a} in (b), and the receding contact angle θ_{r} in (c). Symbols indicate the receding mechanisms detailed in Section 4.3.1: bridge depinning (grey squares), edge depinning (red circles), lip depinning (blue triangles), non-depinning (black pentagons), and hybrid mechanisms (purple diamonds).

Advancing interfaces

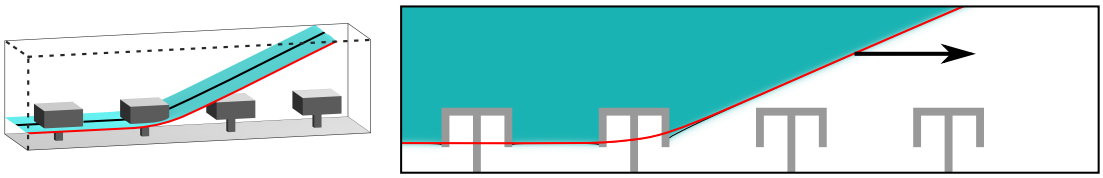

Figure 4.4: Visualisation of the advancing mechanism in 3D, the liquid-vapour interface shown as the blue surface. A 2D cross-section through the centre of the system is also shown, where the black line highlights the position of the liquid-vapour interface at the centre of the system, while the red line marks its position at the edge. The black arrow indicates the advancing direction.

In Fig. 4.3(b), we show the advancing contact angles measured from simulations. Across the simulated parameter range, the same advancing mechanism is observed, illustrated in Fig. 4.4. In this, the advancing occurs when the angle of the approximatively planar liquid-vapour interface results in the liquid contacting the cap of the neighbouring structure. Furthermore, as the liquid-vapour interface never impinges under the cap, θ_{a} is identical for both reentrant and doubly reentrant geometries.

For all practical surfaces used in superomniphobic applications, the advancing contact angle θ_{a} exceeds 160°, shown in Fig. 4.3(b). $\theta_{\mathrm{a}} < 160°$ is only observed for large lip depths and area fractions, both of which are effective at pinning the advancing interface to the

advancing bottom edge of the cap. Although limited, a direct comparison with previous experimental results can be made at $F \approx 0.196$, $D_r = 0.087$ and 0.17, in which octane was found to make a microscopic contact angle with surface of 60° [175]. Experimentally, $\theta_a \approx 157°$ and 152° for each D_r respectively, compared to $\theta_a = 169°$ and 163° measured in this simulation. The 7% difference between each value is negligible compared to the experimental precision of measuring such large contact angles [193].

Receding interfaces

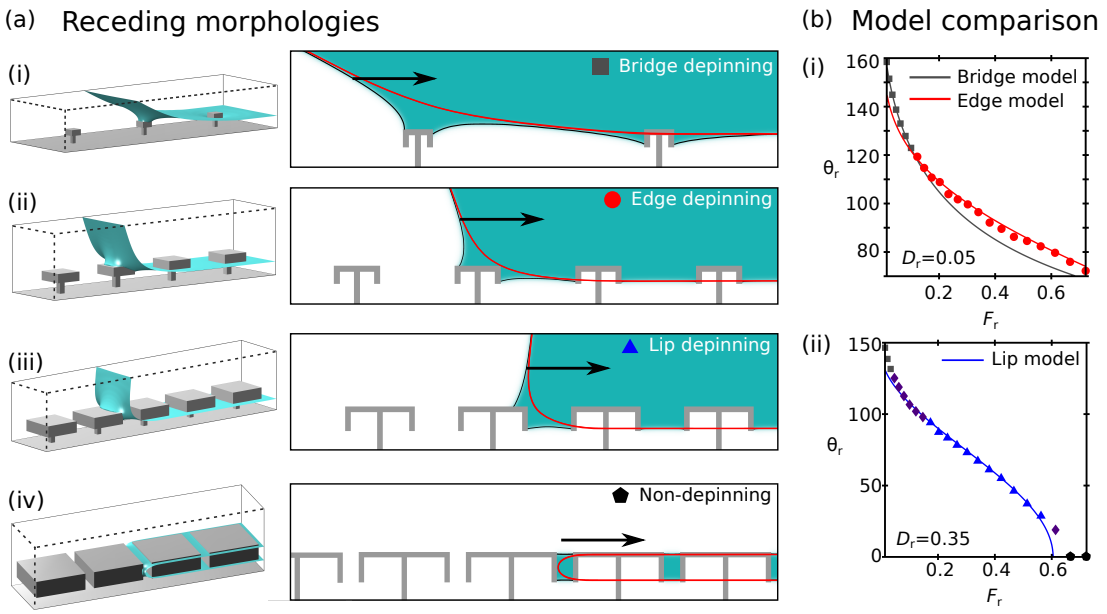

Figure 4.5: (a) Visualisations of the four major receding mechanisms. In 3D, the liquid-vapour interface is shown as the blue surface. In 2D, a cross-section through the centre of the system is shown, where the black line highlights the position of the liquid-vapour interface at the centre of the system, while the red line marks its position at the edge. The black arrow indicates the receding direction. (b) Comparison of the bridge-, edge-, and lip-depinning receding models (solid lines, colour-coded) against the simulated θ_r (data points); examples shown with varying F_r at fixed $D_r = 0.05$ and 0.35. The ±1° error bars in the simulation data are too small to be seen.

In contrast to the advancing contact angles, the receding contact angles shown in Fig. 4.3(c) span almost the entire possible contact angle range. We now compare the simulated θ_r with the same experiments as discussed for θ_a [175]. At $D_r = 0.087$ and 0.17, experimentally $\theta_r \approx 108°$ and 99° respectively. Via simulation, we observe $\theta_r = 108°$ and 103° respectively. Within the error margins (±2° in experiment, ±1° in simulation), the experimental and simulation results are in very good agreement.

The receding mechanisms are found to exhibit significant variation across the parameter

range. This will be shown to lead to the large variation in θ_r observed in Fig. 4.3(c), which is primarily responsible for the large variation in CAH observed in Fig. 4.3(a). Overall, four dominant receding mechanisms are observed: bridge, edge, and lip depinning, and a fourth non-depinning mechanism. Characteristic examples of these are shown in Fig. 4.5(a)(i-iv) respectively. The operative regions of each mechanism are labelled in Fig. 4.3(a) and (c), indicated by grey squares, red circles, blue triangles and black pentagons respectively. The hybrid depinning mechanisms (purple diamonds), indicate the regions in which the dominant mechanisms smoothly interpolate. We now describe and model each of these receding mechanisms in turn.

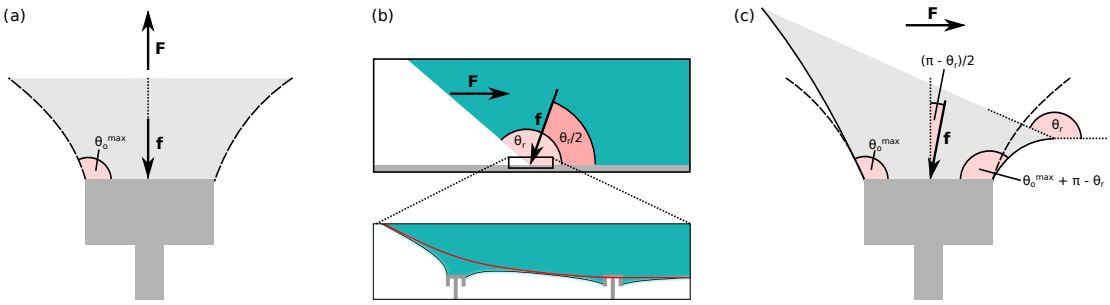

Figure 4.6: Observation and construction of the bridge depinning model. (a) Force balance occurring at the point of depinning for a vertically strained capillary bridge. The solid reentrant geometry is shown in dark grey, the liquid in pale grey. The system is axisymmetric about the vertical dotted line. (b) Macroscopic view of the receding interface (top), with magnification about the three-phase contact line to observe the bridge depinning mechanism (bottom). (c) Model of a single capillary bridge being strained in the receding direction. Dashed black lines indicate the original liquid-vapour interface shape for the vertically strained bridge in (a), whilst the solid black lines indicate the strained interface shape.

Bridge depinning. For the lowest area fractions, at the point of receding, the three-phase contact line is pinned to the outermost pillar around the top perimeter of the cap, shown in Fig. 4.5(a)(i). A capillary bridge is strained between the cap and bulk liquid, such that receding occurs at the point of bridge depinning. This matches what has been observed experimentally [185, 186, 194]. We note that in some experiments, residual droplets are able to be observed on the pillar top after the bridge detachment event [187, 188]. We do not observe this in simulations as the system morphologies we observe are equilibrium morphologies, so that any residual droplet (of higher pressure than the bulk fluid) is evaporated at thermodynamic equilibrium.

We will now outline, quantitatively test, and improve the bridge-depinning receding model proposed by Butt *et al.* [185, 186]. In order to model the bridge depinning mechanism, we

begin by considering the maximum pinning force a capillary bridge can achieve when being strained parallel to its axis, illustrated in Fig. 4.6(a). In this, we show a 2D slice through the centre of an axisymmetric system. The axis of symmetry is denoted by the vertical dotted line. Assuming the contact angle at the three phase contact line is uniform throughout, at the point of depinning the maximum pinning force $\mathbf{f}$ is expressed as

$$|\mathbf{f}| = \gamma_{\mathrm{lv}} m \sin \theta_{\circ}^{\max}, \tag{4.1}$$

where m is the contact line length, and $\theta_{\circ}^{\max}$ is the corrected contact angle. $\theta_{\circ}^{\max}$ is defined as $\theta_{\circ}^{\max} = \max[\theta_{\circ}, \pi/2]$. The form of $\theta_{\circ}^{\max}$ can be rationalised by considering that the maximum pinning force occurs when $\theta_{\circ} = \pi/2$. If $\theta_{\circ} > \pi/2$, before the maximum pinning force is reached, the Gibbs pinning criterion breaks down and the interface slides across the cap, leading to $\theta_{\circ}^{\max} = \theta_{\circ}$. If however $\theta_{\circ} < \pi/2$, Gibbs pinning criterion does not break down before the maximum pinning force is reached, so that for all $\theta_{\circ} < \pi/2$, $\theta_{\circ}^{\max} = \pi/2$.

In receding systems, the capillary bridge is strained along the receding direction, shown in Figs. 4.6(b) and (c). Following a previous derivation [185], but augmented with our treatment of $\theta_{\circ}^{\max}$, two effects arise. Firstly the direction of the pinning force $\mathbf{f}$ balances the capillary forces arising from the front and receding edge of the cap, and so forms an angle which bisects the receding contact angle [195], shown in Fig. 4.6(b). Secondly, the contact angle around the contact line varies between a maximum value at the innermost edge (right hand side of Fig. 4.6(c)), to a minimum value at the outermost edge (left hand side of Fig. 4.6(c)). At the innermost edge, the receding angle increases the local contact angle to $\theta_{\circ}^{\max} + \pi - \theta_{\mathrm{r}}$. At the outermost edge, the contact angle cannot be reduced from $\theta_{\circ}^{\max}$, otherwise the contact line would depin. The pinning force $\mathbf{f}$ is assumed to depend on the average contact angle $\bar{\theta}$, approximated as $\bar{\theta} = \theta_{\circ}^{\max} + (\pi - \theta_{\mathrm{r}})/2$.

At equilibrium, the horizontal component of the microscopic pinning force $\mathbf{f}_{\mathrm{h}}$ must balance the macroscopic receding force $\mathbf{F}$, leading to

$$\begin{aligned} |\mathbf{f}_{\mathrm{h}}| &= \gamma_{\mathrm{lv}} m \sin \bar{\theta} \sin\left(\frac{\pi}{2} - \frac{\theta_{\mathrm{r}}}{2}\right), \\ &= \gamma_{\mathrm{lv}} m \cos\left(\theta_{\circ}^{\max} - \frac{\theta_{\mathrm{r}}}{2}\right) \cos\frac{\theta_{\mathrm{r}}}{2}. \end{aligned} \tag{4.2}$$

On the macroscale, the force $\mathbf{F}$ required to displace a contact line of length B is expressed

via the Young-Dupré equation for the work of adhesion: $|\mathbf{F}| = \gamma_{\mathrm{lv}} B\,(1 + \cos\theta_{\mathrm{r}})$. Thus, by equating $|\mathbf{f}_{\mathrm{h}}| = |\mathbf{F}|$ and manipulating the equality, we arrive at a general expression for the receding contact angle for liquids of all wettabilities:

$$\tan\frac{\theta_{\mathrm{r}}}{2} = \frac{2B}{m\sin\theta_{\circ}^{\max}} - \frac{1}{\tan\theta_{\circ}^{\max}}. \tag{4.3}$$

In the case of wetting liquids, for which $\theta_{\circ}^{\max} = \frac{\pi}{2}$, this simplifies to

$$\tan\frac{\theta_{\mathrm{r}}}{2} = \frac{2B}{m}. \tag{4.4}$$

In the simplest model, it is assumed that at the point of depinning, the three-phase contact line closely follows the square cap perimeter, such that $m = 4W_{\mathrm{r}}$. However, to reflect the actual contact line morphology, the shape parameter α is introduced, so that $m = 4W_{\mathrm{r}}\alpha$. α is equal to 1 if the contact line is perfectly square, and $\pi/4$ for a circle. As the shape parameter cannot be predicted *a priori*, it is treated as a fitting parameter. An example of this is shown in Fig. 4.5(b)(i) (grey curve and square points) for $D_{\mathrm{r}} = 0.05$. Here, $\alpha = 0.861$, reflecting the contact line deviating from perfectly square by depinning at the cap corners. This yields a small average deviation between the simulation and model of 0.4° (average deviation for all D_{r} tested is 0.6°, maximum 2°).

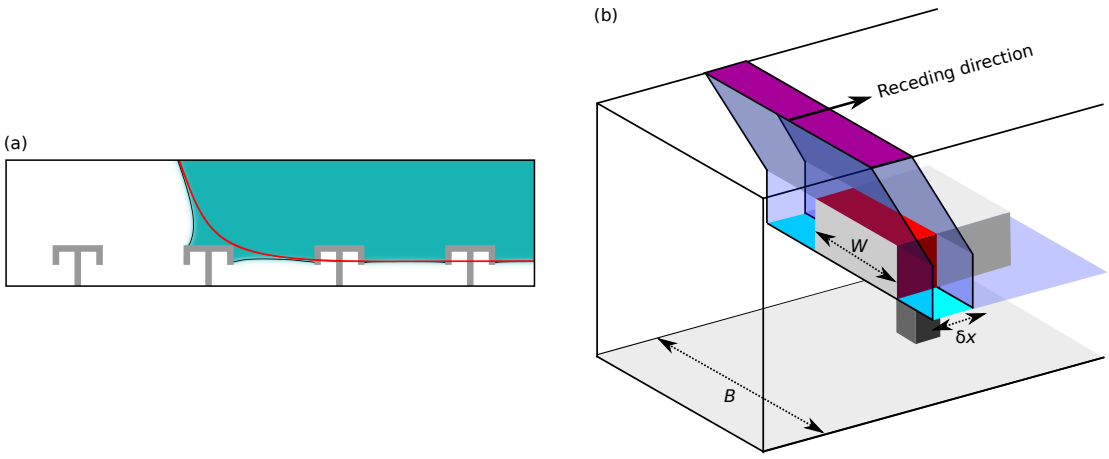

Figure 4.7: Observation and construction of the edge depinning model. (a) A 2D slice along the centre of the microchannel showing the edge depinning mechanism. (b) Model of the edge depinning mechanism in which the liquid vapour interface (translucent blue) is displaced by a distance δx along the length of the microchannel. The areas highlighted in purple, red, and cyan, indicate the change in liquid contact area with the top surface, cap, and vapour phase respectively.

Edge depinning. At intermediate area fractions and lip depths, the depinning mechanism is no longer capillary bridge-mediated. Instead, the edge-pinned receding mechanism is observed, shown in Fig. 4.5(a)(ii). Here, the interface maintains approximately the same morphology as it depins laterally from the edge of the cap. Thus, we are able to analyse the energetic change of sliding the interface laterally by a small distance, in order to obtain the angle at which receding becomes energetically favourable - the receding angle.

The edge depinning model for wetting liquids is constructed in Fig. 4.7. The energy change upon displacement of the contact lines by δx is expressed as the sum of contributions arising from sliding across the top surface of the microchannel, sliding across the surface of the cap, and reducing the liquid-vapour interfacial area, such that

$$\begin{aligned}\delta E =& \gamma_{\mathrm{sv}}^{\mathrm{top}} B\delta x - \gamma_{\mathrm{sl}}^{\mathrm{top}} B\delta x \\ &+ \gamma_{\mathrm{sv}}^{\mathrm{cap}} (W+2D)\,\delta x - \gamma_{\mathrm{sl}}^{\mathrm{cap}} (W+2D)\,\delta x \\ &- \gamma_{\mathrm{lv}} (B-W)\,\delta x. \end{aligned} \tag{4.5}$$

This is readily simplified using the Young equation to yield an expression for the force required to exact the displacement of the contact line,

$$\frac{\delta E}{\delta x} = \gamma_{\mathrm{lv}} \left[B\cos\theta_{\mathrm{top}} + (W+2D)\cos\theta_{\circ} - (B-W) \right]. \tag{4.6}$$

At the point of receding, this force is equal to zero. By realising that $\theta_{\mathrm{r}} = \pi - \theta_{\mathrm{top}}$, this yields

$$\cos\theta_{\mathrm{r}} = (W_{\mathrm{r}} + 2D_{\mathrm{r}})\cos\theta_{\circ} + W_{\mathrm{r}} - 1. \tag{4.7}$$

This represents a generalisation of previous edge-depinning models [179, 181], in which by taking account of the liquid receding from the cap sides, we are now able to describe the edge-depinning mechanism accurately for wetting liquids. This is demonstrated in Fig. 4.5(b)(i) (red curve and circular points). Without any fitting parameters, the average deviation between the model and simulation results is 2°. (average deviation for all D_{r} tested is 3°, maximum 7°).

Lip depinning. At large D_{r} and F_{r}, a new capillary bridge depinning mechanism is observed in which the bridge is strained between the cap edge, and bulk liquid phase. This

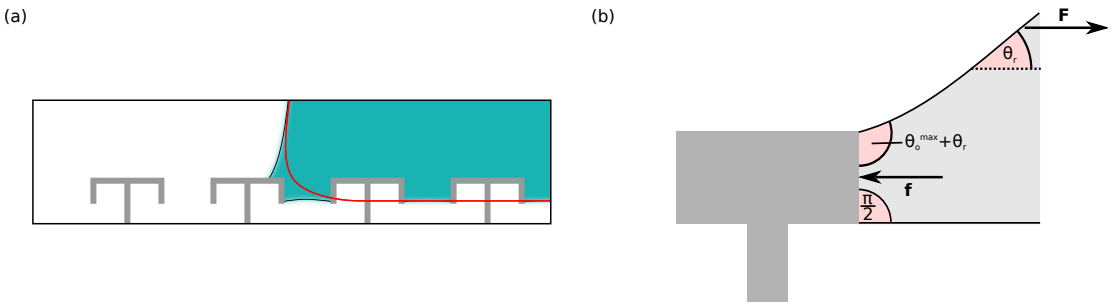

Figure 4.8: Observation and construction of the lip depinning model. (a) A 2D slice along the centre of the microchannel showing the lip depinning mechanism, in which the liquid (blue) is pinned to the side of the cap. (b) Model of the lip depinning mechanism in which the liquid meniscus (pale grey) is strained parallel to the receding direction.

lip-depinning receding mechanism, shown in Fig. 4.5(a)(iii), results in a substantial decrease in θ_r, demonstrated in Fig 4.3(c) (blue triangular points). The model we introduce is to approximate the receding interface as a capillary bridge pinned to the side of the cap, this time strained *parallel* to the receding direction.

In the lip depinning scheme, the geometry of the capillary-bridge depinning mechanism is markedly altered, shown in Fig. 4.8. At zero applied pressure, the liquid-vapour interface pinned to the bottom of the caps is planar, making a contact angle of $\pi/2$ with the cap side. Thus, the microscopic pinning force $\mathbf{f}$ acts anti-parallel to the macroscopic receding force $\mathbf{F}$, as shown in Fig. 4.8(b). The effect of $\mathbf{F}$ is therefore to change the contact angle around the contact line, varying from a maximum value ($\theta_\mathrm{o}^\mathrm{max} + \theta_\mathrm{r}$) at the top of the cap, to a minimum value ($\pi/2$) at the bottom of the cap. We make the assumption that $\mathbf{f}$ depends on the average contact angle $\bar{\theta} = \frac{\theta_\mathrm{o}^\mathrm{max}}{2} + \frac{\theta_\mathrm{r}}{2} + \frac{\pi}{2}$, leading to

$$|\mathbf{f}| = \gamma_\mathrm{lv} m \sin\left(\frac{\theta_\mathrm{o}^\mathrm{max}}{2} + \frac{\theta_\mathrm{r}}{2} + \frac{\pi}{4}\right). \tag{4.8}$$

For wetting liquids with $\theta_\mathrm{o}^\mathrm{max} = \frac{\pi}{2}$, this simplifies to

$$|\mathbf{f}| = \gamma_\mathrm{lv} m \cos\frac{\theta_\mathrm{r}}{2}. \tag{4.9}$$

Finally, we equate $|\mathbf{f}|$ and $|\mathbf{F}|$ to yield an expression for the receding contact angle due to lip depinning,

$$\cos\frac{\theta_\mathrm{r}}{2} = \frac{2(W_\mathrm{r} + D_\mathrm{r})\alpha}{2}, \tag{4.10}$$

where we have substituted the reduced perimeter m/B for that appropriate for rectangular

caps sides with deformation of the contact line capture by the shape parameter α: $m/B = 2(W_r + D_r)\alpha$. We note that for non-wetting surfaces ($\theta_\circ > \pi/2$), as the liquid-vapour interface does not pin to the cap underside in the suspended state, the lip depinning mechanism cannot occur.

The accuracy of this model is demonstrated in Fig. 4.5b(ii) at $D_r = 0.35$, for which $\alpha = 0.887$. This yields a small average deviation between the simulation and model of 1°, (average deviation for all D_r tested is 2°, maximum 6°).

Non-depinning. The lip-depinning model also predicts the existence of systems in which a receding contact angle no longer exists. In these extreme cases of the lip-depinning mechanism, because depinning is not able to occur, a droplet caused to move across the surface would leave a trail of suspended liquid trapped between the caps. We observe this predicted non-depinning mechanism in simulations, indicated by black pentagons in Figs. 4.3(c). This non-receding case is illustrated in Fig. 4.5(a)(iv).

4.3.2 Non-wettable surfaces

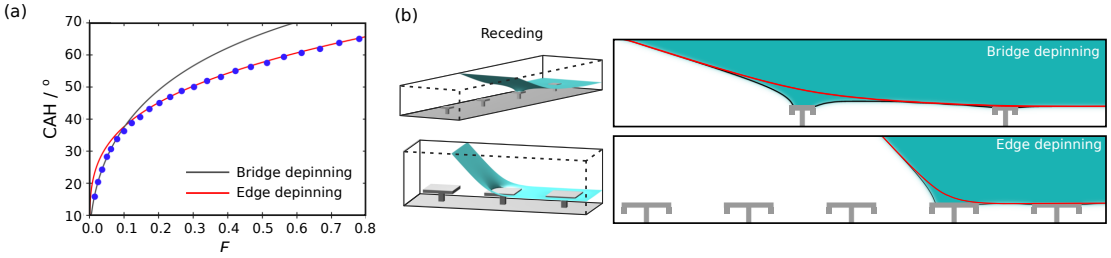

Figure 4.9: (a) Contact angle hysteresis measured via simulation (blue circles), with fitted bridge depinning (grey line) and edge depinning (red line) models. (b) Visualisations of systems at the point of receding via the bridge and edge depinning mechanisms.

We conclude this section by discussing the hysteresis on non-wetting surfaces, in which the microscopic contact angle is fixed at $\theta_\circ = 110°$. This provides a platform to compare the effects of surface wetability on CAH, and also to allow for the first time the rigourous testing of the bridge-depinning model as proposed by Butt *et al.* [185, 186, 195].

The CAH here is quantified in Fig. 4.9(a). Because the liquid-vapour interface is pinned to the top of the cap, the CAH is independent of the underlying cap structure. Thus, the reentrant and doubly reentrant geometries show identical behaviour, as do simple posts with no cap structure at all.

The pinning at the top of the cap leads to a uniform advancing contact angle of 180° for all cap widths W_r, matching experimental observations [178]. Two receding mechanisms are observed, bridge and edge depinning, shown in Fig. 4.9(b). The receding contact angle for the bridge depinning mechanism is described by Eq. (4.3), where the corrected contact angle $\theta_\circ^{\max} = \theta_\circ$ for $\theta_\circ > \pi/2$. Meanwhile, the receding contact angle for the edge-depinning mechanism is described by Eq. (4.7), in which the term $2D_\mathrm{r}$ is neglected as the liquid does not wet the cap sides. In this limit, Eq. (4.7) reduces to the conventional receding model [179]. The bridge and edge depinning mechanisms smoothly interpolate on the non-wetting geometries. We find that the error associated with both models compared to the simulation data is minimised if points with $F < 0.1$ are associated with the bridge depinning model, and points with $F > 0.1$ are associated with the edge depinning model. $F = 0.1$ therefore corresponds to the crossover between analytic models. Overall, for the bridge model, we find the shape parameter $\alpha = 0.65$ yields a maximum difference in θ_r of 1°. It is interesting to note that here, $\alpha < \pi/4$, meaning that the contact line is shorter than a circle of width W. Such small values of α have been previously reported [185], and suggest that not all portions of the contact line contribute equally to the pinning force, as was our assumption in Eq. (4.1). However the excellent agreement between theory and simulation allow us to conclude that the proposed capillary bridge model provides a suitable approximation for the actual receding contact angle. The edge-depinning model also shows excellent agreement with the simulation data, in which the maximum difference in θ_r between theory and simulation is also 1°.

4.4 Critical pressure

4.4.1 Wettable surfaces

Unlike with the contact angle hysteresis, the critical pressure is sensitive to whether the surface geometry is reentrant or doubly reentrant. Throughout, the critical pressure shown ΔP_c is referenced with respect to the pressure γ_lv/B. Here we find that ΔP_c is only dependent upon the area fraction F_r and the pillar height H_r. Although ΔP_c is affected by the presence of a doubly reentrant lip, ΔP_c does not depend on the precise lip depth L_r. The critical pressure dependencies on F_r and H_r are shown for the reentrant and doubly reentrant structures in Figs. 4.10(a)(i,ii) respectively. For both structural types, these dependencies change across

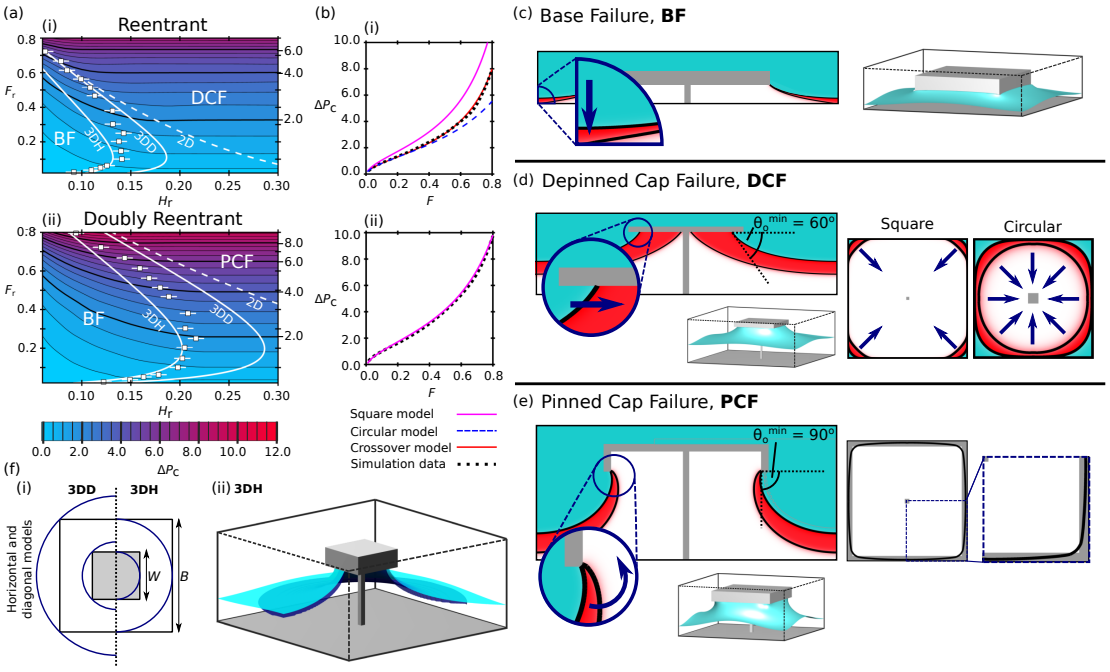

Figure 4.10: Critical pressure analysis for reentrant and doubly reentrant geometries. (a) Contour plots of ΔP_c variation with F_r and H_r for reentrant (i) and doubly reentrant (ii) geometries. Data points mark the critical height at which the failure mechanism switches from Base Failure (BF) to cap failure (CF), error bars indicate the uncertainty in this height due to the diffuse interface width. Solid and dashed white lines show the critical height based on the capillary model and 2D model respectively. (b) Model fits to ΔP_c of the cap failure mechanisms at $H_r = 0.25$ for reentrant (i) and doubly reentrant (ii) geometries. (c-e) The three failure mechanisms shown in 3D, with associated diagonal cross sections. Critical pressure liquid morphologies are shown in blue, the vapour phase shown in white, and the interface indicated with a black solid line. Red regions show how the unstable meniscus evolves upon increasing ΔP above ΔP_c. Panels (d,e) also show under-cap views, highlighting the shapes of the contact lines at the critical pressure. (f) Details of the horizontal and diagonal capillary bridge models used, showing the inner and outer circumferences (blue) against the system configuration. The 3D illustration compares the simulated liquid-vapour interface (light blue) to the horizontal capillary model (dark blue).

the parameter space, due to the presence of two different pressure-induced failure mechanisms: Base Failure and Cap Failure.

For a given area fraction F_r, at low pillar heights the Base Failure mechanism is operative, illustrated in Fig. 4.10(c). In this, the suspended state fails because the sagging liquid-vapour interface touches the base of the system whilst the three-phase contact line remains pinned to the bottom of the cap. By increasing the pillar height, ΔP_c is increased.

However, at H_r above the critical height, H_c, the Cap failure mechanism becomes operative. Here, at the critical pressure the system can no longer simultaneously support the uniform mean curvature of the liquid-vapour interface and the contact line morphology. For

the reentrant geometry, this results in the contact line depinning and sliding inwards, shown in Fig. 4.10(d). For the doubly reentrant geometry with a thin lip width l_r, this results in the liquid-vapour interface ballooning outwards while the contact line remains pinned, shown in fig. 4.10(e). In both of these cases, increasing the pillar height further now results in no change to ΔP_c.

Therefore at fixed F_r, the maximum ΔP_c occurs for $H_r \geq H_c$, in the Cap failure region. However, it is detrimental for design performance if the height is increased above the critical height, as this mechanically weakens the structure without increasing ΔP_c [76, 175]. The optimum pillar height is therefore $H_r = H_c$, which defines the Base Failure - Cap Failure boundary. We therefore focus on discussing the critical pressure due to the Cap failure mechanisms, before analysing the critical height.

Depinned Cap Failure for Reentrant Geometries

In order to understand how ΔP_c is influenced by the area fraction (or alternatively the cap width W_r) in the depinned Cap Failure mechanism, we begin by examining the rudimentary model proposed by Tuteja *et al.* [56, 196]. In this,

$$\Delta P_c = \frac{4\alpha \sin\theta_\circ}{\frac{1}{W_r} - \alpha W_r}. \tag{4.11}$$

For convenience, we incorporate the shape parameter α, the same parameter as defined previously in the CAH section, in order to unify the critical pressure models on circular ($\alpha = \pi/4$) and square ($\alpha = 1$) geometries. To rationalise this model, at ΔP_c the pinning force of the contact line balances the force due to the pressure over the area between the pillars [56, 196]. Two key assumptions are made. Firstly, the contact line is supposed to follow the cap edge, whilst secondly, the contact angle around the contact line is presumed to be uniform and equal to $\theta_\circ$. We test this model in Fig. 4.10(b)(i). The square-cap model is observed to fit the simulation results very poorly, overestimating the critical pressure by between 26% to 95% in the tested range $0.016 \leq F_r \leq 0.8$. If instead, a circular contact line model is employed, we find that this agrees with the simulation data up to moderate area fractions ($F_r < 0.6$). Overall, by observing the contact line shape obtained through simulations, shown in Fig. 4.10(d), we find that the contact line varies in morphology, from circular at low F_r, to approximately square at high F_r.

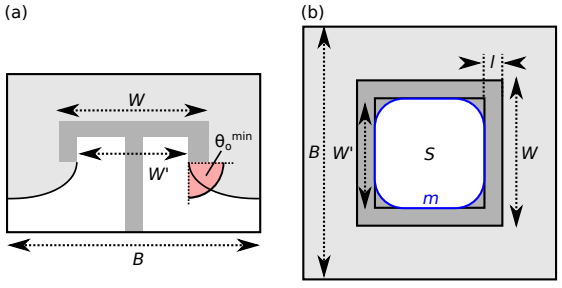

Figure 4.11: (a) Side view of a 3D system at the critical pressure. In this, the liquid (pale grey) sags beneath the cap (dark grey),and the contact line is pinned with contact angle $\theta_\circ^{\min}$. (b) Underside view of the same system, showing the position of the contact line perimeter of length m (blue line), and projected area occupied by the vapour phase, S. W' indicates the pinned width of the contact line (in general different to W).

We now develop a more sophisticated model, capable of accurately describing the critical pressure for reentrant and doubly reentrant geometries, at all contact angles. To do this, we return to the derivation presented by Tuteja *et al.* [56, 196], but take care to capture the actual contact line morphology. We begin by considering a typical system at the critical pressure, of size B, cap width W, illustrated in Fig. 4.11. At the critical pressure, the pinning force of the contact line balances the force due to the pressure, such that

$$(\Delta P_c \gamma_{lv}/B)\left(B^2 - S\right) = \gamma_{lv} m \sin\theta_\circ^{\min}, \tag{4.12}$$

where $\left(B^2 - S\right)$ is the projected area occupied by the liquid phase, shown in Fig. 4.11(b). As in the contact angle hysteresis study, m is the contact line perimeter, and again we take care to correctly capture the true pinning force by using the corrected contact angle, where $\theta_\circ^{\min} = \min[\theta_\circ, \pi/2]$ if the contact line is pinned to the outer cap edge, or $\theta_\circ^{\min} = \pi/2$ if the contact line is pinned to the inner cap edge. These forms of $\theta_\circ^{\min}$ are now rationalised. For pinning on the outer cap edge, the maximum pinning force occurs at $\theta_\circ = \pi/2$. If $\theta_\circ < \pi/2$ however, this maximum pinning force cannot be attained before the Gibbs pinning criterion breaks down (where the interface slides inwards under the cap), leading to $\theta_\circ^{\min} = \theta_\circ$. For all $\theta_\circ > \pi/2$, this maximum force can be attained before the Gibbs pinning criterion breaks down, leading to $\theta_\circ^{\min} = \pi/2$. For doubly reentrant geometries, the undercut cap means that for all contact angles, the Gibbs pinning criterion never breaks down, so that $\theta_\circ^{\min} = \pi/2$. We note pinning on the outer cap edge is appropriate for wetting on (singly) reentrant geometries, or doubly reentrant geometries where $\theta_\circ > \pi/2$. Pinning on the inner cap edge is appropriate for doubly reentrant geometries where $\theta_\circ < \pi/2$. In all cases, we make the assumption that

the average contact angle is equal to $\theta_\circ^{\min}$.

To model the contact line perimeter, we assume that the pinned width of the contact line is W', which is different from the cap width W by a distance a. Since a cannot be predicted *a priori* we treat a as a fitting parameter. For pinning on the inner lip (for wetting liquids on doubly reentrant structures as shown in Fig. 4.11), we expect a to be approximately twice the lip width l_r. For pinning on the outer lip (for reentrant geometries, or non-wetting liquids on doubly reentrant geometries), we expect $a \approx 0$. Overall, $m = 4\alpha W'$, where the shape parameter α is used to smoothly vary the possible perimeter shapes from circular ($\alpha = \pi/4$) to square ($\alpha = 1$). To model the projected vapour-occupied area S, we again use the corrected width W' and shape parameter α to model the contact line shape, yielding $S = \alpha W'^2$. The critical pressure model is obtained by manipulating Eq. (4.12),

$$\begin{aligned}\Delta P_\mathrm{c} &= B \sin\theta_\circ^{\min} \frac{m}{B^2 - S}, \\ &= \sin\theta_\circ^{\min} \frac{4\alpha W' B}{B^2 - \alpha W'^2}, \\ &= \sin\theta_\circ^{\min} \frac{4\alpha}{\frac{1}{W'_\mathrm{r}} - \alpha W'_\mathrm{r}},\end{aligned} \tag{4.13}$$

where W'_r is the reduced corrected width W'/B.

We next make a second update to Tuteja *et al.*'s critical pressure model. Here, we propose that the shape parameter α varies continuously as a function of W'_r between the circular and square limits, such that $\alpha = \frac{\pi}{4} + (1 - \frac{\pi}{4})(W'_\mathrm{r})^x$. The exponent x describes the strength of this crossover, and is a second fitting parameter.

This crossover model is shown in Fig. 4.10(b)(i) to be in excellent agreement with the simulation data, yielding $a = 0.023$ and $x = 6.7$. As anticipated, a is small relative to the cap width, and is of the order of the diffuse interface width ($\epsilon/B = 0.01$). The large exponent x reflects the simultaneous change of both the perimeter and area of the contact line as the system crosses from a circular to square configuration.

Pinned Cap Failure for Doubly Reentrant Geometries

Next, we consider the critical pressures of the doubly reeentrant structure, shown in Fig. 4.10(b)(ii). In the pinned Cap Failure region, the liquid-vapour interface is pinned to the inner cap edge, shown in Fig. 4.10(e). The doubly reentrant lip enforces an approximately square contact line across the entire range of F_r tested, such that excellent agreement between

the simulations and the critical pressure model in Eq. (4.11) is achieved at $x = 0$, $\alpha = 1$ and $a = 0.080$. As anticipated, within the uncertainty introduced by the diffuse interface $a \approx 2L_{\mathrm{r}}$ (where $2L_{\mathrm{r}} = 0.1$). However, the data in Fig. 4.10(b)(ii) are best described by replacing $\theta_{\circ}$ in Eq. (4.11) with 90°. In 2D, and for axisymmetric doubly reentrant wells, it is facile to show that the critical pressure occurs when the contact angle reaches 90° for thin lip widths l_{r} [10]. We conclude here that this remains true, even for 3D, non-axisymmetric caps. This therefore verifies the proposition that the doubly reentrant lip maximises the critical pressure for any surface wettability [60].

Critical heights

At a given F_{r}, the critical heights are obtained both analytically and through simulations by observing the maximum depth which the liquid-vapour interface sags under the pillar in the Cap failure regions. If the pillar height H_{r} is equal to this sagging depth, the failure mechanism is simultaneously Base Failure and Cap failure, so defining the failure mode boundary and the critical height H_{c}. The salient observation based on the simulated critical heights (white data points in Figs. 4.10(a)(i,ii)) is that regardless of cap area fraction, the optimal pillar height is surprisingly short, and should never exceed $\approx 0.2B$. We now rationalise this observation.

By far the most commonly used approximation for liquid-vapour interfaces in 3D systems is the 2D circular arc model (see for example [56, 195, 196]), illustrated in Fig. 4.12(a). For visual clarity we show a reentrant geometry, although the following models and derivations are general for simple pillars, reentrant and doubly reentrant geometries at all contact angles. In this, a circular arc spans the separation between two adjacent pillars. At the critical pressure for cap failure the arc makes a contact angle of $\theta_{\circ}^{\min}$ with each cap underside. To choose which pillars should be spanned by a circular arc, there exist two choices, shown in Fig. 4.12(b), either the arc spans horizontally separated pillars, or diagonally separated pillars. These are labelled as the horizontal and diagonal models respectively. The distance spanned by the circular arc, $s_{\circ}$, is therefore equal to $B - W'$ in the horizontal model, or $\sqrt{2}(B - W')$ in the diagonal model. Generally expressed, the radius of curvature, R is

$$R = \frac{s_{\circ}}{2 \sin \theta_{\circ}^{\min}}, \tag{4.14}$$

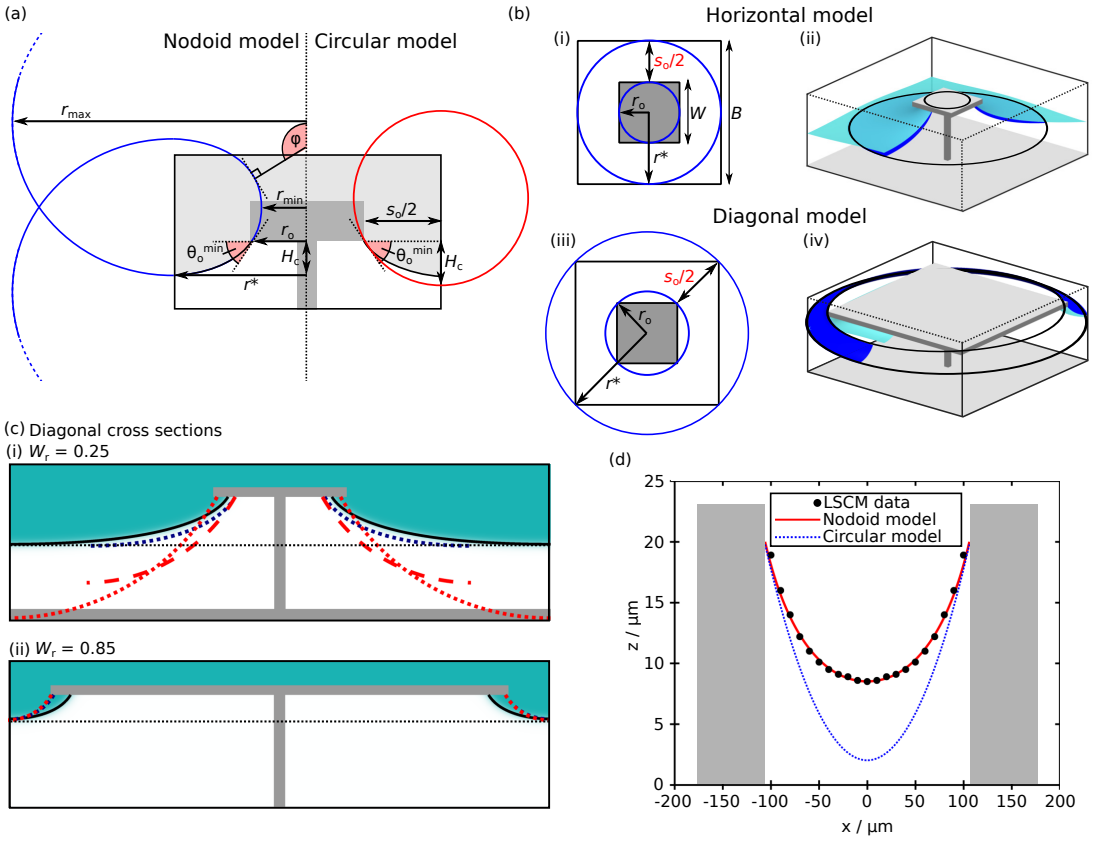

Figure 4.12: (a) Models used to approximate the true liquid-vapour interface morphology (black line). A reentrant geometry is shown for visual clarity, but the models are also valid for doubly reentrant geometries. (Left) The nodoid model for approximating the vapour phase as a capillary bridge (blue line); (right) the circular arc model (red line). All distances and angles used in the model constructions are labelled. (b) In a square system, two choices of distance measurement exist, either horizontal (i,ii) or diagonal (iii,iv). (i,iii) vertical projections of the system, showing inner and outer radii for the nodoid model (blue), and cap separation for the circular model. (ii,iv) Example comparisons with simulations for the horizontal and diagonal models at $W_r = 0.25$ and $W_r = 0.85$ respectively. The simulated liquid-vapour interface is shown in light blue, the nodoid model shown in dark blue. Both interfaces are cut horizontally and diagonally to be able to compare the model and simulation results. Black lines indicate the inner and outer perimeters of the nodoid interface. (c) Diagonal cross sections from the 3D horizontal (i) and vertical (ii) models, the sagging height of the liquid-vapour interface obtained from simulation is indicated by a black dotted line. Also shown are the liquid vapour interfaces from: simulation (black, solid), nodoid model (blue, dotted), diagonal circular model (red, dotted), and horizontal circular model (red, dashed, only shown in (i)). In (ii), the diagonal nodoid and circular models overlap, showing how both agree closely with the simulated critical height. (d) Comparison of the diagonal nodoid (red, solid line) and circular arc models (blue, dashed line) with an experimental laser scanning confocal microscopy (LSCM) diagonal profile (black data) of a liquid-vapour interface on a square array of square pillars (grey). Experimental data extracted from [147]. Note the stretched vertical scale for visual clarity.

and the sagging height H_c is

$$H_c = \frac{s_\circ}{2} \frac{1 - \cos\theta_\circ^{\min}}{\sin\theta_\circ^{\min}}. \tag{4.15}$$

We now test the circular arc model for accuracy at capturing the critical height. In Figs. 4.10(a)(i,ii) (dashed white lines), we show the critical height variation with F_r for the diagonal 2D circular arc model. It can be readily seen that except at very high F_r, a 2D estimation grossly overestimates the critical height. All currently manufactured, low-F_r structures relying on these 2D models are therefore significantly taller than necessary, which can be seen in refs. [177] and [48] for example.

In Fig. 4.12(c), we next test the circular arc model for accuracy at representing the simulated interface shape. In agreement with our previous observation, it can be seen in Fig. 4.12(c)(i) ($W_\mathrm{r} = 0.25$) that the diagonal circular arc model (dotted red line) grossly overestimates the sagging height at the critical pressure by several times. The horizontal circular arc model also overestimates the sagging height (dashed red line). It is only at the largest cap widths that the circular arc is able to accurately estimate H_c, as shown for the diagonal model in Fig. 4.12(c)(ii) ($W_\mathrm{r} = 0.85$). The reason for this 2D-like behaviour at large W_r, is that the principal radius of curvature approximated by the circular arc (R_1) is significantly smaller than the second principal radius of curvature of the interface (R_2). This arises because $s_\circ << W_\mathrm{r}$. Thus, the Laplace pressure $\Delta P \propto 1/R_1 + 1/R_2$ and hence the interface shape, becomes well-approximated by the single radius of curvature R_1.

However, surfaces with large W_r suffer from a severely limited capacity to produce surfaces of low contact angle hysteresis. For practically useful surfaces where the circular arc model is highly inaccurate, we consider an alternative capillary-bridge model. In this, we recognise that the liquid-vapour interface under the cap forms a capillary-bridge-like structure, in which the vapour has a negative pressure relative to the liquid. We therefore look to model the interface as the simplest 3D surface of constant mean curvature. Out of the family of Delaunay surfaces, the nodoid exhibits a negative mean curvature. This is illustrated in Fig. 4.12(a), in which the blue line shows a portion of interfacial profile of the axisymmetric, periodic surface. In the parametrisation shown, the vertical height z of a point on the surface is defined by the local radius r and angle relative to the surface-normal φ. In the following derivation, we only present the nodoid characteristics pertinent to ascertaining the critical height, for a comprehensive treatment see for example [197].

The nodoid is fully characterised by specifying the innermost radius, r_min, outermost radius, r_max, and a single point on the surface. This point can be determined by realising that, at the critical pressure, the interface makes an angle of $\pi - \theta_\circ^\mathrm{min}$ in the vapour phase

with the underside of the cap at the pinning location. However, a choice exists in where to define the point. Because the capillary bridge is axisymmetric, whereas the simulated system is square, there are two limiting cases of where the inner and outer radii contact the structure and simulation boundary respectively, shown in Fig. 4.10(f)(i). Either the inner and outer radii contact the central edges of the structure and simulation boundaries (the horizontal model, representing the minimum possible radii), or contact is made at the corners (the diagonal model, representing the maximum possible radii). Both potential capillary models are shown in Figs. 4.10(a)(i,ii) (solid white lines). Thus, for these two limiting cases, the point is located at ($z_\circ$, $r_\circ$, $\varphi_\circ$) = (H, $W'/2$, $\theta_\circ^{\min}$) for the horizontal nodoid model, and (H, $\sqrt{2}W'/2$, $\theta_\circ^{\min}$) for the diagonal nodoid model, shown in Fig. 4.12(b). We are now able to deduce the appropriate $r_{\min}$ and $r_{\max}$ for each pillar geometry. Firstly, on the portion of the nodoid representing the liquid-vapour interface, there exists a point at radius $r^* = \sqrt{r_{\min} r_{\max}}$ where $dr/dz = 0$. To respect the periodic boundary conditions of the liquid-vapour interface, $r^* = B/2$ or $r^* = \sqrt{2}B/2$ in the horizontal and diagonal models respectively. Secondly, by rearranging the relationship

$$\begin{aligned} \sin\varphi &= \frac{r^2 - r_{\min} r_{\max}}{r(r_{\max} - r_{\min})}, \\ &= \frac{r^2 - r^{*2}}{r(r^{*2}/r_{\min} - r_{\min})}, \end{aligned} \tag{4.16}$$

we are able to find $r_{\min}$ as

$$r_{\min} = \frac{1}{2r\sin\varphi}\left[r^{*2} - r \pm \sqrt{(r - r^{*2})^2 + (rr^*\sin\varphi)^2}\right], \tag{4.17}$$

by taking the negative result and substituting for one of the defined points $(r, \varphi) = (r_\circ, \varphi_\circ)$.

Finally, we are able to obtain the nodoid approximation to the interfacial profile through the relationship

$$z(r) = r_{\min} F(k, \psi) - r_{\max} E(k, \psi), \tag{4.18}$$

$$\text{where} \quad k^2 = 1 - \frac{r_{\min}^2}{r_{\max}^2}, \tag{4.19}$$

$$\text{and} \quad \sin^2\psi = \frac{r_{\max}^2 - r^2}{r_{\max}^2 - r_{\min}^2}, \tag{4.20}$$

which is plotted in Fig. 4.12(c) (blue dashed line). $F(k, \psi)$ and $E(k, \psi)$ are the elliptic

integrals of the first and second kinds respectively. Overall, H_c is obtained through recognising that

$$H_c = z(r_\circ) - z(r^*). \tag{4.21}$$

In all cases in Fig. 4.10(a), it is observed that the simulated critical heights are bounded by the horizontal and diagonal capillary bridge models. Furthermore, at low F_r, the horizontal capillary model accurately predicts the critical height. For structures where the interface is pinned to the outer cap edge, namely reentrant geometries and doubly reentrant geometries with $\theta_\circ > 90^\circ$ (shown in Section 4.4.2), the diagonal model is shown to closely predict the critical height at high F_r. An illustrated comparison of the horizontal and diagonal models is shown in Fig. 4.10(f)(ii). Through this, we are able to successfully capture the critical height suppression at low F_r, and maximum H_c at intermediate F_r.

Experimental validation of the nodoid model is shown in Fig. 4.12(d). Here, experimental data (black points) are extracted from laser scanning confocal microscopy (LSCM) experiments performed in [147], which was able to resolve a diagonal cross-section of the liquid-vapour interfacial profile of a sessile water droplet on a square array of square pillars. For this system, the pillar width $W = 50$ μm, height $H = 23$ μm, system size $B = 200$ μm, and the contact angle is determined to be 109°. As the nodoid and circular arc models only require a knowledge of the contact angle, pillar separation and contact line diameter, both models are equally applicable for simple pillars, reentrant, and doubly reentrant geometries. We compare diagonal variants of both models with the diagonal experimental profile in Fig. 4.12(d). The nodoid model (red, solid line) is observed to closely follow the experimental data, whereas the circular arc model (blue, dashed line) overestimates the sagging height of the interface by 56%.

4.4.2 Non-wettable surfaces

We now examine the critical pressure behaviour on non-wetting geometries, where we again choose the representative contact angle $\theta_\circ = 110^\circ$. The critical pressure contour plots observed in Fig. 4.13 are identical for both reentrant and doubly reentrant geometries, as the contact line is always pinned to the outer cap edge. The behaviour is similar to that observed for the doubly reentrant geometry at $\theta_\circ = 60^\circ$ (pinned to the inner cap edge), and would be identical in the limit that the lip width $l \to 0$. This is because in all three cases, the

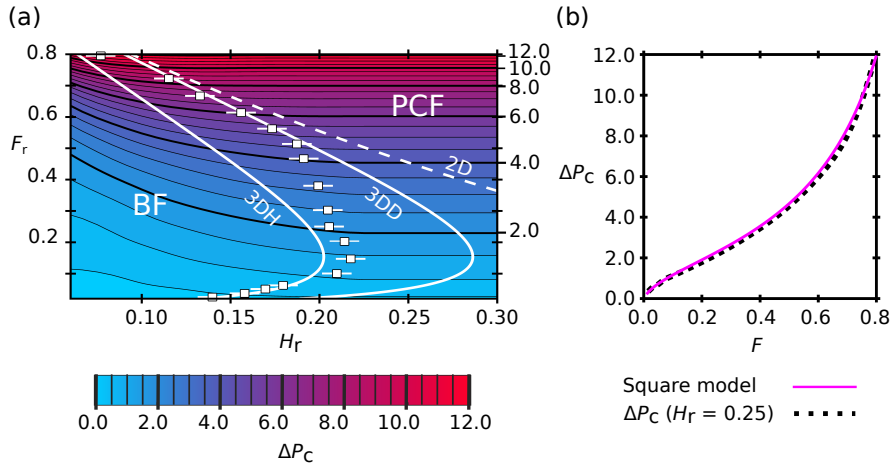

Figure 4.13: (a) Critical pressure variation with area fraction F_r and pillar height H_r. Data points indicate the critical height, and therefore the boundary between Base Failure BF, and pinned Cap Failure PCF. Error bars represent the interface width, and hence the uncertainty in the critical height. Approximations to the critical heights are indicated for circular 2D model (white, dashed line), and both horizontal and diagonal nodoid variants (white, solid line). (b) Comparison of the cap failure model against the simulation data for $H_r = 0.25$.

corrected contact angle in Eq. (4.13) is $\theta_\circ^{\min} = 90°$. As found previously, the 2D circular arc approximation in Eq. (4.15) grossly overestimates the critical height for all but the largest cap widths. The 3D capillary bridge models are again shown to be accurate at low area fractions F_r (horizontal model), and high F_r (diagonal model), and correctly capture the qualitative behaviour at intermediate values.

In Fig. 4.13(b), we show the comparison between the critical pressure model for cap failure, expressed in Eq. (4.13), with the simulation data. As the contact line closely follows the cap edge, excellent agreement between the model and simulation is achieved when the shape parameter $\alpha = 1$ (square contact line), yielding a fitted $a = 0.02$. As anticipated, because the contact line is pinned to the outer cap edge, a is insignificantly different from zero, relative to the interface width = 0.01.

4.5 Simultaneous optimisation

Overall, six structural parameters influence the three key wetting properties: A_r (pillar width), H_r (pillar height), L_r (lip depth), t_r (cap thickness), W_r (cap width), and the system scale B/B_{ref} (where $B_{ref} = 1$ μm). Having studied how these parameters affect each individual wetting property, the parameters which antagonistically couple the wetting properties become apparent. Firstly, in order to reduce the CAH, W_r must be reduced; but this reduces

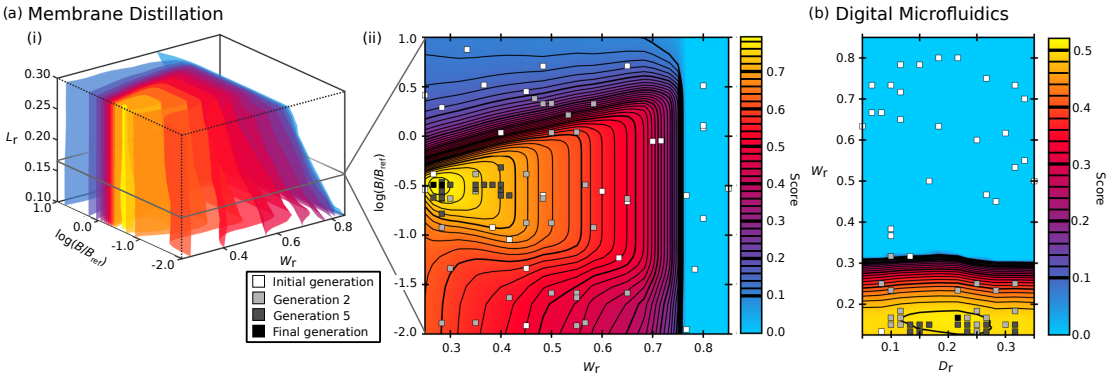

Figure 4.14: (a)(i) 3D contour plot of the membrane distillation scoring function at fixed $H_r = 0.3$, $A_r = 0.05$, $t_r = 0.05$. Each surface is a surface of constant score. (ii) A 2D slice of the 3D contour plot at the optimal $L_r = 0.17$. Square data points show the initial (white), 2nd (light grey), 5th (dark grey), and final (black) generations of the genetic algorithm, projected onto the 2D plane. (b) Scoring function for the digital microfluidics application, projected onto the $H_r = 0.3$ plane at fixed $B = 100$ µm, also showing the successive generations of the genetic algorithm population.

ΔP_c and ΔE_r. Secondly, in order to increase ΔP_c the system scale must be reduced; but this reduces ΔE_r. In order to overcome this unfavourable coupling, we simultaneously optimise the surface structures, which is demonstrated for two example applications: membranes for water purification via membrane distillation, and droplet-based digital microfluidics. In order to perform this simultaneous optimisation, we begin by developing an application-specific scoring function which grades a candidate design against the desired wetting properties. We then optimise the scoring function using two methods. The first is to evaluate the scoring function over the entire parameter range tested, and from this find the optimum structure. In the second method, we demonstrate that for designs where it is not practical to perform comprehensive wetting property surveys, due to increased surface complexity for example, genetic algorithms can be used to efficiently perform the simultaneous optimisation.

Conventionally in membrane distillation, purification is achieved by passing a heated contaminated water source over a hydrophobic membrane, through which water vapour is able to pass to collect in a clean water reservoir. However oils readily foul the membrane leading to breakthrough of the contaminated liquid into the fresh water reservoir [66, 198]. We overcome this using a doubly reentrant structure. To optimise the geometry, we construct a suitable scoring by recognising that the first priority is for the membrane to be pressure-resistant under typical operating conditions: water at 70°C ($\gamma_{lv} = 64.4$ mN·m^{-1}) under pressures of approximately 100 kPa (ΔP_c^{target}) [199]. In order to ensure the suspended state

remains stable, the minimum energy barrier must be of the order of 100 $k_{\mathrm{B}}T$ ($\Delta E_{\mathrm{r}}^{\mathrm{target}}$). This is of particular importance for the doubly reentrant geometry, in order to prevent failure via condensation within the texture [200]. Finally, in order to reduce viscous drag across the membrane the CAH should be minimised, and we impose the condition that the CAH should not exceed 90° ($\mathrm{CAH}^{\mathrm{cutoff}}$). The critical pressure, energy barrier, and CAH conditions generate individual scoring functions S_{P}, S_{E}, and S_{C} respectively,

$$\begin{aligned} S_{\mathrm{P}} &= \frac{1}{2}\left[1+\tanh\left(\frac{\Delta P_{\mathrm{c}}-\Delta P_{\mathrm{c}}^{\mathrm{target}}}{\Delta P_{\mathrm{width}}}\right)\right], \\ S_{\mathrm{B}} &= \frac{1}{2}\left[1+\tanh\left(\frac{\Delta E_{\mathrm{r}}-\Delta E_{\mathrm{r}}^{\mathrm{target}}}{\Delta E_{\mathrm{width}}}\right)\right], \\ S_{\mathrm{C}} &= \max\left(\frac{\mathrm{CAH}^{\mathrm{cutoff}}-\mathrm{CAH}}{\mathrm{CAH}^{\mathrm{cutoff}}},0\right), \end{aligned} \tag{4.22}$$

from which the total score is the geometric mean of these: $\mathrm{Score} = (\mathrm{S_P S_B S_C})^{\frac{1}{3}}$. For S_{P} and S_{B}, a tanh profile is selected to appropriately localise critical pressures and energy barriers within a range of suitable operating conditions. This leads to the widths chosen here as $\Delta P_{\mathrm{width}} = 0.5$ and $\Delta E_{\mathrm{width}} = 5\times10^{-5}$. Meanwhile the linear function for S_{C} aims to ensure that low-CAH structures are always favoured.

By maximising this 6-dimensional scoring function using either the results from the wetting property survey, or a genetic algorithm, the optimal structure is obtained with a score of 0.794. The optimal parameters are (A_{r}, H_{r},L_{r}, t_{r}, W_{r}, B/B_{ref}) = (0.05, ≥0.17, 0.17, 0.05, 0.27, 0.32). The optimum system scale of 320 nm is strikingly similar to that of springtail cuticles [9]. Both the springtail cuticle and membrane design have been selected for pressure-resistant liquid shedding ability, whilst allowing the unimpeded movement of gasses through the surface. The membrane design proposed here may therefore reflect a natural optimum for robust gaseous diffusion. The optimum design yields the properties: $\Delta P_{\mathrm{c}} = 162$ kPa, $\Delta E = 1.25\times10^{3}\ k_{\mathrm{B}}T$, CAH = 42° ($\theta_{\mathrm{a}} = 165°$, $\theta_{\mathrm{r}} = 123°$). This CAH is typical of currently manufactured reentrant microtextures, see for example [48, 175, 196].

By studying the individual wetting properties, we can rationalise the optimal structural design. The optimal value of A_{r} represents the minimum pillar width tested, whose sole function is to maximise ΔE_{r}. H_{r} reflects the observation that the maximum critical pressure is achieved at $H_{\mathrm{r}} \geq H_{\mathrm{c}}$. $L_{\mathrm{r}} + t_{\mathrm{r}}$ optimises the CAH, whilst the specific value of L_{r} maximises ΔE_{r}. Finally, the small value of W_{r} reduces the CAH, whilst retaining a high ΔP_{c} due to

the small system scale.

The scoring function at fixed optimal values of A_r, H_r, and t_r is shown in Fig. 4.14(a)(i) as a 3D contour plot. A 2D cut through this is shown in Fig. 4.14(a)(ii) at the optimal L_r, to show that the optimal structure scale is bounded by the critical pressure criterion from above, and the minimum energy barrier criterion from below. Also shown in Fig. 4.14(a)(ii) are projections of successive generations of the genetic algorithm. The optimal structure was located after 20 generations, requiring the sampling of only 0.01% of the 7.2×10^6 possible structures considered overall.

The four examples of manufactured doubly reentrant surfaces feature system sizes of 1-100 μm, as smaller scales are currently challenging to manufacture [60, 61, 73, 74]. We now choose to optimise a structure whose manufacture has already been demonstrated, so we fix $B = 100$ μm in accordance with the texture designed in a recent work by Liu and Kim [60]. A leading-edge application for this is surfaces designed for digital microfluidics [71,191]. Devices fail when droplets become immobilised by pinning to the surface, particularly problematic for low surface tension solvents [191], or for reactive processes where the surface tension is variable and hard to predict.

Both of these problems are readily overcome using the doubly reentrant geometry. We demonstrate this by optimising a surface structure for use within a particularly challenging scenario - digital microfluidics using microlitre volume droplets of n-hexane ($\gamma_{lv} = 27.4$ mN·m^{-1}). The pressure within such a droplet (88 Pa) introduces the target pressure for use in the scoring scheme Eq. (4.22): $\Delta P_c^{target} = 100$ Pa, with the width $\Delta P_{width} = 0.005$. Furthermore, as the CAH should be minimised, but impose the condition $CAH^{cutoff} = 50°$. At the imposed length scale used, the barrier score $S_B \approx 1$ (ΔE is of the order of 10×10^{10} k_BT), meaning that we choose to optimise the score $(S_P S_C)^{1/2}$.

Overall, the optimum structure, 0.508, is obtained using both the wetting property survey, and the genetic algorithm. The optimum parameters are (H_r,D_r, W_r) = ($\geq$0.13, 0.22, 0.16), yielding the properties: $\Delta P_c = 105$ Pa, CAH = 25°. The pillar width A_r and ratio of L_r to t_r become free parameters to choose. A 2D contour plot of the scoring function at constant $H_r = 0.3$ is shown in Fig. 4.14(b), in which projections of successive generations of the genetic algorithm are shown. Here, the algorithm converged after 14 generations, requiring 2.2% of the entire population to be sampled.

For both the membrane distillation and digital microfluidics applications, the sensitivity

of the optimised structural dimensions and properties can be assessed relative to the choice of scoring function parameters. This is achieved through re-optimising the geometries when each parameter in the scoring functions shown in Eq. (4.22) were varied individually by ±5%. It is found that the optimised membrane distillation geometry is insensitive to the parameter variation. This observation also applies to the optimised digital microfluidics geometry, except in the scenario where $\mathrm{CAH}^{\mathrm{cutoff}}$ is reduced by 5%. In this case, the optimal CAH is reduced by 13%, and the optimal critical pressure is reduced by 17%. However, this variation is due to the $\mathrm{CAH}^{\mathrm{cutoff}}$ reduction (2.5°) being relatively large compared to the low optimal CAH (25°) for this application.

The manufactured structure reported by Liu and Kim [60] is similar to the optimum geometry. However, the key difference is that the optimal geometry has a significantly shorter pillar height H_{r} than the manufactured geometry by a factor of 3.7 times. This is due to the surprisingly short critical height required, as discussed in Section 4.4.1.

4.6 Discussion and conclusions

Overall in this chapter, in order to optimise the wetting properties of the reentrant and doubly reentrant surface texture for a vast variety of potential applications, we began by comprehensively surveying two key surface wetting properties: the contact angle hysteresis, and the critical pressure. This was achieved for both wetting and non-wetting liquids.

In the contact angle hysteresis study, we identified four major receding mechanisms, of which only two had previously been reported, and defined the structural dimensions where each is operative. For all receding mechanisms, we were able to develop and analyse quantitative models which were robustly validated against our simulation results.

In the critical pressure study, three failure mechanisms were observed and quantified as a function of the structural parameters. However, upon comparison with the simulation data, the prevailing and widely-used critical pressure models were found to be significantly over-simplified. This led to a particularly poor description of the liquid-vapour interface morphology, meaning that manufactured structures are many times taller (and mechanically weaker) than necessary. By developing a more sophisticated model, we were able to achieve both quantitative accuracy of the critical pressures, and success at modelling the complex interface morphologies as capillary bridges.

Here, we have studied how a planar interface advances and recedes uniformly in the direction of a single row of pillars, however receding in real systems is shown to be far more complex (see for example [201–203]). In these, it is observed that receding occurs via kinks in the contact line propagating perpendicular to the receding direction. Although our simulations are currently in quantitative agreement with the available experimental data, an interesting perspective for future work will be to see how liquid droplets recede on these surfaces. A related investigation is to study the dependence of CAH on the propagation direction: we suggest that droplet motion may be favoured along specific axes of the texture, a well-known phenomenon for other surfaces such as ridges [204] and ratchets [82]. This would have particular significance for applications such as membrane distillation, in which the flow should be directed along a low-hysteresis axis for efficient oil contaminant removal; and digital microfluidics, in which droplet manipulation would be anisotropic.

Finally, we combined the CAH and critical pressure study, with the minimum energy barrier study from Chapter 3, in order to design optimised surface textures. However, it was found that the wetting properties were antagonistically coupled by the structural parameters: parameters which tended to maximise the critical pressure, minimised the energy barrier and maximised the contact angle hysteresis. As it was not possible to optimise a surface geometry with respect to each individual wetting parameter, we performed the optimisation by considering all three simultaneously. This was achieved in two ways for the optimum design of both membranes for water-purification, and surfaces for digital microfluidics. Firstly, using the comprehensive wetting property surveys, we were able to evaluate and locate the maximum of a combined scoring function. However, we then demonstrated that a genetic algorithm was able to efficiently locate the optimum design in the six-dimensional parameter space. Although the designs tested here featured a relatively small number of structural degrees of freedom, going forward we highlight such optimisation techniques as being powerful tools in designing more complex structures for special wettability applications. The computational techniques developed here are highly versatile, and can be used for any mesoscopically structured surface in contact with multiple fluid phases.

Coupled with recent, significant developments in fabrication techniques (including 3D printing, fluidization of polymer micropillars, and lithographic methods), we believe the multifaceted optimisation strategy presented here will be a powerful approach to designing real-world superomniphobic surfaces.

Chapter 5

Critical pressure asymmetry in the enclosed fluid diode

5.1 Introduction

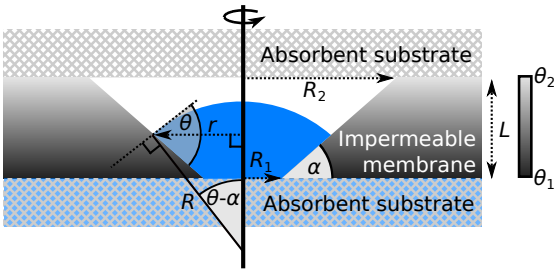

Figure 5.1: 2D illustration of the axisymmetric pore construction and outgoing meniscus profile, the axis of symmetry shown as the thick vertical line. Liquid is shown in blue, with air shown in white.

In previous chapters, we have developed surface structures which are optimised to be maximally liquid-repellent, with uniform physical and chemical texturing. Here, we now advance on this to consider textures with a gradient in surface properties to form a fluid diode. Our primary aim is to show how the physical and chemical gradients interact in a fluid diode, which we will use to produce a diode with optimised directionality. We do this for a structure in which realising strong directionality is particularly challenging: the enclosed pore illustrated in Fig. 5.1. Here, the diode geometry is a conical pore augmented with a chemical gradient. The pore passes through an impermeable membrane, sandwiched between two absorbent substrates. We utilise this simple design to facilitate high-throughput manufacture, for applications we detail below. The diode ability arises from the critical pressure asymmetry - the difference in the maximum Laplace pressure (critical pressure) required to force liquid from the bottom substrate to the top substrate, compared to the reverse direction. The

challenge to obtaining high critical pressure asymmetry in this geometry is twofold: firstly, the two substrates enclosing the pore mean that if a liquid meniscus grows too large within the pore, it will contact an absorbent substrate leading to diode breakdown; and secondly, ratcheting structures which are able to generate high asymmetries are prohibited in this simple design. In Section 5.6 however, we lift this design constraint to generate optimal (but complex) pores.

The enclosed pore is particularly suited to a range of applications in which fluid should be readily absorbed into the diode, but not be able to pass back out. Cleaning and hygiene are two notable areas where such applications are prominent. In these, the diode would both facilitate absorption of liquid from a surface, such as skin, into a porous material while also preventing back-flow out of the material. General and widely-used potential applications include diapers, cloths, and towels [205]. However, the enclosed fluid diode is also gaining interest in high-performance innovations, such as sports textiles which absorb and remove sweat to cool the body, but are waterproof from the outside [206]; and wound dressings, in which excess fluid should be selectively absorbed out of the wound to improve healing and reduce infection risk [207].

Although substantial progress has been made in calculating the maximum Laplace pressures for liquid entering physically textured surfaces (see for example [208, 209]), for the enclosed geometry, the efficacy at preventing back-flow and the impact of chemical patterning have never been discussed. In Section 5.2 we begin by calculating the Laplace pressure for liquid leaving the pore. In Section 5.3, we calculate the Laplace pressure for liquid entering the pore. We then compare the incoming and outgoing maximum Laplace pressures, using the critical pressure asymmetry to measure the strength of the diode in Section 5.4, before optimising the chemical pattern to produce the maximum possible critical pressure asymmetry in Section 5.5. We finally end by lifting the simple design constraints to realise the optimal enclosed pore in Section 5.6.

5.2 Outgoing critical pressures

5.2.1 Setup

The model setup, illustrated in Fig. 5.1, features a liquid-impermeable membrane shown in shaded grey, punctured by an axisymmetric (conical) pore of wedge angle α. Without loss of

generality, we restrict α to the interval $[0, \pi/2]$, so that the smallest pore radius R_1 is always located at the bottom of the system, and the largest pore radius R_2 is located at the top. For $\alpha > \pi/2$, we need not perform additional calculations, but rather turn the pore as shown upside-down, and exchange the roles of incoming and outgoing critical pressure. In addition to a physical gradient, we employ a chemical gradient in the form of the local contact angle $\theta(r)$ which varies from θ_1 at the bottom of the pore to θ_2 at the top. Although any variation in contact angle can be chosen, we employ a linear variation to most closely compare with the linear physical gradient of the conic profile, where

$$\theta(r) = \theta_1 + (\theta_2 - \theta_1)\frac{r - R_1}{R_2 - R_1}. \tag{5.1}$$

In a fully enclosed pore, the top and bottom surfaces of the liquid-impermeable membrane are in contact with liquid-absorbent substrates, shown as cross-hatched areas in Fig. 5.1.

For considering the outgoing critical pressure, the bottom absorbent substrate is modelled as an infinite liquid reservoir from which the liquid meniscus rises upwards into the pore. We consider the surface to be smooth with the only pinning sites occurring at the sharp corners at the top and bottom of the pore, and we work below the capillary length so that the liquid meniscus assumes a spherical cap geometry for all values of the contact line radius r. This can be ensured for the majority of liquids under ambient conditions if $r < 1$ mm. The pressure difference ΔP across the liquid-vapour interface is therefore described by the Young-Laplace equation appropriate for a spherical geometry: $\Delta P = 2\gamma_{\mathrm{lv}}/R$, where γ_{lv} is the liquid-vapour interfacial tension and R is the radius of the sphere. Throughout, we nondimensionalize the Laplace pressure so that $\Delta P_r = \Delta P/(2\gamma_{\mathrm{lv}}/R_1)$. For convenience, we also nondimensionalise all radii with respect to R_1, so that for example, $R' = R/R_1$ and $R'_2 = R_2/R_1$.

We note here that although we label the fluids as 'liquid' and 'vapour', as the methods only require a knowledge of the contact angle at the three-phase contact line and the fluid-fluid interfacial tension, the analyses presented here are entirely general for any pair of immiscible fluids, such as oil and water.

Using the construction in Fig. 5.1, the outgoing Laplace pressure $\Delta P_r^{\mathrm{out}}$ may be described as a function of the reduced contact line radius $r' = r/R_1$,

$$\Delta P_r^{\mathrm{out}} = \frac{1}{r'}\sin\left[\theta_1 + (\theta_2 - \theta_1)\frac{r' - 1}{R'_2 - 1} - \alpha\right]. \tag{5.2}$$

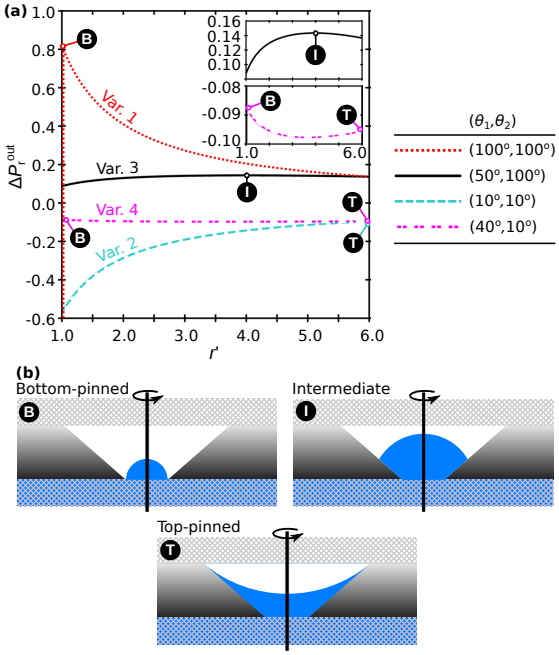

Figure 5.2: (a) Example plots of each of the four outgoing reduced pressure variations with r', with insets magnifying the local maxima/minima. The local maximum of each variation is associated with one of three critical meniscus types, illustrated in (b).

Finding the critical outgoing pressure ΔP_c^{out} then becomes finding the maximum value of ΔP_r in the interval $r' \in [1, R_2']$. ΔP_r^{out} exhibits four characteristic variations with r', depending on $R2'$, θ_1, θ_2, and α; representative examples of each are plotted in Fig. 5.2(a), where we fix $\alpha = 45°$, R_2'=6.

5.2.2 Variation 1 and the bottom-pinned (B) critical meniscus

The first variation, shown as the dotted red line, shows that for $r' > 1$, ΔP_r^{out} decreases monotonically with r'. When $r' = 1$ however, the contact line is pinned to the bottom of the pore. The Gibbs pinning criterion of a contact line at a sharp corner [57,104] then permits a continuum of allowed pressures, as the pinned contact angle may vary from θ_1 with respect to the bottom surface of the impenetrable membrane, to θ_1 with respect to the sloping pore wall. This is shown as the vertical dotted red line at $r' = 1$. The critical pressure here occurs in the bottom-pinned state, labelled the B-state in Fig. 5.2(b), where,

$$\Delta P_c^{\text{out}}(\text{B}) = \sin\left[\min(\theta_1 - \alpha, \frac{\pi}{2})\right]. \tag{5.3}$$

For $\theta_1 - \alpha < \pi/2$, $\Delta P_c^{\text{out}}(\text{B})$ occurs when the interface depins from the sharp corner, such that the contact angle at the contact line is equal to θ_1. For $\theta_1 - \alpha > \pi/2$ however, $\Delta P_c^{\text{out}}(\text{B})$ happens when the contact angle reaches $\pi/2 - \alpha$, before the depinning event, because the maximum possible critical pressure for the system is attained here at $R = R_1$.

5.2.3 Variation 2 and the top-pinned (T) critical meniscus

The second variation, shown as the dashed cyan line in Fig. 5.2(a), shows a monotonic increase of ΔP_r^{out} with r'. The critical pressure therefore occurs at the point when the contact line reaches the top of the system at $r' = R_2'$, where $\theta = \theta_2$. This is labelled the top-pinned (T) state in Fig. 5.2(b). In this case,

$$\Delta P_c^{\text{out}}(\text{T}) = \frac{1}{R_2'} \sin\left(\theta_2 - \alpha\right). \tag{5.4}$$

5.2.4 Variation 3 and the intermediate (I) critical meniscus

The third variation, shown as the solid black line in Fig. 5.2(a), exhibits a local maximum at intermediate values of r', labelled the I-state in Fig. 5.2(b). The upper inset panel highlights the local maximum in a vertical magnification. To solve for the critical pressure, we aim to find stationary points of ΔP_r^{out} in Eq. (5.2), such that the critical contact line radius $r_c' \in (1, R_2')$. This amounts to solving,

$$\begin{aligned} &\frac{1}{r_c'}\left(\frac{\theta_2 - \theta_1}{R_2' - 1}\right)\cos\left(\theta_1 + (\theta_2 - \theta_1)\frac{r_c' - 1}{R_2' - 1} - \alpha\right) \\ &-\frac{1}{r_c'^2}\sin\left(\theta_1 + (\theta_2 - \theta_1)\frac{r_c' - 1}{R_2' - 1} - \alpha\right) = 0, \end{aligned} \tag{5.5}$$

for r_c', such that ΔP_r^{out} is maximal, yielding $\Delta P_c^{\text{out}}(\text{I})$. In general, this is not analytically solvable and instead must be solved numerically. Interestingly, such a local maximum cannot exist for a chemically homogeneous pore: rather it is result of the competition between physical and chemical gradients. To illustrate this, we consider the example shown in Fig .5.2(a) (solid black line), for which $\theta_1 < \pi/2$, but $\theta_2 > \pi/2$. Physically, as the contact line radius r' increases from 1 to R_2', this tends to increase the droplet radius R' and hence reduce the Laplace pressure. Chemically, the simultaneous increase in local contact angle tends to reduce the droplet radius R and so increase the droplet pressure. When the I-state exists, it is therefore due to the balancing of these two effects.

5.2.5 Variation 4 and the B and T critical menisci

Instead of a local maximum, the fourth variation, shown as the double-dashed magenta line in Fig. 5.2(a), exhibits a local minimum. The lower inset panel highlights the local minimum in a vertical magnification. This behaviour is observed when solving Eq. (5.5) which yields a minimal solution of ΔP_r^{out}. Thus, both the B-state at $r' = 1$ and the T-state at $r' = R_2'$ become local maximisers of ΔP_r^{out}. Which state globally maximises ΔP_r^{out} is found by comparing Eq. (5.3) and Eq. (5.4). We detail this comparison in Section 5.2.8.

5.2.6 Influence of top substrate: B' and I' critical menisci

In the four preceding Laplace pressure characteristics, we have neglected the influence of the absorbent substrate at the top of the system. We consider this to be an ideal liquid sink, such that as soon as any point of the liquid meniscus reaches the top of the pore, liquid will escape from the pore. When the liquid meniscus is convex, the centre of meniscus may contact the top of the pore before the B-state or I-state critical pressure is reached. We denote the bottom-pinned contacting state B', and the intermediate contacting state I'. We note that a top-pinned contacting state cannot occur, as this would require the centre of the meniscus to contact the top absorbent substrate before the three-phase contact line. For clarity of notation throughout, we refer to a liquid meniscus as being convex if the droplet forms a converging lens, such as the B-state in Fig. 5.2(b), and concave if the droplet forms a diverging lens, such as the T-state in Fig. 5.2(b). In Fig. 5.3(a), we construct the total height of the liquid meniscus as the sum of the height of the contact line z_c above the pore bottom, and the height of the spherical cap above this h_c. Noticing that $h_c = R_c - s_c$, where s_c is the z-distance from the centre of the spherical cap to the contact line, we derive,

$$h_c = r_c \frac{1 - \cos(\theta(r_c) - \alpha)}{\sin(\theta(r_c) - \alpha)}. \tag{5.6}$$

For the spherical cap to touch the upper substrate, $z_c + h_c = L$ must be satisfied, where $z_c = (r_c - R_1)\tan\alpha$, and the membrane thickness $L = (R_2 - R_1)\tan\alpha$. In reduced units, this amounts to solving,

$$\left(r_c' - R_2'\right)\tan\alpha + r_c' \frac{1 - \cos(\theta(r_c') - \alpha)}{\sin(\theta(r_c') - \alpha)} = 0. \tag{5.7}$$

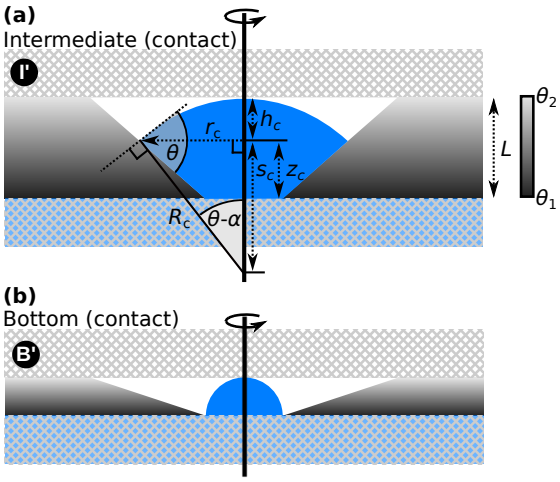

Figure 5.3: (a) Construction used to calculate the critical pressure of the I' state. (b) Illustration of the B' state.

In general this does not have analytic solutions and must be solved numerically. Once r_c' is found in this way, it is straightforward to substitute r' for r_c' in Eq. (5.2) to recover the critical pressure $\Delta P_c^{\text{out}}(\text{I}')$ caused by the cap contacting the upper substrate, while the contact line radius takes an intermediate value between R_1 and R_2.

If instead the contact line is pinned to the bottom of the pore at the point of meniscus contact, as illustrated in Fig. 5.3(b), the B'-type critical meniscus arises, where the outgoing critical pressure may be simply expressed as,

$$\Delta P_c^{\text{out}}(\text{B}') = \frac{2}{L' + \frac{1}{L'}}, \tag{5.8}$$

where $L' = L/R_1$.

5.2.7 Critical morphology existence ranges

Overall, five different critical interface morphologies may occur: B, B', T, I, and I', in which the associated critical pressures feature different dependencies on θ_1, θ_2, α, and R_2'. Despite this complexity, the critical pressure types able to occur within a system can be determined based on whether the liquid meniscus is convex ($\theta > \alpha$) or concave ($\theta < \alpha$) at the top and bottom of the system. This is presented in Table 5.1.

For ($\theta_1 > \alpha$, $\theta_2 < \alpha$), the critical meniscus must occur when contact line is pinned to the bottom of the system in B or B'. For ($\theta_1 < \alpha$, $\theta_2 > \alpha$) however, the Laplace pressure is negative when the contact line is at the bottom of the pore, and positive at the top, so

Table 5.1: The critical outgoing meniscus types able to occur for a convex meniscus, $\theta > \alpha$, or concave meniscus $\theta < \alpha$.

	$\theta_1 > \alpha$	$\theta_1 < \alpha$
$\theta_2 > \alpha$	B, B', I, I'	I, I'
$\theta_2 < \alpha$	B, B'	B, T

the critical meniscus must occur in some intermediate state: I or I'. For ($\theta_1 > \alpha$, $\theta_2 > \alpha$), the meniscus is convex for all r, meaning the B, B', I, or I' states could occur. For ($\theta_1 < \alpha$, $\theta_2 < \alpha$), the meniscus is concave for all r, so that the critical pressure must either occur at the bottom of the system, as B, or top, as T.

5.2.8 Outgoing critical pressures visualisation

We now visualise how the outgoing critical pressure depends on the four parameters θ_1, θ_2, α, and R_2'. To reduce the dimensionality of the representation, in Fig. 5.4 we show a matrix of contour plots at fixed θ_1 and θ_2, both of which may only take the values 10°, 50°, and 100°. We choose these values to capture the range of contact angles exhibited by commonly used liquids and substrates, see for example [192]. Other contact angle combinations may be explored using the matlab code provided as supplementary material.

At each θ_1, θ_2, Fig. 5.4 illustrates the sets of critical pressure states presented in Table 5.1. We now discuss the competition between the states within each set, for the global critical pressure.

When $\theta_1 = 10°$, $\alpha < \theta_2$, B, B', I, or I' are possible, however the I state is not observed within the range of R_2' plotted. The region of existence of B' is shown to not depend on θ_2. This is because the B' meniscus is pinned to the bottom of the well, and so never experiences the chemical gradient. Furthermore, if B' co-exists with I', the I' state must necessarily have a lower critical pressure than B'. This is because, compared to B', the I' meniscus has a wider contact line radius and smaller peak height, leading to a greater radius of curvature and so a smaller critical pressure. Thus, the I' critical pressure (which does depend on θ_2) never out-competes the B' critical pressure, leaving the B' region of existence unaltered by θ_2. I' is however able to out-compete the B state, as exhibited by the B region receding to larger R_2' values as θ_2 is increased from 10° to 50°.

When $\theta_1 = 50°$, two additional features are observed. The first is that the B and T states only coexist and compete when $\theta_1 > \theta_2$ (and $\theta_1, \theta_2 < \alpha$ as described in Table 5.1, meaning the menisci at the top and bottom of the pore are concave). This condition must be satisfied,

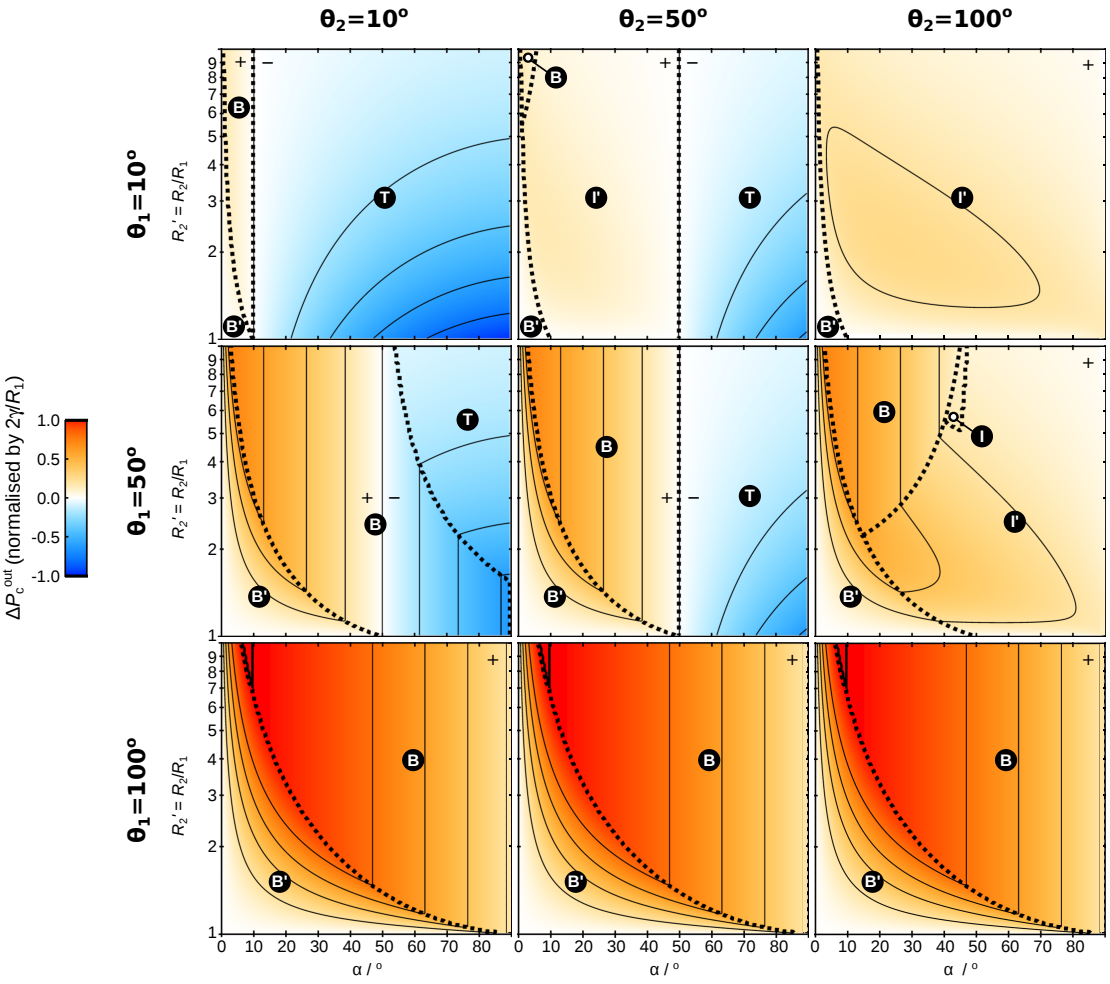

Figure 5.4: Matrix of R_2' - α contour plots of the outgoing critical pressure for a selection of θ_1 and θ_2. The outgoing meniscus types are labelled with black circles. The boundaries between these critical types are shown as dotted black lines. Contours are shown at intervals in ΔP_c^{out} of 0.2. For visual clarity, regions with $\Delta P_c^{\text{out}} > 0$ are marked with a '+', and regions where $\Delta P_c^{\text{out}} < 0$ are marked with a '-'.

otherwise the wider aperture at the top of the pore will always produce a meniscus of larger negative critical radius, and so a greater critical pressure, than when pinned to the bottom of the pore. The second additional feature is that for $\theta_2 = 100°$, we now observe the I state to exist over a small region at large R_2'. For I to occur, the critical meniscus must be produced sufficiently low in the well for the peak to not contact the upper substrate. This requires a delicate balance between the chemical gradient (favouring the critical state at the top of the pore) and the physical gradient (favouring the critical state at the bottom of the pore), which overall produces a narrow existence range of I.

When $\theta_1 = 100°$, only the B and B' states are able to occur, as outlined in Table 5.1. Because the contact line at the critical pressure is always pinned to the bottom of the well,

θ_2 has no impact on the critical pressure. Thus, all three contour plots for $\theta_1 = 100°$ are identical. Since $\theta_1 > 90°$, we also observe here the incidence of the maximum possible critical pressure, $\Delta P^{\text{out}} = 1$, shown bounded by the thick contour. This is shown in Eq. (5.3) to be as a result of the B-state critical pressure occurring when the contact line is pinned to the bottom of the well, with a contact angle of 90° with respect to the horizontal axis.

5.3 Incoming critical pressure

5.3.1 Setup

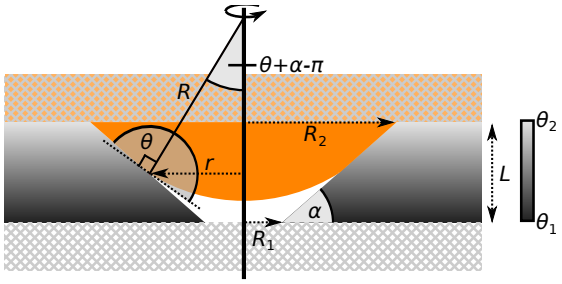

Figure 5.5: 2D illustration of the axisymmetric pore construction and incoming meniscus profile, the axis of symmetry shown as the thick vertical line. Liquid is shown in orange, with air shown in white.

We model the occurrence of liquid entering the pore from above in Fig. 5.5. We utilise the same setup as shown in Fig. 5.1, with the exception that the liquid (orange) now enters from the top absorbent substrate, and the bottom substrate is dry. The same linear physical and chemical gradients are employed as before.

The incoming Laplace pressure ΔP_r^{in} can be derived as

$$\Delta P_r^{\text{in}} = -\frac{1}{r'} \sin\left[\theta_1 + (\theta_2 - \theta_1)\frac{r' - 1}{R_2' - 1} + \alpha\right]. \tag{5.9}$$

It can be seen that Eq. (5.9) can be obtained from ΔP_r^{out} in Eq. (5.2) by exchanging the fluid phases, such that $\theta(r') \to \pi - \theta(r')$. This simple transformation however will be shown to give rise to remarkably different incoming and outgoing critical pressures. Again, the competition between physical and chemical gradients gives rise to four different variations in ΔP_r^{in} with r'. The characteristic examples of each shown in Fig. 5.6(a) illustrate the symmetry between ΔP_r^{in} and ΔP_r^{out}, as it is observed that by making the fluid exchange, Fig. 5.2(a) is reflected in the r' axis to yield Fig. 5.6(a).

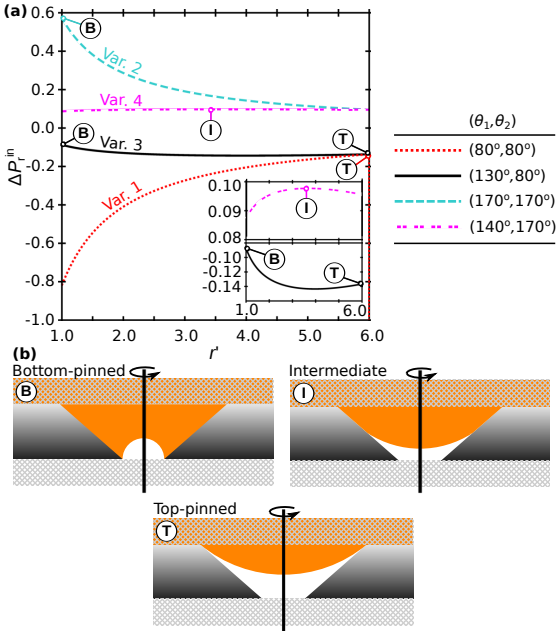

Figure 5.6: (a) Example plots of each of the four incoming reduced pressure variations with r', with insets magnifying the local maxima/minima. The local maxima of each variation is associated with one of three critical meniscus types, illustrated in (b).

5.3.2 Variation 1 and the top-pinned (T) critical meniscus

The first variation is shown as the dotted red line in Fig. 5.6(a). Here, for $r' < R_2'$, ΔP_r^{in} decreases monotonically as r' decreases. When $r' = R_2'$ however, a range of critical pressures is possible as the contact line is pinned to the top of the pore. This is shown as the vertical dotted red line at $r' = R_2'$. The critical pressure here occurs in the top-pinned state, labelled the T-state in Fig. 5.6(b), where,

$$\Delta P_c^{\text{in}}(\text{T}) = -\frac{1}{R_2'}\sin(\theta_2 + \alpha)\,. \tag{5.10}$$

5.3.3 Variation 2 and the bottom-pinned (B) critical meniscus

The second variation is shown as the dashed cyan line in Fig. 5.6(a). This shows a monotonic increase of ΔP_r^{in} as r' is decreased. The critical pressure therefore occurs at the point when the contact line reaches the bottom of the system at $r' = 1$, $\theta = \theta_1$, labelled the B-state in Fig. 5.6(b). In this case,

$$\Delta P_c^{\text{in}}(\text{B}) = -\sin(\theta_1 + \alpha)\,. \tag{5.11}$$

5.3.4 Variation 3 and the T and B critical menisci

The third variation is shown as the solid black line in Fig. 5.6(a). Here, a local minimum exists at intermediate values of r'. The lower inset panel highlights the local minimum in a vertical magnification. In this pressure variation, both the T-state and the B-state become local maximisers of ΔP_r^{in}. Which state globally maximises ΔP_r^{in} is found by comparing Eq. (5.10) and Eq. (5.11). We perform this comparison for selected examples of θ_1 and θ_2 in Section 5.3.8.

5.3.5 Variation 4 and the intermediate (I) critical meniscus

The fourth variation is shown as the double-dashed magenta line in Fig. 5.6(a). Here, a local maximum is observed at intermediate values of r', labelled the I-state in Fig. 5.6(b). The upper inset panel in Fig. 5.6(a) highlights the local maximum in a vertical magnification. This local maximum can be found by finding stationary points of ΔP_r^{in} in Eq. (5.9) which maximise ΔP_r^{in} in the interval $r'_c \in [1, R'_2]$. This is achieved through solving,

$$\begin{aligned} &\frac{1}{r'_c}\left(\frac{\theta_2-\theta_1}{R'_2-1}\right)\cos\left(\theta_1+(\theta_2-\theta_1)\frac{r'_c-1}{R'_2-1}+\alpha\right) \\ &-\frac{1}{r'^2_c}\sin\left(\theta_1+(\theta_2-\theta_1)\frac{r'_c-1}{R'_2-1}+\alpha\right)=0. \end{aligned} \tag{5.12}$$

In general, this is again not analytically solvable and instead must be solved numerically.

5.3.6 Influence of top substrate: T' and I'

In the four preceding incoming Laplace pressure characteristics, we have this time neglected the influence of the absorbent substrate at the bottom of the system. When the liquid meniscus is convex, the centre of meniscus may contact the bottom of the pore before the T-state or I-state critical pressure is reached.

To find the critical pressure of the I-contacting state shown in Fig. 5.7(a) (denoted I'), we begin by finding the total sag depth of the liquid meniscus. This is constructed as the sum of the depth of the contact line z_c below the pore top, and the depth of the spherical cap below this h_c. Using $h_c = R_c - s_c$, we derive,

$$h_c = -r_c\frac{1+\cos(\theta(r_c)+\alpha)}{\sin(\theta(r_c)+\alpha)}. \tag{5.13}$$

The spherical cap will touch the lower substrate if $z_c + h_c = L$. In reduced units, we therefore solve,

$$\left(1 - r_c'\right) \tan\alpha - r_c' \frac{1 + \cos(\theta(r_c') + \alpha)}{\sin(\theta(r_c') + \alpha)} = 0. \tag{5.14}$$

In general this does not have analytic solutions and must be solved numerically. Once r_c' is found in this way, we substitute r' for r_c' in Eq. (5.9) to obtain the critical pressure $\Delta P_c^{\text{in}}(\text{I}')$ caused by the cap contacting the lower substrate, while the contact line radius takes an intermediate value between R_1 and R_2.

If instead the contact line remains pinned to the top of the pore at the point of meniscus contact, as illustrated in Fig. 5.7(b), the top-contacting critical meniscus arises (denoted T'), where the incoming critical pressure is expressed as,

$$\Delta P_c^{\text{in}}(\text{T}') = \frac{2}{L' + \frac{R_2'^2}{L'}}. \tag{5.15}$$

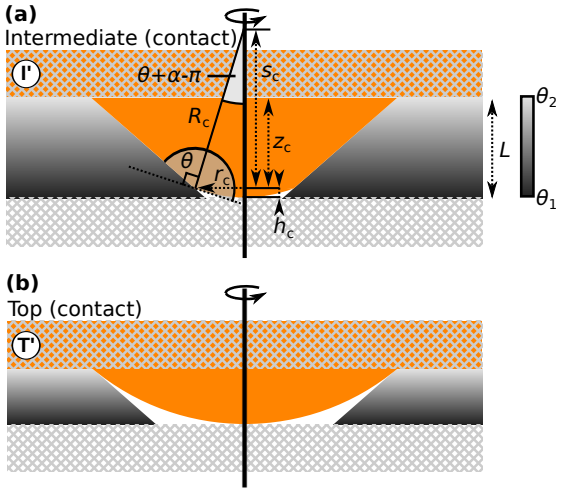

Figure 5.7: (a) Construction used to calculate the critical pressure of the I' state. (b) Illustration of the B' state, with the point of failure highlighted by a red circle.

5.3.7 Critical morphology existence ranges

Overall, five different critical interface morphologies may occur: B, T, T', I, and I', in which the associated critical pressures feature different dependencies on θ_1, θ_2, α, and R_2'. Despite this, the critical pressure types able to occur within a system can be determined based on whether the liquid meniscus is convex ($\theta + \alpha > \pi$) or concave ($\theta + \alpha < \pi$) and the top and bottom of the system. This is presented in Table 5.2.

Table 5.2: The critical incoming meniscus types able to occur for a convex meniscus, $\theta+\alpha > \pi$, or concave meniscus $\theta + \alpha < \pi$.

	$\theta_1 + \alpha > \pi$	$\theta_1 + \alpha < \pi$
$\theta_2 + \alpha > \pi$	T, T', I, I'	T, T'
$\theta_2 + \alpha < \pi$	I, I'	T, B

For ($\theta_1 + \alpha < \pi$, $\theta_2 + \alpha > \pi$), the critical meniscus must occur when contact line is pinned to the top of the system as T or T'. For ($\theta_1 + \alpha > \pi$, $\theta_2 + \alpha < \pi$) however, the Laplace pressure is negative when the contact line is at the top of the pore, and positive at the bottom, so the critical meniscus must occur in some intermediate state: I or I'. For ($\theta_1 + \alpha > \pi$, $\theta_2 + \alpha > \pi$), the meniscus is convex for all r, meaning the T, T', I, or I' states could occur. For ($\theta_1 + \alpha < \pi$, $\theta_2 + \alpha < \pi$), the meniscus is concave for all r, so that the critical pressure must either occur at the top of the system, as T, or bottom, as B.

5.3.8 Incoming critical pressure visualisation

We now visualise how the incoming critical pressure depends on the four parameters θ_1, θ_2, α, and R_2'. To reduce the dimensionality of the representation, in Fig. 5.8 we again show a matrix of contour plots at fixed θ_1 and θ_2, both of which may only take the values 10°, 50°, and 100°.

The incoming critical pressure contour plots in Fig. 5.8 show markedly different behaviour to the outgoing critical pressure plots in Fig. 5.4. This is because under the range of θ_1, θ_2 tested, except at large α, $\theta_1 + \alpha < \pi$ and $\theta_2 + \alpha < \pi$ meaning the liquid meniscus is concave. This means that the pore exerts a pulling force on the liquid in the top substrate, so that to prevent liquid filling the pore, a negative pressure must be applied.

Under such conditions, when $\theta_1 = \theta_2$, the T-type critical meniscus always emerges. This is because the meniscus has a wider contact radius at the top of the pore than the bottom, resulting in the less-negative critical pressure at the top of the pore. When $\theta_1 > \theta_2$, the B-state may out-compete the T-state for largest critical pressure at large α and R_2'. When this happens, the high contact angle at the bottom of the pore negates the small contact line radius, to create a less-negative critical pressure than the T-state. When $\theta_1 < \theta_2$, this time the B-state may out-compete the T-state for largest critical pressure at small α and R_2'. This is because at the bottom of the pore, the low contact angle creates a liquid-vapour interface with a near-spherical shape. The associated large radius of curvature produces a smaller negative critical pressure than the meniscus at the top of the well.

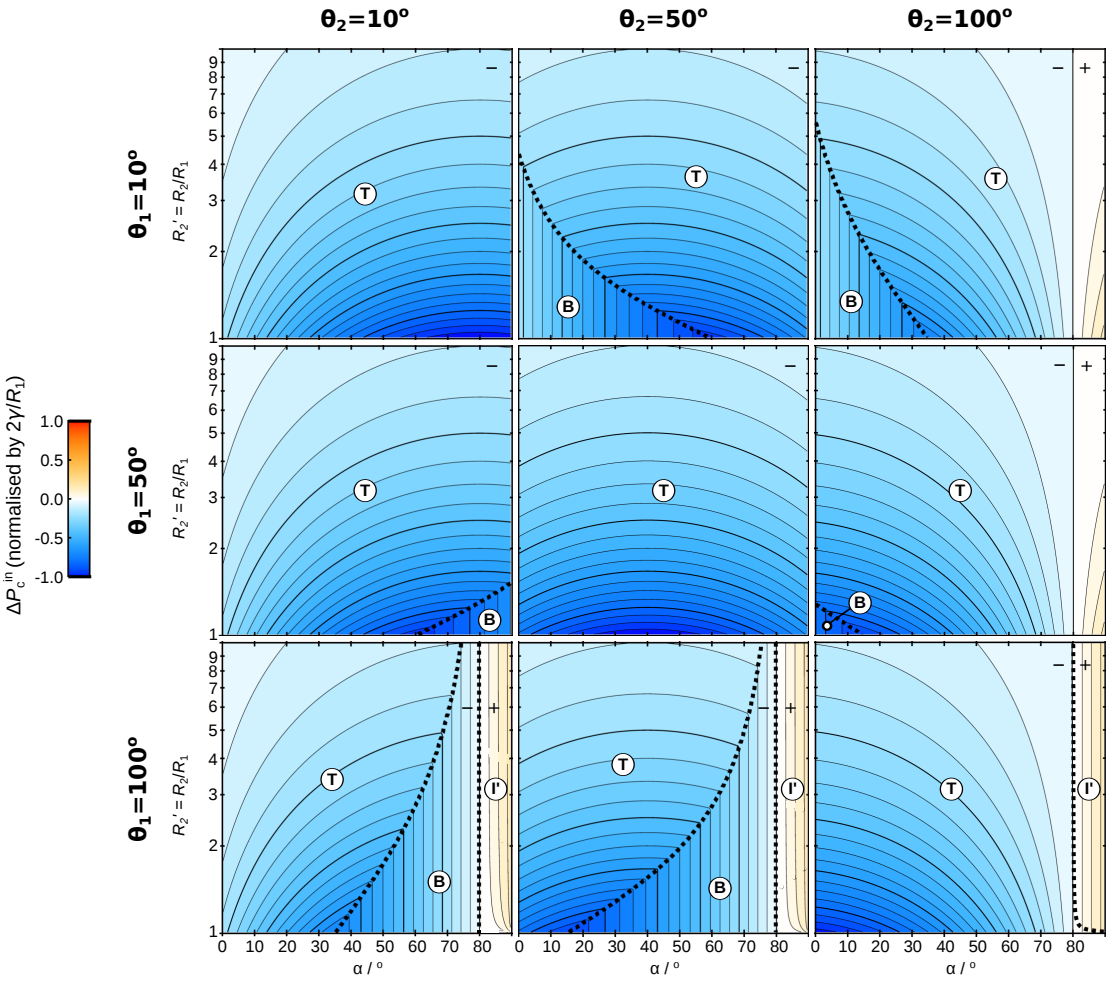

Figure 5.8: Matrix of R_2' - α contour plots of the incoming critical pressure for a selection of θ_1 and θ_2. The incoming meniscus types are labelled with white circles. The boundaries between these critical types are shown as dotted black lines. Contours are shown at intervals in ΔP_c^{in} of 0.05. For visual clarity, regions with $\Delta P_c^{\text{in}} > 0$ are marked with a '+', and regions where $\Delta P_c^{\text{in}} < 0$ are marked with a '-'.

When α is sufficiently large to enable $\theta_1 + \alpha > \pi$, the I' state is observed. This is because a convex meniscus is enabled close to the bottom of the well, resulting in a positive critical pressure.

5.4 Critical pressure asymmetry

We now define the critical pressure asymmetry, A, of a pore: the difference between the outgoing and incoming critical pressures,

$$A = \Delta P_r^{\text{out}} - \Delta P_r^{\text{in}}. \tag{5.16}$$

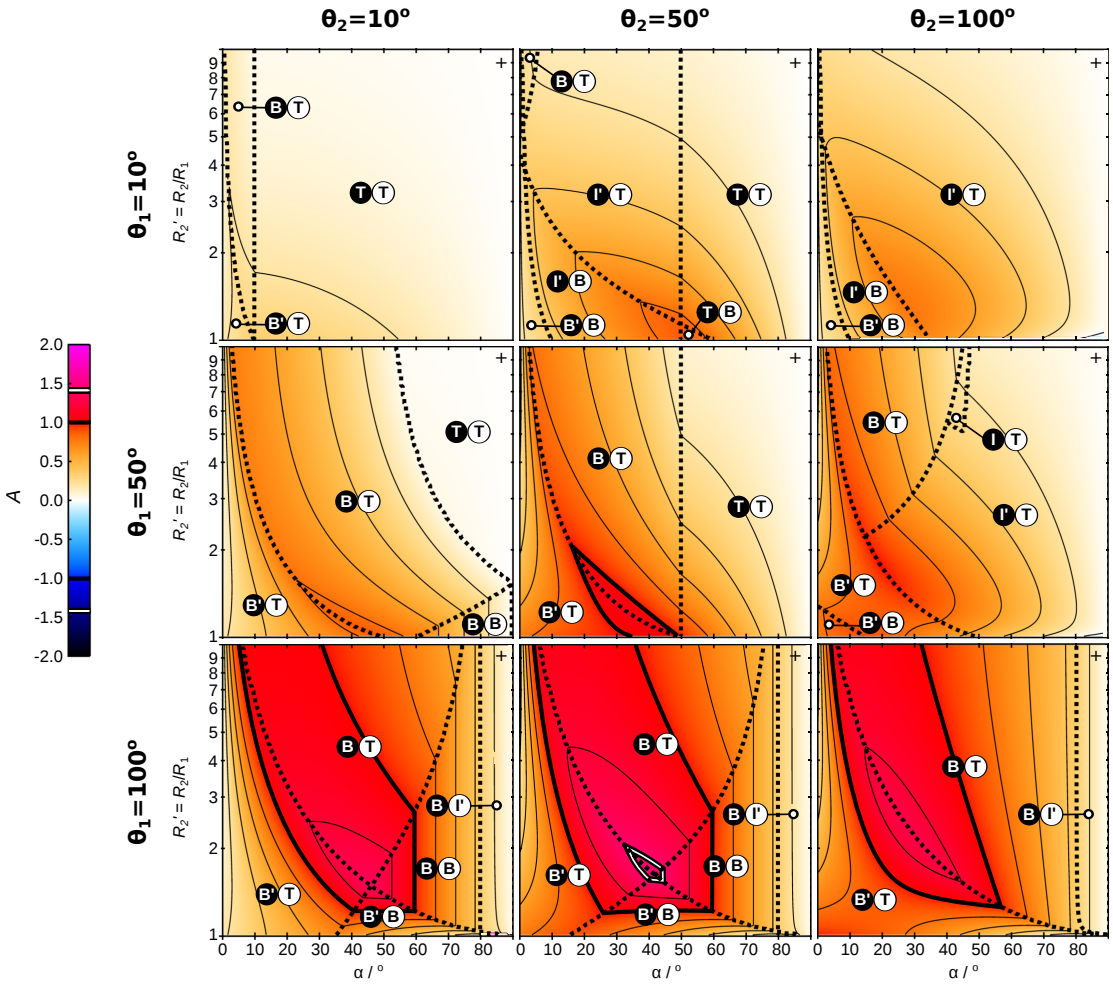

Figure 5.9: Matrix of R_2' - α contour plots of the critical pressure asymmetries for a selection of θ_1 and θ_2. The outgoing meniscus incoming meniscus pair types are labelled with black and white circles. The boundaries between these critical types are shown as dotted black lines. Contours are shown at intervals in A of 0.2. Two significant A contours are also highlighted, $A = 1$ (thick black line), and $A = \sqrt{2}$ (white-centred black line).

A matrix of contour plots shown in Fig. 5.9 illustrates the rich and complex dependence of A on θ_1, θ_2, α, and R_2'. We identify three important values of A to consider, which are deduced in Appendix A. $A = \pm 1$, shown as the thick contour, is the maximum possible asymmetry for a doubly-closed cylindrical pore when $R_2 \to \infty$. $A = \pm\sqrt{2}$ shown as the white-centred black contour, is the maximum possible asymmetry for a semi-open cylindrical pore. $A = 2$ is the maximum possible asymmetry for any pore. We now discuss the features of the critical pressure asymmetries.

It is initially observed that for the range of parameters shown in Fig. 5.9, A is never negative. This can be proved to be true in general for all $\alpha < \pi/2$ in Appendix B. Thus, for $\alpha < \pi/2$, a conical pore will always preferentially intake liquid than expel it.

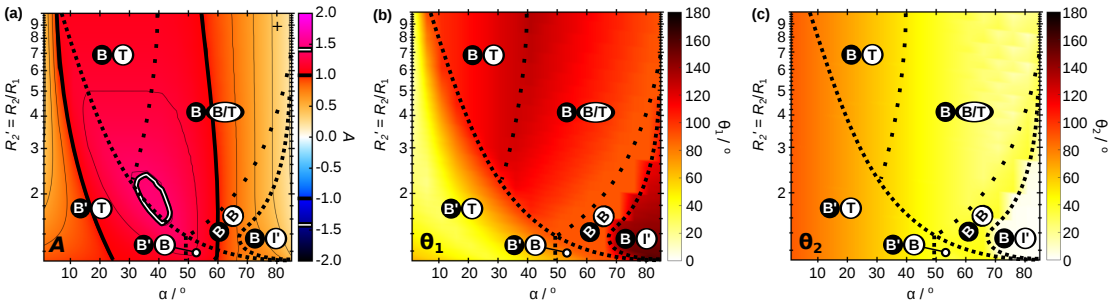

Figure 5.10: (a) Maximum asymmetry possible at each (α, R_2') coordinate. Two significant A limits are highlighted in the contour plots, $A = 1$ (thick black line), and $A = \sqrt{2}$ (white-centred black line). The outgoing meniscus incoming meniscus pair types are labelled with black and white circles, with dense dotted black lines showing the boundaries between these types. The diffuse black dotted line illustrates the approximate region where the incoming B and T states have equal pressure. (b) θ_1 required for maximum asymmetry. (c) θ_2 required for maximum asymmetry.

For $\theta_1 = 10°$, the critical pressure asymmetry remains small. When $\theta_1 < \alpha$, A is small because both the incoming and outgoing critical pressures are negative (with the magnitude of the outgoing being smaller than the incoming). When $\theta_1 > \alpha$, A is also small as although the outgoing critical pressure is positive, it is never large. This is because $\Delta P_c^{\text{out}}(\text{B})$ is small due to the low contact angle, and $\Delta P_c^{\text{out}}(\text{I}')$ is small due to the large contact radius. Overall, the asymmetry is dominated by the negative contribution from the incoming critical pressure, rather than the outgoing critical pressure. Because of the dominance of the incoming critical pressure, the maximal A occurs on the boundary between the incoming B and T critical meniscus types.

For $\theta_1 = 50°$, a similar picture emerges. However, now for $\theta_1 > \alpha$, the B- or B'-type outgoing critical pressure is able to be large and positive. In this region, we therefore begin to see larger A as the contribution of the outgoing critical pressure becomes more significant. The competition also becomes apparent between intermediate positive outgoing critical pressures (at small α, large R_2'), and large negative incoming critical pressures (at intermediate α, small R_2'). The maximum asymmetries occur as an optimal compromise between these extremes, at intermediate α and R_2'. In contrast to $\theta_1 = 10°$, the maximum asymmetries now occur along an outgoing boundary.

For $\theta_1 = 100°$, very large asymmetries are observed, exceeding $A = 1$ in all panels examined, and exceeding $A = \sqrt{2}$ when $\theta_2 = 50°$. Here, the large θ_1 enables large $\Delta P_c^{\text{out}}(\text{B}/\text{B}')$. Thus, the competition between large outgoing and incoming critical pressures observed for $\theta_1 = 50°$ becomes here more extreme. Interestingly, now that both the outgoing and in-

coming critical pressures are able to contribute equally to A, the maximum asymmetries are observed at points where an outgoing-type boundary and incoming-type boundary cross. This is most apparent when $\theta_1 = 100°$, $\theta_2 = 50°$, where at the junction between the outgoing B/B' boundary and incoming T/B boundary, $A > \sqrt{2}$.

5.5 Optimum asymmetry

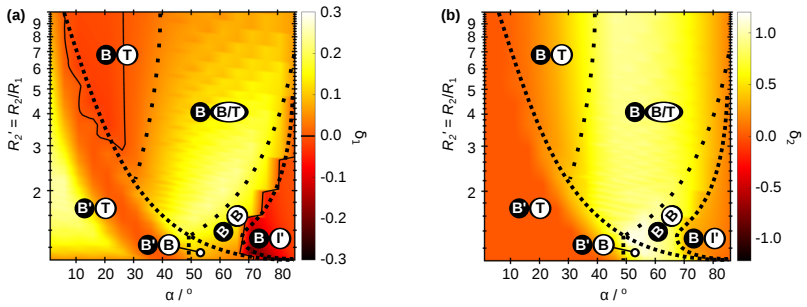

Figure 5.11: Comparison of the asymmetry of the optimal chemically patterned conical pore, with the sum of asymmetries from the same chemical patterning applied to a cylindrical pore, and a chemically homogeneous conical pore. The comparison is made for the chemically homogeneous conical pore with $\theta = \theta_1^{\text{opt}}$ in (a), and $\theta = \theta_2^{\text{opt}}$ in (b). Solid black contours mark the $\delta = 0$ level. Note the larger scale bar range in (b).

We observe in Fig. 5.9 that the (α, R_2') coordinate that maximises the asymmetry depends on both θ_1 and θ_2. We now investigate the maximum possible asymmetry for a specified α and R_2', by varying θ_1 and θ_2. This is achieved by evaluating the asymmetry at each (R_2',α) coordinate, when θ_1 and θ_2 are iteratively incremented in 2° steps from 0° to 180°. The overall optimum asymmetry is shown in Fig. 5.10(a), with the associated optimal θ_1 and θ_2 shown in Fig. 5.10(b) and Fig. 5.10(c) respectively.

Overall, we can conclude that the maximum possible asymmetry, $A = 1.46$, occurs at: $\alpha = 41° \pm 5°$, $R_2' = 1.70 \pm 0.05$, $\theta_1 = 104° \pm 2°$ and $\theta_2 = 49° \pm 2°$. Uncertainties reported indicate the resolution with which the quantities were determined. Across all α and R_2', a key trend we observe is that a high contrast between θ_1 and θ_2 is required in order to produce maximum asymmetries (a homogeneous contact angle will not in general maximise A). We also observe that θ_1 and θ_2 vary non-monotonically with both α and R_2', due to changes in the critical meniscus type.

We now examine the critical meniscus types observed to achieve maximum asymmetry. For the outgoing critical pressure, the observed strategy for maximising A is to ensure the

contact line remains pinned to the bottom of the pore in the B or B' state, thereby ensuring ΔP_c^{out} remains large and positive.

The incoming critical meniscus type is however more variable, particularly in the region where the outgoing critical meniscus is the B-state in the upper right-hand sides of the plots in Fig. 5.10. Here, the incoming meniscus may be in the I', T or B states. In the region where I' is dominant, the incoming critical pressure is positive, making this region unique across all α and R_2'. To maximise the asymmetry in this region, the most effective strategy is to maximise ΔP_c^{out} using $\theta_1 \approx \alpha + \pi/2$, at the expense of enabling a positive incoming critical pressure. However, the large value of α ensures ΔP_c^{in} is never too large, and is minimised further by setting $\theta_2 = 0°$.

When the I' state does not occur however, the B and T incoming states compete for the largest negative ΔP_c^{in}. As is observed in Fig. 5.8, the largest negative critical pressures occur on the boundary between B and T (where this boundary exists). Thus, over the extended region outlined with diffuse dotted lines in Fig. 5.10, the incoming critical pressure is equally described by both the B and T states.

Finally, we examine the cooperativity of the chemical and physical gradients in producing the critical pressure asymmetry. We do this by comparing the optimal critical pressure asymmetry to 'the sum of its parts': the cooperativity δ is defined as

$$\delta = A - \left(A_{\text{het}}^{\text{cyl}} + A_{\text{hom}}^{\text{con}} \right). \tag{5.17}$$

At each (R_2', α) coordinate, $A_{\text{het}}^{\text{cyl}}$ is evaluated as the critical pressure asymmetry of a cylindrical pore, with a chemical gradient the same as the optimal chemical gradient shown in Figs. 5.10(b) and (c). For a fair comparison, we also ensure the pore depth L is the same for the cylindrical and conical pores at each (R_2', α) coordinate. $A_{\text{hom}}^{\text{con}}$ is the critical pressure asymmetry for a chemically homogeneous conical pore. A number of choices exist in deciding which homogeneous contact angle most fairly compares to the optimal chemical gradient. We show in Fig. 5.11 the two limiting cases, when the homogeneous contact angle is: (i) the optimal θ_1 at each (R_2', α) coordinate; (ii) the optimal θ_2 at each (R_2', α) coordinate. To distinguish these two limiting cooperativities, we label these δ_1 in Fig. 5.11(a), and δ_2 in Fig. 5.11(b) respectively.

In Fig. 5.11(a), over the majority of the (R_2', α) plane, the cooperativity $\delta_1 > 0$, meaning

that the optimal asymmetry (arising from both physical and chemical gradients) is greater than the sum of asymmetries arising from the physical gradient and chemical gradient separately. Thus, the physical and chemical gradients act together to produce the high optimal asymmetries. The exceptions to this, when $\delta_1 < 0$ within the solid black contours, arise when the optimal asymmetry is almost wholly achieved through the conical shape and not the chemical patterning. As $A_{\text{het}}^{\text{cyl}} > 0$, in these cases, the optimal asymmetry is less than the sum of its parts.

In Fig. 5.11(b), we observe an extended region at intermediate values of α for which the cooperativity $\delta_2 > 1$. This very large, positive cooperativity is caused in this region by the occurrence of the I-type outgoing critical meniscus for the homogeneous conical pore. The I-type outgoing critical pressure is smaller than the B- or B'-types, hence $A_{\text{hom}}^{\text{con}}$ is small, leading to the large δ_2 observed. The impact of B- or B'-type outgoing critical pressures instead of I can be seen in Fig. 5.11(a). Here, the outgoing type is always B or B', leading to a larger $A_{\text{hom}}^{\text{con}}$, and hence a smaller δ_1.

5.6 Overall optimum pore

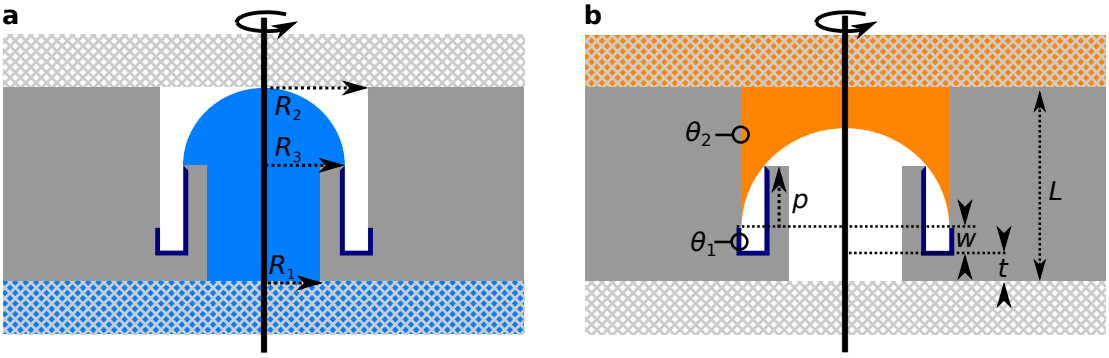

Figure 5.12: Overall optimum pore geometry. (a) Outgoing critical meniscus of radius R_3. (b) Incoming critical meniscus with contact angle $\theta_2 = 0°$ and radius R_2, shown at the point of simultaneous contact with the pore internal lip and non-wetting strip of contact angle θ_1 (dark blue surface).

Throughout, we have explored and optimised the critical pressure asymmetry on a pore of simple physical and chemical patterning for ease of manufacture. Now however, we develop the best possible enclosed pore design, if simple-manufacture constraints are removed. In Fig. 5.12, we develop the reentrant half-enclosed pore design of Agonafer *et al.* [210], to realise a fully enclosed pore design which is capable of yielding $A \to 2$. The design features

a cylindrical pore with an internal lip. In Fig. 5.12(a), we denote the inner cylinder radius as R_1, the outer cylinder radius as R_2, and the outer lip radius as R_3. In Fig. 5.12(b) we show the contact angle everywhere to be $\theta_2 = 0°$, apart from within the lip-cylinder interstice where the contact angle, $\theta_1 > 90°$.

On the lip geometry shown in Fig. 5.12(a), the outgoing critical meniscus is a hemispherical cap of radius R_3, which is pinned to the outer lip edge: $\Delta P_c^{\text{out}} = R_1/R_3$. The incoming critical meniscus, shown in Fig. 5.12(b), is also a hemispherical cap, but of radius $-R_2$: $\Delta P_c^{\text{IN}} = -R_1/R_2$. As the pore is cylindrical, the incoming critical pressure exists over a range of contact line locations, from that shown in Fig. 5.12(b), to the top of the outer cylinder. Combining the incoming and outgoing critical pressures,

$$A = \frac{R_1}{R_3} + \frac{R_1}{R_2}. \tag{5.18}$$

As the R_3 and R_2 are made closer to R_1 (the lip and interstice become thinner), $A \to 2$. Although this limit may not be physically realisable, extremely large asymmetries are possible with finite-thickness structures: for $R_3 = 1.1R_1$ and $R_2 = 1.2R_1$, $A = 1.74$.

For the chemical design, although a uniform contact angle of $\theta_2 = 0°$ is sufficient to achieve these critical menisci, for volatile liquids the base of the lip-cylinder interstice is highly prone to capillary condensation due to the corner geometry [173]. We therefore introduce a non-wetting contact angle within this region, indicated by the dark blue line in Fig. 5.12(a) and (b). This non-wetting region extends up to the top of the lip outer wall, not to prevent condensation there, but to stabilise the outgoing critical meniscus against wetting the outer wall when subject to small perturbations.

For the physical design, we begin by designing the inner lip structure. The lip height p above the non-wetting coating, shown in Fig. 5.12(b), must be sufficiently tall for the incoming meniscus to contact the lip before the contact line reaches the non-wetting coating or bottom of the well. Otherwise, the incoming critical pressure will be less-negative than the optimum. For a hemispherical cap of radius R_2, for this lip-contact to occur,

$$p \geq \sqrt{R_2^2 - R_3^2}. \tag{5.19}$$

Next, the pore thickness L is optimised. As previously described, to maximise the outgoing critical pressure, a hemispherical cap of radius R_3 must be formed. The meniscus therefore

extends above the lip by a height R_3. L must be sufficiently large to accommodate this, so that,

$$L \geq R_3 + p + w + t. \tag{5.20}$$

We are free to choose the non-wetting layer height w and base thickness t, although if a thin membrane is required, these must naturally be minimised.

5.7 Discussion and conclusions

In this chapter we have calculated the maximum Laplace pressures (the critical pressures) required for fluid to both enter and leave a conical, chemically-patterned pore, sandwiched between two absorbent substrates. Across the range of pore designs considered, we found the Laplace pressure to depend on the contact line radius in four different manners; of which two of these arose from a competition between the physical and chemical gradients. This interaction between the two gradients produced three different critical menisci, where the contact line was: pinned to top of the pore, pinned to the bottom of the pore, or located in between. The presence of the top and bottom substrates produced an additional two critical menisci, due to premature contact of the liquid-vapour interface with the substrates.

We then analysed the critical pressure asymmetry, the difference between incoming and outgoing critical pressures, as a measure of the efficacy of the fluid diode across a range of pore geometries. For the pores considered with an opening angle $\alpha < 90°$, the outgoing pressure was always shown to be larger than the incoming pressure. Furthermore, the maximum asymmetry did not in general occur due to the dominance of either the incoming or outgoing critical pressure individually, but as a compromise between the two.

We then optimised the chemical pattering to produce maximal critical pressure asymmetries across the range of pore geometries, showing that a large chemical gradient is required to produce large asymmetries. Across the majority of pore opening angles α and maximum radii R_2, we showed that the optimum asymmetry for the pore with both physical and chemical gradients was greater than the sum of asymmetries of pores with physical gradients and chemical gradients separately. The physical and chemical gradients therefore act together cooperatively to achieve the largest critical pressure asymmetries.

Finally, we lifted the simple design constraints (favouring manufacturability), to design the optimum enclosed pore. We showed that a highly wetting cylinder with internal lip was

capable of generating extremely large asymmetries, which approached the maximum possible asymmetry in the limit of thin lip thickness.

Throughout this chapter, we have modelled the critical liquid menisci under static conditions. Recent results however indicate that under dynamic conditions, in which fluid enters the pore over a finite timescale, the burst pressure required to break through the pore depends on the liquid velocity, and is reduced at high liquid velocities [210]. An interesting perspective for continuation of this work would therefore be to simulate the dynamics of fluid entering the enclosed pore system; particularly relevant for applications where fluid is rapidly introduced to the pore, as in absorbent surface wipes or diapers.

5.8 Note A: Asymmetry limits

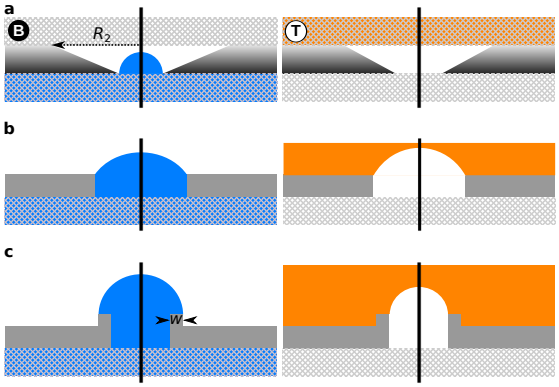

Figure 5.13: Illustrations of the constructions used to calculate the significant critical pressure limits. (a) Critical pressure types for a fully enclosed pore as $R_2' \to \infty$. The maximum asymmetry here is $A = 1$. (b) Critical pressure types for a half-enclosed cylindrical pore. The maximum asymmetry here is $A = \sqrt{2}$. (c) Maximum possible asymmetry on a structured pore. The maximum asymmetry is $A = 2$.

In Fig. 5.13, we show the critical pressure asymmetry limits highlighted in Fig. 5.9. The first highlighted asymmetry, $A = 1$, is the maximum possible asymmetry for a doubly enclosed conical pore when $R_2 \to \infty$, illustrated in Fig. 5.13(a) for $R_2 \to \infty$. When $\theta_1 > \alpha + \pi/2$ and $L' > 1$, but $\theta_1 + \alpha < \pi$ and $\theta_2 + \alpha < \pi$, then $\Delta P_c^{\text{out}}(B) = 1$ and $\Delta P_c^{\text{in}}(T) \to 0$, leading to $A \to 1$.

The second highlighted asymmetry, $A = \sqrt{2}$, is the maximum possible asymmetry for a half-open cylindrical pore, illustrated in Fig. 5.13(b). Here, if $\theta_1 = \theta_2 = \pi/4$, then $\Delta P_c^{\text{out}} = \sqrt{2}/2$ and $\Delta P_c^{\text{in}}(T) = -\sqrt{2}/2$, leading to $A = \sqrt{2}$

The third highlighted asymmetry, $A = 2$, is the maximum possible asymmetry for any

pore geometry, illustrated in Fig. 5.13(c). Here, a lip structure is required on a half-open pore, with $\theta_1 = \theta_2 = 0$. As the lip width $w \to 0$, $\Delta P_c^{\text{out}} \to 1$ and $\Delta P_c^{\text{in}} \to -1$, leading to $A \to 2$. Such an intricately patterned pore design has been recently developed [210]. The disadvantage of this geometry is that it required complex manufacturing procedures, and is not suitable for enclosed-pore applications.

5.9 Note B: Proof of $A > 0$ for $\alpha < \pi/2$

Here we prove that for $\alpha < \pi/2$, the asymmetry $A > 0$. In Fig. 5.14(a), we introduce the angle β_o, which determines the sign and magnitude of the reduced outgoing pressure at a fixed contact line radius. We define β_o with respect to the horizontal axis, such that $\beta_o = \theta - \alpha$. If $\beta_o > 0$, the meniscus is convex, whereas if $\beta_o < 0$, the meniscus is concave. The larger the $|\beta_o|$, the larger the magnitude of the outgoing Laplace pressure. In Fig. 5.14(b), we introduce the angle β_i, which determines the sign and magnitude of the reduced incoming pressure at a chosen contact line radius r_o. We define β_i with respect to the horizontal axis, such that $\beta_i = \theta + \alpha - \pi$. If $\beta_i > 0$, the meniscus is convex, whereas if $\beta_i < 0$, the meniscus is concave. The larger the $|\beta_i|$, the larger the magnitude of the incoming Laplace pressure. When the contact line is at the same location in the pore for the outgoing and incoming interface, we ask whether it is possible for $\beta_o < \beta_i$. This is only possible if $\alpha > \pi/2$, which would require an an inverted pore. For $\alpha < \pi/2$ considered here, $\beta_o > \beta_i$ at all contact line radii. It therefore follows that $\Delta P_r^{\text{out}}(r_o) > \Delta P_r^{\text{in}}(r_o)$. Since ΔP_c^{out} is the maximum of $\Delta P_r^{\text{out}}(r)$, and ΔP_c^{in} is the maximum of $\Delta P_r^{\text{in}}(r)$ for $r \in [1, R_2]$, then it is necessarily true that for $\alpha < \pi/2$, $\Delta P_c^{\text{out}} > \Delta P_c^{\text{in}}$, so that $A > 0$.

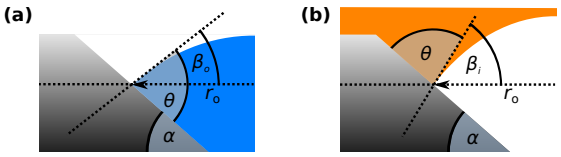

Figure 5.14: Construction of the incoming (a) and outgoing (b) meniscus of a single pore for a fixed contact line radius r_o.

Chapter 6

Conclusions and outlook

Throughout this thesis, a two-tier hierarchy has been presented. At the fundamental level, we have comprehensively investigated four distinct wetting phenomena on structured surfaces: the minimum energy barrier, contact angle hysteresis, the critical pressure on pillared structures, and the critical pressure on gradated, enclosed pores. Without exception, this detailed analysis revealed surprisingly complex wetting phenomena with multiple mechanisms - a direct consequence of multiple stable states in the stability landscapes. On the upper level of this hierarchy, individual wetting phenomena have been combined in order to design structures which are optimal from several aspects simultaneously. This optimal combination proved to be challenging for both structured surfaces, as the properties considered were antagonistically coupled: on the pillared textures, these were the CAH, critical pressure, and minimum energy barrier; while for enclosed pores, these were the incoming and outgoing critical pressures. However, in both cases, this was achieved successfully by developing and maximising application-oriented objective functions: the scoring function for the pillared texture, and the critical pressure asymmetry for the enclosed pores.

We now look to the future. We begin by returning to the pillared geometry to consider an additional wetting property which remains unexplored, but is likely an important factor in future surface design: condensation. This additional factor will be discussed as a representative for a broad range of other design parameters, likely to increase model complexity in the future. Going forwards, the extreme versatility of the stability landscape methods means that many different systems can be investigated. Here, we highlight three potential directions of investigation, although many others are possible, such as liquid crystals and elastic membranes [120].

6.1 Condensation in structured surfaces

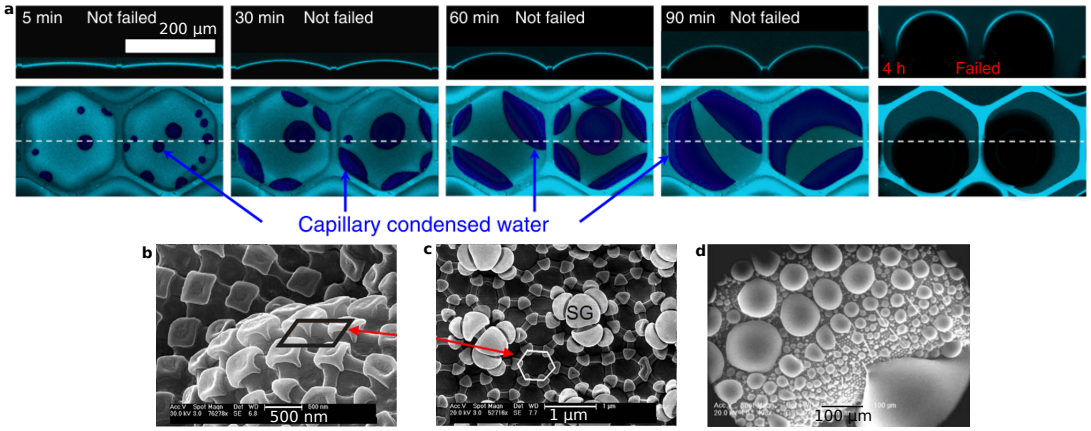

Figure 6.1: (a) Progression of condensation of water inside a hexagonal doubly reentrant well, adapted from [211]. (b) SEM image of the cuticle from the springtail *Tetrodontrophora bilanensis*. (c) SEM image of the cuticle from the springtail *Orthonyciurus stachianus*. (d) Environmental SEM image of condensed droplets forming on top of (but not within) the cuticle of *T. bilanensis*. Panels (b-c) are adapted from [3].

A specific concern for maintaining a suspended state on any structured surfaces is the prevention of condensation, which may otherwise fill the texture and cause collapse when the condensates contact the suspended interface [212]. The diffuse interface model has been successful in this thesis for allowing the study of both the equilibrium morphologies of condensates and the minimum energy condensation mechanism, as shown in Chapter 3. It was shown that for wetting liquids, the corner structures in the doubly reentrant cap presented a low-energy-barrier nucleation site to the liquid, which ultimately led to collapse.

It is tempting to assume that the corner features are responsible for failure via condensation in experiment. In Fig. 6.1(a), we show a recently published sequence of images (from [211]) which observed the nucleation and condensation process of water in a hexagonal, doubly reentrant well. Even though the surface was wetting ($\theta_o = 40°$), the majority of nuclei were not formed in the sharp corner structures - rather the flat surfaces of the well itself. Although our diffuse interface simulations are able to capture the minimum energy nucleation mechanisms, it is clear that in general these are different from the *most likely* nucleation mechanisms. This discrepancy can be explained by placing a forming nucleus randomly on the surface of the system - it is more likely to be located on a planar region than close to a corner structure (assuming the nucleus is small relative to the system size).

A recently proposed solution is to create a texture of reentrant cavities, rather than pillar

structures [212]. In this it was reasoned that for pillared surfaces, the formation and growth of even a single condensate initiates global collapse. Within a system of wells however, failure at a single site only results in local failure, as the collapsing front is not propagated throughout the system. However, we highlight two issues with this approach: firstly, the minimisation of condensation has not been addressed - only the consequences have been reduced in severity; and secondly, well structures have been shown to have exceedingly large CAH, as the liquid contacts a continuous solid structure in which pinning sites span the entire system [176]. Interestingly, this issue may already be resolved on the cuticle of many springtails, two examples of which are shown in Fig. 6.1(b) and (c). In these, the surface structures appear to be a well-pillar hybrids, in which the base of the system is partitioned by ridges, but the pillar caps remain separate. Under repeated condensation experiments, it was found that although water condensed on the top of the texture, shown in Fig. 6.1(d), it remained resistant to condensation within the texture [3]. However, although again well-like features may limit failure via condensation to a local region, how condensation is prevented in these structures remains unknown.

6.2 Complex geometry manufacture

Throughout, a key aim has been to design surface structures with direct relevance to real-world applications. Experimental realisation and testing of our designs would therefore be an important and exciting step forward into achieving this aim. The doubly reentrant geometry for digital microfluidics was designed with a fixed 100 μm system size, which has been demonstrated as an achievable length scale for current fabrication techniques such as lithography [60], fluidisation of polymer micropillars [74] and 3D printing [61]. However, the optimal sub-microscale structure designed for membrane distillation requires a much finer resolution than these manufacture techniques are capable of. The smallest length scale in the system is the cap thickness, with a dimension of 16 nm. Remarkably, this small thickness has been experimentally realised recently, in which Ar^+ ion bombardment of a 20 nm thick gold film resulted in 15 nm thick cap sides on a doubly reentrant geometry. Having therefore demonstrated manufacturability, it will be interesting to see whether, now with clear optimal design targets, advances will be made in high-throughput techniques for manufacturing sub-microscale doubly reentrant geometries.

6.3 Further design aspects

Currently, three wetting properties have been tested for a square array of square geometries, with six variable design parameters, which was sufficient to optimise structures to meet the objective properties. However, a number of further properties may become important for future applications: condensation has been highlighted here, but other examples include slip length in flow, and mechanical stability. Increasing the number of design parameters allows for improved optimal solutions in these cases, but at the cost of vastly increasing the size of the parameter search space. Although the genetic algorithm was highlighted as a general method to perform such complex, multi-variable optimisation, it is not optimal and may still be time consuming to perform. Designed specifically for these high-dimensional optimisation problems, it will be interesting to see whether machine learning and design of experiments (DoE) (see for example [213]) can be incorporated into efficient surface structure design. Largely the preserve of materials scientists currently, these methods allow for highly efficient exploration of the objective function landscape, requiring a minimum number of experiments to perform to achieve optimisation.

6.4 Future applications of landscape methods

The techniques established here for exploring high-dimensional stability landscapes of continuum systems are able to be readily extended to other systems. One key field where this has been applied already is shown in Appendix A, where a continuum elastic shell is discretised into a mesh of springs. In a similar way to how minima and pathways were found for discretised bifluidic systems, different buckled states and the pathways between them are able to be found for thin shells. Three further areas of future development are now highlighted, both within and departing from the field of liquids on surfaces.

6.4.1 Drops on chemically patterned surfaces

Slippery liquid-infused porous surfaces (SLIPS) [215] (also known as liquid-infused surfaces [216], lubricant-impregnated surfaces [217], or lubricant-impregnated rough surfaces [214]) are solid textures which have been imbibed with a highly wetting liquid (typically an oil). Non-miscible drops when placed on these surfaces display exceedingly low CAH, as the infusing liquid minimises the pinning force of the droplet on the solid structures [217].

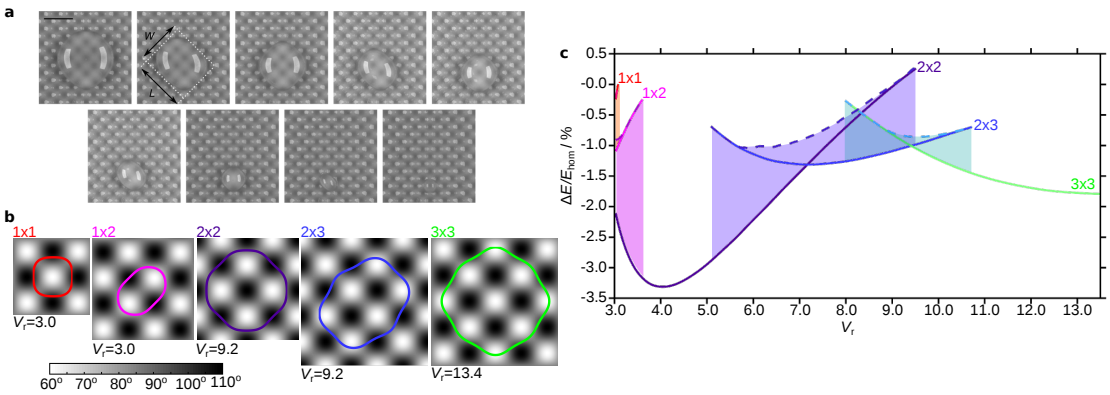

Figure 6.2: (a) Progression of shapes of a droplet evaporating on an eggbox SLIPS surface, adapted from [214]. (b) Simulated shapes obtained for a droplet on a planar, periodic, chemically patterned surface - the local contact angle indicated by the colour bar. (c) The energy of a droplet on the patterned surface, relative to a droplet of the same volume on a planar, chemically homogeneous surface displaying the average contact angle 85°. This relative energy is labelled ΔE, and the homogeneous droplet energy is labelled E_{hom}. The reduced volume V_r is the droplet volume, relative to a cube. Solid lines indicate stable states, dashed lines are transition states. Shaded regions show which stable states are linked via transition states.

Despite the near-complete negation of pinning on the surface texture, recently it has been demonstrated that pinning can be introduced on SLIPS surfaces with non-planar topography [214]. An example of such a surface, described as an 'egg-box' structure, features a periodic sinusoidal height modulation, yielding a square pattern of peaks and troughs as shown in Fig. 6.2(a). Such pinning is able to lead to multiple stable droplet morphologies for a prescribed droplet volume.

The stability landscape methods developed for modelling the interaction of liquids with structured surfaces are readily applicable here. In Fig. 6.2(b) and (c), we are already able to show a selection of results from this investigation. In Fig. 6.2(b), we show the contact line of several stable drop morphologies. Instead of modelling the physical sinusoidal pattern, we employ an analogous, chemically heterogeneous system, where the local contact angle varies sinusoidally. The contact angle modulation on the chemically patterned system is chosen to match that on the physically patterned system, when measured with respect to the horizontal plane. In Fig. 6.2(c), the energy of each state is plotted as solid lines, in which over a range of liquid volumes two or three states may be (meta)stable simultaneously. Using the string method, we are then able to obtain the transition states between these minima, shown as dashed lines in Fig. 6.2(c). Even for this initial system, several interesting results arise. The first is that for the region where the (2×2), (2×3), and (3×3) minima

coexist, the (2×2) converts to (3×3) via (2×3), with no other pathways. The second is that at the end of the volume-existence ranges of each state, a minimum combines with a transition state (or more precisely four symmetry-related transition states). The periodically patterned surface therefore has significant potential for further research from two perspectives. From an application perspective, these systems provide accurate and novel ways to control drop morphology and motion. On a fundamental basis however, they represent convenient systems in which to test how bifurcations and catastrophes occur within parameter-controlled landscapes [218, 219] theoretically, experimentally and via simulation.

6.4.2 Deformation of fibrous biological systems

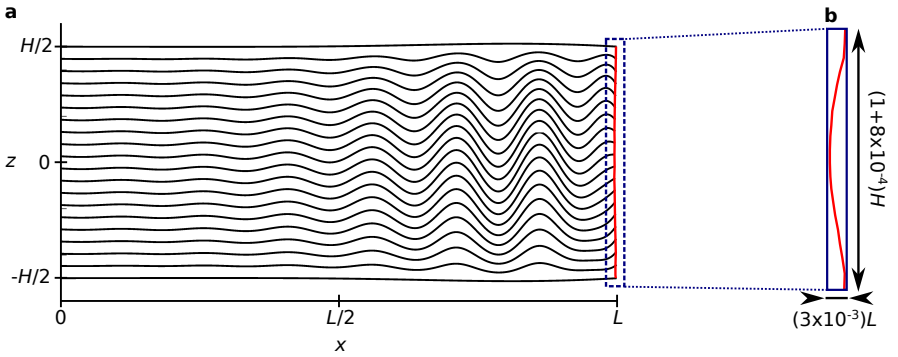

Figure 6.3: (a) Localised deformation of elastic fibres as a model for the optic nerve, subject to a vertical inwards load applied to both outer fibres, and a horizontal load in the $-x$ direction. Here, as L/H=20, the vertical axis is shown stretched to aid visualisation. (b) Magnification of the lamina cribosa deformation (red) where both x and z axes are shown with the same scale.

Increasingly, it is becoming recognised that natural systems exhibit and exploit nonlinearities in elastic deformations [220]. Multistability is a common feature of these systems, as are rapid transitions between (meta)stable states. A characteristic and familiar example of this is the snapping mechanism of the venus flytrap: in which stimulation of the trigger hairs results in a rapid conformational change from a convex, open leaf, to a concave, closed leaf [221]. One biomechanical system that appears within a range of tissues and organisms is elastic fibre bundles, a model of which is shown in Fig. 6.3. These systems have particular biomedical relevance: for example, in healthy individuals the microtubule cytoskeleton in myocytes (heart cells) buckles sinusoidally under heart contraction to regulate the load applied to the cell. Conversely, healthy human optic nerves under normal conditions remain as approximately linear fibre bundles. Recent (unpublished) investigations however suggest

that glaucoma, a disease causing loss of vision, may be initiated through localised buckling of the nerve bundles within the optic fibre.

Our computational techniques are ideally situated to study such nonlinear mechanical response, and recently we have developed and begun to test a 2D model for the optical nerve behind the eye, shown in Fig. 6.3(a). In this, the nerve bundles (shown as black) are discretized into segments, with a mesh of springs linking the bundles. For this specific case, to model the optic nerve structure, the outer bundles are made strongly resistant to bending, the fibre bundles are fixed in location at one end of the nerve, and attached perpendicular to an elastic membrane (modelling the lamina cribosa structure behind the eye) at the other. Mimicking pressure build-up in the eye, the lamina cribosa is subject to forces in the $-x$ direction, and the outer bundles subject to inwards forces along the z-axis. Under certain conditions, the fibre bundles kink as shown in Fig. 6.3(a). This in turn produces a pinching inwards of the lamina cribosa, a magnification of which is shown in Fig. 6.3(b).

Future work will quantify the conditions under which kinking occurs, and attempt to relate this kinking to deformation of the lamina cribosa. As the lamina cribosa can be imaged optically, the ultimate aim would be to develop a diagnostic in which fibre kinking, and hence the risk of developing glaucoma, could be assessed non-invasively, and before nerve damage occurs.

6.4.3 Multifluidic systems

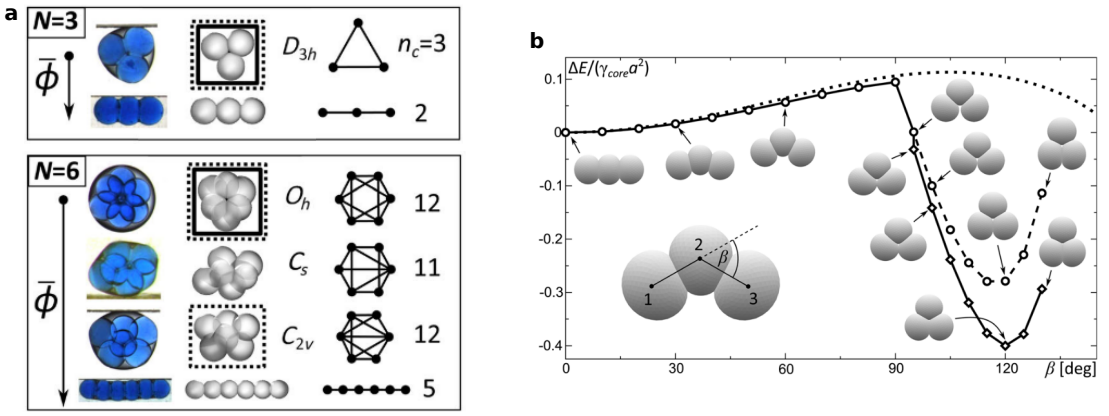

Figure 6.4: (a) Example configurations of droplet clusters (blue) confined within a super-droplet. (b) Proposed transition profile between two 3-droplet states. Adapted from [222].

The final future direction we discuss returns pleasingly to the origin of many of the stability landscape methods discussed throughout this thesis: cluster configurations [115].

However, advancing from Lennard-Jones clusters [223] and sticky-sphere clusters [224], recently Guzowski and Garstecki experimentally realised clusters of liquid droplets, themselves confined within a super-droplet [222]. A selection of example configurations are shown in shown in Fig. 6.4(a).

As the complexity of the system (number of droplets) was increased, the number of stable configurations was also observed to increase. In Fig. 6.4(b), a transition pathway was proposed between two stable 3-droplet states, but only based on the single reaction coordinate β, the opening angle of the 3-droplet chain. Such a system represents a challenging and exciting target to develop our simulation strategies for.

Two major challenges exist. The first is to design a diffuse interface potential which will allow for the simulation of multiple drops in the same system. One promising direction for this is implementation of a multi-phase fluid potential - each droplet represented by a different phase (as proposed in [225] for example). The practical challenge for this scheme however relies on developing parallel minimisation and path-finding methods, to be able to simulate N-component phase fields efficiently.

Bibliography

[1] H. J. Ensikat, P. Ditsche-Kuru, C. Neinhuis, and W. Barthlott, "Superhydrophobicity in perfection: the outstanding properties of the lotus leaf," *Beilstein Journal of Nanotechnology*, vol. 2, no. 1, pp. 152–161, 2011.

[2] W. Barthlott and C. Neinhuis, "Purity of the sacred lotus, or escape from contamination in biological surfaces," *Planta*, vol. 202, no. 1, pp. 1–8, 1997.

[3] R. Helbig, J. Nickerl, C. Neinhuis, and C. Werner, "Smart skin patterns protect springtails," *PLoS ONE*, vol. 6, no. 9, pp. 2–7, 2011.

[4] J. Ju, H. Bai, Y. Zheng, T. Zhao, R. Fang, and L. Jiang, "A multi-structural and multi-functional integrated fog collection system in cactus.," *Nature communications*, vol. 3, p. 1247, 2012.

[5] S. Wang, K. Liu, X. Yao, and L. Jiang, "Bioinspired surfaces with superwettability: New insight on theory, design, and applications," *Chemical Reviews*, vol. 115, pp. 8230–8293, 2015.

[6] S. Zhang, J. Huang, Z. Chen, and Y. Lai, "Bioinspired Special Wettability Surfaces: From Fundamental Research to Water Harvesting Applications," *Small*, vol. 13, no. 3, p. 1602992, 2017.

[7] M. Liu, S. Wang, and L. Jiang, "Nature-inspired superwettability systems," *Nature Reviews Materials*, vol. 2, no. 7, p. 17036, 2017.

[8] A. Marmur, "The Lotus Effect: Superhydrophobicity and Metastability," *Langmuir*, vol. 20, no. 9, pp. 3517–3519, 2004.

[9] J. Nickerl, R. Helbig, H. J. Schulz, C. Werner, and C. Neinhuis, "Diversity and potential correlations to the function of Collembola cuticle structures," *Zoomorphology*, vol. 132, no. 2, pp. 183–195, 2013.

[10] R. Hensel, R. Helbig, S. Aland, H. G. Braun, A. Voigt, C. Neinhuis, and C. Werner, "Wetting resistance at its topographical limit: The benefit of mushroom and serif T structures," *Langmuir*, vol. 29, no. 4, pp. 1100–1112, 2013.

[11] H. Gundersen, H. P. Leinaas, and C. Thaulow, "Surface Structure and Wetting Characteristics of Collembola Cuticles," *PLoS ONE*, vol. 9, no. 2, p. e86783, 2014.

[12] R. Hensel, C. Neinhuis, and C. Werner, "The springtail cuticle as a blueprint for omniphobic surfaces.," *Chemical Society reviews*, vol. 45, pp. 323–341, 2016.

[13] T. Young, "An essay on the cohesion of fluids," *Philosophical Transactions of the Royal Society of London*, vol. 95, pp. 65–87, 1805.

[14] W. Bu, D. Kim, and D. Vaknin, "Density Profiles of Liquid/Vapor Interfaces Away from Their Critical Points," *The Journal of Physical Chemistry C*, vol. 118, no. 23, pp. 12405–12409, 2014.

[15] P. G. de Gennes, F. Brochard-Wyart, and D. Quéré, *Capillarity and Wetting Phenomena: Drops, Bubbles, Pearls, Waves*. New York, USA: Springer Science + Business Media, Inc., 2010.

[16] B. M. Law, S. P. McBride, J. Y. Wang, H. S. Wi, G. Paneru, S. Betelu, B. Ushijima, Y. Takata, B. Flanders, F. Bresme, H. Matsubara, T. Takiue, and M. Aratono, "Line tension and its influence on droplets and particles at surfaces," *Progress in Surface Science*, vol. 92, no. 1, pp. 1–39, 2017.

[17] V. H. Dalvi and P. J. Rossky, "Molecular origins of fluorocarbon hydrophobicity," *Proceedings of the National Academy of Sciences*, vol. 107, no. 31, pp. 13603–13607, 2010.

[18] A. B. D. Cassie and S. Baxter, "Wettability of Porous Surfaces," *Trans. Faraday. Soc.*, vol. 40, pp. 546–551, 1944.

[19] R. N. Wenzel, "Resistance of solid surfaces to wetting by water.," *Industrial and Engineering Chemistry*, vol. 28, no. 8, pp. 988–994, 1936.

[20] E. Bormashenko, "A variational approach to wetting of composite surfaces: Is wetting of composite surfaces a one-dimensional or two-dimensional phenomenon?," *Langmuir*, vol. 25, no. 18, pp. 10451–10454, 2009.

[21] L. Gao and T. J. McCarthy, "An attempt to correct the faulty intuition perpetuated by the wenzel and cassie "laws"," *Langmuir*, vol. 25, no. 13, pp. 7249–7255, 2009.

[22] M. Ma and R. M. Hill, "Superhydrophobic surfaces," *Current Opinion in Colloid & Interface Science*, vol. 11, no. 4, pp. 193–202, 2006.

[23] E. Celia, T. Darmanin, E. Taffin de Givenchy, S. Amigoni, and F. Guittard, "Recent advances in designing superhydrophobic surfaces," *Journal of Colloid and Interface Science*, vol. 402, pp. 1–18, 2013.

[24] H. Kusumaatmaja and J. M. Yeomans, "Modeling contact angle hysteresis on chemically patterned and superhydrophobic surfaces," *Langmuir*, vol. 23, no. 7, pp. 6019–6032, 2007.

[25] A. Marmur, "Solid-Surface Characterization by Wetting," *Annual Review of Materials Research*, vol. 39, no. 1, pp. 473–489, 2009.

[26] D. Quéré, "Wetting and Roughness," *Annual Review of Materials Research*, vol. 38, pp. 71–99, 2008.

[27] P. Zhang, L. Lin, D. Zang, X. Guo, and M. Liu, "Designing Bioinspired Anti-Biofouling Surfaces based on a Superwettability Strategy," *Small*, vol. 13, no. 4, p. 1503334, 2017.

[28] R. Fürstner, W. Barthlott, C. Neinhuis, and P. Walzel, "Wetting and self-cleaning properties of artificial superhydrophobic surfaces," *Langmuir*, vol. 21, pp. 956–961, 2005.

[29] I. Sas, R. E. Gorga, J. A. Joines, and K. A. Thoney, "Literature review on superhydrophobic self-cleaning surfaces produced by electrospinning," *Journal of Polymer Science Part B: Polymer Physics*, vol. 50, no. 12, pp. 824–845, 2012.

[30] E. J. Falde, S. T. Yohe, Y. L. Colson, and M. W. Grinstaff, "Superhydrophobic materials for biomedical applications," *Biomaterials*, vol. 104, pp. 87–103, 2016.

[31] X. Zhang, L. Wang, and E. Levänen, "Superhydrophobic surfaces for the reduction of bacterial adhesion," *RSC Advances*, vol. 3, no. 30, p. 12003, 2013.

[32] J. P. Rothstein, "Slip on Superhydrophobic Surfaces," *Annual Review of Fluid Mechanics*, vol. 42, pp. 89–109, 2010.

[33] Y. Lai, L. Lin, F. Pan, J. Huang, R. Song, Y. Huang, C. Lin, H. Fuchs, and L. Chi, "Bioinspired Patterning with Extreme Wettability Contrast on TiO 2 Nanotube Array Surface: A Versatile Platform for Biomedical Applications," *Small*, vol. 9, no. 17, pp. 2945–2953, 2013.

[34] P. Roach, N. J. Shirtcliffe, and M. I. Newton, "Progess in superhydrophobic surface development," *Soft Matter*, vol. 4, no. 2, pp. 224–240, 2008.

[35] N. Gao and Y. Yan, "Characterisation of surface wettability based on nanoparticles," *Nanoscale*, vol. 4, no. 7, p. 2202, 2012.

[36] A. Checco, A. Rahman, and C. T. Black, "Robust superhydrophobicity in large-area nanostructured surfaces defined by block-copolymer self assembly," *Advanced Materials*, vol. 26, no. 6, pp. 886–891, 2014.

[37] A. Ghicov and P. Schmuki, "Self-ordering electrochemistry: a review on growth and functionality of TiO2 nanotubes and other self-aligned MOx structures," *Chemical Communications*, no. 20, p. 2791, 2009.

[38] D. Tian, Y. Song, and L. Jiang, "Patterning of controllable surface wettability for printing techniques," *Chemical Society Reviews*, vol. 42, no. 12, pp. 5184–5209, 2013.

[39] Y. Li, J. Bi, S. Wang, T. Zhang, X. Xu, H. Wang, S. Cheng, B.-W. Zhu, and M. Tan, "Bio-inspired Edible Superhydrophobic Interface for Reducing Residual Liquid Food," *Journal of Agricultural and Food Chemistry*, vol. 66, no. 9, pp. 2143–2150, 2018.

[40] L. Li, V. Breedveld, and D. W. Hess, "Design and fabrication of superamphiphobic paper surfaces," *ACS Applied Materials and Interfaces*, vol. 5, no. 11, pp. 5381–5386, 2013.

[41] B. Liu and F. F. Lange, "Pressure induced transition between superhydrophobic states: Configuration diagrams and effect of surface feature size," *Journal of Colloid and Interface Science*, vol. 298, no. 2, pp. 899–909, 2006.

[42] J. Zhang, Z. Yao, and P. Hao, "Formation and evolution of air–water interfaces between hydrophilic structures in a microchannel," *Microfluidics and Nanofluidics*, vol. 21, no. 135, pp. 1–8, 2017.

[43] P. Papadopoulos, D. Vollmer, and H.-J. Butt, "Long-Term Repellency of Liquids by Superoleophobic Surfaces," *Physical Review Letters*, vol. 117, p. 046102, 2016.

[44] A. Susarrey-Arce, Á. G. Marín, H. Nair, L. Lefferts, J. G. E. Gardeniers, D. Lohse, and A. van Houselt, "Absence of an evaporation-driven wetting transition on omniphobic surfaces," *Soft Matter*, vol. 8, p. 9765, 2012.

[45] C. Dorrer and J. Rühe, "Condensation and wetting transitions on microstructured ultrahydrophobic surfaces," *Langmuir*, vol. 23, no. 7, pp. 3820–3824, 2007.

[46] B. Zhang and X. Zhang, "Elucidating Nonwetting of Re-Entrant Surfaces with Impinging Droplets," *Langmuir*, vol. 31, pp. 9448–9457, 2015.

[47] L.-Y. Chen, C.-H. Lai, P.-W. Wu, and S.-K. Fan, "Electrowetting of Superhydrophobic ZnO Inverse Opals," *Journal of The Electrochemical Society*, vol. 158, no. 8, pp. 93–99, 2011.

[48] A. Grigoryev, I. Tokarev, K. G. Kornev, I. Luzinov, and S. Minko, "Superomniphobic magnetic microtextures with remote wetting control," *Journal of the American Chemical Society*, vol. 134, pp. 12916–12919, 2012.

[49] M. Amabili, E. Lisi, A. Giacomello, and C. M. Casciola, "Wetting and cavitation pathways on nanodecorated surfaces," *Soft Matter*, vol. 12, no. 12, pp. 3046–3055, 2016.

[50] M. Xu, G. Sun, and C. J. Kim, "Infinite lifetime of underwater superhydrophobic states," *Physical Review Letters*, vol. 113, pp. 1–5, 2014.

[51] P. R. Jones, X. Hao, E. R. Cruz-Chu, K. Rykaczewski, K. Nandy, T. M. Schutzius, K. K. Varanasi, C. M. Megaridis, J. H. Walther, P. Koumoutsakos, H. D. Espinosa, and N. A. Patankar, "Sustaining dry surfaces under water.," *Scientific reports*, vol. 5, p. 12311, 2015.

[52] Y. Li, D. Quéré, C. Lv, and Q. Zheng, "Monostable superrepellent materials," *Proceedings of the National Academy of Sciences*, vol. 114, no. 13, pp. 3387–3392, 2017.

[53] A. Giacomello, L. Schimmele, S. Dietrich, and M. Tasinkevych, "Perpetual superhydrophobicity," *Soft Matter*, vol. 12, no. 43, pp. 8927–8934, 2016.

[54] J. Yong, F. Chen, Q. Yang, J. Huo, and X. Hou, "Superoleophobic surfaces," *Chemical Society Reviews*, vol. 46, no. 14, pp. 4168–4217, 2017.

[55] Z. Chu and S. Seeger, "Superamphiphobic surfaces.," *Chemical Society reviews*, vol. 43, pp. 2784–98, 2014.

[56] A. Tuteja, W. Choi, J. M. Mabry, G. H. McKinley, and R. E. Cohen, "Robust omniphobic surfaces.," *Proceedings of the National Academy of Sciences of the United States of America*, vol. 105, no. 47, pp. 18200–18205, 2008.

[57] J. W. Gibbs, *The Scientific Papers of J. Willard Gibbs, Volume 1. Thermodynamics*. London: Longmans, Green and Co., 1906.

[58] P. S. Laplace, *Supplément au dixième livre du Traité de Mécanique Céleste*. Courcier, Paris, France, 1805.

[59] H. Kusumaatmaja and R. Lipowsky, "Equilibrium Morphologies and Effective Spring Constants of Capillary Bridges," *Langmuir*, vol. 26, no. 24, pp. 18734–18741, 2010.

[60] T. Liu and C.-J. Kim, "Turning a surface superrepellent even to completely wetting liquids," *Science*, vol. 346, no. 6213, pp. 1096–1100, 2014.

[61] X. Liu, H. Gu, M. Wang, X. Du, B. Gao, A. Elbaz, L. Sun, J. Liao, P. Xiao, and Z. Gu, "3D Printing of Bioinspired Liquid Superrepellent Structures," *Advanced Materials*, vol. 30, no. 22, pp. 1–8, 2018.

[62] R. W. Webb, "The evolution of enhanced surface geometries for nucleate boiling," *Heat Transfer Engineering*, vol. 2, no. 3-4, pp. 46–69, 1981.

[63] C.-J. Kim, *Structured Surfaces for Enhanced Nucleate Boiling*. PhD thesis, Iowa State University, 1985.

[64] Y. T. Cheng and D. E. Rodak, "Is the lotus leaf superhydrophobic?," *Applied Physics Letters*, vol. 86, no. 14, pp. 1–3, 2005.

[65] A. K. Epstein, B. Pokroy, A. Seminara, and J. Aizenberg, "Bacterial biofilm shows persistent resistance to liquid wetting and gas penetration," *Proceedings of the National Academy of Sciences*, vol. 108, no. 3, pp. 995–1000, 2011.

[66] D. González, J. Amigo, and F. Suárez, "Membrane distillation: Perspectives for sustainable and improved desalination," *Renewable and Sustainable Energy Reviews*, vol. 80, pp. 238–259, 2017.

[67] A. Ali, R. A. Tufa, F. Macedonio, E. Curcio, and E. Drioli, "Membrane technology in renewable-energy-driven desalination," *Renewable and Sustainable Energy Reviews*, vol. 81, pp. 1–21, 2018.

[68] A. Elbourne, R. J. Crawford, and E. P. Ivanova, "Nano-structured antimicrobial surfaces: From nature to synthetic analogues," *Journal of Colloid and Interface Science*, vol. 508, pp. 603–616, 2017.

[69] Y. Su, C. Luo, Z. Zhang, H. Hermawan, D. Zhu, J. Huang, Y. Liang, G. Li, and L. Ren, "Bioinspired surface functionalization of metallic biomaterials," *Journal of the Mechanical Behavior of Biomedical Materials*, vol. 77, pp. 90–105, 2018.

[70] M. Belhadjamor, M. El Mansori, S. Belghith, and S. Mezlini, "Anti-fingerprint properties of engineering surfaces: a review," *Surface Engineering*, vol. 34, no. 2, pp. 85–120, 2018.

[71] S. L. Freire, "Perspectives on digital microfluidics," *Sensors and Actuators, A: Physical*, vol. 250, pp. 15–28, 2016.

[72] L. Chen, Z. Guo, and W. Liu, "Outmatching superhydrophobicity: bio-inspired reentrant curvature for mighty superamphiphobicity in air," *J. Mater. Chem. A*, vol. 5, no. 28, pp. 14480–14507, 2017.

[73] G.-T. Yun, W.-B. Jung, M. S. Oh, G. M. Jang, J. Baek, and N. I. Kim, "Springtail-inspired superomniphobic surface with extreme pressure resistance," *Science Advances*, vol. 4, p. eaat4978, 2018.

[74] J. Choi, W. Jo, S. Y. Lee, Y. S. Jung, S. H. Kim, and H. T. Kim, "Flexible and Robust Superomniphobic Surfaces Created by Localized Photofluidization of Azopolymer Pillars," *ACS Nano*, vol. 11, no. 8, pp. 7821–7828, 2017.

[75] X. Deng, L. Mammen, H.-J. Butt, and D. Vollmer, "Candle Soot as a Template for a Transparent Robust Superamphiphobic Coating," *Science*, vol. 335, pp. 67–71, 2012.

[76] B. P. Dyett, A. H. Wu, and R. N. Lamb, "Mechanical Stability of Surface Architecture - Consequences for Superhydrophobicity," *ACS Appl Mater Interfaces*, vol. 6, no. 21, pp. 18380 – 18394, 2014.

[77] X. Jing and Z. Guo, "Biomimetic super durable and stable surfaces with superhydrophobicity," *Journal of Materials Chemistry A*, vol. 6, no. 35, pp. 16731–16768, 2018.

[78] J. E. Mates, T. M. Schutzius, J. Qin, D. E. Waldroup, and C. M. Megaridis, "The fluid diode: Tunable unidirectional flow through porous substrates," *ACS Applied Materials and Interfaces*, vol. 6, no. 15, pp. 12837–12843, 2014.

[79] J. Li, J. Li, J. Sun, S. Feng, and Z. Wang, "Biological and Engineered Topological Droplet Rectifiers," *Advanced Materials*, vol. 31, no. 14, p. 1806501, 2019.

[80] M. J. Hancock, K. Sekeroglu, and M. C. Demirel, "Bioinspired Directional Surfaces for Adhesion, Wetting, and Transport," *Advanced Functional Materials*, vol. 22, no. 11, pp. 2223–2234, 2012.

[81] H. Bai, X. Tian, Y. Zheng, J. Ju, Y. Zhao, and L. Jiang, "Direction Controlled Driving of Tiny Water Drops on Bioinspired Artificial Spider Silks," *Advanced Materials*, vol. 22, no. 48, pp. 5521–5525, 2010.

[82] H. Kusumaatmaja and J. M. Yeomans, "Anisotropic hysteresis on ratcheted superhydrophobic surfaces," *Soft Matter*, vol. 5, no. 14, p. 2704, 2009.

[83] J. Li, Y. Song, H. Zheng, S. Feng, W. Xu, and Z. Wang, "Designing biomimetic liquid diodes," *Soft Matter*, vol. 15, no. 9, pp. 1902–1915, 2019.

[84] S. Zhang, J. Huang, Z. Chen, S. Yang, and Y. Lai, "Liquid mobility on superwettable surfaces for applications in energy and the environment," *Journal of Materials Chemistry A*, vol. 7, no. 1, pp. 38–63, 2019.

[85] Y. Zhao, H. Wang, H. Zhou, and T. Lin, "Directional Fluid Transport in Thin Porous Materials and its Functional Applications," *Small*, vol. 13, no. 4, p. 1601070, 2017.

[86] P. Gupta and B. Kandasubramanian, "Directional Fluid Gating by Janus Membranes with Heterogeneous Wetting Properties for Selective Oil–Water Separation," *ACS Applied Materials & Interfaces*, vol. 9, no. 22, pp. 19102–19113, 2017.

[87] P. S. Brown and B. Bhushan, "Bioinspired materials for water supply and management: water collection, water purification and separation of water from oil," *Philosophical Transactions of the Royal Society A: Mathematical, Physical and Engineering Sciences*, vol. 374, no. 2073, p. 20160135, 2016.

[88] A. J. DeMello, "Control and detection of chemical reactions in microfluidic systems," *Nature*, vol. 442, no. 7101, pp. 394–402, 2006.

[89] L. Shang, Y. Cheng, and Y. Zhao, "Emerging Droplet Microfluidics," *Chemical Reviews*, vol. 117, no. 12, pp. 7964–8040, 2017.

[90] J. Li, X. Zhou, J. Li, L. Che, J. Yao, G. McHale, M. K. Chaudhury, and Z. Wang, "Topological liquid diode," *Science Advances*, vol. 3, no. 10, p. eaao3530, 2017.

[91] D. Shou and J. Fan, "An All Hydrophilic Fluid Diode for Unidirectional Flow in Porous Systems," *Advanced Functional Materials*, vol. 28, no. 36, p. 1800269, 2018.

[92] M. Zimmermann, P. Hunziker, and E. Delamarche, "Valves for autonomous capillary systems," *Microfluidics and Nanofluidics*, vol. 5, no. 3, pp. 395–402, 2008.

[93] H. Cho, H.-Y. Kim, J. Y. Kang, and T. S. Kim, "How the capillary burst microvalve works," *Journal of Colloid and Interface Science*, vol. 306, pp. 379–385, 2007.

[94] J. M. Chen, C.-Y. Chen, and C.-H. Liu, "Pressure Barrier in an Axisymmetric Capillary Microchannel with Sudden Expansion," *Japanese Journal of Applied Physics*, vol. 47, no. 3, pp. 1683–1689, 2008.

[95] A. Taher, B. Jones, P. Fiorini, and L. Lagae, "Analytical, numerical and experimental study on capillary flow in a microchannel traversing a backward facing step," *International Journal of Multiphase Flow*, vol. 107, pp. 221–229, 2018.

[96] L. Hou, N. Wang, X. Man, Z. Cui, J. Wu, J. Liu, S. Li, Y. Gao, D. Li, L. Jiang, and Y. Zhao, "Interpenetrating Janus Membrane for High Rectification Ratio Liquid Unidirectional Penetration," *ACS Nano*, vol. 13, no. 4, pp. 4124–4132, 2019.

[97] T. Li, F. Liu, S. Zhang, H. Lin, J. Wang, and C. Y. Tang, "Janus Polyvinylidene Fluoride Membrane with Extremely Opposite Wetting Surfaces via One Single-Step Unidirectional Segregation Strategy," *ACS Applied Materials & Interfaces*, vol. 10, no. 29, pp. 24947–24954, 2018.

[98] X. Tian, H. Jin, J. Sainio, R. H. A. Ras, and O. Ikkala, "Droplet and Fluid Gating by Biomimetic Janus Membranes," *Advanced Functional Materials*, vol. 24, no. 38, pp. 6023–6028, 2014.

[99] F. Brochard, "Motions of droplets on solid surfaces induced by chemical or thermal gradients," *Langmuir*, vol. 5, no. 2, pp. 432–438, 1989.

[100] Y. Ito, M. Heydari, A. Hashimoto, T. Konno, A. Hirasawa, S. Hori, K. Kurita, and A. Nakajima, "The Movement of a Water Droplet on a Gradient Surface Prepared by Photodegradation," *Langmuir*, vol. 23, no. 4, pp. 1845–1850, 2007.

[101] B. Zhao, J. S. Moore, and D. J. Beebe, "Principles of Surface-Directed Liquid Flow in Microfluidic Channels," *Analytical Chemistry*, vol. 74, no. 16, pp. 4259–4268, 2002.

[102] P. Renvoisé, J. W. M. Bush, M. Prakash, and D. Quéré, "Drop propulsion in tapered tubes," *EPL (Europhysics Letters)*, vol. 86, no. 6, p. 64003, 2009.

[103] L. Lorenceau and D. Quéré, "Drops on a conical wire," *Journal of Fluid Mechanics*, vol. 510, pp. 29–45, 2004.

[104] M. L. Blow, H. Kusumaatmaja, and J. M. Yeomans, "Imbibition through an array of triangular posts," *Journal of Physics: Condensed Matter*, vol. 21, no. 46, p. 464125, 2009.

[105] G. Buchberger, A. Kogler, A. Weth, R. Baumgartner, P. Comanns, S. Bauer, and W. Baumgartner, ""Fluidic diode" for passive unidirectional liquid transport bioinspired by the spermathecae of fleas," *Journal of Bionic Engineering*, vol. 15, no. 1, pp. 42–56, 2018.

[106] P. Comanns, G. Buchberger, A. Buchsbaum, R. Baumgartner, A. Kogler, S. Bauer, and W. Baumgartner, "Directional, passive liquid transport: the Texas horned lizard as a model for a biomimetic 'liquid diode'," *Journal of The Royal Society Interface*, vol. 12, no. 109, p. 20150415, 2015.

[107] J. Rowlinson, "English translation of J. D. van der Waals' The thermodynamic theory of capillarity under the hypothesis of a continuous variation of density," *Journal of Statistical Physics*, vol. 20, no. 2, pp. 197–200, 1979.

[108] J. W. Cahn and J. E. Hilliard, "Free Energy of a Nonuniform System . I . Interfacial Free Energy," *J. Chem. Phys.*, vol. 28, no. 2, pp. 258–267, 1958.

[109] D. Jacqmin, "Calculation of Two-Phase Navier–Stokes Flows Using Phase-Field Modeling," *Journal of Computational Physics*, vol. 155, no. 1, pp. 96–127, 1999.

[110] A. J. Briant, A. J. Wagner, and J. M. Yeomans, "Lattice Boltzmann simulations of contact line motion. I. Liquid-gas systems," *Physical Review E*, vol. 69, no. 3, p. 031602, 2004.

[111] A. J. Briant and J. M. Yeomans, "Lattice Boltzmann simulations of contact line motion. II. Binary fluids," *Physical Review E*, vol. 69, no. 3, p. 031603, 2004.

[112] J. Lowengrub and L. Truskinovsky, "Quasi–incompressible Cahn–Hilliard fluids and topological transitions," *Proceedings of the Royal Society of London. Series A: Mathematical, Physical and Engineering Sciences*, vol. 454, no. 1978, pp. 2617–2654, 1998.

[113] J. Nocedal, "Updating Quasi-Newton Matrices With Limited Storage," *Math. Comp.*, vol. 35, no. 151, pp. 773–782, 1980.

[114] D. Liu and J. Nocedal, "On the Limited Memory BFGS Method for Large Scale Optimization," *Math. Program.*, vol. 45, pp. 503–528, 1989.

[115] D. J. Wales, *Energy Landscapes*. Cambridge University Press, Cambridge, 2003.

[116] P. J. Hoogerbrugge and J. M. V. A. Koelman, "Simulating Microscopic Hydrodynamic Phenomena with Dissipative Particle Dynamics," *Europhysics Letters (EPL)*, vol. 19, no. 3, pp. 155–160, 1992.

[117] P. Español and P. Warren, "Statistical Mechanics of Dissipative Particle Dynamics," *Europhysics Letters (EPL)*, vol. 30, no. 4, pp. 191–196, 1995.

[118] T. Krüger, H. Kusumaatmaka, A. Kuzmin, O. Shardt, G. Silva, and E. M. Vigen, *The Lattice Boltzmann Method: Principles and Practie*. Springer International Publishing Switzerland, 2017.

[119] G. R. Liu and L. M. B., *Smoothed particle hydrodynamics: A meshfree particle method*. World Scientific Publishing, Singapore, 2003.

[120] H. Kusumaatmaja, "Surveying the free energy landscapes of continuum models: Application to soft matter systems," *The Journal of Chemical Physics*, vol. 142, no. 12, p. 124112, 2015.

[121] M. Plapp, "Phase-Field Models," in *Multiphase Microfluidics: The Diffuse Interface Model. CISM Courses and Lectures, vol 538.* (R. Mauri, ed.), ch. Phase-Fiel, pp. 129–175, Vienna: Springer, 2012.

[122] H. Kusumaatmaja and J. M. Yeomans, "Lattice boltzmann simulations of wetting and drop dynamics," in *Simulating Complex Systems by Cellular Automata* (A. Hoekstra, J. Kroc, and P. Sloot, eds.), Springer Berlin Heidelberg, 2010.

[123] D. Beysens and M. Robert, "Thickness of fluid interfaces near the critical point from optical reflectivity measurements," *The Journal of Chemical Physics*, vol. 87, no. 5, pp. 3056–3061, 1987.

[124] J. W. Cahn, "Critical point wetting," *The Journal of Chemical Physics*, vol. 66, no. 8, pp. 3667–3672, 1977.

[125] D. M. Anderson, G. B. McFadden, and A. A. Wheeler, "Diffuse-Interface Methods in Fluid Mechanics," *Annual Review of Fluid Mechanics*, vol. 30, no. 1, pp. 139–165, 1998.

[126] P. G. de Gennes, "Wetting: Statistics and Dynamics," *Rev. Mod. Phys.*, vol. 57, no. 3, pp. 827–863, 1985.

[127] P. Papatzacos, "Macroscopic two-phase flow in porous media assuming the diffuse-interface model at pore level," *Transport in Porous Media*, vol. 49, pp. 139–174, 2002.

[128] K. Connington and T. Lee, "Lattice Boltzmann simulations of forced wetting transitions of drops on superhydrophobic surfaces," *Journal of Computational Physics*, vol. 250, pp. 601–615, 2013.

[129] J.-J. Huang, H. Huang, and X. Wang, "Wetting boundary conditions in numerical simulation of binary fluids by using phase-field method: some comparative studies and new development," *International Journal for Numerical Methods in Fluids*, vol. 77, no. 3, pp. 123–158, 2015.

[130] C. T. Kelley, *Iterative Methods for Optimization*. Society for Industrial and Applied Mathematics, 1999.

[131] J. E. Dennis, Jr. and J. J. Moré, "Quasi-Newton Methods, Motivation and Theory," *SIAM Review*, vol. 19, no. 1, pp. 46–89, 1977.

[132] G. Henkelman and H. Jónsson, "Improved tangent estimate in the nudged elastic band method for finding minimum energy paths and saddle points," *The Journal of Chemical Physics*, vol. 113, no. 22, pp. 9978–9985, 2000.

[133] S. A. Trygubenko and D. J. Wales, "A doubly nudged elastic band method for finding transition states," *The Journal of Chemical Physics*, vol. 120, no. 5, pp. 2082–2094, 2004.

[134] W. E, W. Ren, and E. Vanden-Eijnden, "Simplified and improved string method for computing the minimum energy paths in barrier-crossing events," *The Journal of Chemical Physics*, vol. 126, no. 16, p. 164103, 2007.

[135] D. J. Wales, "Optim: A program for optimizing geometries and calculating reaction pathways," 2016. http://www-wales.ch.cam.ac.uk/OPTIM.doc/OPTIM.

[136] H. Jonsson, G. Mills, and K. W. Jacobsen, "Nudged elastic band method for finding minimum energy paths of tranisitons," in *Classical and Quantum Dynamics in Condensed Phase Simulations* (B. J. Berne, G. Ciccotti, and D. F. Coker, eds.), World Scientific, Singapore, 1998.

[137] D. Sheppard, R. Terrell, and G. Henkelman, "Optimization methods for finding minimum energy paths," *The Journal of Chemical Physics*, vol. 128, p. 134106, 2008.

[138] W. E, W. Ren, and E. Vanden-Eijnden, "String method for the study of rare events," *Physical Review B*, vol. 66, no. 5, p. 052301, 2002.

[139] W. Ren and E. Vanden-Eijnden, "A climbing string method for saddle point search," *The Journal of Chemical Physics*, vol. 138, no. 13, p. 134105, 2013.

[140] Y. Choi and P. McKenna, "A mountain pass method for the numerical solution of semilinear elliptic problems," *Nonlinear Analysis: Theory, Methods & Applications*, vol. 20, no. 4, pp. 417–437, 1993.

[141] S. Maeda, K. Ohno, and K. Morokuma, "Systematic exploration of the mechanism of chemical reactions: the global reaction route mapping (GRRM) strategy using the ADDF and AFIR methods," *Physical Chemistry Chemical Physics*, vol. 15, no. 11, p. 3683, 2013.

[142] A. L. Dewyer, A. J. Argüelles, and P. M. Zimmerman, "Methods for exploring reaction space in molecular systems," *Wiley Interdisciplinary Reviews: Computational Molecular Science*, vol. 8, no. 2, pp. 1–20, 2018.

[143] J. P. K. Doye and D. J. Wales, "Saddle points and dynamics of Lennard-Jones clusters, solids, and supercooled liquids," *The Journal of Chemical Physics*, vol. 116, no. 9, pp. 3777–3788, 2002.

[144] W. C. Rheinboldt, "Numerical continuation methods: a perspective," *Journal of Computational and Applied Mathematics*, vol. 124, no. 1-2, pp. 229–244, 2000.

[145] J. Duncan, Q. Wu, K. Promislow, and G. Henkelman, "Biased gradient squared descent saddle point finding method," *Journal of Chemical Physics*, vol. 140, p. 194102, 2014.

[146] M. Reyssat, J. M. Yeomans, and D. Quéré, "Impalement of fakir drops," *Epl*, vol. 81, p. 26006, 2008.

[147] P. Papadopoulos, L. Mammen, X. Deng, D. Vollmer, and H.-J. Butt, "How superhydrophobicity breaks down," *Proceedings of the National Academy of Sciences of the United States of America*, vol. 110, no. 9, pp. 3254–3258, 2013.

[148] H. Rathgen and F. Mugele, "Microscopic shape and contact angle measurement at a superhydrophobic surface," *Faraday discussions*, vol. 146, pp. 49–56, 2010.

[149] P. Lv, Y. Xue, Y. Shi, H. Lin, and H. Duan, "Metastable states and wetting transition of submerged superhydrophobic structures," *Physical Review Letters*, vol. 112, p. 196101, 2014.

[150] P. Lv, Y. Xue, H. Liu, Y. Shi, P. Xi, H. Lin, and H. Duan, "Symmetric and Asymmetric Meniscus Collapse in Wetting Transition on Submerged Structured Surfaces," *Langmuir*, vol. 31, no. 4, pp. 1248–1254, 2015.

[151] N. A. Patankar, "Transition between superhydrophobic states on rough surfaces," *Langmuir*, vol. 20, no. 17, pp. 7097–7102, 2004.

[152] H. Kusumaatmaja, M. L. Blow, A. Dupuis, and J. M. Yeomans, "The collapse transition on superhydrophobic surfaces," *EPL*, vol. 81, p. 36003, 2008.

[153] H. J. Butt, I. V. Roisman, M. Brinkmann, P. Papadopoulos, D. Vollmer, and C. Semprebon, "Characterization of super liquid-repellent surfaces," *Current Opinion in Colloid and Interface Science*, vol. 19, pp. 343–354, 2014.

[154] E. Bormashenko, "Progress in understanding wetting transitions on rough surfaces," *Advances in Colloid and Interface Science*, vol. 222, pp. 92–103, 2015.

[155] Y. C. Jung and B. Bhushan, "Wetting transition of water droplets on superhydrophobic patterned surfaces," *Scripta Materialia*, vol. 57, pp. 1057–1060, 2007.

[156] N. A. Patankar, "Consolidation of hydrophobic transition criteria by using an approximate energy minimization approach," *Langmuir*, vol. 26, no. 11, pp. 8941–8945, 2010.

[157] C. Dorrer and J. Rühe, "Some thoughts on superhydrophobic wetting," *Soft Matter*, vol. 5, no. 1, pp. 51–61, 2009.

[158] A. Shahraz, A. Borhan, and K. A. Fichthorn, "Kinetics of droplet wetting mode transitions on grooved surfaces: Forward flux sampling," *Langmuir*, vol. 30, pp. 15442–15450, 2014.

[159] G. Pashos, G. Kokkoris, and a.G. Boudouvis, "A modified phase-field method for the investigation of wetting transitions of droplets on patterned surfaces," *Journal of Computational Physics*, vol. 283, pp. 258–270, 2015.

[160] A. Giacomello, S. Meloni, M. Chinappi, and C. M. Casciola, "Cassie-baxter and wenzel states on a nanostructured surface: Phase diagram, metastabilities, and transition mechanism by atomistic free energy calculations," *Langmuir*, vol. 28, pp. 10764–10772, 2012.

[161] A. Giacomello, S. Meloni, M. Müller, and C. M. Casciola, "Mechanism of the Cassie-Wenzel transition via the atomistic and continuum string methods," *J. Chem. Phys.*, vol. 142, no. 10, p. 104701, 2015.

[162] S. Prakash, E. Xi, and A. J. Patel, "Spontaneous Recovery of Superhydrophobicity on Nanotextured Surfaces," *PNAS*, vol. 113, no. 20, pp. 5508–5513, 2016.

[163] M. Amabili, A. Giacomello, S. Meloni, and C. M. Casciola, "Unraveling the Salvinia Paradox: Design Principles for Submerged Superhydrophobicity," *Advanced Materials Interfaces*, vol. 2, p. 1500248, 2015.

[164] E. S. Savoy and F. A. Escobedo, "Simulation Study of Free-Energy Barriers in the Wetting Transition of an Oily Fluid on a Rough Surface with Reentrant Geometry," *Langmuir*, vol. 28, pp. 16080–16090, 2012.

[165] E. S. Savoy and F. A. Escobedo, "Molecular simulations of wetting of a rough surface by an oily fluid: effect of topology, chemistry, and droplet size on wetting transition rates," *Langmuir*, vol. 28, no. 7, pp. 3412–3419, 2012.

[166] W. Ren, "Wetting transition on patterned surfaces: Transition states and energy barriers," *Langmuir*, vol. 30, no. 10, pp. 2879–2885, 2014.

[167] Y. Zhang and W. Ren, "Numerical study of the effects of surface topography and chemistry on th wetting transition using the string method," *J. Chem. Phys.*, vol. 141, p. 244705, 2014.

[168] M. Amabili, A. Giacomello, S. Meloni, and C. M. Casciola, "Collapse of superhydrophobicity on nanopillared surfaces," *Physical Review Fluids*, vol. 2, p. 034, 2017.

[169] M. Amabili, S. Meloni, A. Giacomello, and C. Casciola, "Activated Wetting of Nanostructured Surfaces: Reaction Coordinates, Finite Size Effects, and Simulation Pitfalls," *The Journal of Physical Chemistry B*, vol. 122, pp. 200–212, 2018.

[170] G. Pashos, G. Kokkoris, A. G. Papathanasiou, and A. G. Boudouvis, "Wetting transitions on patterned surfaces with diffuse interaction potentials embedded in a Young-Laplace formulation," *The Journal of Chemical Physics*, vol. 144, p. 034105, 2016.

[171] Q. S. Zheng, Y. Yu, and Z. H. Zhao, "Effects of hydraulic pressure on the stability and transition of wetting modes of superhydrophobic surfaces," *Langmuir*, vol. 21, no. 26, pp. 12207–12212, 2005.

[172] A. O. Parry and C. Rascón, "Scaling properties of fluid adsorption near the base of a cylinder," *Physical Review E*, vol. 85, p. 031606, 2012.

[173] K. Rejmer, S. Dietrich, and M. Napiórkowski, "Filling transition for a wedge," *Physical review. E*, vol. 60, no. 4, pp. 4027–4042, 1999.

[174] J. R. Panter and H. Kusumaatmaja, "The impact of surface geometry, cavitation, and condensation on wetting transitions: posts and reentrant structures," *Journal of Physics: Condensed Matter*, vol. 29, no. 8, p. 084001, 2017.

[175] H. Zhao, K.-C. Park, and K.-Y. Law, "Effect of Surface Texturing on Superoleophobicity, Contact Angle Hysteresis, and "Robustness"," *Langmuir*, vol. 28, no. 42, pp. 14925–14934, 2012.

[176] E. M. Domingues, S. Arunachalam, and H. Mishra, "Doubly Reentrant Cavities Prevent Catastrophic Wetting Transitions on Intrinsically Wetting Surfaces," *ACS Applied Materials and Interfaces*, vol. 9, pp. 21532–21538, 2017.

[177] Z. Wang and T. Wu, "Modeling pressure stability and contact-angle hysteresis of superlyophobic surfaces based on local contact line," *Journal of Physical Chemistry C*, vol. 119, no. 23, pp. 12916–12922, 2015.

[178] F. Schellenberger, N. Encinas, D. Vollmer, and H. J. Butt, "How Water Advances on Superhydrophobic Surfaces," *Physical Review Letters*, vol. 116, p. 096101, 2016.

[179] W. Choi, A. Tuteja, J. M. Mabry, R. E. Cohen, and G. H. McKinley, "A modified Cassie-Baxter relationship to explain contact angle hysteresis and anisotropy on non-wetting textured surfaces," *Journal of Colloid and Interface Science*, vol. 339, pp. 208–216, 2009.

[180] A. L. Dubov, J. Teisseire, and E. Barthel, "Elastic instability and contact angles on hydrophobic surfaces with periodic textures," *EPL*, vol. 97, no. 2, p. 26003, 2012.

[181] B. M. Mognetti and J. M. Yeomans, "Modeling receding contact lines on superhydrophobic surfaces," *Langmuir*, vol. 26, no. 23, pp. 18162–18168, 2010.

[182] M. Reyssat and D. Quéré, "Contact Angle hysteresis generated by strong dilute defects," *Journal of Physical Chemistry B*, vol. 113, no. 12, pp. 3906–3909, 2009.

[183] R. Dufour, M. Harnois, V. Thomy, R. Boukherroub, and V. Senez, "Contact angle hysteresis origins: Investigation on super-omniphobic surfaces," *Soft Matter*, vol. 7, pp. 9380–9387, 2011.

[184] Y. H. Yeong, A. Milionis, E. Loth, and I. S. Bayer, "Microscopic Receding Contact Line Dynamics on Pillar and Irregular Superhydrophobic Surfaces," *Scientific Reports*, vol. 5, no. 1, p. 8384, 2015.

[185] H.-J. Butt, D. Vollmer, and P. Papadopoulos, "Super liquid-repellent layers: The smaller the better," *Advances in Colloid and Interface Science*, vol. 222, pp. 104–109, 2015.

[186] H. J. Butt, N. Gao, P. Papadopoulos, W. Steffen, M. Kappl, and R. Berger, "Energy dissipation of moving drops on superhydrophobic and superoleophobic surfaces," *Langmuir*, vol. 33, pp. 107–116, 2017.

[187] J. W. Krumpfer, P. Bian, P. Zheng, L. Gao, and T. J. McCarthy, "Contact angle hysteresis on superhydrophobic surfaces: An ionic liquid probe fluid offers mechanistic insight," *Langmuir*, vol. 27, pp. 2166–2169, 2011.

[188] R. Dufour, P. Brunet, M. Harnois, R. Boukherroub, V. Thomy, and V. Senez, "Zipping Effect on Omniphobic Surfaces for Controlled Deposition of Minute Amounts of Fluid or Colloids," *Small*, vol. 8, no. 8, pp. 1229–1236, 2012.

[189] K. W. Lawson and D. R. Lloyd, "Membrane distillation," *Journal of Membrane Science*, vol. 124, pp. 1–25, 1997.

[190] M. Washizu, "Electrostatic actuation of liquid droplets for microreactor applications," *IEEE Transactions on Industry Applications*, vol. 34, no. 4, pp. 732–737, 1998.

[191] H. Ding, S. Sadeghi, G. J. Shah, S. Chen, P. Y. Keng, C.-J. Kim, and R. M. van Dam, "Accurate dispensing of volatile reagents on demand for chemical reactions in EWOD chips," *Lab on a Chip*, vol. 12, no. 18, p. 3331, 2012.

[192] S. Lee, J.-S. Park, and T. R. Lee, "The Wettability of Fluoropolymer Surfaces : Influence of Surface Dipoles," *Langmuir*, vol. 24, no. 9, pp. 4817–4826, 2008.

[193] T. Liu and C.-J. Kim, "Contact Angle Measurement of Small Capillary Length Liquid in Super-repelled State," *Scientific Reports*, vol. 7, no. 1, p. 740, 2017.

[194] A. T. Paxson and K. K. Varanasi, "Self-similarity of contact line depinning from textured surfaces," *Nature Communications*, vol. 4, p. 1492, 2013.

[195] H.-J. Butt, C. Semprebon, P. Papadopoulos, D. Vollmer, M. Brinkmann, and M. Ciccotti, "Design principles for superamphiphobic surfaces," *Soft Matter*, vol. 9, pp. 418–428, 2013.

[196] A. Tuteja, W. Choi, M. Ma, J. M. Mabry, S. A. Mazzella, G. C. Rutledge, G. H. McKinley, and R. E. Cohen, "Designing Superoleophobic Surfaces," *Science*, vol. 318, pp. 1618–1622, 2007.

[197] V. V. Krotov and A. I. Rusanov, *Physicochemical hydrodynamics of capillary systems*. London: Imperial College Press, 1999.

[198] Z. Wang and S. Lin, "Membrane fouling and wetting in membrane distillation and their mitigation by novel membranes with special wettability," *Water Research*, vol. 112, pp. 38–47, 2017.

[199] A. Alkhudhiri, N. Darwish, and N. Hilal, "Membrane distillation: A comprehensive review," *Desalination*, vol. 287, pp. 2–18, 2012.

[200] Y. Xue, P. Lv, H. Lin, and H. Duan, "Underwater Superhydrophobicity: Stability, Design and Regulation, and Applications," *Applied Mechanics Reviews*, vol. 68, no. 3, p. 030803, 2016.

[201] C. Dorrer and J. Rühe, "Advancing and Receding Motion of Droplets on Ultrahydrophobic Post Surfaces," *Langmuir*, vol. 22, no. 18, pp. 7652–7657, 2006.

[202] S. Iliev and N. Pesheva, "Contact-angle hysteresis on periodic microtextured surfaces: Strongly corrugated liquid interfaces," *Physical Review E*, vol. 93, no. 6, p. 062801, 2016.

[203] D. Li, Y. Xue, P. Lv, S. Huang, H. Lin, and H. Duan, "Receding dynamics of contact lines and size-dependent adhesion on microstructured hydrophobic surfaces," *Soft Matter*, vol. 12, no. 18, pp. 4257–4265, 2016.

[204] H. Zhao and K.-y. Law, "Directional Self-Cleaning Superoleophobic Surface," *Langmuir*, vol. 28, pp. 11812–11818, 2012.

[205] H.-J. G. Diersch, V. Clausnitzer, V. Myrnyy, R. Rosati, M. Schmidt, H. Beruda, B. J. Ehrnsperger, and R. Virgilio, "Modeling Unsaturated Flow in Absorbent Swelling Porous Media: Part 1. Theory," *Transport in Porous Media*, vol. 83, no. 3, pp. 437–464, 2010.

[206] D. Miao, Z. Huang, X. Wang, J. Yu, and B. Ding, "Continuous, Spontaneous, and Directional Water Transport in the Trilayered Fibrous Membranes for Functional Moisture Wicking Textiles," *Small*, vol. 14, no. 32, pp. 1–10, 2018.

[207] L. Shi, X. Liu, W. Wang, L. Jiang, and S. Wang, "A self-pumping dressing for draining excessive biofluid around wounds," *Advanced Materials*, vol. 1804187, p. 1804187, 2018.

[208] Y. Kaufman, S.-Y. Chen, H. Mishra, A. M. Schrader, D. W. Lee, S. Das, S. H. Donaldson, and J. N. Israelachvili, "Simple-to-Apply Wetting Model to Predict Thermodynamically Stable and Metastable Contact Angles on Textured/Rough/Patterned Surfaces," *The Journal of Physical Chemistry C*, vol. 121, no. 10, pp. 5642–5656, 2017.

[209] J. R. Panter, Y. Gizaw, and H. Kusumaatmaja, "Multifaceted design optimization for superomniphobic surfaces," *Science Advances*, vol. 5, no. 6, p. eaav7328, 2019.

[210] D. D. Agonafer, H. Lee, P. A. Vasquez, Y. Won, K. W. Jung, S. Lingamneni, B. Ma, L. Shan, S. Shuai, Z. Du, T. Maitra, J. W. Palko, and K. E. Goodson, "Porous micropillar structures for retaining low surface tension liquids," *Journal of Colloid and Interface Science*, vol. 514, pp. 316–327, 2018.

[211] E. M. Domingues, S. Arunachalam, J. Nauruzbayeva, and H. Mishra, "Biomimetic coating-free surfaces for long-term entrapment of air under wetting liquids," *Nature Communications*, vol. 9, no. 1, pp. 1–11, 2018.

[212] K. L. Wilke, D. J. Preston, Z. Lu, and E. N. Wang, "Toward Condensation-Resistant Omniphobic Surfaces," *ACS Nano*, vol. 12, no. 11, pp. 11013–11021, 2018.

[213] B. Cao, L. A. Adutwum, A. O. Oliynyk, E. J. Luber, B. C. Olsen, A. Mar, and J. M. Buriak, "How To Optimize Materials and Devices via Design of Experiments and Machine Learning: Demonstration Using Organic Photovoltaics," *ACS Nano*, vol. 12, no. 8, pp. 7434–7444, 2018.

[214] G. G. Wells, É. Ruiz-Gutiérrez, Y. Le Lirzin, A. Nourry, B. V. Orme, M. Pradas, and R. Ledesma-Aguilar, "Snap evaporation of droplets on smooth topographies," *Nature Communications*, vol. 9, p. 1380, 2018.

[215] T.-S. Wong, S. H. Kang, S. K. Y. Tang, E. J. Smythe, B. D. Hatton, A. Grinthal, and J. Aizenberg, "Bioinspired self-repairing slippery surfaces with pressure-stable omniphobicity.," *Nature*, vol. 477, no. 7365, pp. 443–7, 2011.

[216] A. K. Epstein, T. S. Wong, R. A. Belisle, E. M. Boggs, and J. Aizenberg, "Liquid-infused structured surfaces with exceptional anti-biofouling performance," *Proceedings of the National Academy of Sciences of the United States of America*, vol. 109, no. 33, pp. 13182–13187, 2012.

[217] J. D. Smith, R. Dhiman, S. Anand, E. Reza-Garduno, R. E. Cohen, G. H. McKinley, and K. K. Varanasi, "Droplet mobility on lubricant-impregnated surfaces," *Soft Matter*, vol. 9, no. 6, pp. 1772–1780, 2013.

[218] P. T. Saunders, *An introduction to catastrophe theory*. Cambridge University Press, Cambridge, 1980.

[219] I. V. I. Arnol'd, "Singularities, bifurcations, and catastrophes," *Soviet Physics Uspekhi*, vol. 26, pp. 1025–1037, 1983.

[220] S. Lin, Y. M. Xie, Q. Li, X. Huang, Z. Zhang, G. Ma, and S. Zhou, "Shell buckling: from morphogenesis of soft matter to prospective applications," *Bioinspiration & Biomimetics*, vol. 13, no. 5, p. 051001, 2018.

[221] Y. Forterre, J. M. Skotheim, J. Dumais, and L. Mahadevan, "How the Venus flytrap snaps," *Nature*, vol. 433, no. 7024, pp. 421–425, 2005.

[222] J. Guzowski and P. Garstecki, "Droplet Clusters: Exploring the Phase Space of Soft Mesoscale Atoms," *Physical Review Letters*, vol. 114, no. 18, p. 188302, 2015.

[223] D. L. Freeman and J. D. Doll, "Computational studies of clusters: methods and results," *Annual Review of Physical Chemistry*, vol. 47, no. 1, pp. 43–80, 1996.

[224] N. Arkus, V. N. Manoharan, and M. P. Brenner, "Minimal Energy Clusters of Hard Spheres with Short Range Attractions," *Physical Review Letters*, vol. 103, no. 11, p. 118303, 2009.

[225] C. Semprebon, T. Krüger, and H. Kusumaatmaja, "Ternary free-energy lattice Boltzmann model with tunable surface tensions and contact angles," *Physical Review E - Statistical, Nonlinear, and Soft Matter Physics*, vol. 93, no. 3, pp. 1–11, 2016.

Appendix A

Throughout this thesis, the energy landscape methods detailed in Chapter 2 have been applied to study the interaction of fluids with complex surface structures. However, through changing the choice of free energy functional, a vast range of other applications can be studied. In this appendix, we show one such example: the buckling states of thin shells, with a specific focus on the cylindrical shell. In this, we shall see the implementation of a lattice-spring discretisation of a continuum thin shell, which coupled with the energy landscape methods allows a large number of minimum energy states to be obtained. We then connect each of these state via minimum energy pathways to produce disconnetivity graphs which describe the energy landscape. These range from being simple funnel shapes, to complex, rough, and 'glassy'. Finally, we introduce *landscape biasing* as a method to exploit the landscapes in order to control the buckling responses. These methods can be generalised, such that in the future, a host of buckling responses on different thin shell morphologies may be tested and controlled.

Harnessing energy landscape exploration to control the buckling of cylindrical shells

Panter J. R.[1], Chen J.[2], Zhang T.[2] and Kusumaatmaja H.[1]

[1]Department of Physics, Durham University, South Road, Durham, DH1 3LE, UK
[2]Department of Mechanical and Aerospace Engineering, Syracuse University, Syracuse, NY 13244, USA

Abstract

The complexity and unpredictability of postbuckling responses in even simple thin shells have raised great challenges to emerging technologies exploiting buckling transitions. Here we comprehensively survey the buckling landscapes to show the full complexity of the stable buckling states and the transition mechanisms between each of them. This is achieved by combining a simple and versatile triangulated lattice model for modelling the shell morphologies with efficient high-dimensional free-energy minimisation and transition path finding algorithms. We show how the simple free energy landscapes of short, lightly compressed cylinders become vastly more complex at high compressive strains or aspect ratios. We then exploit these landscapes to introduce an effective method for targeted design landscape biasing. This is used to inform thickness modifications enabling landscape redesign, and the development of structures which are highly resistant to lateral perturbations. Our methods are general, and can be extended to studying postbuckling responses of other geometries.

1 Introduction

Having shed the perception of being a purely problematic phenomenon [1], postbuckling responses are rapidly being shown to enable a broad range of emerging technologies [2–5]. Such applications include soft robotics and actuation [6, 7], mechanical metamaterials [8] including origami- and kirigami-inspired designs [9], morphable soft electronics [10, 11], logic gates [12], energy harvesting [13], damping devices [14], information storage [15], and bioinspired design [16]. However, in general the extreme complexity of these responses [17] has largely limited studies to investigate simple structures with very few local postbuckled states [18–21]. Predicting and controlling buckling responses on more complex structures is an open and increasingly active problem in as diverse a range of applications as mechanical engineering [3] to biological morphogenesis [22].

Here, we demonstrate how the buckled states and buckling transitions of complex systems can be comprehensively surveyed and controlled. Our key methodological contribution is to combine a simple and versatile triangulated lattice model for modelling the shell morphologies with efficient high-dimensional free-energy minimisation and transition path finding algorithms, in order to develop a powerful computational methodology for exploring the buckling landscapes. We apply this approach to the problem of cylindrical shell buckling, where the extreme landscape complexity arises from a combination of subcritcality, multiplicity and snaking in the postbuckled states [17]. Harnessing these tools we also explore the landscape biasing technique as an effective method to design and control buckling responses.

We begin by surveying the (meta) stable states - the free energy minima in the landscape. It has long been recognised that the cylindrical postbuckling states are strongly subcritical; coexisting with the unbuckled states in a loading interval which spans between the lower buckling load [23], and critical load (see [24] for a detailed review). This means that, as has been revealed historically, cylindrical shells are capable of failing at even 20% of their critical load [25]. Furthermore, the particular sensitivity to lateral loads [26], lead to NASA's development of empirical predictions for the practical load bearing capacity of imperfect cylinders [27]. Previously, buckled states have been elucidated by solving the von Kármán-Donell equations relating the stress to the radial displacement in an elastic cylindrical shell, but only by assuming the solutions exhibit axial periodicity (see for example [28, 29]), reminiscent of the diamond pattern shown by Yoshimura to enable global, inextensible buckling [30]. Similarly, group theory has also enabled the study of high-symmetry solutions [31]. However, a plethora of postbuckling solutions exist, discussed recently in the context of spatial localisation of the elastic deformation leading to snaking (pinning) in the solution space [17].

The energy landscape approach is then used to survey how the minima transform into each other by the lowest energy routes. We connect all postbuckling morphologies via such transition pathways, and so explore the entire stability landscape of cylindrical buckling. In this we reveal a diverse variation in the landscape properties, ranging from

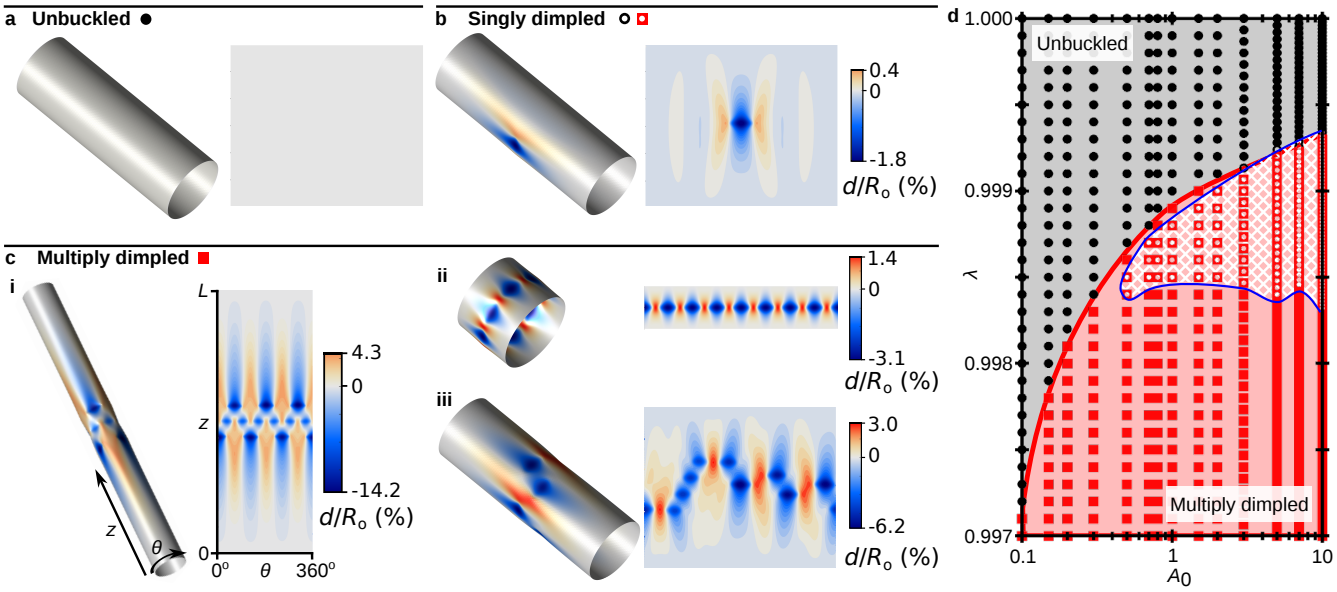

Figure 1: Summary of the stable buckling morphology classes and the minimum energy states, surveyed across a range of aspect ratios A_0 and end shortening ratios λ. **a-c** Visualisations of representative minima, shown in 3D and as radial displacement field contour plots. The axial and angular coordinates z and θ of the contour plots are shown in **c**(**i**), with the displacement d expressed as a fraction of R_0. **d** Phase diagram indicating the global free energy minimum across a range of A_0 and λ. The control ratio, $k^{\text{stretch}}R_0^2/k^{\text{bend}}$ is fixed throughout at 2.5×10^5. The global minimum is either unbuckled (grey region, simulation data shown as black circles), or multiply dimpled (pink region, simulation data shown as red squares). The singly dimpled state is never the global minimum, but the existence region is shown outlined in blue with unfilled data points.

very simple funnel-shaped landscapes at low aspect ratios and end shortenings, to broad and highly complex glassy landscapes at long aspect ratios.

Previously, only the first transition capable of buckling the unbuckled cylinder has been investigated [32, 33]. This has received significant interest as capturing the minimum energy pathway (MEP) enables the minimum energy barrier to be obtained, which provides an absolute lower bound to the energy required for a compressed cylinder to buckle. An explicit link has therefore been made between the ease of single dimple formation and the sensitivity of loaded cylinders to lateral loading [32]. As important for structural applications, it has been suggested that these theoretical minimum energy barriers can be accessed experimentally via a local probing technique for cylindrical [26, 34–36] and spherical shells [37, 38]. However, it is only via comparison to the minimum energy pathways obtained here that we are able to verify this.

Finally, we introduce a new method to begin to exert control over the buckling landscape - landscape biasing. In this, we are able to stabilise or destabilise targeted features in the landscape, such as transition states and minima. This is achieved by making local modifications to the elastic spring constants in the triangular lattice model to simulate thickness modifications. Thus, the knowledge of the energy landscape proves highly complimentary to experimental processes aimed at exerting postbuckling control [39–41]. We demonstrate the principal of landscape biasing by first showing how biasing against the unbuckled-single dimple transition state produces a 20% increase in buckling resistance of the unbuckled cylinder for a 1% increase in mass. We then show how biasing for a multiply dimpled state simplifies the local landscape, tripling the targeted state stability at 0% mass change.

2 Results and Discussions

2.1 Free energy minima

The triangular lattice model, detailed in Methods, discretises the shell into a triangulated mesh of extensional and angular elastic springs. Respectively, these allow for the decomposition of the total free energy into a sum of stretching and bending terms. To begin with, the stretching and bending spring constants, k^{stretch} and k^{bend}, are uniform throughout the shells. Each shell is generated with a well-defined aspect ratio $A_0 = L_0/(2R_0)$, where L_0 and R_0 are the length and radius of the cylinder when all springs assume their equilibrium configurations. When axially compressed, the shortening ratio is defined $\lambda = L/L_0$, where L is the length of the compressed cylinder. The top and bottom edged of the cylinder are simply supported: the coordinates of the mesh are fixed, but the planes attached to the ends can bend freely. We also choose k^{stretch}, k^{bend}, and R_0 to maintain a constant dimensionless elastic con-

trol ratio $k^{\text{stretch}}R_0^2/k^{\text{bend}}=2.5\times10^5$, and free energies E reported throughout are nondimensionalized such that the reduced free energy $E_{\text{r}} = E/k^{\text{bend}}$. The elastic control ratio is chosen to be representative of a physical system, corresponding to an aluminium drinks can. The choice of elastic control ratio and nondimensionalization are discussed further in Methods.

The construction of the free energy landscape begins by surveying the free energy minima. To access the many different buckled states for each fixed aspect ratio A_0 and shortening ratio λ, a basin hopping step is employed prior to energy minimisation [42], detailed in Methods. Three characteristic cylinder morphologies are observed: unbuckled, singly dimpled, and multiply dimpled, visualised in 3D and as radial displacement fields d in Fig. 1a-c respectively.

The multiply dimpled states in Fig. 1c form the largest set of minima, within which is contained the often-studied morphologies of high rotational symmetry - the Yoshimura-like diamond dimpling pattern, an example of which is shown in Fig. 1c(ii) [30]. However the largest multiply dimpled subset is the irregularly dimpled morphologies, a characteristic example of which is shown in Fig. 1c(iii). A random perturbation applied to these cylindrical shells is therefore most likely to result an irregularly dimpled state, showing that cylindrical shell buckling responses are inherently hard to predict.

The phase diagram in Fig. 1d summarises the minimum survey. At high λ in the phase diagram, the global free energy configuration is the unbuckled state, indicated by black circles. Upon decreasing λ the multiply dimpled states become the global minima, indicated by red squares. The solid red line indicates the point at which the buckled and multiply dimpled states are isoenergetic, at which the shortening ratio therefore produces an axial load equal to the Maxwell load (a detailed discussion regarding the loading limits is given in [24] for example). Across all tested scenarios, the most stable multiply dimpled states are those exhibiting a high degree of rotational symmetry, most commonly those with Yoshimura-like diamond patterns. However, we also find examples where more exotic high-symmetry multiply dimpled states form the global free energy minima, such as the example shown in Fig. 1c(i) at $A_0 = 10, \lambda = 0.999$.

The singly dimpled state, shown in Fig. 1b is of significant interest due to it's frequent role in the first buckling transition (which we consider further in the proceeding section), and also it's characteristic role of being the unit excitation in the postbuckling landscape. However, across a broad range of aspect ratios and elastic control ratios, detailed further in SI, we observed that the single dimple is never the global free energy minimum. When it is energetically unfavourable to form a dimple, the unbuckled state is lower in energy; when it is energetically favourable to form a dimple, the energy is always lowered further by subsequent dimpling. The single dimple is therefore only metastable. This metastability region is outlined in blue in Fig. 1d. The non-monotonic form of the low-λ boundary arises from the complex deformation profile surrounding the dimple. At high aspect ratios, this profile extends around the circumference of the cylinder, such that self-interaction effects contribute to the dimple stability (detailed further in SI).

2.2 Buckling transitions

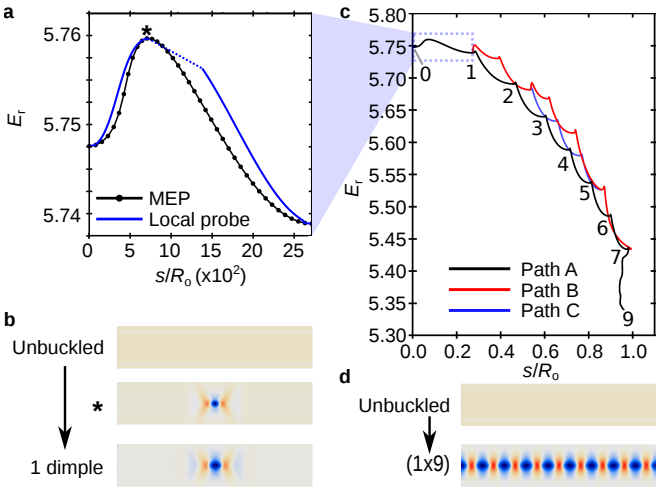

Figure 2: Comparison of the minimum energy pathway with the local probe technique, and examples of multi-step pathways through the buckling landscape. **a** Reduced free energy profile along the MEP (black) and local probe pathway (blue) for the unbuckled - single dimple transition on a cylinder of $A_0 = 0.8$, $\lambda = 0.9986$. The end points and transition state (*) are illustrated in **b**. The path length s describes the normalised distance of a point along the profile from the unbuckled state shown in Eq. (1). **c** Three example transition pathways connecting the unbuckled state and 1-row by 9-dimples (1×9) state illustrated in **d**. All pathways are shown to begin with the unbuckled - single dimple transition, which is magnified in **a**, and the number of dimples are labelled at each minimum in Path A.

In order to describe the minimum energy mechanisms by which the cylindrical buckling morphologies interconvert, we must obtain the minimum energy pathways (MEP). Between any two states in the free energy landscape, the MEP is defined as a path in which the gradient of the free energy is parallel to the path tangent vector. The MEP will also pass through at least one saddle point in the landscape, a local energy maximum along the pathway. The buckling morphology at this point is known as the transition state. Several methods exist for finding the MEP and transition states, see for example refs. [43–47]. The string methods we use here are detailed in Methods.

Computationally, the only transition which has been followed previously is the simplest unbuckled-singly dimpled pathway, where the dimple is centrally located on the cylinder [32, 33]. Meanwhile, local probing of cylindrical shells has been suggested as an experimental technique which

may allow the true dimpling transition state to be accessed [26, 34–36]. In Fig. 2a, we compare the reduced-energy profiles $E_{\mathrm{r}}(s)$ of the MEP (black series) with the pathway generated by simulating the local probe technique (blue line) for an example cylinder with $A_0 = 0.8, \lambda = 0.9986$. Local probe simulation methodologies are detailed in Methods. In order to usefully compare the paths, the path distance coordinate *s* is the Euclidean distance between the triangulated mesh of a point along the pathway, with that of the initial (unbuckled) state

$$s = \sum_{i=1}^{N_{\mathrm{nodes}}} |\underline{\mathbf{a}_i} - \underline{\mathbf{a}_i^o}| \tag{1}$$

where $\underline{\mathbf{a}_i}$ and $\underline{\mathbf{a}_i^o}$ are the position vectors of node i in the buckled and unbuckled mesh respectively.

On comparison, we observe that the local probe technique does meet the MEP at the transition state (labelled '*' and shown in shown in Fig. 2b), but does not access the minimum energy pathway generally. At the point of crossing the barrier, the locally-probed system snaps to a dimpled-like configuration: a small probe displacement resulting in a large change to the surrounding morphology, and a concomitant jump in E_{r} and s.

This comparison shows that the local probe technique is capable of measuring the minimum energy barrier to the first dimpling transition. This is consistently shown across all the test cases summarised in SI. Previous studies were unable to prove that the local probe technique could access the minimum energy barrier, as it was assumed that the true MEP was not too curved [26]: namely the direction of motion along the transition always has a component in the direction of the applied force (i.e the path never curves against the applied force).

However, the methodology presented here allows for the pathway between any two states to be investigated, not only the 0-1 transition. We therefore extend the first pathway found in Fig. 2a to find complete pathways from the unbuckled state to the multiply-dimpled global minimum. Examples are shown in Fig. 2c, with Fig. 2d showing the pathway endpoints: the unbuckled state, and the (1×9) global minimum. Two key observations are made: multiple competing pathways exist between the end points, and each pathway is complex, featuring many intervening minima. Out of the large number of possible pathways, three examples are highlighted in Fig. 2c, labelled A, B, and C. Movies showing the conformational changes along each pathway are shown in Supplementary Movies 1, 2, and 3 respectively. Path A is distinguished from other paths: out of the set of barriers along path A, the maximum energy barrier is the smallest out of all possible pathways. In Path A, eight separate dimpling transitions occur. In the first seven, a single dimpling event occurs to build a train of dimples. The final transition sees two dimples forming simultaneously to complete the ring of nine dimples. In this final transition, the path distance decreases as all dimples become shallower on formation of the final two. However, the system is capable of undergoing dimpling transitions not linked to the growing dimple train, leading to example alternative pathways B and C.

2.3 Energy landscapes

By connecting any pair of minima with an MEP, we may thus explore the complete energy landscape for any fixed A_0 and λ. Here we examine the extent of the landscape complexity as a function of A_0 and λ (varying the elastic constants is presented in SI). As will be shown, cylindrical shells exhibit a diverse range of landscape types. We will first compare the energy landscape of a lightly compressed short cylinder where the single dimple is stable ($A_0 = 0.8$,$\lambda = 0.9986$), with a heavily compressed short cylinder where the single dimple is unstable ($A_0 = 0.8$,$\lambda = 0.9980$). We then compare the short, lightly compressed cylinder, with a long, lightly compressed cylinder ($A_0 = 3.0$,$\lambda = 0.9990$), where the single dimple is stable in both cases.

As the network of minima connected by MEPs is in general highly complex, it is instructive to consider simplified network representations. In Fig. 3, the free energy landscapes are visualised as disconnectivity graphs (for a comprehensive discussion of the disconnectivity graph representation of energy landscapes, we refer the reader to refs. [42, 48]). In this, the network of minima and pathways is reduced to a spanning tree showing only the energy of the minima (the end points of each branch) and the lowest energy barrier connecting any two minima, read by tracing the path between two branches and finding the highest energy point. For example, in Fig. 3a, unbuckled state and singly dimpled state are labelled '0' and '1' respectively. On tracing between the two branches, the highest energy point along the path, labelled '*' marks the largest transition state energy. In this case, this is the 0-1 transition state shown in Fig. 2b. However, as the 1D disconnectivity graph does not show which states are directly connected, in general the highest energy point between two states is simply the largest energy encountered in the possible multi-step transition pathway.

In Fig. 3a, the disconnectivity graph is presented for A_0 = 0.8, $\lambda = 0.9986$, and represents the full energy landscape which was partially described in Fig. 2. Under these subcritical conditions, the unbuckled, singly dimpled, and multiply dimpled states coexist. However, the buckling landscape is remarkably simple: qualitatively, the states are (approximately) uniformly distributed across the stable energy range. To quantify this and subsequent observations, we partition the minimum-energy range into 100 bins of equal width and total the number of minima within each bin; this histogram is shown in SI. We then calculate the variance in bin populations as a measure of the distribution uniformity. Here, the small variance in the bin frequency, 0.38, describes a relatively uniform distribution of minima across the energy range. The uniformity of the landscape is further reflected in the range of energy barriers - almost all have similar minimum energy barriers, of energy $\mathcal{O}(10^{-3})$. The

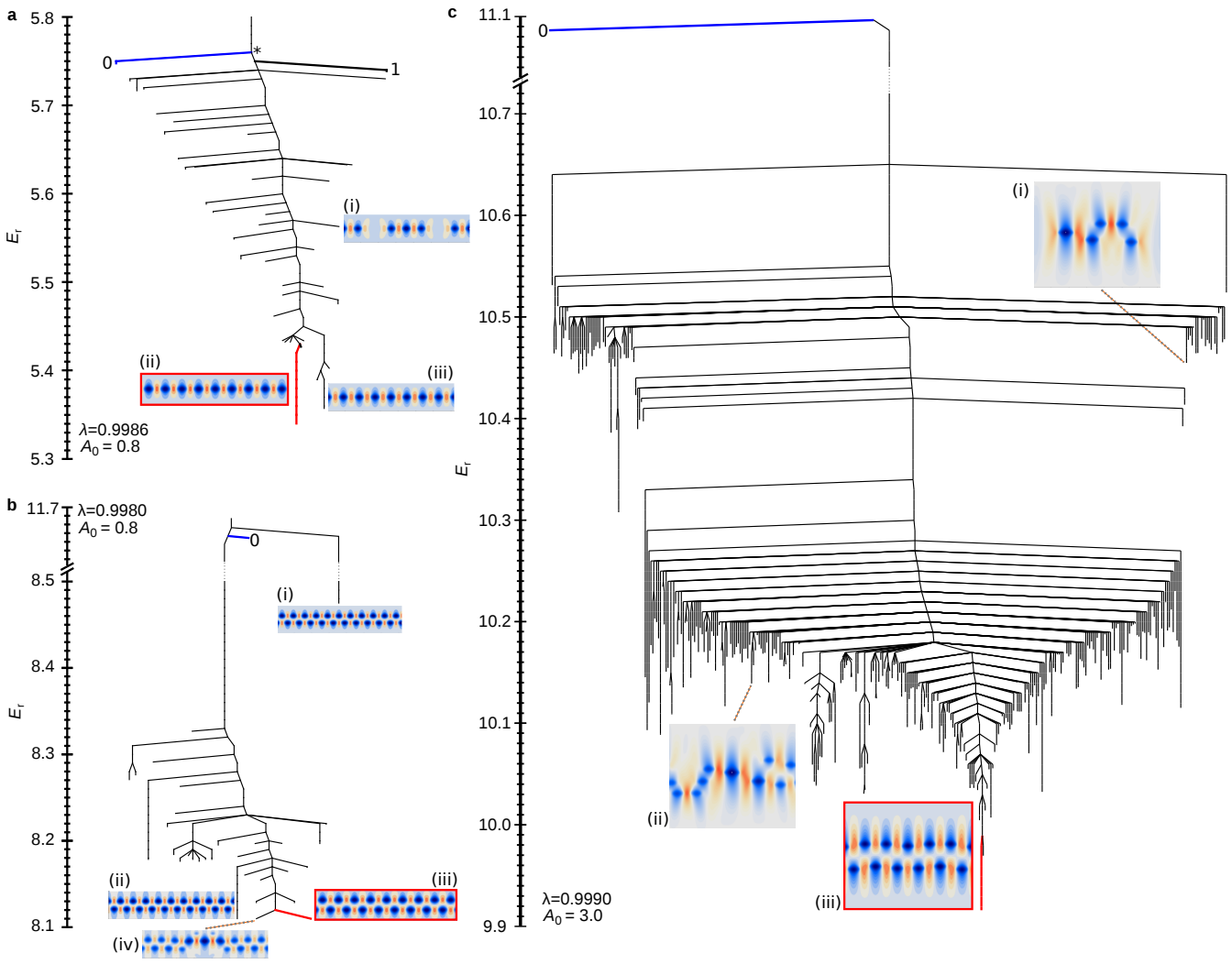

Figure 3: Disconnectivity graphs showing the minimum energetic barrier between any pair of states. The unbuckled and global minimum branches are coloured in blue (labelled '0') and red respectively. Representative minima radial displacement plots are also shown, with the global minimum outlined in red. **a** $A_0 = 0.8$, $\lambda = 0.9986$, the single dimple branch is labelled '1', the 0-1 transition state labelled '*'. **b** $A_0 = 0.8$, $\lambda = 0.9980$, no additional minima are present in the vertical axis break. **c** $A_0 = 3.0$, $\lambda = 0.999$, a small number of multiply dimpled states not pertinent to the discussion are present in the vertical break.

distribution of the barriers is also shown in SI.

The example minimum (i) is a characteristic state of the system, featuring clusters of dimples closely aligned around the central circumference. The (1×9) global energy minimum (highlighted in red) exists in a deep well, with the minimum energy barrier greater than the first transition by a factor of 7. Thus, if an unbuckled state is subject to perturbations with sufficient energy to overcome the first dimpling transition, although other states may be sampled along the way, the tendency is to quickly become trapped in the global energy minimum. The notable exception to this picture however is that a second deep branch also exists at the base of the disconnectivity graph. This represents a competing set of deep states which are likely to split the population between the lowest minimum (1×9), and second-lowest minimum (1×8), labelled (iii) in Fig. 3a.

Upon decreasing λ to 0.9980, although the system is still subcritical, the singly dimpled state looses stability. The disconnectivity graph for this landscape is shown in Fig. 3b. Here, the landscape is markedly different to the less-compressed case shown in Fig. 3a: although the number of minima is $\mathcal{O}(10)$ in both cases, at $\lambda = 0.9980$ the majority of states are concentrated at the lower stable energy range, indicated by the greater variance in bin population, 2.09, detailed further in SI. Additionally, the range of energy barriers is large, varying from 10^{-3} to 10^{1}, with many states featuring high energetic barriers. This latter point is most pronounced when considering the (2×11) multiply dimpled state, labelled (i), which has an energy barrier 1000× greater than the minimum energy barrier from the

unbuckled state. A further contrast in this disconnectivity graph is that the global minimum (2×9) does not have a large energy barrier compared to other transitions. Thus, random perturbations made to the unbuckled state may result in the system becoming trapped in several states different from the global minimum. Two highlighted examples of these which are close in energy to the global minima are the (2×10) system, labelled (iii), and a defective (2×9) system with two adjacent dimple vacancies, labelled (iv).

Finally, we return to a subcritical shortening ratio where the unbuckled, singly dimpled, and multiply dimpled states coexist, but now extend the aspect ratio: $A_0 = 3.0$, $\lambda = 0.999$. The disconnectivity graph for this system is shown in Fig. 3c. Three prominent features of this landscape offer significant contrast to the short aspect-ratio landscapes: the number of minima has increased by a factor of 100 compared to the $A_0 = 0.8$ systems, the minimum distribution is highly non-uniform - the bin population variance is 93, and the landscape becomes rough over a range of energy scales.

Expanding on these observations, the increase in the number of minima is due to two effects. Firstly, at large aspect ratios, all minima observed are no longer characterised uniquely by a single well-defined energy and morphology, but exist as clusters in which the intra-cluster energy variability is approximately $\Delta E_{\mathrm{r}} < \times 10^{-3}$. Thus, on the finest scale, the stability landscape is rough and glass-like. In the stability landscape shown in Fig. 3c, we have clustered minima which share the same number of dimples with interconversion barriers $< 10^{-3}$, reducing the number of minima shown by a factor of 10. The second effect is due to dimple confinement introduced by the fixed ends. At $A_0 = 0.8$, the fixed ends tightly constrain the dimples to lie within either one or two rows, due to the characteristic dimple size being similar to L_0. At the longer aspect ratio of $A_0 = 3.0$, the constraining strength of the fixed ends is diminished, yielding a larger number of possibilities of dimple arrangements.

The large phase space for dimple arrangements within certain energy ranges enables numerous minima to exhibit similar energies and similar barriers. This is most pronounced in the range $10.1 < E_{\mathrm{r}} < 10.3$, dominated by irregular systems with between 7 and 11 dimples. A representative example is shown, labelled (ii). In this region, the number of dimples is large enough to produce a significant number of variations in arrangement, yet not so large that packing constraints become dominant. On average, the inter-cluster energy barrier is $\mathcal{O}(10^{-2})$. A similar glassy region exists at larger energies, where irregularly dimpled systems feature between 3 and 6 dimples. A representative example here is shown, labelled (i). Thus, the stability landscape becomes rough on two energy scales: (1) $\Delta E_{\mathrm{r}} \approx \times 10^{-3}$ associated with intra-cluster variability, and (2) $\Delta E_{\mathrm{r}} \approx \times 10^{-2}$ associated with inter-cluster variability in the absence of packing constraints (when comparing clusters of similar numbers of dimples). The distributions of energy barriers associated with this roughness are shown in the SI.

For larger dimple numbers than 11, efficient packing on the cylinder is required, leading to a severe reduction in the phase space of dimple arrangements. Thus, in the vicinity of the global minimum, the (2×6) regularly dimpled state highlighted in red, the local landscape becomes significantly less glassy. Nonetheless, the overall landscape roughness coupled with a large number of deep states means that a perturbed unbuckled cylinder may buckle to any number of states, explaining the difficulty in designing cylindrical postbuckling states.

2.4 Controlling the landscape

Despite the complexity of the buckling landscapes, we now demonstrate how to control the stability of target features, by introducing a process we term *landscape biasing*. This enables us to design buckling responses by locally thickening or thinning the cylinder, complimentary to experimental realisation; see for example [39–41]. We demonstrate two examples of landscape biasing, by first biasing *against* a target transition state, and then biasing *for* a target minimum. The examples shown here significantly increase the stability of the target structures to lateral perturbations. These biased structures are therefore highly suited to scenarios where sudden morphological changes would be detrimental to device performance, a key example being aeronautical applications [27]. For these examples, we apply this method to A_0=0.8, λ=0.9986 system, for which the buckling landscape is shown in Fig. 3a.

To begin with, it is observed that the minimum energy barrier from the unbuckled state to the singly dimpled state is small compared to both the overall landscape energy range, and other deep states, generating the extreme imperfection sensitivity of cylinders to sub-critical buckling transitions. The energy profile for this transition, shown originally in Fig. 2a, is re-plotted in Fig. 4a (solid black line), in which the reduced energy is referenced to the energy of the unbuckled state, E_o. We aim to increase the energy barrier of this transition, in order to make the unbuckled cylinder more robust against lateral perturbations, by biasing the landscape against the transition state.

The landscape biasing workflow is shown in Fig 4b-d, and detailed further in SI. Firstly, as shown in Fig. 4b, we obtain the radial deformation field for the unbiased transition state (as well as that of the unbuckled state). Secondly, we compute the fractional change in local elastic potential energy E_{f} when transforming from the unbuckled to the transition state. It is observed that the stored elastic potential energy is highly localised about the centre of the dimple deformation. We then reason that in order to increase the energy of this transition state (and hence the barrier to the transition), we must modify the cylinder to energetically penalise this localisation of the potential energy, effectively biasing the landscape against the transition state. A choice exists in how to perform this modification, but for this example we choose to simulate a local thickening of the shell by modifying k^{stretch} ($\propto t$) and k^{bend} ($\propto t^3$), facilitating experimen-

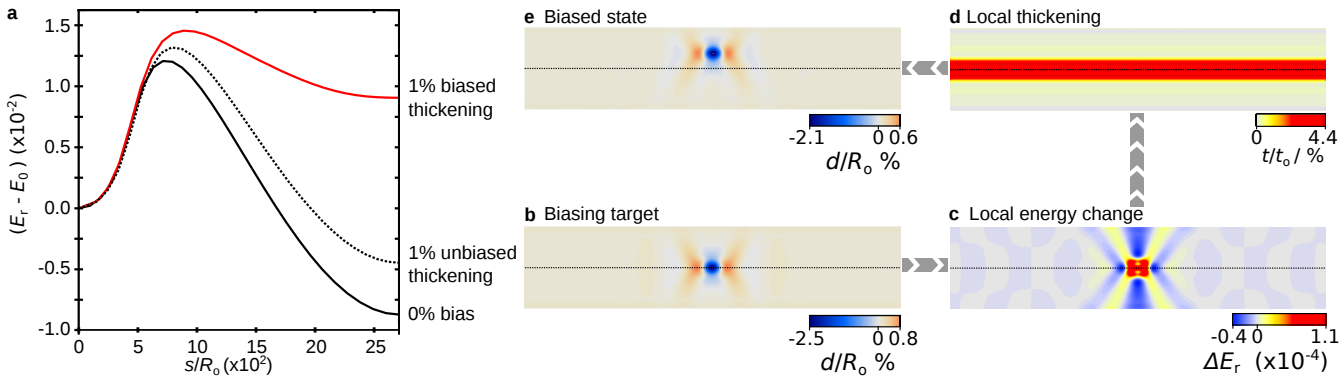

Figure 4: The landscape biasing workflow and the effect when biasing against the unbuckled-single dimple transition state. **a** Unbuckled to single dimple transition energy profiles for three local thickening schemes: A_0=0.8, λ=0.9986. **b-e** Illustrative workflow for the landscape biasing procedure, a black dotted line indicates the centre of the cylinder. **b** Radial deformation field of the unbiased transition state. **c** Local elastic potential energy change of the transition state relative to the unbuckled cylinder. **d** Local thickening profile of the 1% biased cylinder. **e** Unbuckled to single dimple transition state of the 1% biased cylinder.

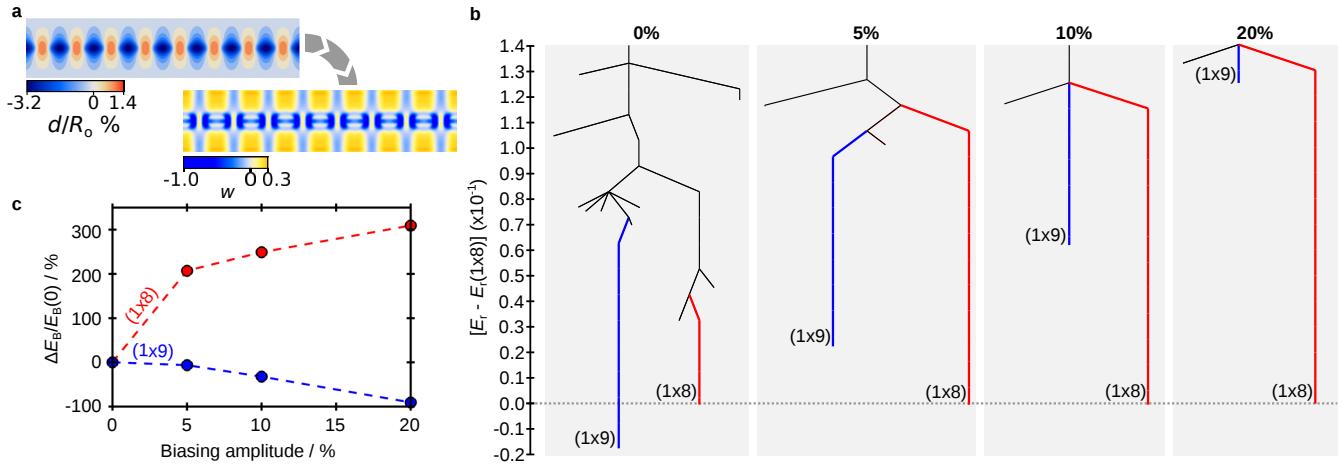

Figure 5: Changes in the local landscape upon biasing for the (1×8) state. **a** Workflow showing how the radial deformation field of the (1×8) state at A_0=0.8, λ=0.9986 is transformed into the thickness weighting field for landscape biasing. **b** Evolution of the bottom of the landscape as the biasing amplitude increases, all energies shown relative to the (1×8) state. The (1×8) well is highlighted in red and the (1×9) well is highlighted in blue. **c** Evolution of the change in minimum energy barrier ΔE_B out of the (1×8) state (red), and (1×9) state (blue) upon increase in biasing amplitude. ΔE_B is shown relative to the unbiased barrier, $E_B(0)$, for the (1×8) state and (1×9) state respectively. The dotted lines are shown as guides for the eye.

tal realisation. A more sophisticated yet complex treatment would alter k^{stretch} and k^{bend} independently, according to the separate local stretching and bending energies respectively. A comparison of alternative geometric methods to modify cylindrical shell buckling are presented in [39]. In the local thickening treatment, detailed in SI, we weight the thickening according to the local energy change. Due to the symmetry breaking of the transition, in order to suppress dimple formation anywhere around the circumference of the cylinder, at each z we average the thickening profile over all θ. Finally, the thickening profile is rescaled in order to achieve a prescribed total mass increase, which is set as 1% for the results presented in Fig. 4. The final thickening profile is shown in Fig. 4d, which sees the a thickness increase localised around the centre of the cylinder.

On attempting to dimple this biased cylinder, the transition state is now forced off-centre, shown in Fig. 4e. The energy profile for this transition is shown as the solid red line in Fig. 4, showing that for a 1% increase in mass, a 20% increase in buckling resistance is achieved. This improvement is over twice that of a uniformly thickened cylinder, 9%, with the same mass increase, the transition profile for which is shown as the dotted black line. This landscape biasing against the transition is the antithesis to modal nudging [49], the recently formalised technique for slender structures in which minimal structural modifications

are made in order to select a specific failure mode.

The second way to design the bucking landscape is to bias *for* a target structure. We observe the landscape shown in Fig. 3a to exhibit a deep global minimum (1×9) and the shallower (1×8) state. Here, we choose to stabilise the (1×8) state through minimum-targeted landscape biasing. It will be shown how a target minimum can be significantly stabilised, thus realising a postbuckled state which is highly resistant to lateral perturbation. Furthermore, this example will show that through biasing we can select which high-symmetry morphology forms the global minimum.

In Fig. 5a, we show the radial displacement field of the (1×8) state. As before, we evaluate the local stored elastic potential energy, then weight the local elastic constants to exact a local thickening, detailed further in SI. As the (1×8) state is to be stabilised, in regions of high stored elastic energy we locally thin the structure to reduce the energetic cost of the specific buckling mode. We also weight the thickening so that there is no overall mass change, and prescribe a biasing amplitude - the maximum percentage change in thickness allowed. To obtain the local thickness change, we therefore scale the weighting field w shown in fig. 5a by the biasing amplitude.

By systematically increasing the biasing amplitude from 0% to 20%, we observe how the buckling landscape changes at the bottom of the funnel, shown in Fig. 5b. At 0% bias, we show a magnification of the low-energy portion of the disconnectivity graph shown in Fig. 3a, featuring the two deep wells decorated with multiple stable minima. The wells corresponding to the (1×8) state and (1×9) state are shown highlighted in red and blue respectively. In Fig. 5c, the percentage change in the (1×8) and (1×9) barriers are shown relative to their respective barriers at 0% bias.

On application of a 5% bias, the landscape changes significantly relative to the unbiased case: the landscape is simplified as the biasing destabilises many minima, the (1×9) state increases in energy, and the targeted (1×8) state decreases in energy to such an extent that it becomes the global minimum. Furthermore, the landscape simplification and (1×8) state stabilisation effects act cooperatively to increase the barrier out of the target (1×8) state by 207% relative to the unbiased (0%) landscape. At 10% bias, these effects are further magnified. At 20% bias, there is no further change in the lower landscape structure, but the stabilisation of the (1×8) state and destabilisation of the (1×9) state continues. This leads to an ultimate barrier increase 302% for the (1×8) state, and barrier decrease of 91% for the (1×9) state.

3 Conclusions and Outlook

In this work, a triangular lattice model is used to evaluate the free energy of postbuckled states of elastic thin shells. This is implemented in efficient energy-minimisation and path finding algorithms in order to fully describe the buckling landscapes. Here, we have demonstrated this for the complex problem of buckling of fixed-end cylindrical shells, subject to axial compressive strains. To begin with, we surveyed the free energy minima, observing unbuckled, singly dimpled, and multiply dimpled states whose stabilities were evaluated for different aspect ratios and compressive strains. We then systematically used the string method to connect pairs of minima within the same cylindrical system in order to find the minimum energy pathways and transition states between these states. This enabled a global description of the buckling landscape: in which a simple funnel-shaped landscape became complex and glassy when increasing the aspect ratio, or featured many deep states when increasing the compressive strain. We then finally introduced the landscape biasing method to control the stability of targeted features of the landscape, in order to design structures with improved resistance to lateral forces.

Overall, by being able to both survey the free energy landscape and design specific transition modes through landscape biasing, we may now design dynamic buckling responses for diverse applications, ranging from energy harvesting devices to complex morphable materials.

One important consideration we highlight for future work is that of the role of imperfections in buckling responses, a significant concern in real-world applications. The ability to generalise our model to consider shapes other than the perfect cylinder, as well as including diverse elastic modulations and boundary conditions, lead us to emphasise the applicability of this model to studying the impact of a large range of different geometric or elastic imperfections on the buckling landscape.

4 Methods

4.1 Discretisation and free energy

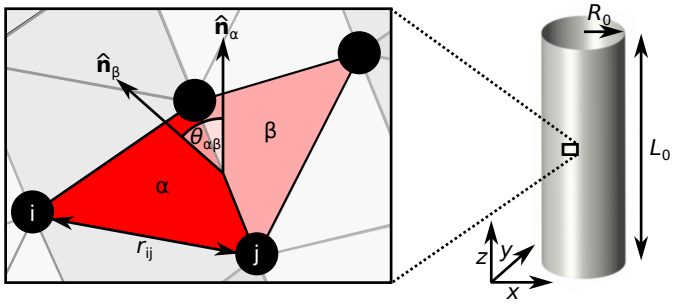

Figure 6: The thin shell discretisation scheme. The nodes are indicated with black circles, in which nodes i and j are separated by a distance r_{ij}. The planes are indicated with coloured triangles, in which the dihedral angle between planes α and β, $\theta_{\alpha\beta}$, is shown as the angle between the respective normal vectors $\hat{\mathbf{n}}_\alpha$ and $\hat{\mathbf{n}}_\beta$.

To evaluate the free energy of an arbitrary thin shell (or composite of thin shells), we discretise the surface into a triangulated mesh of nodes, defining a set of neighbouring

nodes and a set of neighbouring planes, in a manner based on [50] although other similar methods have also been reported, for example [51]. The local form of this discretisation is shown in Fig. 6. In this, neighbouring nodes i and j are connected by an extensional spring of equilibrium bond length r_{ij}^0 and elastic constant k_{ij}^{stretch}. Neighbouring planes α and β are connected by an angular spring of equilibrium angle $\theta_{\alpha\beta}^0$ and elastic constant $k_{\alpha\beta}^{\text{bend}}$. In general, as in our triangulation scheme, r_{ij}^0 and $\theta_{\alpha\beta}^0$ are non-uniform across the lattice. The discretisation of the shell into a set of extensional and angular springs allows the total free energy to be decomposed into a sum of stretching and bending energies such that generally,

$$E = \sum_{ij} k_{ij}^{\text{stretch}} \left(r_{ij} - r_{ij}^0\right)^2 + \sum_{\alpha\beta} k_{\alpha\beta}^{\text{bend}} \left(1 - \cos\left(\theta_{\alpha\beta} - \theta_{\alpha\beta}^0\right)\right), \quad (2)$$

where r_{ij} is the separation distance between nodes i and j; $\theta_{\alpha\beta}$ is the dihedral angle between planes α and β, defined as the angle between the respective normal vectors $\hat{\mathbf{n}}_\alpha$ and $\hat{\mathbf{n}}_\beta$.

Throughout this work, we report the nondimensionalised free energy $E_r = E/k_{\text{ref}}^{\text{bend}}$, where $k_{\text{ref}}^{\text{bend}}$ is a reference dihedral elastic constant. For cylinders of uniform elasticity, we define $k_{ij}^{\text{bend}} = k_{\text{ref}}^{\text{bend}}$. Furthermore, the bond lengths are nondimensioanlised by expressing r_{ij} and r_{ij}^0 relative to a reference length scale R_0, which we choose to be the cylinder radius.

The single parameter defining the cylinder's elastic behaviour then becomes the control ratio $k_{\text{ref}}^{\text{stretch}} R_0^2/k^{\text{bend}}$ which unless otherwise stated we fix at 2.5×10^5. Through comparison with continuum elastic theory [50], in terms of Young's modulus Y, plate thickness t, and Poisson ratio ν we have $k^{\text{stretch}} = \frac{\sqrt{3}}{4} Y t$ and $k^{\text{bend}} = \frac{2}{\sqrt{3}} \frac{Y t^3}{12(1-\nu^2)}$. Hence, the control ratio is given by $\frac{9(1-\nu^2)}{2} \left(\frac{R_0}{t}\right)^2$. To demonstrate the physical significance of our prescribed control ratio of 2.5×10^5, if we choose a Poisson ratio appropriate for aluminium, $\nu = 0.3$, the resulting ratio R_0/t=247 is similar to that of aluminium drinks cans ($R_0/t \approx 300$).

The cylinder radius R_0 is fixed throughout, such that to change the uncompressed aspect ratio A_0, only the length L_0 is varied. In order to accurately calculate the free energy while balancing computational cost, the number of nodes must be sufficient to capture the deformation profiles of single dimples, the length scale of which depends on A_0 and the control ratio. For the cylinders studied here, $\approx 10^4$ nodes per cylinder are required (an illustrative resolution test is shown in SI). Our triangulated lattice model is also validated against ABAQUS/Explicit commercial software [52], shown in SI.

4.2 Minimisation and path finding

The L-BFGS algorithm [53, 54] is employed to efficiently minimise the free energy with respect to the large number of degrees of freedom ($\mathcal{O}(10^4 - 10^5)$). For this, the total free energy is required as well as the derivatives of E with respect to each degree of freedom (the x, y and z coordinates of each node). By setting selected derivatives to zero prior to minimisation, we can constrain specific node positions. Here, we fix the x and y coordinates of the nodes which cap each end of the cylinder to the uncompressed configuration, forbidding deformation or relative rotation of the ends. By choosing the z coordinates at which to fix these nodes, we can achieve the desired cylinder end shortening.

To simulate local probe experiments, in addition to fixing the end caps we also fix the position of a single node in the centre of the cylinder (thus mimicking a point probe). This point is moved radially inwards by a small increment and the free energy minimised. This increment-minimisation procedure is repeated until the entire pathway from the unbuckled state to a second minimum has been obtained.

In the free energy minimum survey, we access the many different dimpled states by performing a basin hopping step prior to each minimisation [42]. To perform this step, we begin with the unbuckled cylinder, and make a random number of trial dimples to the initial node coordinates. Each trial dimple consists of a paraboloidic indentation radially into the cylinder, in which the indentation depth is allowed to vary up to $R_0/2$.

The minimum energy pathways (MEPs) between any two minima of equal end shortening are found using the string method [55], which we augment for use with high-dimensional systems. To begin with, the end points are maximally aligned through rotation and reflection of the displacement fields. An initial string of 30 images is then formed which interpolates the coordinates of the two end points. One iteration of the algorithm consists of evolving each image in the downhill direction, then re-interpolating the images along the new string. The Euler and Runge-Kutta methods used in [55] are however highly inefficient for the high-dimensional energy landscape considered here. Instead, we use 300 L-BFGS steps to rapidly converge the string to the MEP. A simple linear re-interpolation scheme is used, with the image density concentrated at the highest energy points along the string. This process is iterated until the E_r of the highest energy point along the string changes by less than 10^{-6} from the previous iteration. If intermediate minima exist along the pathway, a separate string is evolved for each, such that each pathway connects two minima via a single transition state. The Euler method is employed in the final stage to fine-tune the pathway, such that convergence is achieved when the RMS distance between the strings is less than 10^{-6}. The transition state is then fine-tuned using the climbing string method with Euler steps [44], finishing once the RMS gradient is reduced below 10^-5. Repeating the string algorithm to connect multiple end points forms a network of connected minima.

In order to show the general validity of this model, we further apply it to analyze the energy landscapes of the buckling of spherical caps in the SI. The preliminary work

shows our model has the same accuracy as the finite element model implemented in ABAQUS, and successful captures the stable axisymmetrically inverted configuration of the spherical cap [56]. The analysis is suitably rich that we reserve further discussion for another publication.

References

[1] P. M. Reis, F. Brau, and P. Damman, "The mechanics of slender structures," *Nature Physics*, vol. 14, no. 12, pp. 1150–1151, 2018.

[2] P. M. Reis, "A Perspective on the Revival of Structural (In)Stability With Novel Opportunities for Function: From Buckliphobia to Buckliphilia," *Journal of Applied Mechanics*, vol. 82, no. 11, p. 111001, 2015.

[3] N. Hu and R. Burgueño, "Buckling-induced smart applications: recent advances and trends," *Smart Materials and Structures*, vol. 24, no. 6, p. 063001, 2015.

[4] Y. Zhang, F. Zhang, Z. Yan, Q. Ma, X. Li, Y. Huang, and J. A. Rogers, "Printing, folding and assembly methods for forming 3D mesostructures in advanced materials," *Nature Reviews Materials*, vol. 2, no. 4, p. 17019, 2017.

[5] K. Bertoldi, V. Vitelli, J. Christensen, and M. van Hecke, "Flexible mechanical metamaterials," *Nature Reviews Materials*, vol. 2, no. 11, p. 17066, 2017.

[6] D. Rus and M. T. Tolley, "Design, fabrication and control of soft robots," *Nature*, vol. 521, no. 7553, pp. 467–475, 2015.

[7] L. Hines, K. Petersen, G. Z. Lum, and M. Sitti, "Soft Actuators for Small-Scale Robotics," *Advanced Materials*, vol. 29, no. 13, p. 1603483, 2017.

[8] H. Yang and L. Ma, "Multi-stable mechanical metamaterials by elastic buckling instability," *Journal of Materials Science*, vol. 54, no. 4, pp. 3509–3526, 2019.

[9] Z. Zhai, Y. Wang, and H. Jiang, "Origami-inspired, on-demand deployable and collapsible mechanical metamaterials with tunable stiffness," *Proceedings of the National Academy of Sciences*, vol. 115, no. 9, pp. 2032–2037, 2018.

[10] H. Fu, K. Nan, W. Bai, W. Huang, K. Bai, L. Lu, C. Zhou, Y. Liu, F. Liu, J. Wang, M. Han, Z. Yan, H. Luan, Y. Zhang, Y. Zhang, J. Zhao, X. Cheng, M. Li, J. W. Lee, Y. Liu, D. Fang, X. Li, Y. Huang, Y. Zhang, and J. A. Rogers, "Morphable 3D mesostructures and microelectronic devices by multistable buckling mechanics," *Nature Materials*, vol. 17, no. 3, pp. 268–276, 2018.

[11] X. Ning, X. Yu, H. Wang, R. Sun, R. E. Corman, H. Li, C. M. Lee, Y. Xue, A. Chempakasseril, Y. Yao, Z. Zhang, H. Luan, Z. Wang, W. Xia, X. Feng, R. H. Ewoldt, Y. Huang, Y. Zhang, and J. A. Rogers, "Mechanically active materials in three-dimensional mesostructures," *Science Advances*, vol. 4, no. 9, p. eaat8313, 2018.

[12] Y. Song, R. M. Panas, S. Chizari, L. A. Shaw, J. A. Jackson, J. B. Hopkins, and A. J. Pascall, "Additively manufacturable micro-mechanical logic gates," *Nature Communications*, vol. 10, p. 882, 2019.

[13] C. Dagdeviren, P. Joe, O. L. Tuzman, K.-I. Park, K. J. Lee, Y. Shi, Y. Huang, and J. A. Rogers, "Recent progress in flexible and stretchable piezoelectric devices for mechanical energy harvesting, sensing and actuation," *Extreme Mechanics Letters*, vol. 9, no. 3, pp. 269–281, 2016.

[14] B. Haghpanah, A. Shirazi, L. Salari-Sharif, A. Guell Izard, and L. Valdevit, "Elastic architected materials with extreme damping capacity," *Extreme Mechanics Letters*, vol. 17, pp. 56–61, 2017.

[15] J. Y. Chung, A. Vaziri, and L. Mahadevan, "Reprogrammable Braille on an elastic shell," *Proceedings of the National Academy of Sciences*, vol. 115, no. 29, p. 201722342, 2018.

[16] M. A. Meyers, J. McKittrick, and P.-Y. Chen, "Structural Biological Materials: Critical Mechanics-Materials Connections," *Science*, vol. 339, no. 6121, pp. 773–779, 2013.

[17] E. Knobloch, "Spatial Localization in Dissipative Systems," *Annual Review of Condensed Matter Physics*, vol. 6, no. 1, pp. 325–359, 2015.

[18] R. H. Plaut, "Snap-through of arches and buckled beams under unilateral displacement control," *International Journal of Solids and Structures*, vol. 63, pp. 109–113, 2015.

[19] G. Napoli and S. Turzi, "Snap buckling of a confined thin elastic sheet," *Proceedings of the Royal Society A: Mathematical, Physical and Engineering Sciences*, vol. 471, no. 2183, 2015.

[20] A. Pandey, D. E. Moulton, D. Vella, and D. P. Holmes, "Dynamics of snapping beams and jumping poppers," *EPL (Europhysics Letters)*, vol. 105, no. 2, p. 24001, 2014.

[21] Y. Forterre, J. M. Skotheim, J. Dumais, and L. Mahadevan, "How the Venus flytrap snaps," *Nature*, vol. 433, no. 7024, pp. 421–425, 2005.

[22] C. M. Nelson, "On Buckling Morphogenesis," *Journal of Biomechanical Engineering*, vol. 138, no. 2, p. 021005, 2016.

[23] T. von Karman and H.-S. Tsien, "The Buckling of Thin Cylindrical Shells Under Axial Compression," *Journal of the Aeronautical Sciences*, vol. 8, no. 8, pp. 303–312, 1941.

[24] J. M. T. Thompson, "Advances in Shell Buckling: Theory and Experiments," *International Journal of Bifurcation and Chaos*, vol. 25, no. 01, p. 1530001, 2015.

[25] P. Seide, V. I. Weingarten, and E. J. Morgan, "The development of design criteria for elastic stability of thin shell structures," tech. rep., Space Technology Laboratories, Inc., Los Angeles, CA, 1960.

[26] J. M. T. Thompson and J. Sieber, "Shock-Sensitivity in Shell-Like Structures: With Simulations of Spherical Shell Buckling," *International Journal of Bifurcation and Chaos*, vol. 26, no. 02, p. 1630003, 2016.

[27] NASA, "Buckling of Thin-Walled Circular Cylinders," tech. rep., NASA Space Vehicle Design Criteria; National Aeronautics and Space Administration, Washington, DC, 1965.

[28] G. J. Lord, A. R. Champneys, and G. W. Hunt, "Computation of localized post buckling in long axially compressed cylindrical shells," *Philosophical Transactions of the Royal Society A: Mathematical, Physical and Engineering Sciences*, vol. 355, no. 1732, pp. 2137–2150, 1997.

[29] G. W. Hunt, M. A. Peletier, A. R. Champneys, P. D. Woods, M. A. Wadee, C. J. Budd, and G. J. Lord, "Cellular buckling in long structures," *Nonlinear Dynamics*, vol. 21, no. 1, pp. 3–29, 2000.

[30] Y. Yoshimura, "On the mechanism of buckling of a circular cylindrical shell under axial compression," tech. rep., National Advisory Committee for Aeronautics, Washington, DC, 1955.

[31] J. Wohlever and T. Healey, "A group theoretic approach to the global bifurcation analysis of an axially compressed cylindrical shell," *Computer Methods in Applied Mechanics and Engineering*, vol. 122, no. 3-4, pp. 315–349, 1995.

[32] J. Horák, G. J. Lord, and M. A. Peletier, "Cylinder Buckling: The Mountain Pass as an Organizing Center," *SIAM Journal on Applied Mathematics*, vol. 66, no. 5, pp. 1793–1824, 2006.

[33] T. Kreilos and T. M. Schneider, "Fully localized post-buckling states of cylindrical shells under axial compression," *Proceedings of the Royal Society A: Mathematical, Physical and Engineering Science*, vol. 473, no. 2205, p. 20170177, 2017.

[34] E. Virot, T. Kreilos, T. M. Schneider, and S. M. Rubinstein, "Stability Landscape of Shell Buckling," *Physical Review Letters*, vol. 119, no. 22, p. 224101, 2017.

[35] S. Gerasimidis, E. Virot, J. W. Hutchinson, and S. M. Rubinstein, "On Establishing Buckling Knockdowns for Imperfection-Sensitive Shell Structures," *Journal of Applied Mechanics*, vol. 85, no. 9, p. 091010, 2018.

[36] J. M. T. Thompson, J. W. Hutchinson, and J. Sieber, "Probing Shells Against Buckling: A Nondestructive Technique for Laboratory Testing," *International Journal of Bifurcation and Chaos*, vol. 27, no. 14, p. 1730048, 2017.

[37] J. W. Hutchinson and J. M. T. Thompson, "Nonlinear Buckling Interaction for Spherical Shells Subject to Pressure and Probing Forces," *Journal of Applied Mechanics*, vol. 84, no. 6, p. 061001, 2017.

[38] J. Marthelot, F. López Jiménez, A. Lee, J. W. Hutchinson, and P. M. Reis, "Buckling of a Pressurized Hemispherical Shell Subjected to a Probing Force," *Journal of Applied Mechanics*, vol. 84, no. 12, p. 121005, 2017.

[39] N. Hu and R. Burgueño, "Tailoring the elastic post-buckling response of cylindrical shells: A route for exploiting instabilities in materials and mechanical systems," *Extreme Mechanics Letters*, vol. 4, pp. 103–110, 2015.

[40] N. Hu and R. Burgueño, "Harnessing Seeded Geometric Imperfection to Design Cylindrical Shells With Tunable Elastic Postbuckling Behavior," *Journal of Applied Mechanics*, vol. 84, p. 011003, 2016.

[41] X. Kuang, J. Wu, K. Chen, Z. Zhao, Z. Ding, F. Hu, D. Fang, and H. J. Qi, "Grayscale digital light processing 3D printing for highly functionally graded materials," *Science Advances*, vol. 5, no. 5, p. eaav5790, 2019.

[42] D. J. Wales, *Energy Landscapes*. Cambridge University Press, Cambridge, 2003.

[43] D. Sheppard, R. Terrell, and G. Henkelman, "Optimization methods for finding minimum energy paths," *The Journal of Chemical Physics*, vol. 128, p. 134106, 2008.

[44] W. Ren and E. Vanden-Eijnden, "A climbing string method for saddle point search," *The Journal of Chemical Physics*, vol. 138, no. 13, p. 134105, 2013.

[45] S. A. Trygubenko and D. J. Wales, "A doubly nudged elastic band method for finding transition states," *The Journal of Chemical Physics*, vol. 120, no. 5, pp. 2082–2094, 2004.

[46] G. Henkelman, B. P. Uberuaga, and H. Jónsson, "A climbing image nudged elastic band method for finding saddle points and minimum energy paths," *The Journal of Chemical Physics*, vol. 113, no. 22, pp. 9901–9904, 2000.

[47] H. Kusumaatmaja, "Surveying the free energy landscapes of continuum models: Application to soft matter systems," *The Journal of Chemical Physics*, vol. 142, no. 12, p. 124112, 2015.

[48] D. J. Wales, M. A. Miller, and T. R. Walsh, "Archetypal energy landscapes," *Nature*, vol. 394, no. 6695, pp. 758–760, 1998.

[49] B. Cox, R. Groh, D. Avitabile, and A. Pirrera, "Modal nudging in nonlinear elasticity: Tailoring the elastic post-buckling behaviour of engineering structures," *Journal of the Mechanics and Physics of Solids*, vol. 116, pp. 135–149, 2018.

[50] H. S. Seung and D. R. Nelson, "Defects in flexible membranes with crystalline order," *Physical Review A*, vol. 38, no. 2, pp. 1005–1018, 1988.

[51] K. Liu and G. H. Paulino, "Nonlinear mechanics of non-rigid origami: an efficient computational approach," *Proceedings of the Royal Society A: Mathematical, Physical and Engineering Sciences*, vol. 473, no. 2206, p. 20170348, 2017.

[52] Hibbitt, Karlsson, and Sorensen, *ABAQUS/Explicit: user's manual, Vol. 1*. Hibbitt, Karlsson and Sorenson Incorporated, 2001.

[53] J. Nocedal, "Updating Quasi-Newton Matrices With Limited Storage," *Math. Comp.*, vol. 35, no. 151, pp. 773–782, 1980.

[54] D. Liu and J. Nocedal, "On the Limited Memory BFGS Method for Large Scale Optimization," *Math. Program.*, vol. 45, pp. 503–528, 1989.

[55] W. E, W. Ren, and E. Vanden-Eijnden, "Simplified and improved string method for computing the minimum energy paths in barrier-crossing events," *The Journal of Chemical Physics*, vol. 126, no. 16, p. 164103, 2007.

[56] M. Taffetani, X. Jiang, D. P. Holmes, and D. Vella, "Static bistability of spherical caps," *Proceedings of the Royal Society A: Mathematical, Physical and Engineering Sciences*, vol. 474, no. 2213, p. 20170910, 2018.

Acknowledgements

H.K. would like to acknowledge EPSRC for funding, Grant No. EP/P007139/1.

Supplementary Materials. Extended discussions for: Harnessing energy landscape exploration to control the buckling of cylindrical shells

Panter J. R.[1], Chen J.[2], Zhang T.[2] and Kusumaatmaja H.[1]

[1]Department of Physics, Durham University, South Road, Durham, DH1 3LE, UK
[2]Department of Mechanical and Aerospace Engineering, Syracuse University, Syracuse, NY 13244, USA

1 Single dimple stability

1.1 Global free energy minima

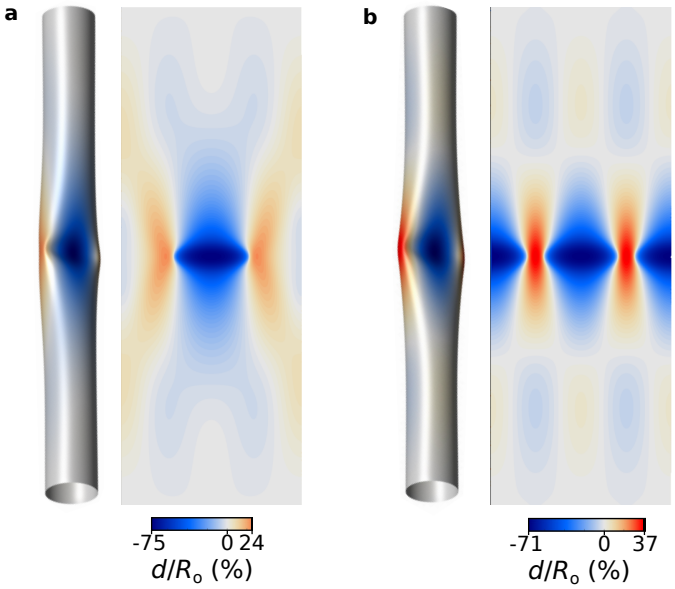

Figure S1: Free energy minima 3D visualisations and radial displacement maps for a cylinder of A_0=10, λ=0.990, and an elastic control ratio = 2.5×10^3. **a** Single dimple. **b** Two dimples.

Across the range of aspect ratios A_0 and shortening ratios λ, it was observed in Fig. 1d (main text) that the singly dimpled state was never the global free energy minimum. For cylinders of low aspect ratio, this observation is explained by the high localisation in both the axial and azimuthal directions, such that multiples dimples may form on the structure which have sufficient spacial separation to not interact. If a single dimple reduces the overall free energy of the system by exchanging stretching contributions for bending contributions, then a second spatially separated dimple reduces the free energy further by an equal amount. Thus, for any system with physical or elastic properties that enable multiple non-interacting dimples to form, the single dimple may never be the global energy minimum.

We next consider the alternative case where multiple dimples interact strongly, an extreme example of which is illustrated in Fig. S1. As will be shown in Fig. S2 and Fig. S3, spatial localisation of a dimple is reduced on increasing A_0 and reducing the elastic control ratio, allowing for multiple dimples to interact over the shell. We therefore aim to probe the single dimple stability at extreme values of A_0 and elastic control ratios. The limit of this investigation is shown in Fig. S1, where A_0=10, λ=0.990, and the elastic control ratio = 2.5×10^3. For reference, a material with Poisson ratio = 0.3 and elastic control ratio = 2.5×10^3 yields a shell with radius to thickness ratio R_0/t=25. The singly dimpled state shown in Fig. S1a exhibits extreme deformation, with a maximum radial displacement of 75% of R_0, and a reduced free energy of E_r=34.8. The free energy is still reduced on forming a second dimple however, shown in Fig. S1b, where E_r=31.9. Overall, over a large range of physically relevant conditions, the singly dimpled state is never the global free energy minimum.

1.2 Self-interaction

The low-λ single dimple stability limit, shown in Fig. 1d (main text), exhibits a non-monotonic variation with A_0 when $A_0 \geq$5. In Fig. S2, we plot the radial displacement of the single dimple about the centre of the cylinder at the low-λ stability limit. It is observed that for A_0=2, the dimple is highly localised in the azimuthal direction, and does not extend around the full circumference. This is shown in Fig. S2(inset) as the radial deformation tending to zero far from the dimple centre. This angular localisation decreases however as A_0 is increased, so that for $A_0 \geq$5, the radial displacement far from the dimple centre is of the order of 1% of R_0. Thus, self-interaction effects modify the single dimple stability for $A_0 \geq$5, leading to the non-monotonic low-λ stability limit on increasing A_0.

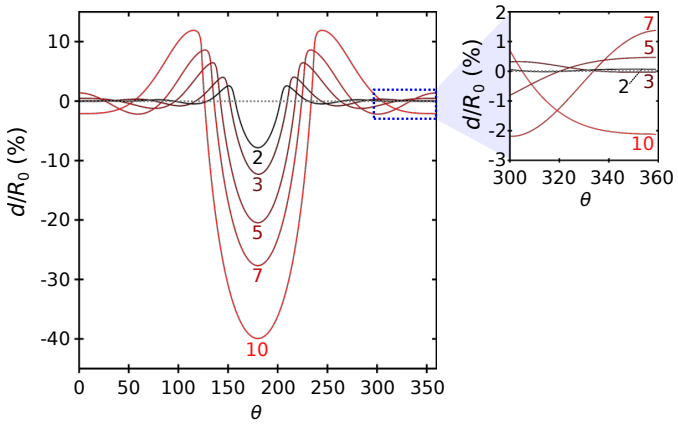

Figure S2: Radial deformation profiles at the large-λ stability limit of the the singly dimpled states, taken about the centre of the cylinder. Each profile is labelled with the corresponding A_0, and for each the elastic control ratio is $2.5{\times}10^5$. Inset: a magnification of the deformation profile far from the dimple centre at $\theta = 180°$.

2 Elastic property effects on the free energy landscape

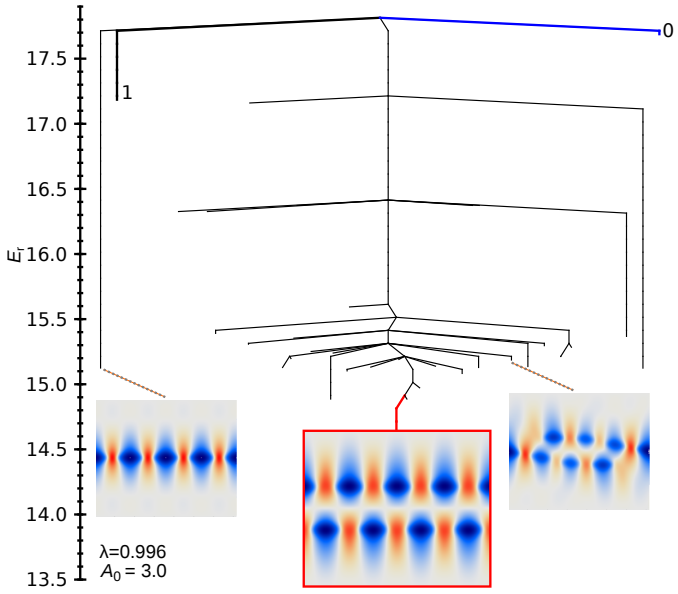

Figure S3: Disconnectivity graph showing the minimum energetic barrier between any pair of states. The unbuckled and global minimum branches are coloured in blue (labelled '0') and red respectively. The global minimum radial displacement field is outlined in red. Representative examples of other minima are also shown. $A_0 = 3.0$, $\lambda = 0.996$, elastic control ratio to $2.5{\times}10^4$. The single dimple branch is labelled '1'.

In Fig. 3c (main text), it was observed that for cylinders of high aspect ratio and thin shell thickness, at compression ratios where the unbuckled, singly dimpled and multiply dimpled states coexisted, the energy landscape became highly complex. This was observed for the cylinder of aspect ratio $A_0 = 3.0$, elastic control ratio $2.5{\times}10^5$, and compression ratio λ=0.999. This complexity was manifest both in the number of minima, $\mathcal{O}(10^3)$, and multiple energy scales over which the landscape was 'rough'. Here, we observe the effect of decreasing the elastic control ratio (equivalent to increasing the shell thickness) on the landscape complexity. In Fig. S3, we illustrate the energy landscape for a cylinder of the same aspect ratio, $A_0 = 3.0$, and use a compression ratio where the unbuckled, singly dimpled and multiply dimpled states also coexist, $\lambda = 0.996$, but decrease the elastic control ratio to $2.5{\times}10^4$. This decrease in the elastic control ratio, equivalent to a thickness increase of $\approx 3{\times}$, has a marked, simplifying affect on the energy landscape. The landscape is transformed from being rough and glassy ($\mathcal{O}(10^3)$ minima, bin population variance = 93), to being funnel-shaped with several deep states($\mathcal{O}(10^1)$ minima, bin population variance = 0.9). The global minimum is a $(2{\times}4)$ diamond pattern, but a deep (1×4) state also exists. At low energies the landscape is dominated by systems with 7 to 8 dimples.

The dominating reason for this pronounced simplification is due to the size of each dimple relative to the cylinder area: whereas 8 dimples pack round the cylinder at the global minimum here, when the elastic control ratio was $2.5{\times}10^5$, 12 were able to do so. The number of dimple arrangements possible on the cylinder here is therefore markedly reduced. It is also instructive to compare Fig. 3b (main text) where $A_0 = 0.8$, elastic control ratio $2.5{\times}10^5$, and compression ratio λ=0.998, with the disconnectivity graph here. In Fig. 3b (main text), the strong confinement introduced by the dimples interacting with the fixed ends caused numerous deep states to exist, as well as for the majority of states to occur in the low-energy region of the landscape. Both of these observations are also made here in Fig. S3, suggesting that by decreasing the elastic control ratio, the dimples are confined by the fixed ends. This is in contrast to the cylinder with $A_0 = 3.0$, elastic control ratio $2.5{\times}10^5$, in which the dimples were weakly confined, giving rise to the glassy landscape.

3 Further analyses of the local probe technique

3.1 Accuracy of the unbuckled-single dimple local probe

In Tables 1 and 2, we compare the transition state energy E_{TS} from the MEP, with that obtained via the local probe technique for the unbuckled-single dimpled transition. In every case tested, the local probe achieves highly accurate estimates of the MEP transition state energy with a small percentage difference between the two (typically of the order of 10^{-3}%). This is consistent with the typical accuracy of

λ	E_{TS}(MEP)	E_{TS}(Probe)	Difference / %
0.9990	7.42679	7.42709	0.00399
0.9989	8.96955	8.96976	0.00236
0.9988	10.66295	10.66329	0.00315
0.9987	12.50415	12.50452	0.00290
0.9986	14.49440	14.49477	0.00257
0.9985	16.63210	16.63242	0.00191

Table 1: Comparision of the unbuckled-single dimpled transition state energy E_{TS}(MEP) for the MEP and local probe technique at different compression ratios λ. All other physical and elastic parameters remain fixed: $A_0 = 2.0$, $k_{\mathrm{stretch}}R_0^2/k_{\mathrm{bend}} = 2.5 \times 10^5$.

A_0	E_{TS}(MEP)	E_{TS}(Probe)	Difference / %
0.8	5.75967	5.75968	0.00007
1.0	7.25528	7.25555	0.00374
2.0	14.49440	14.49477	0.00257
3.0	11.09301	11.09242	-0.00524

Table 2: Comparision of the unbuckled-single dimpled transition state energy E_{TS}(MEP) for the MEP and local probe technique at different aspect ratios A_0. All other physical and elastic parameters remain fixed: $\lambda = 0.9986$, $k_{\mathrm{stretch}}R_0^2/k_{\mathrm{bend}} = 2.5 \times 10^5$.

the local probe: successive increments change the energy by $10^{-5} - 10^{-4}$ close to the transition state.

3.2 Efficacy of multiple local probes

We have shown that the unbuckled-single dimple minimum energy barrier can be accurately accessed through the local probing technique for $A_0 = 0.8$, $\lambda = 0.9986$. In Fig. S4, we investigate whether local probing can access more complex pathways. This is tested via attempting to reproduce the sets of transitions which occur in the multi-step unbuckled-(1×9) pathways. This is attempted for the selected paths A, B, and C. We focus on Path A initially, reproduce in Fig. S4a.

To begin the local probe setup, we must estimate where the dimples will form without prior knowledge of the MEP. It is reasonable to assume the (1×9) state is formed by nine separate dimpling transitions. which are equally spaced around the circumference of the cylinder centre. These locations are labelled in Fig. S4b. A number of choices exist with how to proceed with locally probing at nine locations, regarding in particular: whether the probes are applied individually or in unison, the depth each probe should be tested to, and whether probes should be removed or remain in place after a dimpling event. Here, we choose to test the pathway as simply as possible, in which: (1) A single probe is initiated at radius $R = R_O$; (2) this probe is incremented radially inwards, up to the point where the energy of the system begins to reduce; (3) the system is then relaxed with the probe removed to form a new (dimpled) equilibrium configuration; (4) The next single probe is applied, and steps (1-3) repeated. By selecting the order of the probes, we may access different dimpling pathways. To compare as closely as possible to the MEPs here, we observe the dimpling order in paths A, B, and C, and perform the local probes in this order. The dimpling order is shown for paths A, B, and C, in Fig. S4a,c, and d respectively. The parenthesised pair of dimples in these orders indicate both dimples form in a single transition, but this would not be known *a priori*.

For path A in Fig. S4a, each of the eight separate transitions are labelled **Ai**-**Aviii**, and shown individually magnified. It can be seen that transition **Ai** is well reproduced in both energy and location by the local probe. As the series of transitions proceeds up to **Avii** however, although the local probe is able to accurately capture the transition state energy, the transition state location is obtained with decreasing accuracy. This can be rationalised by observing the movie of path A in Supplementary Movie 1. It can be seen that the dimples shift slightly in their location as the transition proceeds, which cannot be accommodated for in the fixed local probe simulation. In **Aviii**, the local probing technique fails to capture the MEP, as two dimples form in the same transition in the MEP, but not the probing simulation. As can be seen at the end of Supplementary Movie 1, the start of the transition sees one dimple partially form, then the other grows to match it, before both grow together to complete the transition.

For path B Fig. S4c, the nine-point probing scheme departs from the MEP after only two transitions. This is because for this sequence of dimples, a probe applied at one point causes a large shift in the previously-formed dimple locations. Successive probing therefore continues to deviate further from the MEP. The same observation is made later in the pathway for path C in Fig. S4d.

Overall, this multiple local probing scheme is able to closely estimate the minimum energy barrier, but only when: (1) The dimpling event is single-dimpled; (2) the probe does not cause a large shift in previously-formed dimples; (3) the dimple formed by the probe does not undergo a large shift on removal of the probe. This latter point would be particularly challenging to maintain for irregularly dimpled structures, where a best estimate of the probe location may not be readily available.

4 Minimum and barrier distributions in the free energy landscapes

Throughout our disconnectivity graph discussions, two key properties have become useful comparative metrics between different buckling landscapes: the range of minimum energy barrier heights, and the uniformity of minimum distributions. In Fig. S5 (upper panels), we begin by plotting the minimum energy barrier height as a function of the en-

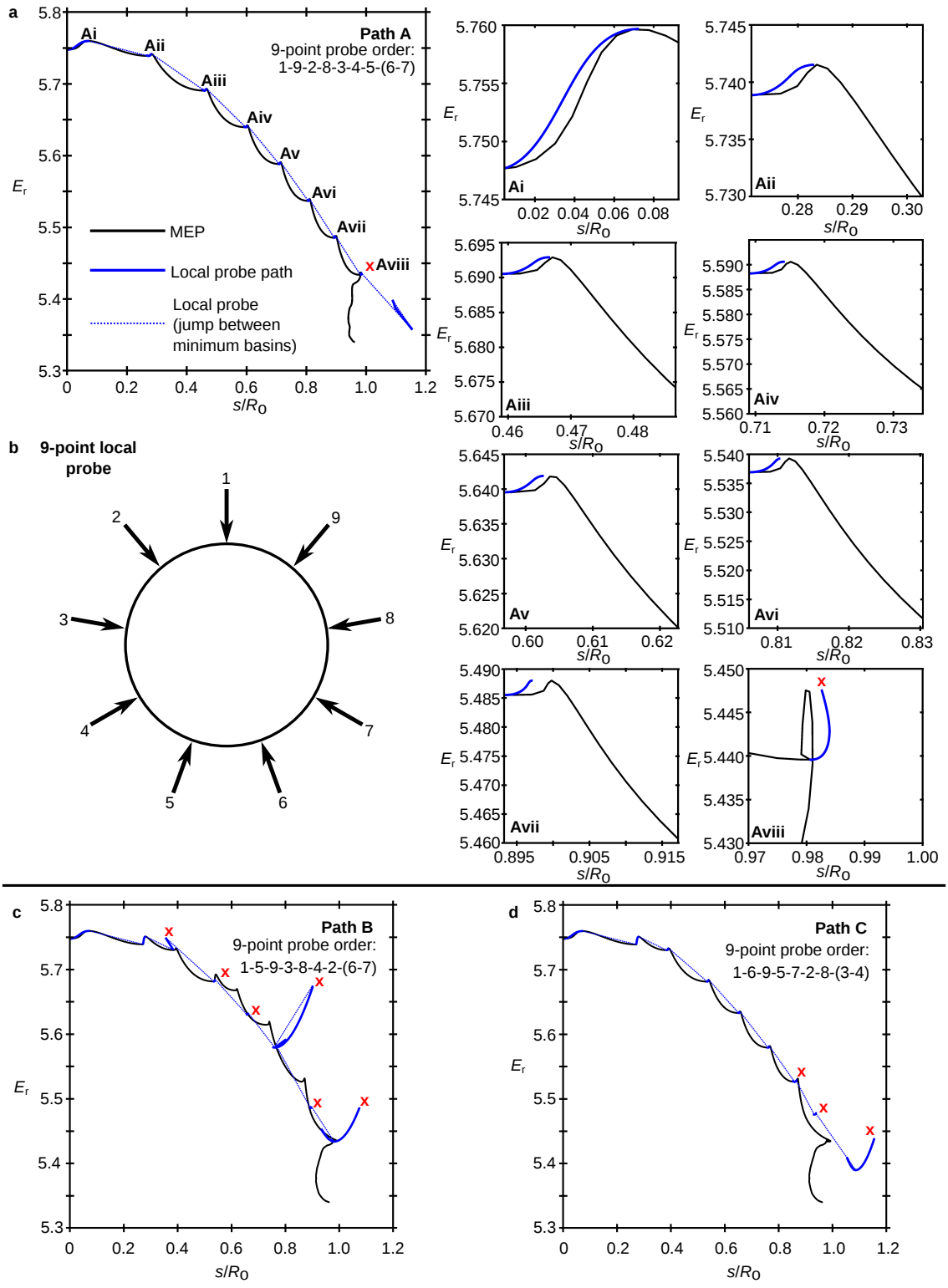

Figure S4: Investigation of the accuracy of multiple local probing at recovering the MEP. **a** Path A: the multi-step unbuckled-(1×9) global minimum energy pathway (black), compared to the nine-point local probing technique (blue). For the probing technique, discontinuous jumps between local basins of attraction are shown as dashed lines. Magnifications of each of the eight dimpling events are shown in **Ai**-**Aviii**. Red crosses indicate where the probing transition does not correspond to the transition in the MEP. **b** Labelling scheme of the nine local probes. **c** Nine-point local probing of Path B, showing early failure. **c** Nine-point local probing of Path C, showing late failure. For all paths, the path distance s measures the distance in the lattice points from the current state to the unbuckled state. The order of the dimpling event is also shown for paths A, B, and C, with parenthesised locations indicating both dimples occur in the same transition.

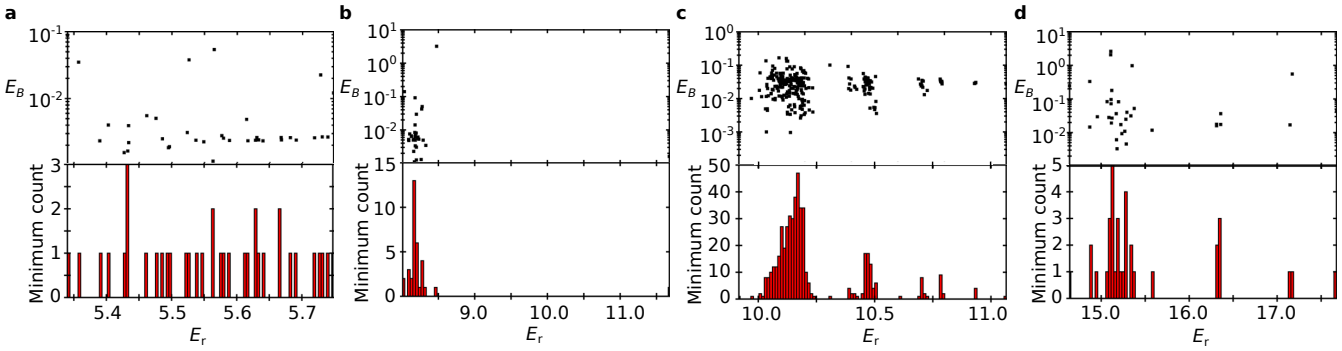

Figure S5: Distributions of minimum energy barriers with stable state energies (top panels), and histograms of state frequency (lower panels) when states are counted within 100 bins over the landscape energy range. **a** $A_0 = 0.8$, λ=0.9986, elastic control ratio 2.5×10^5. **b** $A_0 = 0.8$, λ=0.998, elastic control ratio 2.5×10^5. **c** $A_0 = 3.0$, λ=0.999, elastic control ratio 2.5×10^5. **d** $A_0 = 3.0$, λ=0.996, elastic control ratio 2.5×10^4.

A_0	λ	Control ratio	Barrier range (decades)	Bin count variance
0.8	0.9986	2.5×10^5	1.87	0.38
0.8	0.998	2.5×10^5	3.46	2.1
*3.0	0.999	2.5×10^5	2.24	93
3.0	0.996	2.5×10^4	2.90	0.93

Table 3: Comparative metrics for the four cylindrical systems reviewed. *Analysis performed after clustering.

ergy of each state. The range in barrier energies are shown in Table 3. The deep states exhibited by the $A_0 = 0.8$, λ=0.998; and $A_0 = 3.0$, λ=0.996 systems mean the range of barrier energies for both span approximately 3 decades. This is compared to the 2 decade range in energy barriers for the systems lacking deep states: $A_0 = 0.8$, λ=0.9986; and $A_0 = 3.0$, λ=0.999.

Next, we partition each landscape minimum energy range into 100 bins of equal width, and count the associated number of states within each. These state density distributions are plotted in Fig. S5 (lower panels). Uniquely in our study, for each dimpling configuration in the $A_0 = 3.0$, λ=0.999 system, a number of similarly structured minima exist with small energy barriers to their interconversion. For this reason, we clustered states with the same number of dimples and energy barrier less than 10^{-3}. The uniformity of each distribution is quantified by calculating the variance in the bin populations, listed in Table 3. The glassy landscape of the $A_0 = 3.0$, λ=0.999 system is readily distinguishable from the large population variance, 93. The two roughness scales of the energy landscape also become apparent here: within clusters, barriers of less than 10^{-3} are present, associated with local movement of dimples in the same configuration, whereas the typical energy barrier between clusters is shown in Fig. S5c to be of the order of 10^{-2}.

5 Landscape biasing for targeted design

5.1 General workflow

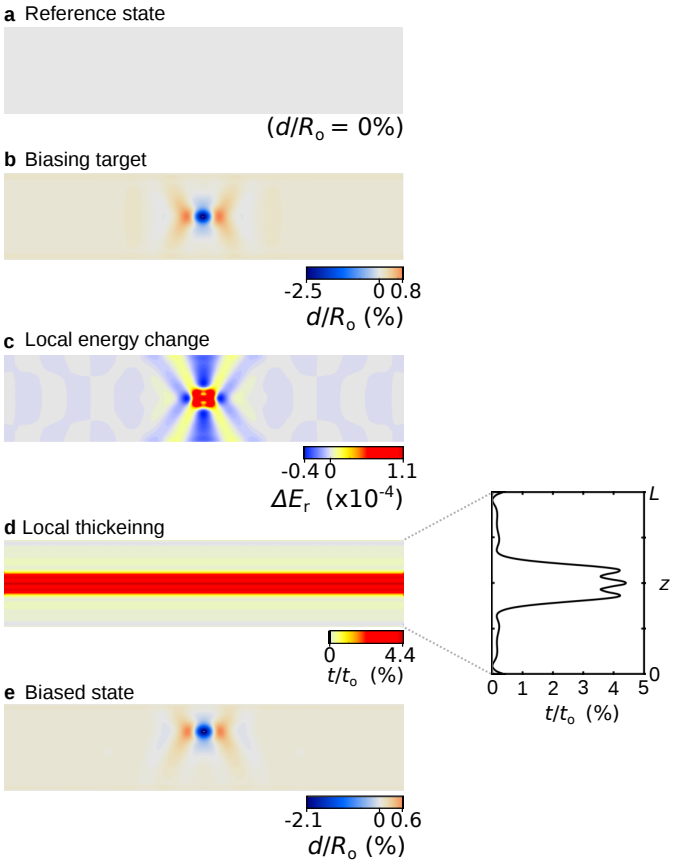

Figure S6: Sequential workflow for the landscape biasing process to design the buckling responses.

The sequence of steps required for landscape biasing is shown in Fig. S6. To begin with, a reference state is chosen which undergoes the target buckling response. The exam-

ple reference shown in Fig. S6a is the unbuckled state for the $A_0 = 0.8$, λ=0.9986 system, with the example biasing target shown as the 0-1 dimple transition state in Fig. S6b.

Next, the elastic potential energy associated with each node, i, in the triangulated mesh is calculated for both the biasing target, $E_{\rm target}(i)$, and the reference $E_{\rm ref}(i)$. The difference,

$$\Delta E(i) = E_{\rm target}(i) - E_{\rm ref}(i), \tag{1}$$

is shown for the biasing example in Fig. S6c.

Numerous choices now exist in using the local energy difference to inform the local thickening. We now demonstrate two example methods: one was used to bias against the 0-1 transition state, and the other for the (1×8) minimum.

To bias against the 0-1 transition state, $\Delta E(i)$ is shifted by the minimum value of $\{\Delta E(i)\}$, then normalised, so that the weighting of element i is expressed:

$$w_i = \frac{\Delta E(i) - \min\{\Delta \mathrm{E(i)}\}}{\sum_i \left[\Delta E(i) - \min\{\Delta \mathrm{E(i)}\}\right]}. \tag{2}$$

The local weights are then used to simulate a local thickening of the elastic shell, so that the ratio of the new thickness of element i, t_i, to the local thickness of the reference state, t_i^o, is

$$\frac{t_i}{t_i^o} = 1 + \alpha w_i, \tag{3}$$

where α is the biasing amplitude, and represents the prescribed fractional increase in mass of the shell, if we make the reasonable assumption that the mass increases in proportion to the simulated shell thickness. For the 0-1 transition state example, we make a preliminary step in which the $\Delta E(i)$ are averaged about the circumference of the cylinder. The resultant local thickening of this treatment, using a biasing amplitude $\alpha = 0.01$, yields the thickening map illustrated in Fig. S6d. The inset shows the z-variation in the local thickening profile.

To bias for the (1×8) minimum, the local weighting w_i is obtained via shifting $\Delta E(i)$ with respect to the average value of $\{\Delta E(i)\}$, and rescaled by the maximum value of $\{|\Delta E(i)|\}$, such that,

$$w_i = \frac{\Delta E(i) - \mathrm{average}\{\Delta \mathrm{E(i)}\}}{\max\{|\Delta \mathrm{E(i)}|\}}. \tag{4}$$

The local thickening ratio, t_i/t_o is then expressed,

$$\frac{t_i}{t_i^o} = 1 - \alpha w_i. \tag{5}$$

This treatment ensures that the total mass increase of the biased cylinder is zero, as $\sum_i w_i = 0$, and the magnitude of the greatest local fractional change in thickness is the biasing amplitude α.

The final step is to transform the local elastic constants to effectively simulate the local thickening. The new local stretching constant between nodes i and j, $k_{\rm ij}^{\rm stretch}$, relative to the local reference constant $k_{\rm o}^{\rm stretch}$ is

$$k_{\rm ij}^{\rm stretch} = \frac{k_{\rm o}^{\rm stretch}}{2}\left[\frac{t_i}{t_i^o} + \frac{t_j}{t_j^o}\right]. \tag{6}$$

Similarly, the new local dihedral bending constant associated with nodes i, j, k, and l, $k_{\rm ijkl}^{\rm bend}$, relative to the local reference constant $k_{\rm o}^{\rm bend}$ is

$$k_{\rm ijkl}^{\rm bend} = \frac{k_{\rm o}^{\rm bend}}{4}\left[\left(\frac{t_i}{t_i^o}\right)^3 + \left(\frac{t_j}{t_j^o}\right)^3 + \left(\frac{t_k}{t_k^o}\right)^3 + \left(\frac{t_l}{t_l^o}\right)^3\right]. \tag{7}$$

The example result of the local thickening treatment for the 0-1 transition state is shown in Fig. S6e: the transition state has been shifted off-centre, increasing the minimum energy barrier.

5.2 Interpolated biasing

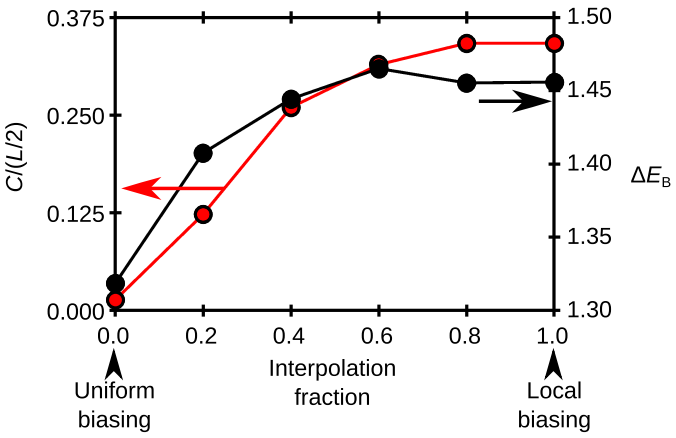

Figure S7: Impact of the biasing localisation on the displacement of the dimple C from the centre of the cylinder length (red data, left axis), and on the energy barrier $\Delta E_{\rm B}$ (black data, right axis).

Upon biasing against the unbuckled-single dimple transition state for the A_0=0.8, λ=0.9986 system, the biased transition state is observed to form off-centre. This displacement is caused by the energetic penalty associated with deforming the locally thickened central region of the cylinder. As it is also energetically unfavourable to deform the cylinder close to the simply supported ends, the dimple is expected to form at a location C between 0 and $L/2$ from the centre of the cylinder. We test the hypothesis that symmetry breaking is caused by local thickening about the centre with the following set of simulations (all at the prescribed 1% mass increase). We begin by testing the energy barrier $\Delta E_{\rm B}$ on the uniformly thickened cylinder, which we assign an 'interpolation fraction' of 0. We then

obtain the energy barriers a series of cylinders with interpolated thickening fields between the uniform cylinder, and the fully biased cylinder (which we assign an interpolation fraction of 1). The dimple position and energy barrier of these interpolations are shown in Fig. S7.

As anticipated, the more localised the biasing is to the centre, the larger the energetic penalty for deforming the centre, so the further away the dimple forms. However, interestingly there is an optimum interpolation fraction between local and uniform, at approximately 0.6. We can rationalise this observation by considering that to maximise the barrier to dimpling, the interpolation fraction should be large enough to force the dimple off-centre, but not so large that the dimple forms in a region of low thickness.

6 Model tests

6.1 Model validation

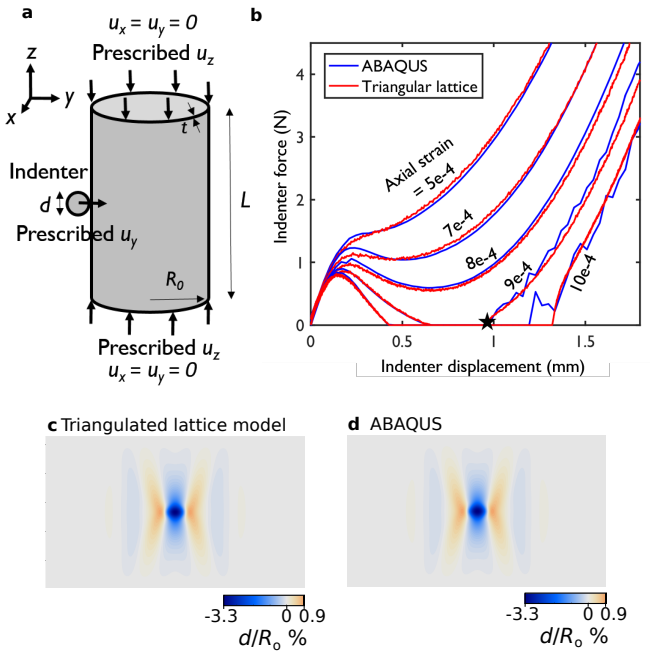

Figure S8: Validation of the triangulated lattice model against ABAQUS. **a** Triangular lattice model for cylindrical shell. **b** Indenting force-displacement curves obtained from ABAQUS and triangular lattice simulations at different axial compressions. **c**, **d** Contour plots of the radial displacement fields at the local energy minima of the axial strain $= 9 \times 10^{-4}$ curves (black star in b)

To verify the triangular lattice model, we first conducted simulations of indenting a cylindrical shell under axial compression [1] using the triangular lattice model and ABAQUS/Explicit [2]. The cylindrical shell has radius $R_0 = 28.6$ mm, length $L_0 = 107$ mm, and thickness t=0.104 mm. It is made of linear elastic material with Youngs modulus $Y = 71000$ N mm^{-2} and Poissons ratio $\nu = 0.3$. The indenter is a rigid sphere with diameter $D = 4.7$ mm. The cylindrical shell is modelled with 4-node shell element (S4R) in ABAQUS. The shell is first compressed axially by assigning a constant velocity at the bottom and top edges. This corresponds to the simply supported boundary conditions for thin shells. After a targeted axial compressive strain is reached, the velocities of the top and bottom edges are set to zeros. The indenter is then approached to the cylinder with a constant velocity perpendicular to the shell surface to generate local probe deformation. (Fig. S8a). Different loading rates are checked to make sure it is a quasi-static process. The indenting force-displacement curves of the triangular lattice model and the shell element in ABAQUS are in agreement, as shown in Fig. S8b. The displacement maps of the dimpled structures are also compared in Fig. S8c,d, and are in agreement to within 2%. Moreover, our simulations captured the instabilities during indentation, which have been reported in experiments [1].

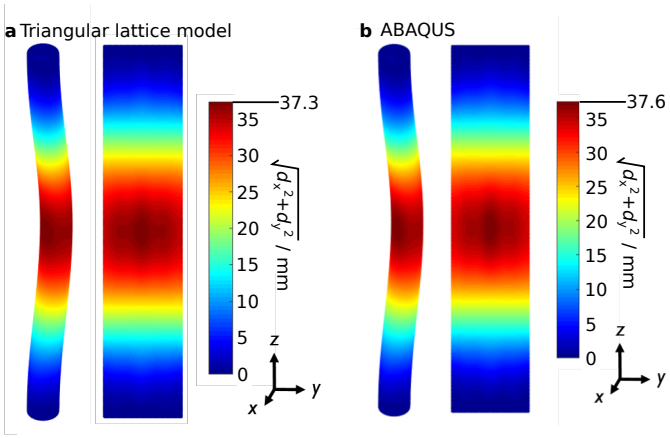

Figure S9: Bending tests for a cylindrical shell of R_0=28.6 mm, L_0=858 mm, t=3.575 mm, Y=71000 N mm^{-2}, and ν=0.3. **a**,**b** Contour plots of lateral deflection fields obtained from ABAQUS and triangular lattice simulations under the an axial strain of 0.024.

We then simulated bending of a slender cylindrical shell under an axial compressive strain slightly above Eulers buckling load of a beam using the same boundary conditions. The comparison between our triangulated lattice model and ABAQUS is presented in Fig. S9. Although there is no constraints for shell edge rotating, the bottom and top surfaces remain flat due to the finite size of the cross section. Therefore we need to apply the "clamped boundary in the framework of beam theory. The parameters for cylindrical shell were chosen to be R_0=28.6 mm, L_0=858 mm, t=3.575 mm, Y=71000 N mm^{-2} and ν=0.3. This makes sure its global (beam bending) buckling strain $\epsilon_{cr}^{\text{global}} = \frac{\pi^2 I}{A(0.5L)^2} \approx 0.0220$ [3] is much smaller than its local (plate bending)

buckling strain $\epsilon_{cr}^{\text{local}} = \frac{t}{\sqrt{3(1-\nu^2)}R} \approx 0.0756$ [4], where I and A are the second area moment and area of cross section. The shell is rst compressed until its axial strain reaches 0.024, slightly above $\epsilon_{cr}^{\text{global}}$. After applying a small indenting force to initiate global buckling, the cylinder relaxes to an equilibrium post-buckling shape, shown in Fig. S9a and b. The lateral deflection fields of both models are in agreement, as shown in S9a and b, with a difference of less than 1% in maximum values.

6.2 Resolution tests

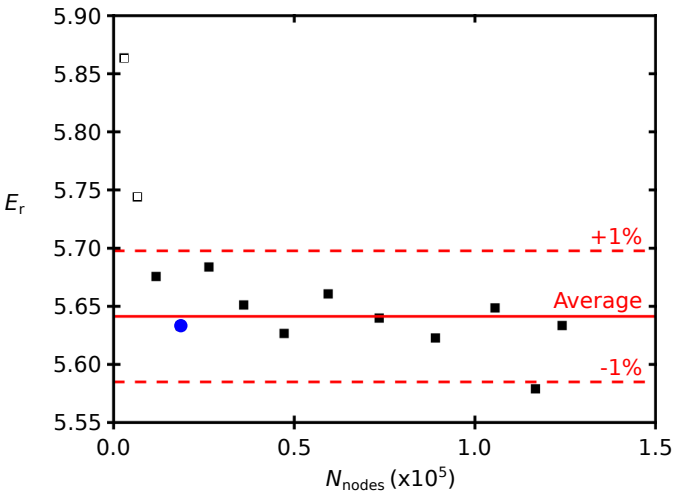

Figure S10: Energy of a multiply dimpled state for A_0=0.8 and λ=0.9986, as computed with meshes using different numbers of nodes, N_{nodes}. The average energy of the filled data is shown in as the red solid line, with ±1% margins shown as the red dashed lines. The N_{nodes} used in this work is plotted as the blue circle.

In Fig. S10, the influence of the triangulated mesh node density on the computed energy is tested. To perform the test, a multiply dimpled state on the A_0=0.8, λ=0.9986 cylinder was chosen. The energy for this state was then calculated using different numbers of nodes, N_{nodes}. Fig. S10 shows for $N_{\text{nodes}} > 10^4$ (filled data), the accuracy of the computed energy cannot be further improved. By averaging the energies of systems with $N_{\text{nodes}} > 10^4$, we show that all meshes produce energies consistent to within ≈1% of this average. The resolution we choose to perform further simulations at is highlighted with a blue circle, balancing accuracy with computational efficiency.

6.3 Generalising the model

In the continuum limit, it has been shown that the effective bending energy of the perfect triangular lattice can be expressed as [5, 6],

$$E_{\text{bending}} = \frac{k_{ref}^{\text{bend}}}{4\sqrt{3}} \int (3H^2 - 8K) dA, \qquad (8)$$

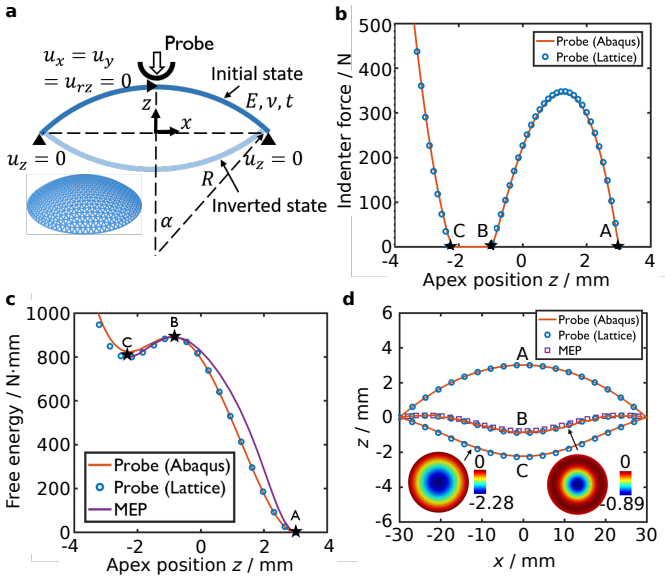

Figure S11: **a** Parameters and boundary conditions in the spherical cap problem. The parameters chosen in our study are Y=71000 MPa, ν=-0.3, t=0.7984 mm, R=151 mm and α=0.2 rad. **b** Indenter force-apex position curves. **c** Free energy profile along the minimum energy path (MEP) connecting the initial state A and inverted state C and passing through the transition state B, compared with the free energy profile along the probe paths . **d** Deformation profiles of the cylindrical cap corresponding to the three states on the MEP.

where H is the mean curvature, and K is the Gaussian Curvature. For a continuum sheet, the bending energy can be written as [6, 7],

$$E_b = \int \left(\frac{1}{2}\kappa H^2 + \kappa_G K \right) dA, \qquad (9)$$

where $\kappa = \left(\frac{Yt^3}{12(1-\nu^2)} \right)$ is the bending rigidity, and the Gaussian rigidity $\kappa_G = -\left(\frac{Yt^3}{12(1+\nu)} \right)$. Y and ν denote Youngs modulus and Poissons ratio respectively.

By comparing Eqs. (8) and (9), the effective Poissons ratio of the triangular lattice is $\nu_{\text{bending}} = -1/3$. It should be pointed out that the in-plane stretching energy and out-of-plane bending energy in the triangular lattice model are decoupled. Therefore the effective Poissons ratio derived from bending energy has no effect on the Poissons ratio in the in-plane deformation, which has been shown to be $\nu_{\text{stretching}}$=1/3 [8].

To show our method can be generalized to other geometries, we consider the buckling of a spherical cap shell shown in Fig. S11a. The undeformed zero-energy shape of the shell is cut from a sphere with radius R, Youngs modulus Y, Poissons ratio ν and thickness t, with angle α between the pole and the edge, represented by the dark blue arc. Its edge is free to rotate but restricted to move within the z=0 plane (u_z=0), and its apex is fixed in the $x-y$ direction

(u_x=u_y=0). For a spherical cap with large enough R/t, when probed with an indenter moving down along the z axis, the shell will snap to an inverted local minimum, represented by the light blue arc, once the indenter displacement reaches a critical value [9].

For the triangular lattice model, we mesh the spherical cap with arbitrarily shaped triangles instead of equilateral triangles in cylindrical shells, as spherical shells cannot be isometrically mapped to simple planar shapes. The corresponding bending energy elastic constants for general triangulated meshes are [10]:

$$k_{\alpha\beta}^{\mathrm{bend}} = \frac{l_{\alpha\beta}^2}{A_\alpha + A_\beta} \frac{Yt^3}{12(1-\nu^2)}, \tag{10}$$

where A_α,A_β are the triangular areas and $l_{\alpha\beta}$ is the length of the shared edge of two triangles. The equilibrium values of the dihedral angle $\theta_{\alpha\beta}^0$ are also computed based on the initial coordinates of the nodes on the spherical cap. To verify the results of triangular lattice model, we also conduct finite element (FE) simulations using shell elements in ABAQUS. It should also be pointed out that we take Poissons ratio ν to be -0.3 in the FE model to match the ratio between Gaussian and bending rigidities in the triangular lattice model. This issue is not a concern in the main text as Gaussian rigidity does not play a significant role in the buckling of cylindrical shells, whose Gaussian curvature is zero. But in our preliminary indenting simulations of spherical caps, the force-displacement curves vary significantly after choosing different Poissons ratios in the continuum model. In principle, the in-plane stretching energy will be also changed when varying Poissons ratios in FE simulation, as the bending and stretching energy are coupled in the continuum model. However, the in-plane stiffness has little influence in the current study because buckling of spherical caps is dominated by bending energy. The parameters chosen in this study are Y=71000 N mm^{-2}, ν =-0.3, t=0.7984 mm, R=151 mm and α=0.2 rad, so that the spherical cap has an inverted local minimum [9]. We first simulate probing the shell with a hemispherical indenter modeled with triangular lattice and finite element in ABAQUS. Fig. S11b compares the indenter force apex position z_a curve of the two methods, and marks in black star the undeformed local minimum A, transition state B and inverted local minimum C. Fig. S11c compares the free energy profiles along the probe paths and the minimum energy path (MEP) connecting A and C obtained by string method. Similar to the unbuckled single dimple transition of cylindrical shells, probing meets the MEP at the transition state B, but does not access the MEP generally. Fig. S11d compares the deformation profiles of the three states obtained by probing and string method. This preliminary work demonstrates that the methodology of integrating triangular lattice model and string method can capture the snap-through buckling of a spherical cap shell. Future work needs to be done to explore the energy barriers and MEP for more complicated buckling states, such as non-axisymmetric modes [9]. In addition, the current triangular lattice has a fixed ratio between Gaussian and bending rigidities, corresponding to a Poissons ratio ν=-0.3. This is also understandable because there is only one parameter associated with bending in the current triangular lattice model, which cannot produce two different bending rigidities independently. It will be of great interests in developing a more general lattice model capable of describing materials with a wide range of Poissons ratios.

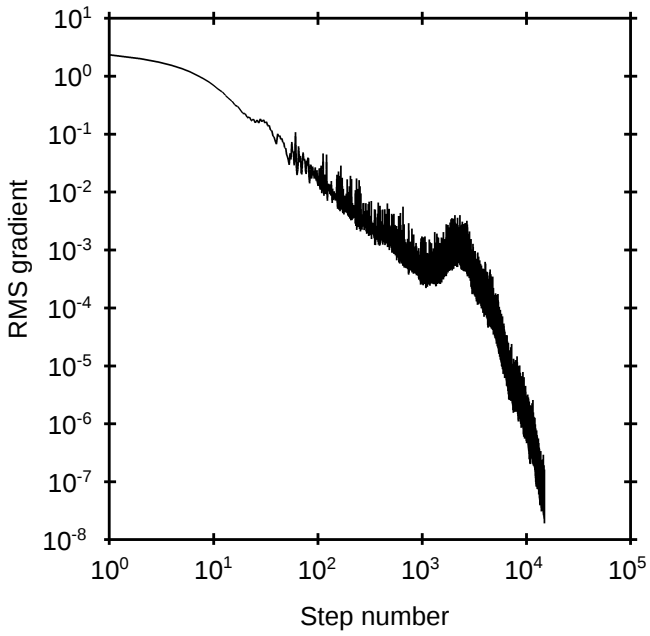

Figure S12: Example convergence of a perturbed cylinder to a buckled state using the L-BFGS algorithm.

7 L-BFGS convergence

We show an example convergence plot in Fig. S12 for the minimisation of a perturbed cylinder to a buckled state using the L-BFGS algorithm. Typically, convergence occurs when the energy change on successive steps is less than 10-11% of the energy of a minimum.

References

[1] E. Virot, T. Kreilos, T. M. Schneider, and S. M. Rubinstein, "Stability Landscape of Shell Buckling," *Physical Review Letters*, vol. 119, no. 22, p. 224101, 2017.

[2] Hibbitt, Karlsson, and Sorensen, *ABAQUS/Explicit: user's manual, Vol. 1*. Hibbitt, Karlsson and Sorenson Incorporated, 2001.

[3] Z. Bazant and L. Cedolin, *Stability of structures: elastic, inelastic, fracture and damage theories*. World Scientific, 2010.

[4] J. W. Hutchinson and J. M. T. Thompson, "Imperfections and energy barriers in shell buckling," *International Journal of Solids and Structures*, vol. 148-149, pp. 157–168, 2018.

[5] B. Schmidt and F. Fraternali, "Universal formulae for the limiting elastic energy of membrane networks," *Journal of the Mechanics and Physics of Solids*, vol. 60, pp. 172–180, 2012.

[6] D. Wan, M. J. Bowick, and R. Sknepnek, "Effects of scars on icosahedral crystalline shell stability under external pressure," *Physical Review E*, vol. 91, no. 3, p. 033205, 2015.

[7] H. Liang and L. Mahadevan, "The shape of a long leaf," *Proceedings of the National Academy of Sciences*, vol. 106, no. 52, pp. 22049–22054, 2009.

[8] H. S. Seung and D. R. Nelson, "Defects in flexible membranes with crystalline order," *Physical Review A*, vol. 38, no. 2, pp. 1005–1018, 1988.

[9] M. Taffetani, X. Jiang, D. P. Holmes, and D. Vella, "Static bistability of spherical caps," *Proceedings of the Royal Society A: Mathematical, Physical and Engineering Sciences*, vol. 474, no. 2213, p. 20170910, 2018.

[10] A. Garg, E. Grinspun, M. Wardetzky, and D. Zorin, "Cubic shells," *Symposium on Computer Animation 2007 - ACM SIGGRAPH / Eurographics Symposium Proceedings, SCA 2007*, pp. 91–98, 2007.